Intramolecular Crosslinking as a Robust Methodology to Manipulate Microphase-Separated Structures of Block Copolymers

A Dissertation for the Degree of Doctor of Philosophy

KODAI WATANABE

Hokkaido University

March, 2020

Acknowledgements

The study presented in this dissertation has been performed under the direction of Professor Toshifumi Satoh, Division of Applied Chemistry, Faculty of Engineering, Hokkaido University, from 2017 to 2020. I would like to express the deepest appreciation to him for his kind instruction, valuable suggestions, and unstinting encouragement throughout the course of this work as well as for his kindness in everything.

I owe my inexpressible gratitude to Assistant Professor Takuya Isono, Division of Applied Chemistry, Faculty of Engineering, Hokkaido University. Since I started this research project when I was in my fourth year in undergraduate school, he has always discussed my research with me and inspired me over and over again. This dissertation would not have been possible without his guidance and persistent help. It was seriously great to be able to spend the first six years of my chemist life with him.

I also would like to show my deep appreciation to Associate Professor Kenji Tajima and Associate Professor Takuya Yamamoto, Division of Applied Chemistry, Faculty of Engineering, Hokkaido University, and Professor Jae-Suk Lee, School of Materials Science and Engineering, Gwangju Institute of Science and Technology (GIST), Korea, for all the meticulous comments, generous support, and fruitful collaborations.

I have greatly benefitted from Professor Hajime Ito, Division of Applied Chemistry, Faculty of Engineering, Hokkaido University, for the AFM experiments, Dr. Hiroaki Mamiya, Quantum Beam Unit, Advanced Key Technologies Division, National Institute for Materials Science (NIMS), for the SAXS experiments, Dr. Yukihiko Kawamura, Neutron Science and Technology Center, Comprehensive Research Organization for Science and Society (CROSS), for the SANS experiments, and Mr. Toshiaki Ito, Electron Microscope Laboratory, Research Faculty of Agriculture, Hokkaido University, for the TEM experiments.

Special thanks goes to Ryoto Tanaka, Satoshi Katsuhara, and Noya Kaizawa. We have discussed the direction and interesting aspects of our works and carried out a lot of experiments together. Although I was sometimes very strict with them, I hope I was of some help. Also, I sincerely hope that they will continuously enjoy the chemist life in their future.

It was definitely my pleasure to meet Brian Jiwon Ree and Hsu Li-Che, my colleagues in the Ph.D program. We have had numerous discussions about our research projects, shared the highs and lows of the doctoral course, and talked about many things as sincere friends. We will walk different paths from now on, but I hope we will make sure to fulfill our own dreams in the future. Also, I thank all the members, including the alumni, of Polymer Chemistry groups and all the students from overseas for having nice

research activities and a vibrant laboratory life. In particular, I appreciate Dr. Kenji Takada, Mr. Takuhiko Matsuno, and Dr. Kohei Yoshida for their generous instructions and support, and Junya Ohba, Eiji Ichinohe, Yusuke Aizawa, Syoichi Takashima, and Tian Lin, my colleagues in the master's course, for their close friendship.

Friends have been an irreplaceable and precious part of my university life. Without "fullness of daily life," I could not have done this big research project. My heartfelt appreciation goes to all of my friends, including friends in Sapporo, friends in my hometown, and friends who I met in the other counties.

This work was supported by the Research Fellowship of Japan Society for the Promotion of Science (JSPS) for Young Scientists during 2017–2019. The SAXS experiment at the Photon Factory (PF) of the High Accelerator Research Organization (KEK) was performed under the approval of the PF Program Advisory Committee (Proposal No. 2017G589 and 2019G579). The SANS experiment at the Material and Life Science Experimental Facility (MLF) of the Japan Proton Accelerator Research Complex (J-PARC) was performed under a user program (Proposal No. 2018B0265).

Finally, I wish to give my thanks and love to my family from the bottom of my heart. Since my elementary school days, I have always looked up to my father, a great researcher and the family breadwinner. I have learned numerous lessons and gained much wisdom from you that have led me to become the man I am today. Now that I have finished this dissertation, I hope I could get closer to you. Without my mother's bottomless love, I could definitely not survive university life. I would like to return the favor to you with this dissertation, the culmination of my nine years of studying chemistry, precisely because I worried and troubled you a lot. As for my two younger brothers, I want to be a big brother who can show you the way to have a vivid dream and make it come true. Why don't we continually inspire and motivate each other based on our brotherhood with the strong bonds?

This is the end of my student life, but it is a new starting line at the same time. I will embark on a new chapter in my chemist life without forgetting to thank everyone who has taken care of me.

March, 2020

Kodai Watanabe

Contents

Chapter 1

General Introduction

1.1 Microphase Separation of Block Copolymer (BCP)

1.1.1 Theory of microphase separation behavior

Block copolymers (BCPs) are macromolecules consisting of two or more chemically distinct polymer segments that are covalently tethered to each other. In this introductory section, the theoretical argument of phase separation behavior (self-assembly) of the simplest AB diblock copolymer, composed of A and B homopolymers linked end to end, will be described, although more complex architectures, such as the ABC triblock terpolymer,[1] starblock copolymer,[2] and bottle-brush BCP,[3] have also been widely studied.

The self-assembling behavior of the BCPs in the bulk and thin film states is dominated by two important factors, *i.e.*, the overall degree of polymerization N (N_A+N_B for AB diblock) and the Flory-Huggins interaction parameter χ (repulsion between unlike segments). When the product χN, referred to as the segregation strength, does not exceed a critical value, the disordered state, where the A and B block chains are mixed on a molecular level, occurs as illustrated in **Figure 1.1**(a). Alternatively, when the χN is sufficiantly large, the segments segregate into A- and B-rich domains forming periodically-ordered nanostructures. Such a local segregation, the so-called "microphase separation", occurs in the BCP system because the chemical junction of the A and B blocks prevents the macroscopic segregation as is the common case in binary mixtures of the homopolymers (**Figure 1.1**(b)). As a consequence, the dimensions of the domains formed by the self-aassembly of the BCPs are on the order of the radius of gyration (R_g) of each block chain (nm-scale).

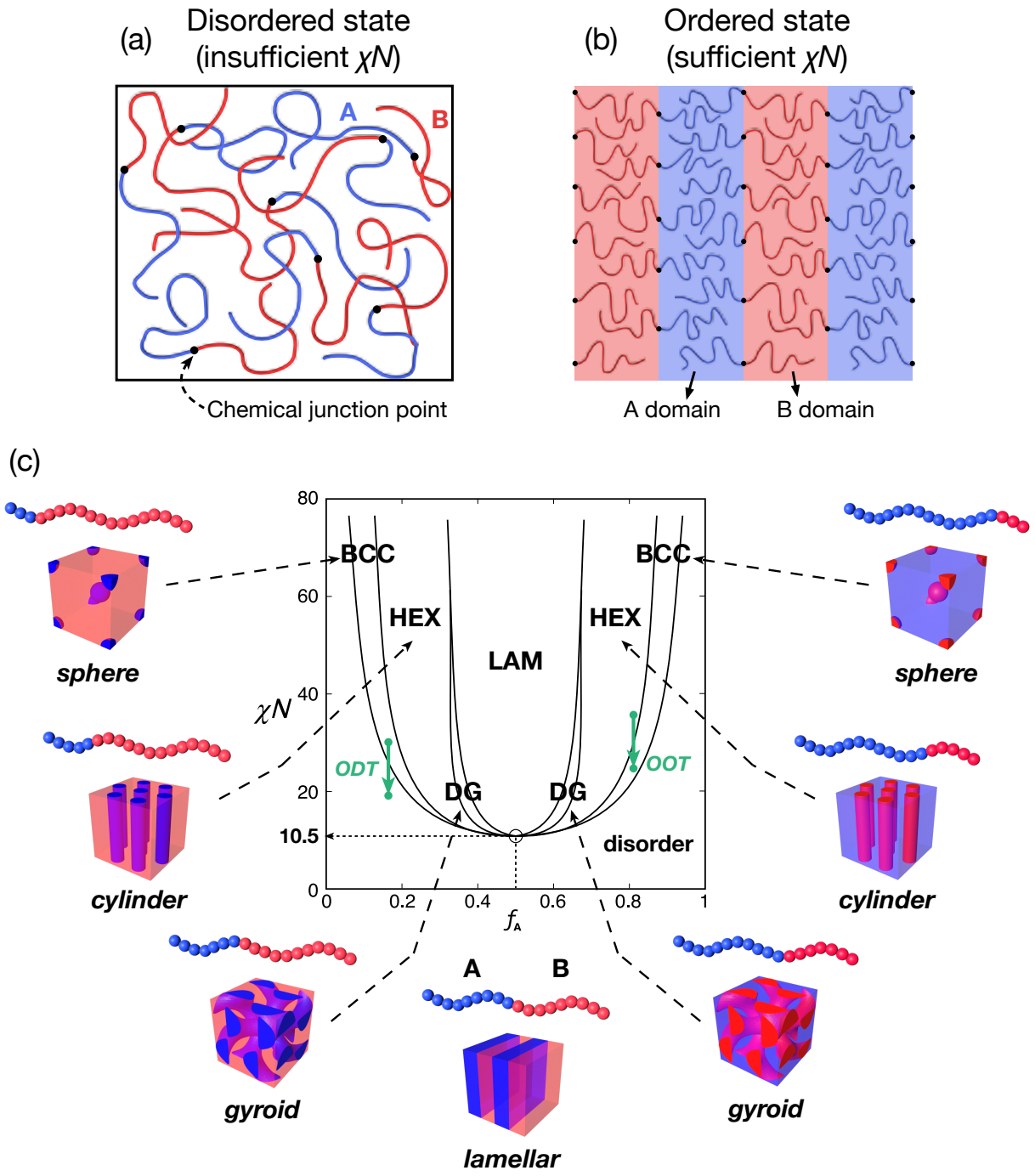

Figure 1.1. Schematic illustration of the BCP chains in the (a) disordered and (b) ordered states. (c) The theoretical phase diagram of AB diblock copolymers constructed based on SCFT. All the typical morphologies (LAM, DG, HEX, and BCC) are schematically represented with the BCP chains having the corresponding volume fraction. The green arrows indicate the order–disorder transition (ODT) and order–order transition (OOT) upon increasing the temperature (decreasing χ).

Figure 1.1(c) shows the classical phase diagram of the AB diblock copolymers constructed by Matsen *et al.* using the self-consistent field theory (SCFT).[4] As can be seen, the various kinds of morphologies are generated by the microphase separation, highly dependent on the volume fraction (*f*) of the blocks. By varying the volume fraction of the A polymer block, f_A, the following common morphologies are observed: lamellar (LAM), hexagonally close-packed cylinder (HEX), body-centered-cubic sphere (BCC), and ordered bicontinuous double gyroid network (DG), wherein the minority and majority blocks form the microdomain and the matrix, respectively. Since χ is inversely proportional to the tempereture ($\chi = a/T + b$, where a and b are system dependent constats and T is absolute temperature), the ordered BCP undergoes the order−disorder transition (ODT) as well as the order−order transition (OOT) by increasing the temperature (decreasing χ and thus χN).[5] It is worth mentioning that the ODT occurs at $\chi N = 10.5$ for the symmetric block composition ($f_A = 0.5$), which is often stated as the representative critical point to achieve the microphase separation. In addition, we shall refer to the regimes corresponding to the situation of $\chi N < 10$ and $\chi N \gg 10$ as the weak segregation limit (WSL) and the strong segregation limit (SSL), respectively.[5] The BCP self-assembly also produces more complex morphologies, such as hexagonally-perforated lamellar (HPL),[6] ordered bicontinuous double diamond network (DD),[7] orthorhombic network having an *Fddd* space group (*Fddd*),[8] and Frank-Kasper phases (σ and A15)[9]; however, these phases are known as metastable states and thus missing from the phase diagram.

1.1.2 BCP lithography

The microphase-separated structures of the BCPs are attracting tremendous interest as promising templates and scaffolds in the nanomanufacturing fields. The various kinds of functional nanomaterials, *e.g.*, filtration membranes,[10] memory devices,[11] nanoporous and mesoporous carbons,[12] photonic crystals,[13] etc.,[14] have been developed due to the variety of morphologies as discussed above and the wide range of achievable sizes (typically 10–50 nm for AB diblock copolymers, which can be extended even over 100 nm by adjusting the BCP architecture). Among these practical technologies, a nanolithographic technique using the self-assembled BCP thin films, the so-called "BCP lithography", is considered as one of the most significant applications contributing to the advancement of the microelectronics industry.

Nanolithography is a technology to fabricate the nanopatterned integrated circuits (ICs), quantum dots, diffraction gratings, etc., which has been conventionally achieved by the photo-lithographic processes with the aid of optical light exposure. However, such "top-down" methods are reaching an intrinsic limitation, *i.e.*, limits of optical diffraction and light wavelength, to achieve sub-30 nm patterns.[15] Although state-of-the-art extreme ultraviolet (EUV) and nanoimprint lithography as well as multiple patterning technique could realize sub-10 nm features, these approaches are arguably high-cost and/or time-consuming. As an alternative "bottom-up" strategy, the BCP lithography technology has been extensively studied over the past two decades because of its promising advantages, such as ultra-small feature size (potentially sub-5 nm), relatively low-cost and simple processing, and high-throughput potential.

The typical line and space (L/S) patterning is accessible with the use of a perpendicularly oriented LAM morphology relative to the underlying substrate as an etching

mask, as illustrated in **Figure 1.2**. However, since the spontaneous formation of the microdomains generally occurs quite randomly, the structural orientation as well as the lateral ordering have to be precisely controlled in the BCP thin film. As a breakthrough approach to fulfill these demands, the directed self-assembly (DSA) technique, where the microdomains are guided to be placed at specific positions on the substrate, has received a great deal of research attention. The DSA principle is generally classified into two methodologies, *i.e.*, graphoepitaxy[16] and chemoepitaxy,[17] wherein the topologically and chemically pre-patterned substrate, respectively, are employed for guiding the self-assembly of the BCPs. Additionally, the perpendicular orientation is also achievable by applying the neutralized layer at the bottom and/or top interface of the thin film,[18] balancing the interfacial affinities of both blocks,[19] and utilizing the solvent vapor annealing.[20] As the BCP needs to satisfy several requirements for successful lithographic processing, the selection of the combination of block segments is quite important. Polystyrene-*block*-poly(methyl methacrylate) (PS-*b*-PMMA, **Figure 1.3**(a))[21] is the most extensively studied material due to several strengths, including facileness to achieve a perpendicular orientation, sufficient etching selectivity to remove the PMMA domain, and production on a pilot-scale. Besides, the other classical BCPs, such as polystyrene-*block*-poly(*rac*-lactide) (PS-*b*-PLA, **Figure 1.3**(b)) [22] polystyrene-*block*-poly(2-vinylpyridine) (PS-*b*-P2VP, **Figure 1.3**(c)), [23] and polystyrene-*block*-poly(dimethylsiloxane) (PS-*b*-PDMS, **Figure 1.3**(d)),[24] were also studied as the candidates with some strong advantages.

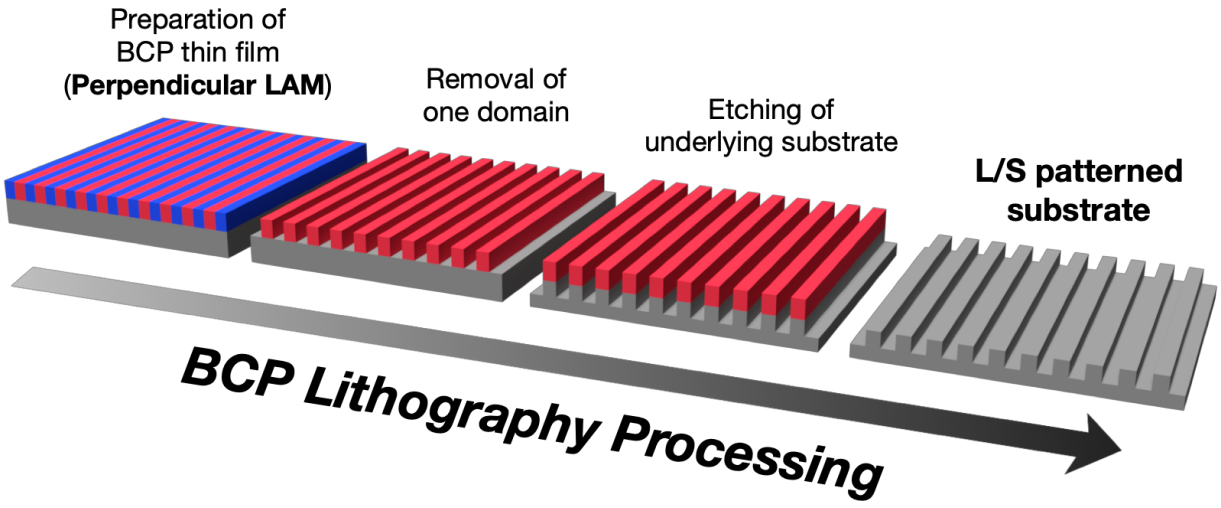

Figure 1.2. Schematic illustration of the BCP lithography processing.

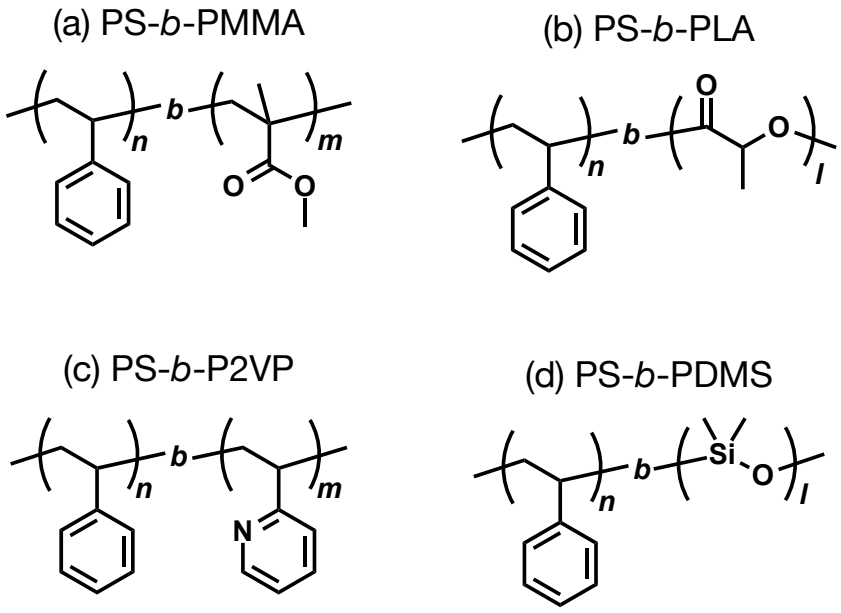

Figure 1.3. The classical BCPs considered as the candidate for BCP lithography.

Despite the significant progress on the related technologies and knowledge, the BCP lithography has yet to see industrial use due to the several unmet practical requirements, such as further downscaling of the nanostructure dimensions,[25] enhancement of the etching selectivity,[26] variation in the patterning geometry,[27] and reduction of structural defects[28] and edge roughness.[29] Although numerous researchers are committed to develop novel solutions to solve these aspects, there is still a gap between the ideal technological level and the current accomplishments.

1.2 Practical Requirements for Advancement of BCP Lithography

1.2.1 Downsizing of feature dimensions

Although the BCP lithography is a promising competitor to the current advanced technologies, such as EUV and nanoimprint lithography as well as multiple patterning, typical microphase-separated structures are still not small enough to satisfy the ever-increasing demand of miniaturization of ICs. Thus, the downsizing of the structure dimensions is considered as one of the nontrivial practical issues. Since the feature size of the microphase-separated structures reflect the R_g of the BCP, the d value could be essentially decreased by reducing the overall N. Yet, this approach is restricted by the limitation regarding the segregation strength; the product χN must be greater than the critical value to ensure the sufficient driving force for the formation of ordered nanostructures as previously described. Due to this limitation, the minimum d value of PS-*b*-PMMA, the current standard material, is around 22 nm[30] whereas a sub-10 nm resolution is generally demanded for next-generation lithography. For achieving the smaller features, therefore, decreasing the N value while increasing the χ value is rationally required. To this end, a number of "high-χ BCPs", such as Si-containing,[31] OH-containing,[32] and oligosaccharides-based[33] BCPs have been developed. However, there are some serious problems with these types of BCPs; only limited pairs of monomers are available for this approach, the high level of repulsion between the blocks commonly cause the difficulty in the structural orientation control in the thin film, and the very low molecular weight of the BCPs result in an insufficient processability.

Thereby, the development of an alternative approach, which is applicable to a wide range of polymers, especially to the usual conventional BCPs, is of significant importance. One such strategy should be reducing the R_g of the BCP by introducing the non-linear

macromolecular architecture without changing the overall molecular weight and composition. Based on numerous previous reports, it has been reported that polymers bearing the cyclic, star (branched), and other non-linear architectures apparently exhibit reduced R_g values compared to linear polymers with the same N.[34] In the pioneering work by Hawker *et al.*, the macrocyclic BCP was found to exhibit a microphase-separated structure with a 25% smaller d value than the linear counterpart (**Figure 1.4**(a)).[35] Importantly, a similar sized nanostructure could not be produced by a linear BCP with half the molecular weight due to the insufficient overall N, highlighting the robustness of such an architectural control approach. According to a recent simulation study, the percentage of d reduction upon cyclization increases up to ca. 35% with the increasing molecular weight of BCP.[36] Furthermore, ours and several other groups reported that the miktoarm star architecture, wherein the A and/or B blocks are branched into some arms, is also effective for decreasing the d value by increasing the branching number while retaining the total molecular weight and block composition (**Figure 1.4**(b)).[37] Thus, the preparation of BCPs with specific chain architectures is a promising strategy for downscaling the dimensions of microphase-separated structures without decreasing the N value.

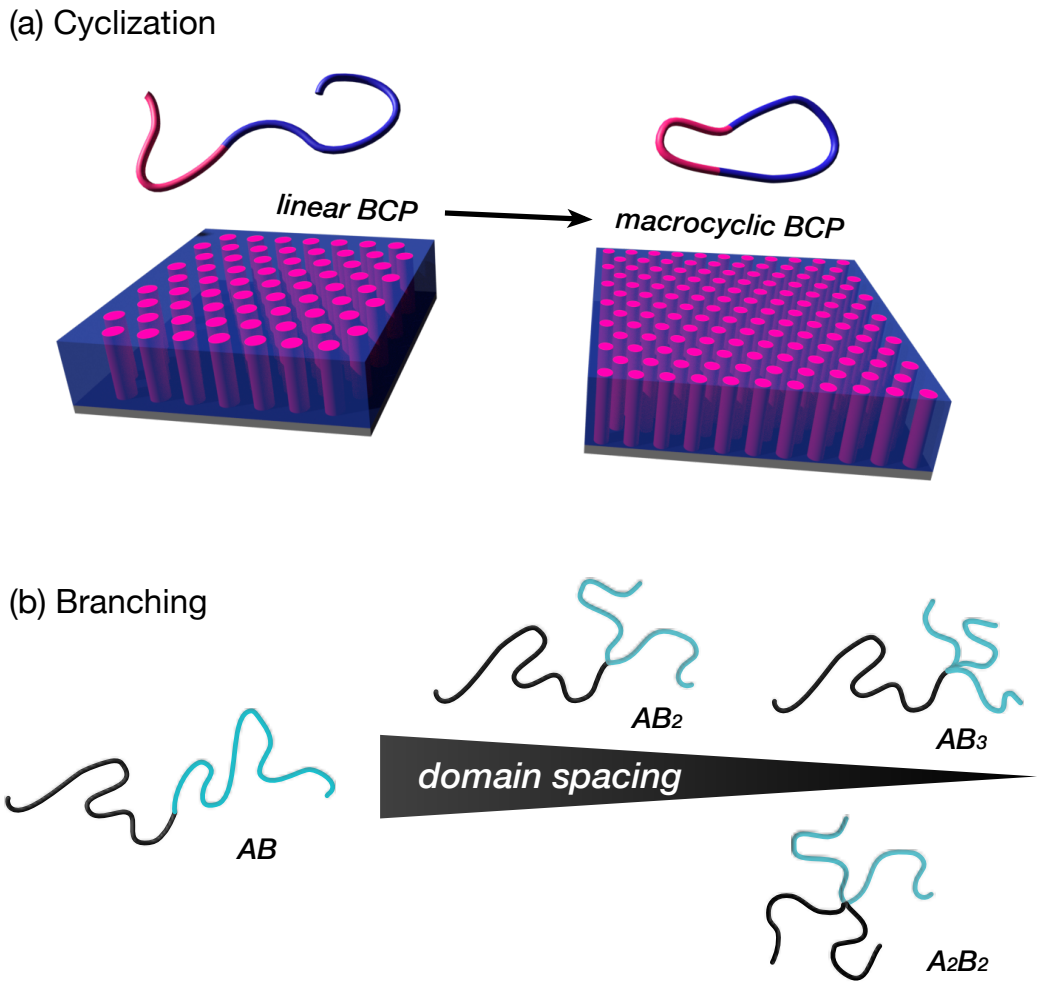

Figure 1.4. Schematic representation of change in the feature size of the microphase-separated structures by introducing (a) cyclic and (b) branched architectures into the BCP molecules.

1.2.2 Pattern diversity and asymmetric lamellar morphology

The pattern geometries created by BCP lithography is typically limited to the holes (and corresponding dots) with the hexagonally close-packed array and the L/S with the width ratio of ca. 1:1 (**Figure 1.5**(a)(b)). This is caused by the fact that only a limited set of morphologies including LAM, HEX, and BCC is available for the lithographic mask application. As can be seen in the current IC design, however, a more diverse pattern geometry is essentially required for the practical devise fabrication. Although a variety of the geometries based on the L/S structure, like bends, jogs, and T-junctions, has been achieved with the aid of chemoepitaxial DSA,[27] the pattern variation via diversifying the fundamental self-assembling morphology is necessary for further advancement of the BCP lithography. As a representative example, Ross *et al.* demonstrated the fabrication of the holes and dots with a square array (**Figure 1.5**(c)) by utilizing the microphase-separated structure of triblock terpolymer.[38]

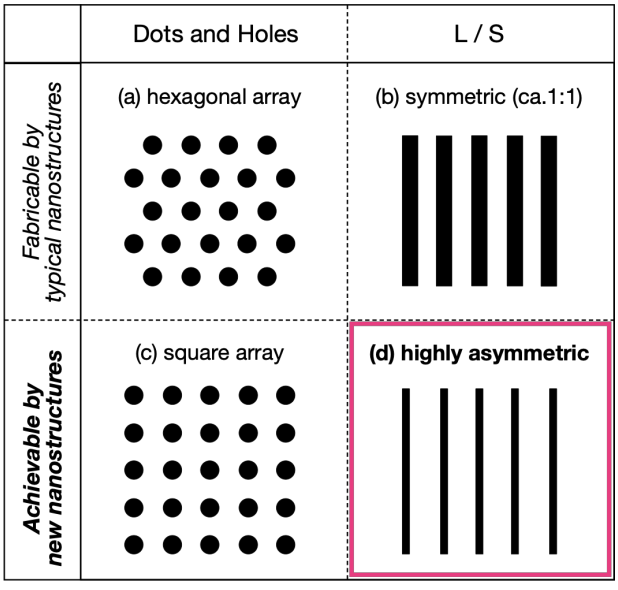

Figure 1.5. Schematic illustration of the representative geometries (dots (and holes) and L/S) created using typical microphase-separated structures (upper) and non-typical ones (lower) via BCP lithography. Fabrication of the highly-asymmetric L/S pattern has not been dedicated.

Among the essential set of geometries required for fabricating an IC, one of the important patterns, especially for logic IC design, should be the highly-asymmetric L/S structure wherein the space width is much larger than the line width (**Figure 1.5**(d)). This particular patterning is accessible by the use of a highly-asymmetric lamellar (A-LAM) morphology. However, since the volume fraction of the BCP is the dominant factor for dictating the morphology of the microphase-separated structures, LAM has merely emerged in the narrow window with an almost symmetric block composition ($f \approx 0.5$). In other words, the curved morphologies, such as HEX and BCC, are formed at the asymmetric block compositions because the interfacial curvature occurs at the microdomain boundary. Consequently, achievement of the A-LAM morphology is quite challenging as long as the BCP is composed of typical linear polymer segments. One of the classical approaches to access the A-LAM is introducing the structural asymmetry into the BCP molecule (molecular asymmetry), by which the interfacial curvature in the nanostructure is dramatically changed. In the phase diagram of the BCPs wherein one block is branched into 5 arms, namely, the AB_5 miktoarm star BCPs, the morphological windows are largely skewed compared to that of typical linear BCPs as a consequence of the molecular asymmetry.[39] Nevertheless, the LAM formation has been observed up to $f \approx 0.8$ despite the remarkable arm number, which is not considered as "highly" asymmetric.

Recently, the achievements of the A-LAM morphologies were demonstrated by introducing a further molecular asymmetry to the BCPs. Lynd *et al*. found that the $A(BA)_3$ miktoarm star BCP could produce the A-LAM morphologies by blending with the A homopolymer even at the extremely high f_A of 0.97 (**Figure 1.6**(a)).[40] On the other hand, Cheng *et al*. designed the BCPs consisting of multiple polyhedral oligomeric silsesquioxane

(POSS) derivatives and long linear PS chain, which in turn produced the A-LAM with the ratio between the widths of the PS and POSS domains up to ca. 5 (**Figure 1.6**(b)).[41] However, these reports were based on the fundamental study of the microphase separation and not intended for practical use in BCP lithoglaphy technology.

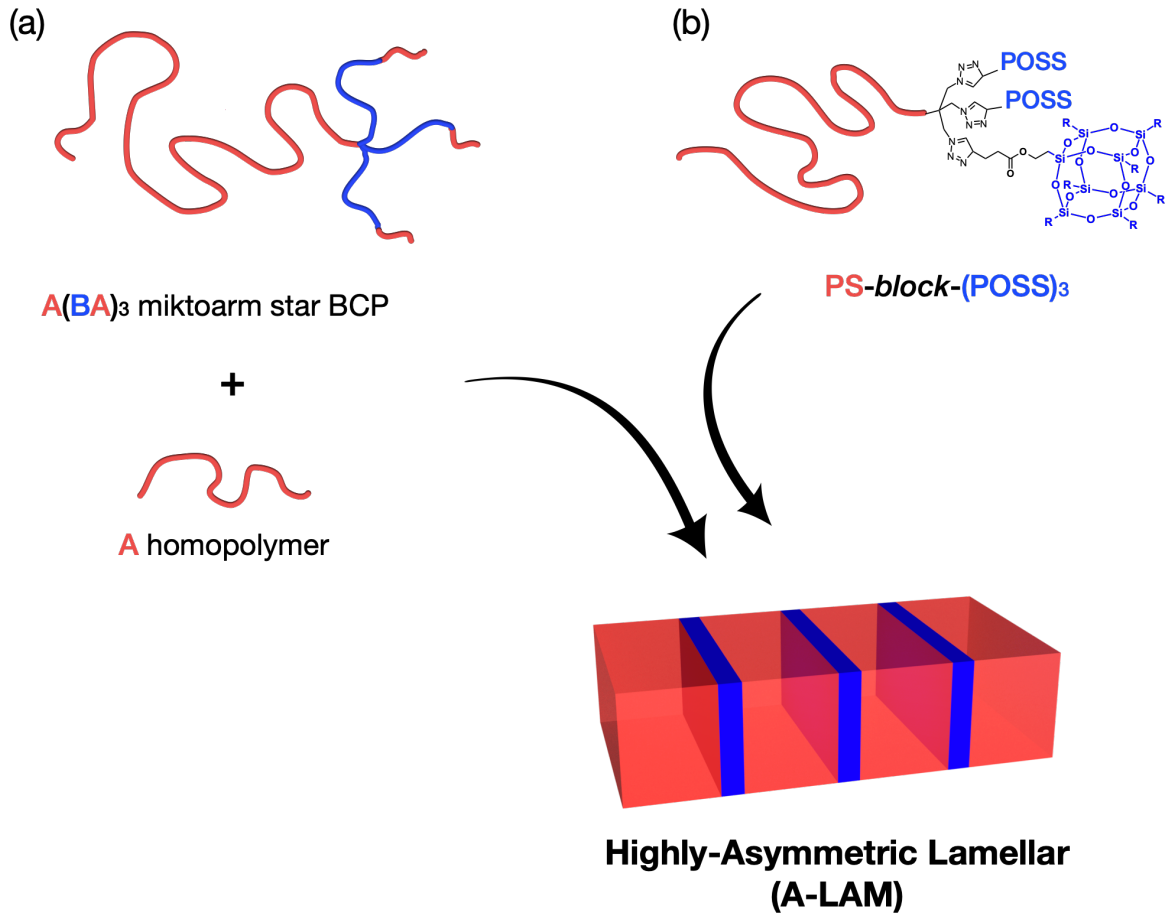

Figure 1.6. Schematic representation of the A-LAM formation by (a) blend of the A(BA)$_3$ miktoarm star BCP and A homopolymer and (b) BCP consisting of the PS chain and three POSS molecules.

When we take the practical applications into account, the important aspects regarding the polymer material should be the easy preparation itself and adjustment of the structural characteristics. Although the miktoarm star BCPs, for instance, are the representatives for solving both of the above issues (Section 1.2.1 and 1.2.2), the arm number (structural characteristics) has to be controlled via a different synthetic pathway as well as the higher-number branched architectures impose a significant synthetic hurdle. Therefore, the development of a novel strategy, which is analogous to the presented ways, such as branching and cyclization, but more suitable for the applicational field is of particular interest.

1.3 Intramolecular Crosslinking Technique

1.3.1 Concept of intramolecular crosslinking

One of the approaches to satisfy both the reduction of the chain dimensions and the introduction of molecular asymmetry into the BCP system should be "polymer chain folding (compaction)". Inspired by the self-folding of the biomacromolecules, such as proteins, the intramolecular crosslinking technique has recently emerged, leading to the novel polymer architecture and the respective properties.[42] The intramolecular crosslinking process is quite simple in principle as follows: a crosslinkable prepolymer, typically prepared via a controlled/living polymerization technique, is diluted much below its overlap concentration (c^*) followed by an individual crosslinking reaction, giving a corresponding product, the so-called "single chain nanoparticle (SCNP)" (**Figure 1.7**). Notably, the intramolecular crosslinking was found to lead to the change in the polymer properties as compared to the linear precursor,[43] such as reduction of the chain dimensions (R_g and hydrodynamic radius, R_h), decrease in the intrinsic viscosity, and increase in the glass transition temperature. Importantly, intramolecular crosslinking has the advantages in not only being a simple procedure itself, but also the capability of controlling the chain dimensions by adjusting the crosslink density.[44]

The intramolecular cross-linking technique was first reported by Kuhn and Majer in 1956.[45] Since then, a variety of highly-efficient covalent cross-linking chemistries has been applied to generate SCNPs from the linear prepolymers possessing the corresponding cross-linkable functionalities.[46] For a representative example, the copper-mediated azide-alkyne click reaction has been reported as a facile and robust strategy of intramolecular cross-linking by several researchers (**Figure 1.8**(a)).[47] Although the covalent bonding has

been broadly studied, non-covalent interactions, such as hydrogen bonding[48] and metal complexation[49], are also capable of synthesizing SCNPs. Meijer *et al.* demonstrated the single chain compaction of a polymer by the 2-uriedopyrimidinone (UPy) dimerization system involving the deprotection and the formation of strong quadruple hydrogen bonds (**Figure 1.8**(b))[50].

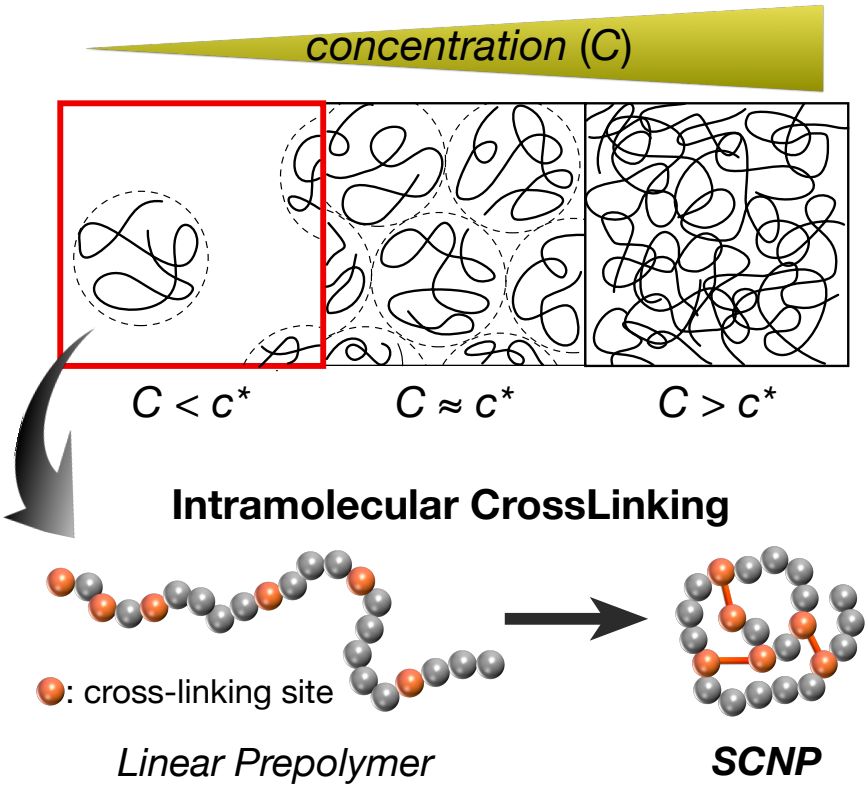

Figure 1.7. Schematic representation of the concept of intramolecular crosslinking.

(a) copper-mediated azide-alkyne click reaction

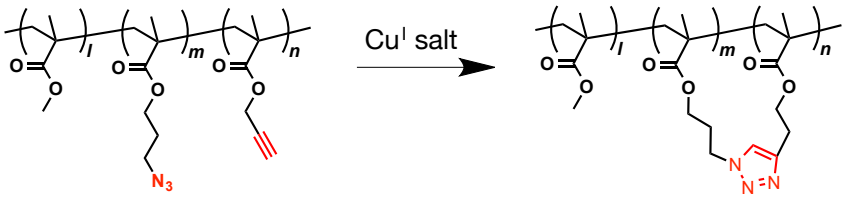

(b) UPy dimerization

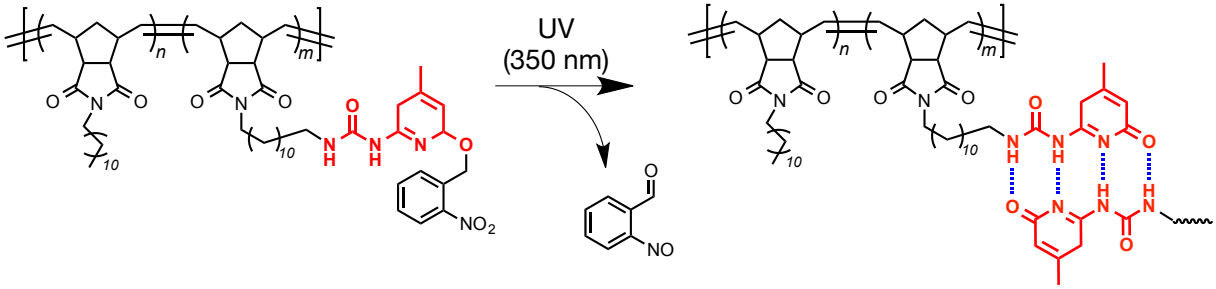

Figure 1.8. Representative examples of the intramolecular crosslinking via (a) covalent bond and (b) non-covalent reaction.

Recent research focus in this field is being transferred to the discovery of the practical uses of SCNPs, for instance, catalytic nanoreactors[51] and photosensitive agents[52]. In addition, some advanced studies on fabricating unusual polymer architectures, such as the intramolecularly-crosslinked cyclic polymer[53] and BCPs[54] as well as a polymer with multiple crosslinked compartments[55], have been reported, which would create new opportunities for the intramolecular crosslinking applications.

1.3.2 Application for BCP ystem

Expanding the intramolecular crosslinking technique to the BCP system should be capable of opening novel vistas in the BCP science due to the unusual molecular architecture of the resultant products. The simplest example should be the diblock copolymer consisting of an intramolecularly crosslinked segment and a linear one, namely, the crosslinked–linear BCP, as first reported by Hawker *et al*.[56] The crosslinked–linear BCPs are typically prepared with the simple synthetic pathway, involving the synthesis of the linear diblock copolymer incorporating crosslinkable moieties in one block segment and the following intramolecular crosslinking (**Figure 1.9**). Interestingly, some research groups have demonstrated the interesting self-assembling behavior of the crosslinked–linear amphiphilic BCPs in certain solvent media. For instance, it was revealed that their micellization behavior was similar to the small molecular surfactant system rather than that of typical linear–linear amphiphilic BCPs.[57] This phenomenon should result from the fact that the crosslinked segment should undergo a less conformational change and chain entanglement during self-assembly as compared to the linear one. Furthermore, the intramolecularly crosslinked nature was also found to impact the resulting self-assembled morphologies. Chen *et al.* successfully demonstrated the unusual morphological variation, *i.e.*, tubular assemblies, bowl-like particles, saddle-shaped lamellar, and typical sphere, upon varying the degree of crosslinking as well as the block composition.[58] It is worth mentioning that these unique self-assembling behaviors of the crosslinked–linear amphiphilic BCPs absolutely arose from their molecular asymmetry and the unique properties. Therefore, the intramolecular crosslinking technique is of significant interest for fine-tuning and diversifying the BCP self-assembling behaviors.

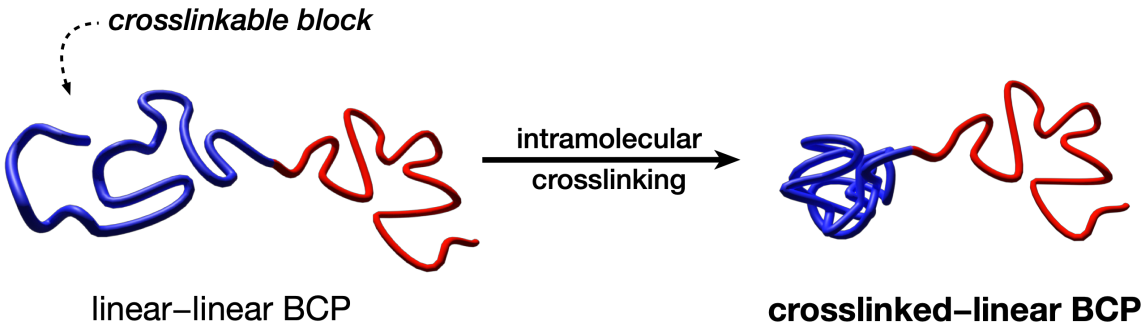

Figure 1.9. Schematic representation of the preparation of the crosslinked–linear BCP.

Quite recently, the crosslinked–crosslinked BCPs, in which two block segments are separately crosslinked or folded, have been synthesized by utilizing the two distinct crosslinking or self-folding chemistries. Sawamoto *et al.* demonstrated the synthesis of the amphiphilic random (A/C–B/C) BCPs, wherein two disparate hydrophobic monomers (A and B) were incorporated into the different blocks while a hydrophilic one (C) was distributed along the entire chain, and subsequent intramolecular self-folding in water (**Figure 1.10**(a)).[59] The resulting single-chain products surely bore the double-core structure, which was an innovative achievement to provide a new possibility for single-chain polymer design. More importantly, Chen *et al.* discovered that the crosslinked–crosslinked BCPs could self-assemble into nanostructured aggregates with an ultra-small periodicity (ca. 4 nm) under certain solvent conditions, indicating the promising potential of the intramolecularly crosslinked BCPs to generate the unusual assembled nano-objects (**Figure 1.10**(b)).[60]

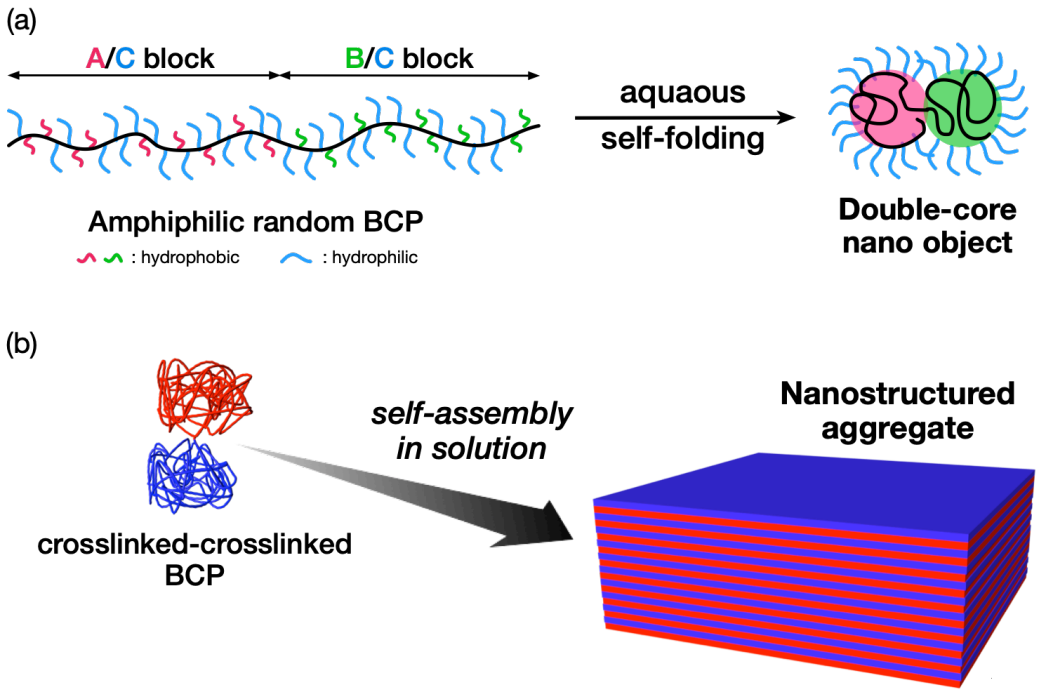

Figure 1.10. Schematic representation of (a) self-folding of A/C–B/C amphiphilic BCPs in water and (b) self-assembly of the crosslinked–crosslinked BCP into the ultra-small nanostructure in the solution state.

As just described, the application of the intramolecular crosslinking to the BCP system has recently been started, which could potentially provide some knowledge about the BCP self-assembly as yet undiscovered. However, none of the previous reports have addressed the self-assembling system of the intramolecularly crosslinked BCPs in the bulk and the thin film state, *i.e.*, microphase-separation, and also intended for the technological applications.

1.4 Objective and Outline of the Dissertation

"Bottom-up" BCP lithography has received substantial attention as a next-generation technology to replace the conventional "top-down" photo-lithography, as mentioned in Section 1.1.2. As a consequence of prolonged research efforts over the last two decades, the significant knowledge about microphase separation and the advanced technologies, represented by DSA techniques, have been remarkably built-up. The practical applications, however, are not widely realized due to several unmet requirements, including further downsizing of the feature dimensions and fabrication of the highly-asymmetric L/S patterns. Although the tiny-sized microphase-separated structures were recently achieved as a result of numerous research studies for developing "high-χ and low-N" BCP systems, the alternative approach for downscaling without changing the molecular weight is of significant importance for practical use. On the other hand, the fabrication of the A-LAM morphology, which is capable of fabricating the asymmetric L/S, has not been dedicated, representing the new research area especially for the BCP lithography field. The now highlights the intramolecular crosslinking technique, as described in Section 1.3.1., to propose the novel solution which can overcome both of the above demands. In order to successfully introduce the intramolecularly crosslinked structure into the BCP molecules, the olefin metathesis reaction was selected as a highly efficient and facile crosslinking chemistry in the presented study.[61] Thereby, the primary objective of this dissertation is the establishment of the "intramolecular olefin metathesis" protocol, which could be accomplished by the extensive study with the homopolymer system. The established method was then extended to the BCP system to investigate the as-yet-unrevealed microphase separation behaviors of the intramolecularly crosslinked BCPs. PS-*b*-PLA, one of classical BCPs, was employed as a

model case through this dissertation because of its strengths for BCP lithographic processing, *i.e.*, a sufficiently high χ to achieve small features,[22(a)] capability to form perpendicular morphologies,[22(c),62] and easy removal of the PLA domain.[22(b),63] Since the intramolecularly crosslinked polymers exhibit reduced chain dimensions analogous to the macrocyclic ones emphasized in Section 1.2.1, the size of the resulting microphase-separated structures of the intramolecularly crosslinked BCPs would be dramatically decreased. In addition, the combination of the typical l inear segment and the crosslinked one could provide a sufficient molecular asymmetry to BCPs in terms of both topology and property, suggesting the promising potential to skew the phase diagram like the miktoarm star BCPs discussed in Section 1.2.2. The goal of this dissertation, therefore, is to demonstrate that the application of the intramolecular crosslinking to the BCP system is an effective and striking way to overcome two important issues, *i.e.*, downsizing of microphase-separated structures and fabrication of A-LAM structures.

An outline of this dissertation is as follows:

Chapter 2 describes the comprehensive examination of the synthesis of SCNPs from the statistical copolymers of *n*-butyl methacrylate (BMA) and 3-butenyl methacrylate (3BMA), *i.e.*, P(BMA-*co*-3BMA)s, via the intramolecular olefin metathesis reaction under a highly diluted condition. The olefin metathesis reaction of P(BMA-*co*-3BMA) using the Grubbs 2nd generation catalyst (G2) in CH_2Cl_2 efficiently gave the corresponding SCNPs under mild conditions. The author achieved the size-controlled synthesis of the SCNPs by adjusting the following factors: (1) the olefin content in the precursor, (2) the molecular weight of the precursor, and (3) the solvent quality of the reaction medium. Furthermore, the above-established intramolecular olefin metathesis approach was successfully applied to the poly(acrylate), poly(ester), and poly(styrene-*block*-methacrylate) precursors, which proved the versatility of the present approach (**Figure 1.11**).

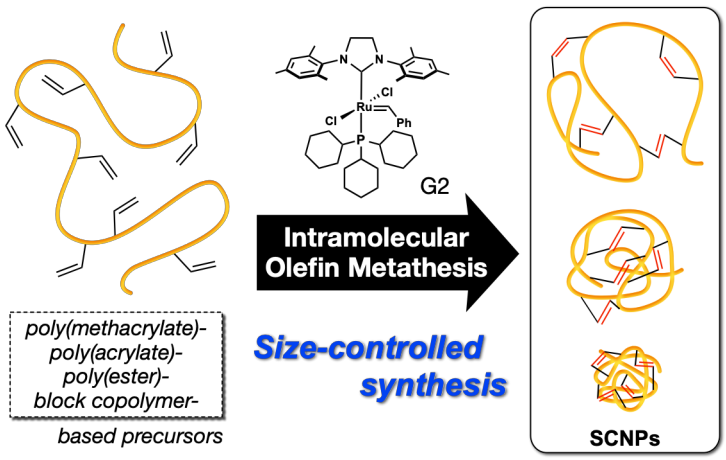

Figure 1.11. Schematic representation of the size-controlled synthesis of the SCNPs from various kinds of olefin-containing prepolymers via the intramolecular olefin metathesis reaction.

Chapter 3 describes a novel strategy for downsizing the feature of the microphase-separated structures via intramolecular crosslinking of BCPs without changing the molecular weight. A series of the BCPs with one olefin-containing-block; i.e., poly[styrene-*st*-(*p*-3-butenyl styrene)]-*block*-poly(*rac*-lactide) (SBS–LA), was subjected to the Ru-catalyzed olefin metathesis under highly diluted conditions to produce the crosslinked–linear BCPs (SBS(*cl*)–LAs) (**Figure 1.12**). Small-angle X-ray scattering (SAXS) measurements and transmission electron microscopy observations of the SBS(*cl*)–LAs revealed the featured size reduction in the LAM and HEX structures in the bulk state, which was surely due to the restricted chain dimensions of the intramolecularly crosslinked SBS block. Notably, the degree of the size reduction was controllable by varying the crosslink density with a maximum decrease of 22% in the LAM spacing. In addition, we successfully observed the downsizing of the HEX structure in the thin film state using atomic force microscopy (AFM), indicating the applicability of the present methodology as the next-generation lithography technology.

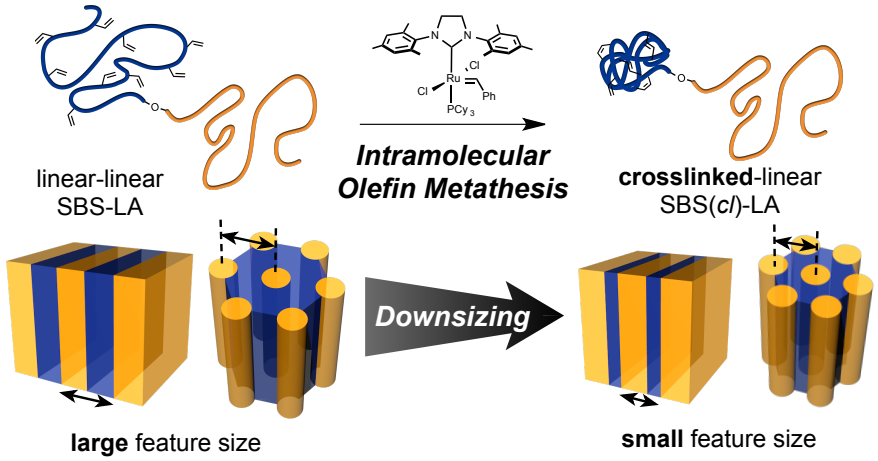

Figure 1.12. Schematic representation of the downsizing of the microphase-separated structures via intramolecular olefin metathesis of the BCPs with one crosslinkable block.

Chapter 4 describes the "one-shot" intramolecular crosslinking of the BCP bearing the olefin side-chains in both blocks aimed at further downsizing the microphase-separated structure (**Figure 1.13**). The intensive solution studies clearly revealed not only the compact conformation, but also the compartmentalized block localization of the resulting intramolecularly crosslinked product, which was highly reminiscent of the Janus particles. Strikingly, the bulk microphase-separated structure of the obtained Janus particle-like product was found to be 47% smaller as compared to that of the linear prepolymer, representing the unprecedented potential of the one-shot intramolecular crosslinking to downsize the microphase-separated structures.

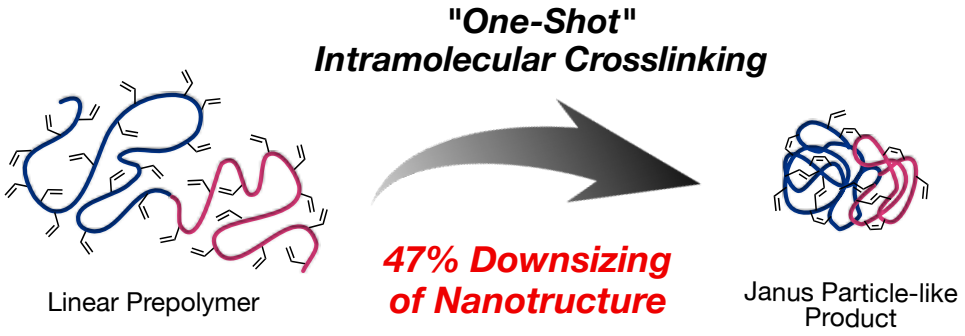

Figure 1.13. Schematic representation of one-shot intramolecular crosslinking of the BCP bearing crosslinkable olefin in a whole chain to further downsize the microphase-separated structure.

Chapter 5 describes the comprehensive study on the microphase separation behavior of the compositionally asymmetric SBS(*cl*)–LAs, in which the molecular weight of the linear LA block is much larger than that of the crosslinked SBS(*cl*) one. The phase diagram was constructed on the basis of the SAXS results in the bulk, which clearly demonstrated the astonishing capability of the SBS(*cl*)–LAs to form the A-LAM morphology even with the

considerably high volume fraction of the linear LA block (F_{LA}) (**Figure 1.14**). This unusual phase behavior arguably arose from the bulky and stiff conformation of the intramolecularly crosslinked SBS(*cl*) block. Significantly, the author successfully produced the perpendicularly-oriented A-LAM morphology in the thin film with the aid of the neutral underlayer, which was confirmed by grazing incidence SAXS and AFM. An intensive morphological study in both the bulk and thin film states thus revealed the promising potential of the crosslinked–linear BCPs as a candidate material for the asymmetric L/S fabrication in the BCP lithography.

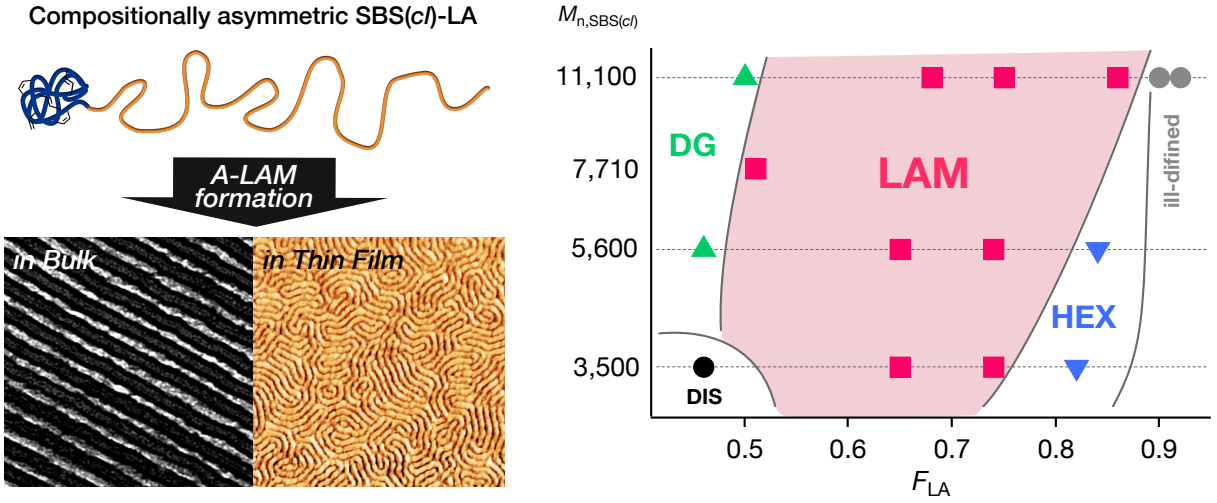

Figure 1.14. Schematic representation of the A-LAM formation by the compositionally asymmetric SBS(*cl*)–LA and its phase behaviors depending on F_{LA} and the molecular weight of the SBS(*cl*) block ($M_{n,SBS(cl)}$).

The concluding Chapter 6 summarizes the established intramolecular olefin metathesis methodology and the microphase separation behavior of the intramolecularly crosslinked BCPs.

1.5 References

1. (a) Cochran, E. W.; Morse, D. C.; Bates, F. S. Design of ABC Triblock Copolymers near the ODT with the Random Phase Approximation. *Macromolecules* **2003**, *36* (3), 782–792. (b) Bates, F. S.; Hillmyer, M. A.; Lodge, T. P.; Bates, C. M.; Delaney, K. T.; Fredrickson, G. H. Multiblock Polymers : Panacea or Pandora's Box? *Science* **2012**, *336* (6080), 434–440. (c) Aissou, K.; Kwon, W.; Mumtaz, M.; Antoine, S.; Maret, M.; Portale, G.; Fleury, G.; Hadziioannou, G. Archimedean Tilings and Hierarchical Lamellar Morphology Formed by Semicrystalline Miktoarm Star Terpolymer Thin Films. *ACS Nano* **2016**, *10* (4), 4055–4061. (d) Ge, H.; Zhang, F.; Huang, H.; He, T. Interplay between Stereocomplexation and Microphase Separation in PS-*b*-PLLA-*b*-PDLA Triblock Copolymers. *Macromolecules* **2019**, *52* (3), 1004–1012.
2. (a) Matsen, M. W.; Schick, M. Microphase Separation in Starblock Copolymer Melts. *Macromolecules* **1994**, *27* (23), 6761–6767. (b) Wang, Y.; Zhong, M.; Park, J. V.; Zhukhovitskiy, A. V.; Shi, W.; Johnson, J. A. Block Co-PolyMOCs by Stepwise Self-Assembly. *J. Am. Chem. Soc.* **2016**, *138* (33), 10708–10715. (c) Seo, Y.; Jang, S.; Ahn, S.; Mishra, A. K.; Kim, J. K.; Lee, W. B. Phase Behavior of 18-Arm Star-Shaped Polystyrene-*block*-Poly(methyl Methacrylate) Copolymers with Different Second Block Initiations. *Macromolecules* **2018**, *51* (7), 2750–2755.
3. (a) Xia, Y.; Olsen, B. D.; Kornfield, J. A.; Grubbs, R. H. Efficient Synthesis of Narrowly Dispersed Brush Copolymers and Study of Their Assemblies: The Importance of Side Chain Arrangement. *J. Am. Chem. Soc.* **2009**, *131* (51), 18525–18532. (b) Rzayev, J. Synthesis of Polystyrene-Polylactide Bottlebrush Block Copolymers and Their Melt Self-Assembly into Large Domain Nanostructures. *Macromolecules* **2009**, *42* (6), 2135–2141. (c) Dalsin, S. J.; Rions-Maehren, T. G.; Beam, M. D.; Bates, F. S.; Hillmyer, M. A.; Matsen, M. W. Bottlebrush Block Polymers: Quantitative Theory and Experiments. *ACS Nano* **2015**, *9* (12), 12233–12245. (d) Pelras, T.; Mahon, C. S.; Müllner, M. Synthesis and Applications of Compartmentalised Molecular Polymer Brushes. *Angew. Chem. Int. Ed.* **2018**, *57* (24), 6982–6994. (e) Guo, Z. H.; Le, A. N.; Feng, X.; Choo, Y.; Liu, B.; Wang, D.; Wan, Z.; Gu, Y.; Zhao, J.; Li, V.; Osuji, C. O.; Johnson, J. A.; Zhong. M. Janus Graft Block Copolymers: Design of a Polymer Architecture for Independently Tuned Nanostructures and Polymer Properties. *Angew. Chem. Int. Ed.* **2018**, *57* (28), 8493–8497.
4. Matsen, M. W.; Bates, F. S. Unifying Weak- and Strong-Segregation Block Copolymer Theories. *Macromolecules* **1996**, *29* (4), 1091–1098.
5. Bates, F. S; Fredrickson, G. H. BLOCK COPOLYMER THERMODYNAMICS: Theory and Experiment. *Annu. Rev. Phys. Chem.* **1990**, *41*, 525–557.
6. (a) Matsen, M. W.; Bates, F. S. Origins of Complex Self-Assembly in Block Copolymers. *Macromolecules* **1996**, *29* (23), 7641–7644. (b) Zhu, L.; Huang, P.; Ge, Q.; Quirk, R. P.; Thomas, E. L.; Lotz, B.; Wittmann, J. C.; Hsiao, B. S.; Yeh, F.; Liu, L.; et

al. Dislocation-Controlled Perforated Layer Phase in a PEO-*b*-PS Diblock Copolymer. *Phys. Rev. Lett.* **2001**, *86* (26 I), 6030–6033. (c) Mastroianni, S. E.; Patterson, J. P.; O'Reilly, R. K.; Epps, T. H. Poly(Methyl Methacrylate-*block*-Vinyl-*m*-Triphenylamine): Synthesis by RAFT Polymerization and Melt-State Self-Assembly. *Soft Matter* **2013**, *9* (42), 10146–10154. (d) Pester, C. W.; Schmidt, K.; Ruppel, M.; Schoberth, H. G.; Böker, A. Electric-Field-Induced Order-Order Transition from Hexagonally Perforated Lamellae to Lamellae. *Macromolecules* **2015**, *48* (17), 6206–6213.

7. (a) Winey, K. I.; Thomas, E. L.; Fetters, L. J. The Ordered Bicontinuous Double-Diamond Morphology in Diblock Copolymer/Homopolymer Blends. *Macromolecules* **1992**, *25* (1), 422–428. (b) Chu, C. Y.; Lin, W. F.; Tsai, J. C.; Lai, C. S.; Lo, S. C.; Chen, H. L.; Hashimoto, T. Order-Order Transition between Equilibrium Ordered Bicontinuous Nanostructures of Double Diamond and Double Gyroid in Stereoregular Block Copolymer. *Macromolecules* **2012**, *45* (5), 2471–2477. (c) Lin, C. H.; Higuchi, T.; Chen, H. L.; Tsai, J. C.; Jinnai, H.; Hashimoto, T. Stabilizing the Ordered Bicontinuous Double Diamond Structure of Diblock Copolymer by Configurational Regularity. *Macromolecules* **2018**, *51* (11), 4049–4058.
8. (a) Yamada, K.; Nonomura, M.; Ohta, T. *Fddd* Structure in AB-Type Diblock Copolymers. *J. Phys. Condens. Matter* **2006**, *18* (32). (b) Takenaka, M.; Wakada, T.; Akasaka, S.; Nishitsuji, S.; Saijo, K.; Shimizu, H.; Kim, M. I.; Hasegawa, H. Orthorhombic *Fddd* Network in Diblock Copolymer Melts. *Macromolecules* **2007**, *40* (13), 4399–4402. (c) Jung, J.; Park, H. W.; Lee, J.; Huang, H.; Chang, T.; Rho, Y.; Ree, M.; Sugimori, H.; Jinnai, H. Structural Characterization of the *Fddd* Phase in a Diblock Copolymer Thin Film by Electron Microtomography. *Soft Matter* **2011**, *7* (21), 10424–10428.
9. (a) Lee, S.; Bluemle, M. J.; Bates, F. S. Discovery of a Frank-Kasper σ Phase in Sphere-Forming Block Copolymer Melts. *Science* **2010**, *330* (15), 349–353. (b) Liu, M.; Qiang, Y.; Li, W.; Qiu, F.; Shi, A. C. Stabilizing the Frank-Kasper Phases via Binary Blends of AB Diblock Copolymers. *ACS Macro Lett.* **2016**, *5* (10), 1167–1171. (c) Li, W.; Duan, C.; Shi, A. C. Nonclassical Spherical Packing Phases Self-Assembled from AB-Type Block Copolymers. *ACS Macro Lett.* **2017**, *6* (11), 1257–1262. (d) Bates, M. W.; Lequieu, J.; Barbon, S. M.; Lewis, R. M.; Delaney, K. T.; Anastasaki, A.; Hawker, C. J.; Fredrickson, G. H.; Bates, C. M. Stability of the A15 Phase in Diblock Copolymer Melts. *Proc. Natl. Acad. Sci. U. S. A.* **2019**, *116* (27), 13194–13199.
10. (a) Pai, R. A.; Humayun, R.; Schulberg, M. T.; Sengupta, A.; Sun, J. N.; Watkins, J. J. Mesoporous Silicates Prepared Using Preorganized Templates in Supercritical Fluids. *Science* **2004**, *303* (5657), 507–510. (b) Yang, S. Y.; Park, J.; Yoon, J.; Ree, M.; Jang, S. K.; Kim, J. K. Virus Filtration Membranes Prepared from Nanoporous Block Copolymers with Good Dimensional Stability under High Pressures and Excellent Solvent Resistance. *Adv. Funct. Mater.* **2008**, *18* (9), 1371–1377. (c) Phillip, W. A.; O'neill, B.; Rodwogin, M.; Hillmyer, M. A.; Cussler, E. L. Self-Assembled Block

Copolymer Thin Films as Water Filtration Membranes. *ACS Appl. Mater. Interfaces* **2010**, *2* (3), 847–853. (d) Yao, L.; Woll, A. R.; Watkins, J. J. Directed Assembly of Block Copolymer Templates for the Fabrication of Mesoporous Silica Films with Controlled Architectures via 3-D Replication. *Macromolecules* **2013**. *46*, 6132–6144. (e) Schöttner, S.; Schaffrath, H. J.; Gallei, M. Poly(2-Hydroxyethyl Methacrylate)-Based Amphiphilic Block Copolymers for High Water Flux Membranes and Ceramic Templates. *Macromolecules* **2016**, *49* (19), 7286–7295.

11. (a) Chiu, Y. C.; Otsuka, I.; Halila, S.; Borsali, R.; Chen, W. C. High-Performance Nonvolatile Transistor Memories of Pentacence Using the Green Electrets of Sugar-Based Block Copolymers and Their Supramolecules. *Adv. Funct. Mater.* **2014**, *24* (27), 4240–4249. (b) Hung, C. C.; Chiu, Y. C.; Wu, H. C.; Lu, C.; Bouilhac, C.; Otsuka, I.; Halila, S.; Borsali, R.; Tung, S. H.; Chen, W. C. Conception of Stretchable Resistive Memory Devices Based on Nanostructure-Controlled Carbohydrate-*block*-Polyisoprene Block Copolymers. *Adv. Funct. Mater.* **2017**, *27* (13), 1606161.
12. (a) Meng, Y.; Gu, D.; Zhang, F.; Shi, Y.; Cheng, L.; Feng, D.; Wu, Z.; Chen, Z.; Wan, Y.; Stein, A.; et al. A Family of Highly Ordered Mesoporous Polymer Resin and Carbon Structures from Organic-Organic Self-Assembly. *Chem. Mater.* **2006**, *18* (18), 4447–4464. (b) Deng, Y.; Wei, J.; Sun, Z.; Zhao, D. Large-Pore Ordered Mesoporous Materials Templated from Non-Pluronic Amphiphilic Block Copolymers. *Chem. Soc. Rev.* **2013**, *42* (9), 4054–4070. (c) Fei, H. F.; Li, W.; Bhardwaj, A.; Nuguri, S.; Ribbe, A.; Watkins, J. J. Ordered Nanoporous Carbons with Broadly Tunable Pore Size Using Bottlebrush Block Copolymer Templates. *J. Am. Chem. Soc.* **2019**, *141* (42), 17006–17014.
13. (a) Kang, Y.; Walish, J. J.; Gorishnyy, T.; Thomas, E. L. Broad-Wavelength-Range Chemically Tunable Block-Copolymer Photonic Gels. *Nat. Mater.* **2007**, *6* (12), 957–960. (b) Sveinbjörnsson, B. R.; Weitekamp, R. A.; Miyake, G. M.; Xia, Y.; Atwater, H. A.; Grubbs, R. H. Rapid Self-Assembly of Brush Block Copolymers to Photonic Crystals. *Proc. Natl. Acad. Sci. U. S. A.* **2012**, *109* (36), 14332–14336. (c) Noro, A.; Tomita, Y.; Shinohara, Y.; Sageshima, Y.; Walish, J. J.; Matsushita, Y.; Thomas, E. L. Photonic Block Copolymer Films Swollen with an Ionic Liquid. *Macromolecules* **2014**, *47* (12), 4103–4109. (d) Liberman-Martin, A. L.; Chu, C. K.; Grubbs, R. H. Application of Bottlebrush Block Copolymers as Photonic Crystals. *Macromol. Rapid Commun.* **2017**, *38* (13), 1–15. (e) Yu, Y. G.; Chae, C. G.; Kim, M. J.; Seo, H. Bin; Grubbs, R. H.; Lee, J. S. Precise Synthesis of Bottlebrush Block Copolymers from ω-End-Norbornyl Polystyrene and Poly(4-Tert-Butoxystyrene) via Living Anionic Polymerization and Ring-Opening Metathesis Polymerization. *Macromolecules* **2018**, *51* (2), 447–455.
14. (a) Thurn-Albrecht, T.; Schotter, J.; Kastle, G. A.; Emley, N.; Shibauchi, T.; Krusin-Elbaum, L.; Guarini, K.; Black, C. T.; Tuominen, M. T.; Russell, T. P.

Ultrahigh-Density Nanowire Arrays Grown in Self-Assembled Diblock Copolymer Templates. *Science* **2000**, *290* (5499), 2126–2129. (b) Hsueh, H. Y.; Yao, C. T.; Ho, R. M. Well-Ordered Nanohybrids and Nanoporous Materials from Gyroid Block Copolymer Templates. *Chem. Soc. Rev.* **2015**, *44* (7), 1974–2018. (c) Wang, W.; Schlegel, R.; White, B. T.; Williams, K.; Voyloy, D.; Steren, C. A.; Goodwin, A.; Coughlin, E. B.; Gido, S.; Beiner, M.; Hong, K.; Kang, N.-G.; Mays, J. High Temperature Thermoplastic Elastomers Synthesized by Living Anionic Polymerization in Hydrocarbon Solvent at Room Temperature. *Macromolecules* **2016**, *49* (7), 248–270. (d) Zhang, Q.; Hua, W.; Ren, Q.; Feng, J. Regulation of Physical Networks and Mechanical Properties of Triblock Thermoplastic Elastomer through Introduction of Midblock Similar Crystalline Polymer with Multiblock Architecture. *Macromolecules* **2016**, *49* (19), 7379–7386.

15. (a) Peace, F.; Chou, S. Y. Lithography and Other Patterning Techniques for Future Electronics. *Proc. IEEE* **2008**, *96* (2), 493–496. (b) Editorial: Beyond the Diffraction Limit. *Nat. Photonics* **2009**, *3* (7), 361. (c) Galatsis, K.; Wang, K. L.; Ozkan, M.; Ozkan, C. S.; Huang, Y.; Chang, J. P.; Monbouquette, H. G.; Chen, Y.; Nealey, P.; Botros, Y. Patterning and Templating for Nanoelectronics. *Adv. Mater.* **2010**, *22* (6), 769–778.
16. (a) Cheng, J. Y.; Mayes, A. M.; Ross, C. A. Nanostructure Engineering by Templated Self-Assembly of Block Copolymers. *Nat. Mater.* **2004**, *3* (11), 823–828. (b) Park, S.; Dong, H. L.; Xu, J.; Kim, B.; Sung, W. H.; Jeong, U.; Xu, T.; Russell, T. P. Macroscopic 10-Terabit-per-Square-Inch Arrays from Block Copolymers with Lateral Order. *Science* **2009**, *323* (5917), 1030–1033. (c) Moon, H.-S.; Shin, D. O.; Kim, B. H.; Jin, H. M.; Lee, S.; Lee, M. G.; Kim, S. O. Large-Area, Highly Oriented Lamellar Block Copolymer Nanopatterning Directed by Graphoepitaxially Assembled Cylinder Nanopatterns. *J. Mater. Chem.* **2012**, *22* (13), 6307–6310. (d) Borah, D.; Rasappa, S.; Salaun, M.; Zellsman, M.; Lorret, O.; Liontos, G.; Ntetsikas, K.; Avgeropoulos, A.; Morris, M. A. Soft Graphoepitaxy for Large Area Directed Self-Assembly of Polystyrene-*block*-Poly(dimethylsiloxane) Block Copolymer on Nanopatterned Poss Substrates Fabricated by Nanoimprint Lithography. *Adv. Funct. Mater.* **2015**, *25* (22), 3425–3432.
17 . (a) Craig, G. S. W.; Nealey, P. F. Self-Assembly of Block Copolymers on Lithographically Defined Nanopatterned Substrates. *J. Photopolym. Sci. Technol.* **2007**, *20* (4), 511–517. (b) Ruiz, R.; Kang, H.; Detcheverry, F. A.; Dobisz, E.; Kercher, D. S.; Albrecht, T. R.; de Pablo, J. J.; Nealey, P. F. Density Multiplication and Improved Lithography by Directed Block Copolymer Assembly. *Science.* **2008**, *321* (5891), 936–939. (c) Wan, L.; Ruiz, R.; Gao, H.; Patel, K. C.; Albrecht, T. R.; Yin, J.; Kim, J.; Cao, Y.; Lin, G. The Limits of Lamellae-Forming PS-*b*-PMMA Block Copolymers for Lithography. *ACS Nano* **2015**, *9* (7), 7506–7514. (d) Xiong, S.; Wan, L.; Ishida, Y.; Chapuis, Y. A.; Craig, G. S. W.; Ruiz, R.; Nealey, P. F. Directed Self-Assembly of

Triblock Copolymer on Chemical Patterns for Sub-10-nm Nanofabrication via Solvent Annealing. *ACS Nano* **2016**, *10* (8), 7855–7865.

18 . (a) Mansky, P.; Liu, Y.; Huang, E.; Russell, T. P.; Hawker, C. Controlling Polymer-Surface Interactions with Random Copolymer Brushes. *Science.* **1997**, *275* (5305), 1458–1460. (b) Bates, C. M.; Seshimo, T.; Maher, M. J.; Durand, W. J.; Cushen, J. D.; Dean, L. M.; Blachut, G.; Ellison, C. J.; Willson, C. G. Polarity-Switching Top Coats Enable Copolymer Domains. *Science.* **2012**, *338* (9), 775–779. (c) Maher, M. J.; Bates, C. M.; Blachut, G.; Sirard, S.; Self, J. L.; Carlson, M. C.; Dean, L. M.; Cushen, J. D.; Durand, W. J.; Hayes, C. O.; Ellison, C. J.; Willson, C. G. Interfacial Design for Block Copolymer Thin Films. *Chem. Mater.* **2014**, *26* (3), 1471–1479. (d) Kim, S.; Wang, H. S.; Choe, Y.; Choi, S. H.; Bang, J. Controlling the Microdomain Orientation in Block Copolymer Thin Films via Cross-Linkable Random Copolymer Neutral Layer. *Polym. J.* **2016**, *48* (4), 333–340. (e) Lee, W.; Kim, Y.; Jo, S.; Park, S.; Ahn, H.; Ryu, D. Y. Irreversible Physisorption of PS-*b*-PMMA Copolymers on Substrates for Balanced Interfacial Interactions as a Versatile Surface Modification. *ACS Macro Lett.* **2019**, 519–524.

19. (a) Nakatani, R.; Takano, H.; Chandra, A.; Yoshimura, Y.; Wang, L.; Suzuki, Y.; Tanaka, Y.; Maeda, R.; Kihara, N.; Minegishi, S.; et al. Perpendicular Orientation Control without Interfacial Treatment of RAFT-Synthesized High-χ Block Copolymer Thin Films with Sub-10 nm Features Prepared via Thermal Annealing. *ACS Appl. Mater. Interfaces* **2017**, *9* (37), 31266–31278. (b) Seshimo, T.; Maeda, R.; Odashima, R.; Takenaka, Y.; Kawana, D.; Ohmori, K.; Hayakawa, T. Perpendicularly Oriented Sub-10-nm Block Copolymer Lamellae by Atmospheric Thermal Annealing for One Minute. *Sci. Rep.* **2016**, *6*, 19481. (c) Yoshimura, Y.; Chandra, A.; Nabae, Y.; Hayakawa, T. Chemically Tailored High-χ Block Copolymers for Perpendicular Lamellae via Thermal Annealing. *Soft Matter* **2019**, *15* (17), 3497–3506.

20. (a) Kim, S. H.; Misner, M. J.; Xu, T.; Kimura, M.; Russell, T. P. Highly Oriented and Ordered Arrays from Block Copolymers via Solvent Evaporation. *Adv. Mater.* **2004**, *16* (3), 226–231. (b) Metwalli, E.; Perlich, J.; Wang, W.; Diethert, A.; Roth, S. V.; Papadakis, C. M.; Müller-Buschbaum, P. Morphology of Semicrystalline Diblock Copolymer Thin Films upon Directional Solvent Vapor Flow. *Macromol. Chem. Phys.* **2010**, *211* (19), 2102–2108. (c) Son, J. G.; Gotrik, K. W.; Ross, C. A. High-Aspect-Ratio Perpendicular Orientation of PS-*b*-PDMS Thin Films under Solvent Annealing. *ACS Macro Lett.* **2012**, *1* (11), 1279–1284. (d) Kim, E.; Kim, W.; Lee, K. H.; Ross, C. A.; Son, J. G. A Top Coat with Solvent Annealing Enables Perpendicular Orientation of Sub-10 nm Microdomains in Si-Containing Block Copolymer Thin Films. *Adv. Funct. Mater.* **2014**, *24* (44), 6981–6988.

21. (a) Welander, A. M.; Kang, H.; Stuen, K. O.; Solak, H. H.; Müller, M.; De Pablo, J. J.; Nealey, P. F. Rapid Directed Assembly of Block Copolymer Films at Elevated

Temperatures. *Macromolecules* **2008**, *41* (8), 2759–2761. (b) Ruiz, R.; Bosworth, J. K.; Black, C. T. Effect of Structural Anisotropy on the Coarsening Kinetics of Diblock Copolymer Striped Patterns. *Phys. Rev. B* **2008**, *77* (5), 054204. (c) Stoykovich, M. P.; Müller, M.; Kim, S. O.; Solak, H. H.; Erik, W.; Pablo, J. J. de; Nealey, P. F. Directed Assembly of Block Copolymer Blends into Nonregular Device-Oriented Structures. *Science* **2012**, *308* (5727), 1442–1446. (d) Kim, E.; Ahn, H.; Park, S.; Lee, H.; Lee, M.; Lee, S.; Kim, T.; Kwak, E. A.; Lee, J. H.; Lei, X.; Huh, J.; Bang, J.; Lee, B.; Ryu, D. Y. Directed Assembly of High Molecular Weight Block Copolymers: Highly Ordered Line Patterns of Perpendicularly Oriented Lamellae with Large Periods. *ACS Nano* **2013**, *7* (3), 1952–1960. (e) Yoshida, K.; Tian, L.; Miyagi, K.; Yamazaki, A.; Mamiya, H.; Yamamoto, T.; Tajima, K.; Isono, T.; Satoh, T. Facile and Efficient Modification of Polystyrene-*block*-Poly(Methyl Methacrylate) for Achieving Sub-10 nm Feature Size.

22. (a) Zalusky, A. S.; Olayo-Valles, R.; Wolf, J. H.; Hillmyer, M. A. Ordered Nanoporous Polymers from Polystyrene-Polylactide Block Copolymers. *J. Am. Chem. Soc.* **2002**, *124* (43), 12761–12773. (b) Baruth, A.; Rodwogin, M. D.; Shankar, A.; Erickson, M. J.; Hillmyer, M. A.; Leighton, C. Non-Lift-off Block Copolymer Lithography of 25 nm Magnetic Nanodot Arrays. *ACS Appl. Mater. Interfaces* **2011**, *3* (9), 3472–3481. (c) Baruth, A.; Seo, M.; Lin, C. H.; Walster, K.; Shankar, A.; Hillmyer, M. A.; Leighton, C. Optimization of Long-Range Order in Solvent Vapor Annealed Poly(styrene)-*block*-Poly(lactide) Thin Films for Nanolithography. *ACS Appl. Mater. Interfaces* **2014**, *6* (16), 13770–13781. (d) Keen, I.; Cheng, H. H.; Yu, A.; Jack, K. S.; Younkin, T. R.; Leeson, M. J.; Whittaker, A. K.; Blakey, I. Behavior of Lamellar Forming Block Copolymers under Nanoconfinement: Implications for Topography Directed Self-Assembly of Sub-10 nm Structures. *Macromolecules* **2014**, *47* (1), 276–283. (e) Li, X.; Liu, Y.; Wan, L.; Li, Z.; Suh, H.; Ren, J.; Ocola, L. E.; Hu, W.; Ji, S.; Nealey, P. F. Effect of Stereochemistry on Directed Self-Assembly of Poly(styrene-*b*-Lactide) Films on Chemical Patterns. *ACS Macro Lett.* **2016**, *5* (3), 396–401.

23. (a) Wu, N. L. Y.; Zhang, X.; Murphy, J. N.; Chai, J.; Harris, K. D.; Buriak, J. M. Density Doubling of Block Copolymer Templated Features. *Nano Lett.* **2012**, *12* (1), 264–268. (b) Murphy, J. N.; Harris, K. D.; Buriak, J. M. Automated Defect and Correlation Length Analysis of Block Copolymer Thin Film Nanopatterns. *PLoS One* **2015**, *10* (7), e0133088. (c) Sun, Z.; Chen, Z.; Zhang, W.; Choi, J.; Huang, C.; Jeong, G.; Coughlin, E. B.; Hsu, Y.; Yang, X.; Lee, K. Y.; Kuo, D. S.;Xiao, S.; Russel, T. P. Directed Self-Assembly of Poly(2-Vinylpyridine)-*b*-Polystyrene-*b*-Poly(2-Vinylpyridine) Triblock Copolymer with Sub-15 nm Spacing Line Patterns Using a Nanoimprinted Photoresist Template. *Adv. Mater.* **2015**, *27* (29), 4364–4370. (d) Sun, Z.; Zhang, W.; Hong, S.; Chen, Z.; Liu, X.; Xiao, S.; Coughlin, E. B.; Russell, T. P. Using Block Copolymer Architecture to Achieve Sub-10 nm Periods. *Polymer* **2017**, *121* (14), 297–303.

24. (a) Jung, Y. S.; Ross, C. A. Orientation-Controlled Self-Assembled Nanolithography Using a Polystyrene-Polydimethylsiloxane Block Copolymer. *Nano Lett.* **2007**, *7* (7), 2046–2050. (b) Jung, Y. S.; Chang, J. B.; Verploegen, E.; Berggren, K. K.; Ross, C. A. A Path to Ultranarrow Patterns Using Self-Assembled Lithography. *Nano Lett.* **2010**, *10* (3), 1000–1005. (c) Park, W. I.; Kim, K.; Jang, H. I.; Jeong, J. W.; Kim, J. M.; Choi, J.; Park, J. H.; Jung, Y. S. Directed Self-Assembly with Sub-100 Degrees Celsius Processing Temperature, Sub-10 Nanometer Resolution, and Sub-1 Minute Assembly Time. *Small* **2012**, *8* (24), 3762–3768. (d) Chang, J. B.; Son, J. G.; Hannon, A. F.; Alexander-Katz, A.; Ross, C. A.; Berggren, K. K. Aligned Sub-10-nm Block Copolymer Patterns Templated by Post Arrays. *ACS Nano* **2012**, *6* (3), 2071–2077. (e) Girardot, C.; Böhme, S.; Archambault, S.; Salaün, M.; Latu-Romain, E.; Cunge, G.; Joubert, O.; Zelsmann, M. Pulsed Transfer Etching of PS-PDMS Block Copolymers Self-Assembled in 193 nm Lithography Stacks. *ACS Appl. Mater. Interfaces* **2014**, *6* (18), 16276–16282. (f) Garnier, J.; Arias-Zapata, J.; Marconot, O.; Arnaud, S.; Böhme, S.; Girardot, C.; Buttard, D.; Zelsmann, M. Sub-10 nm Silicon Nanopillar Fabrication Using Fast and Brushless Thermal Assembly of PS-*b*-PDMS Diblock Copolymer. *ACS Appl. Mater. Interfaces* **2016**, *8* (15), 9954–9960.

25. (a) Woo, S.; Jo, S.; Ryu, D. Y.; Choi, S. H.; Choe, Y.; Khan, A.; Huh, J.; Bang, J. Molecular Tailoring of Poly(styrene-*b*-Methyl Methacrylate) Block Copolymer Toward Perpendicularly Oriented Nanodomains with Sub-10 nm Features. *ACS Macro Lett.* **2017**, *6* (12), 1386–1391. (b) Yang, G. W.; Wu, G. P.; Chen, X.; Xiong, S.; Arges, C. G.; Ji, S.; Nealey, P. F.; Lu, X. B.; Darensbourg, D. J.; Xu, Z. K. Directed Self-Assembly of Polystyrene-*b*-Poly(Propylene Carbonate) on Chemical Patterns via Thermal Annealing for Next Generation Lithography. *Nano Lett.* **2017**, *17* (2), 1233–1239. (c) Van Genabeek, B.; Lamers, B. A. G.; De Waal, B. F. M.; Van Son, M. H. C.; Palmans, A. R. A.; Meijer, E. W. Amplifying (Im)perfection: The Impact of Crystallinity in Discrete and Disperse Block Co-Oligomers. *J. Am. Chem. Soc.* **2017**, *139* (42), 14869–14872. (d) Kwak, J.; Mishra, A. K.; Lee, J.; Lee, K. S.; Choi, C.; Maiti, S.; Kim, M.; Kim, J. K. Fabrication of Sub-3 nm Feature Size Based on Block Copolymer Self-Assembly for Next-Generation Nanolithography. *Macromolecules* **2017**, *50* (17), 6813–6818. (e) Zhang, X.; He, Q.; Chen, Q.; Nealey, P. F.; Ji, S. Directed Self-Assembly of High Poly(styrene-*b*-(lactic Acid- *alt*-Glycolic Acid)) Block Copolymers on Chemical Patterns via Thermal Annealing. *ACS Macro Lett.* **2018**, *7* (6), 751–756.

26. Nunns, A.; Gwyther, J.; Manners, I. Inorganic Block Copolymer Lithography. *Polymer* **2013**, *54* (4), 1269–1284.

27. (a) Stoykovich, M. P.; Muller, M.; Kim, S. O.; Solak, H. H.; Edwards, E. W.; de Pablo, J. J.; Nealey, P. F. Directed Assembly of Block Copolymer Blends into Nonregular Device-Oriented Structures. *Science* **2005**, *308* (5727), 1442–1446. (b) Stoykovich, M. P.; Kang, H.; Daoulas, K. C.; Liu, G.; Liu, C. C.; De Pablo, J. J.; Müller, M.; Nealey, P. F.

Directed Self-Assembly of Block Copolymers for Nanolithography: Fabrication of Isolated Features and Essential Integrated Circuit Geometries. *ACS Nano* **2007**, *1* (3), 168–175. (c) Chuang, V. P.; Gwyther, J.; Mickiewicz, R. A.; Manners, I.; Ross, C. A. Templated Self-Assembly of Square Symmetry Arrays from an ABC Triblock Terpolymer. *Nano Lett.* **2009**, *9* (12), 4364–4369. (d) Doerk, G. S.; Liu, C. C.; Cheng, J. Y.; Rettner, C. T.; Pitera, J. W.; Krupp, L. E.; Topuria, T.; Arellano, N.; Sanders, D. P. Pattern Placement Accuracy in Block Copolymer Directed Self-Assembly Based on Chemical Epitaxy. *ACS Nano* **2013**, *7* (1), 276–285. (e) Luo, M.; Epps, T. H. Directed Block Copolymer Thin Film Self-Assembly: Emerging Trends in Nanopattern Fabrication. *Macromolecules* **2013**, *46* (19), 7567–7579.

28. Hur, S. M.; Thapar, V.; Ramírez-Hernández, A.; Nealey, P. F.; De Pablo, J. J. Defect Annihilation Pathways in Directed Assembly of Lamellar Block Copolymer Thin Films. *ACS Nano* **2018**, *12* (10), 9974–9981.
29. Lee, K. S.; Lee, J.; Kwak, J.; Moon, H. C.; Kim, J. K. Reduction of Line Edge Roughness of Polystyrene-*block*-Poly(methyl Methacrylate) Copolymer Nanopatterns by Introducing Hydrogen Bonding at the Junction Point of Two Block Chains. *ACS Appl. Mater. Interfaces* **2017**, *9* (37), 31245–31251.
30. Sivaniah, E.; Matsubara, S.; Zhao, Y.; Hashimoto, T.; Fukunaga, K.; Kramer, E. J.; Mates, T. E. Symmetric Diblock Copolymer Thin Films on Rough Substrates: Microdomain Periodicity in Pure and Blended Films. *Macromolecules* **2008**, *41* (7), 2584–2592.
31 . (a) Rodwogin, M. D.; Spanjers, C. S.; Leighton, C.; Hillmyer, M. A. Polylactide-Poly(Dimethylsiloxane)-Polylactide Triblock Copolymers as Multifunctional Materials for Nanolithographic Applications. *ACS Nano* **2010**, *4* (2), 725–732. (b) Cushen, J. D.; Bates, C. M.; Rausch, E. L.; Dean, L. M.; Zhou, S. X.; Willson, C. G.; Ellison, C. J. Thin Film Self-Assembly of Poly(Trimethylsilylstyrene-*b*-D,L-Lactide) with Sub-10 nm Domains. *Macromolecules* **2012**, *45* (21), 2584–2592. (c) Luo, Y.; Montarnal, D.; Kim, S.; Shi, W.; Barteau, K. P.; Pester, C. W.; Hustad, P. D.; Christianson, M. D.; Fredrickson, G. H.; Kramer, E. J.; Hawker, C. J. Poly(dimethylsiloxane-*b*-Methyl Methacrylate): A Promising Candidate for Sub-10 nm Patterning. *Macromolecules* **2015**, *48* (11), 3422–3430. (d) Maher, M. J.; Rettner, C. T.; Bates, C. M.; Blachut, G.; Carlson, M. C.; Durand, W. J.; Ellison, C. J.; Sanders, D. P.; Cheng, J. Y.; Willson, C. G. Directed Self-Assembly of Silicon-Containing Block Copolymer Thin Films. *ACS Appl. Mater. Interfaces* **2015**, *7* (5), 3323–3328. (e) Legrain, A.; Fleury, G.; Mumtaz, M.; Navarro, C.; Arias-Zapata, J.; Chevalier, X.; Cayrefourcq, I.; Zelsmann, M. Straightforward Integration Flow of a Silicon-Containing Block Copolymer for Line-Space Patterning. *ACS Appl. Mater. Interfaces* **2017**, *9* (49), 43043–43050.
32. (a) Kwak, J.; Mishra, A. K.; Lee, J.; Lee, K. S.; Choi, C.; Maiti, S.; Kim, M.; Kim, J. K. Fabrication of Sub-3 nm Feature Size Based on Block Copolymer Self-Assembly for

Next-Generation Nanolithography. *Macromolecules* **2017**, *50* (17), 6813–6818. (b) Zhang, W.; Huang, M.; Abdullatif, S. Al; Chen, M.; Shao-Horn, Y.; Johnson, J. A. Reduction of (Meth)acrylate-Based Block Copolymers Provides Access to Self-Assembled Materials with Ultrasmall Domains. *Macromolecules* **2018**, *51* (17), 6757–6763. (c) Yu, D. M.; Mapas, J. K. D.; Kim, H.; Choi, J.; Ribbe, A. E.; Rzayev, J.; Russell, T. P. Evaluation of the Interaction Parameter for Poly(solketal Methacrylate)-Block-Polystyrene Copolymers. *Macromolecules* **2018**, *51* (3), 1031–1040. (d) Chen, Q. P.; Barreda, L.; Oquendo, L. E.; Hillmyer, M. A.; Lodge, T. P.; Siepmann, J. I. Computational Design of High-χ Block Oligomers for Accessing 1 nm Domains. *ACS Nano* **2018**, *12* (5), 4351–4361. (e) Wang, C.; Li, X.; Deng, H. Synthesis of a Fluoromethacrylate Hydroxystyrene Block Copolymer Capable of Rapidly Forming Sub-5 nm Domains at Low Temperatures. *ACS Macro Lett.* **2019**, *8* (4), 368–373.

33. (a) Cushen, J. D.; Otsuka, I.; Bates, C. M.; Halila, S.; Fort, S.; Rochas, C.; Easley, J. A.; Rausch, E. L.; Thio, A.; Borsali, R.; Willson, C. G.; Ellison, C. J. Oligosaccharide/Silicon-Containing Block Copolymers with 5 nm Features for Lithographic Applications. *ACS Nano* **2012**, *6* (4), 3424–3433. (b) Otsuka, I.; Tallegas, S.; Sakai, Y.; Rochas, C.; Halila, S.; Fort, S.; Bsiesy, A.; Baron, T.; Borsali, R. Control of 10 nm Scale Cylinder Orientation in Self-Organized Sugar-Based Block Copolymer Thin Films. *Nanoscale* **2013**, *5* (7), 2637–2641. (c) Sakai-Otsuka, Y.; Zaioncz, S.; Otsuka, I.; Halila, S.; Rannou, P.; Borsali, R. Self-Assembly of Carbohydrate-*block*-Poly(3-Hexylthiophene) Diblock Copolymers into Sub-10 nm Scale Lamellar Structures. *Macromolecules* **2017**, *50* (8), 3365–3376. (d) Isono, T.; Ree, B. J.; Tajima, K.; Borsali, R.; Satoh, T. Highly Ordered Cylinder Morphologies with 10 nm Scale Periodicity in Biomass-Based Block Copolymers. *Macromolecules* **2018**, *51* (2), 428–437.
34. (a) Hogen-Esch, T. E. Synthesis and Characterization of Macrocyclic Vinyl Aromatic Polymers. *J. Polym. Sci. Part A: Polym. Chem.* **2006**, *44* (7), 2139–2155. (b) Kricheldorf, H. R. Cyclic polymers: Synthetic strategies and physical properties. *J. Polym. Sci. Part A: Polym. Chem.* **2010**, *48* (2), 251–284. (c) Ren, J. M.; McKenzie, T. G.; Fu, Q.; Wong, E. H. H.; Xu, J.; An, Z.; Shanmugam, S.; Davis, T. P.; Boyer, C.; Qiao, G. G. Star Polymers. *Chem. Rev.* **2016**, *116* (12), 6743–6836. (d) Iwamoto, T.; Doi, Y.; Kinoshita, K.; Ohta, Y.; Takano, A.; Takahashi, Y.; Nagao, M.; Matsushita, Y. Conformations of Ring Polystyrenes in Bulk Studied by SANS. *Macromolecules* **2018**, *51* (4), 1539–1548.
35. Poelma, J. E.; Ono, K.; Miyajima, D.; Aida, T.; Satoh, K.; Hawker, C. J. Cyclic Block Copolymers for Controlling Feature Sizes in Block Copolymer Lithography. *ACS Nano* **2012**, *6* (12), 10845–10854.
36. Goodson, A. D.; Troxler, J. E.; Rick, M. S.; Ashbaugh, H. S.; Albert, J. N. L. Impact of Cyclic Block Copolymer Chain Architecture and Degree of Polymerization on Nanoscale

Domain Spacing : A Simulation and Scaling Theory Analysis. *Macromolecules* **2019**, *52* (23), 9389–9397.

37. (a) Isono, T.; Otsuka, I.; Kondo, Y.; Halila, S.; Fort, S.; Rochas, C.; Satoh, T.; Borsali, R.; Kakuchi, T. Sub-10 nm Nano-Organization in AB_2- and AB_3-Type Miktoarm Star Copolymers Consisting of Maltoheptaose and Polycaprolactone. *Macromolecules* **2013**, *46* (4), 1461–1469. (b) Shi, W.; Tateishi, Y.; Li, W.; Hawker, C. J.; Fredrickson, G. H.; Kramer, E. J. Producing Small Domain Features Using Miktoarm Block Copolymers with Large Interaction Parameters. *ACS Macro Lett.* **2015**, *4* (11), 1287–1292. (c) Minehara, H.; Pitet, L. M.; Kim, S.; Zha, R. H.; Meijer, E. W.; Hawker, C. J. Branched Block Copolymers for Tuning of Morphology and Feature Size in Thin Film Nanolithography. *Macromolecules* **2016**, *49* (6), 2318–2326. (d) Yue, K.; Liu, C.; Huang, M.; Huang, J.; Zhou, Z.; Wu, K.; Liu, H.; Lin, Z.; Shi, A. C.; Zhang, W.-B.; Cheng, S. Z. D. Self-Assembled Structures of Giant Surfactants Exhibit a Remarkable Sensitivity on Chemical Compositions and Topologies for Tailoring Sub-10 nm Nanostructures. *Macromolecules* **2017**, *50* (1), 303–314.
38. Choi, H. K.; Gwyther, J.; Manners, I.; Ross, C. A. Square Arrays of Holes and Dots Patterned from a Linear ABC Triblock Terpolymer. *ACS Nano* **2012**, *6* (9), 8342–8348.
39. Grason, G. M.; Kamien, R. D. Interfaces in Diblocks: A Study of Miktoarm Star Copolymers. *Macromolecules* **2004**, *37* (19), 7371–7380.
40. Shi, W.; Hamilton, A. L.; Delaney, K. T.; Fredrickson, G. H.; Kramer, E. J.; Ntaras, C.; Avgeropoulos, A.; Lynd, N. A. Creating Extremely Asymmetric Lamellar Structures via Fluctuation-Assisted Unbinding of Miktoarm Star Block Copolymer Alloys. *J. Am. Chem. Soc.* **2015**, *137* (19), 6160–6163.
41. Huang, M.; Yue, K.; Huang, J.; Liu, C.; Zhou, Z.; Wang, J.; Wu, K.; Shan, W.; Shi, A. C.; Cheng, S. Z. D. Highly Asymmetric Phase Behaviors of Polyhedral Oligomeric Silsesquioxane-Based Multiheaded Giant Surfactants. *ACS Nano* **2018**, *12* (2), 1868–1877.
42. (a) Huo, M.; Wang, N.; Fang, T.; Sun, M.; Wei, Y.; Yuan, J. Single-Chain Polymer Nanoparticles: Mimic the Proteins. *Polymer* **2015**, *66*, A11–A21. (b) Mavila, S.; Eivgi, O.; Berkovich, I.; Lemcoff, N. G. Intramolecular Cross-Linking Methodologies for the Synthesis of Polymer Nanoparticles. *Chem. Rev.* **2016**, *116* (3), 878–961. (c) Huurne, G. M. ter; Palmans, A. R. A.; Meijer, E. W. Supramolecular Single-Chain Polymeric Nanoparticles. *CCS Chem.* **2019**, 64–82.
43. (a) Artar, M.; Huerta, E.; Meijer, E. W.; Palmans, A. R. A. Dynamic Single Chain Polymeric Nanoparticles: From Structure to Function. *ACS Symp. Ser.* **2014**, *1170*, 313–325. (b) Frank, P.; Prasher, A.; Tuten, B.; Chao, D.; Berda, E. Characterization of Single-Chain Polymer Folding Using Size Exclusion Chromatography with Multiple Modes of Detection. *Appl. Petrochemical Res.* **2014**, 9–17. (c) Lyon, C. K.; Prasher,

A.; Hanlon, A. M.; Tuten, B. T.; Tooley, C. A.; Frank, P. G.; Berda, E. B. A Brief User's Guide to Single-Chain Nanoparticles. *Polym. Chem.* **2015**, *6*, 181–197.

44. (a) Beck, J. B.; Killops, K. L.; Kang, T.; Sivanandan, K.; Bayles, A.; Mackay, M. E.; Wooley, K. L.; Hawker, C. J. Facile Preparation of Nanoparticles by Intramolecular Cross-Linking of Isocyanate Functionalized Copolymers. *Macromolecules* **2009**, *42* (15), 5629–5635. (b) Hansell, C. F.; Lu, A.; Patterson, J. P.; O'Reilly, R. K. Exploiting the Tetrazine-Norbornene Reaction for Single Polymer Chain Collapse. *Nanoscale* **2014**, *6*, 4102–4107. (c) Song, C.; Li, L.; Dai, L.; Thayumanavan, S. Responsive Single-Chain Polymer Nanoparticles with Host-Guest Features. *Polym. Chem.* **2015**, *6* (26), 4828–4834.
45. V. W. Kuhn, H. Majer, Die Selbstvernetzung von Fadenmolekülen. *Macromol. Chem. Phys.* **1956**, *18* (1), 239–253.
46. (a) Mecerreyes, D.; Lee, V.; Hawker, C. J.; Hedrick, J. L.; Wursch, A.; Volksen, W.; Magbitang, T.; Huang, E.; Miller, R. D. Novel Approach to Functionalized Nanoparticles: Self-Crosslinking of Macromolecules in Ultradilute Solution. *Adv. Mater.* **2001**, *13* (3), 204–208. (b) Zhu, B.; Ma, J.; Li, Z.; Hou, J.; Cheng, X.; Qian, G.; Liu, P.; Hu, A. Formation of Polymeric Nanoparticles via Bergman Cyclization Mediated Intramolecular Chain Collapse. *J. Mater. Chem.* **2011**, *21* (8), 2679–2683. (c) Tuten, B. T.; Chao, D.; Lyon, C. K.; Berda, E. B. Single-Chain Polymer Nanoparticles via Reversible Disulfide Bridges. *Polym. Chem.* **2012**, *3* (11), 3068–3071. (d) Chao, D.; Jia, X.; Tuten, B.; Wang, C.; Berda, E. B. Controlled Folding of a Novel Electroactive Polyolefin via Multiple Sequential Orthogonal Intra-Chain Interactions. *Chem. Commun.* **2013**, *49* (39), 4178–4180. (e) Sanchez-Sanchez, A.; Arbe, A.; Colmenero, J.; Pomposo, J. A. Metallo-Folded Single-Chain Nanoparticles with Catalytic Selectivity. *ACS Macro Lett.* **2014**, *3* (5), 439–443. (f) Frank, P. G.; Tuten, B. T.; Prasher, A.; Chao, D.; Berda, E. B. Intra-Chain Photodimerization of Pendant Anthracene Units as an Efficient Route to Single-Chain Nanoparticle Fabrication. *Macromol. Rapid Commun.* **2014**, *35* (2), 249–253.
47. (a) De Luzuriaga, A. R.; Ormategui, N.; Grande, H. J.; Odriozola, I.; Pomposo, J. A.; Loinaz, I. Intramolecular Click Cycloaddition: An Efficient Room-Temperature Route towards Bioconjugable Polymeric Nanoparticles. *Macromol. Rapid Commun.* **2008**, *29* (12-13), 1156–1160. (b) De Luzuriaga, A. R.; Perez-Baena, I.; Montes, S.; Loinaz, I.; Odriozola, I.; García, I.; Pomposo, J. A. New Route to Polymeric Nanoparticles by Click Chemistry Using Bifunctional Cross-Linkers. *Macromol. Symp.* **2010**, *296* (1), 303–310. (c) Perez-Baena, I.; Loinaz, I.; Padro, D.; García, I.; Grande, H. J.; Odriozola, I. Single-Chain Polyacrylic Nanoparticles with Multiple Gd(Ⅲ) Centres as Potential MRI Contrast Agents. *J. Mater. Chem.* **2010**, *20* (33), 6916–6922. (d) Ormategui, N.; Garcia, I.; Padro, D.; Cabanero, G.; Grande, H. J.; Loinaz, I. Synthesis of Single Chain Thermoresponsive Polymer Nanoparticles. *Soft Matter* **2012**, *8* (3), 734–740.

48. (a) Seo, M.; Beck, B. J.; Paulusse, J. M. J.; Hawker, C. J.; Kim, S. Y. Polymeric Nanoparticles via Noncovalent Cross-Linking of Linear Chains. *Macromolecules* **2008**, *41* (17), 6413–6418. (b) Mes, T.; Van Der Weegen, R.; Palmans, A. R. A.; Meijer, E. W. Single-Chain Polymeric Nanoparticles by Stepwise Folding. *Angew. Chem. Int. Ed.* **2011**, *50* (22), 5085–5089. (c) Romulus, J.; Weck, M. Single-Chain Polymer Self-Assembly Using Complementary Hydrogen Bonding Units. *Macromol. Rapid Commun.* **2013**, *34* (19), 1518–1523. (d) Cheng, C. C.; Chang, F. C.; Yen, H. C.; Lee, D. J.; Chiu, C. W.; Xin, Z. Supramolecular Assembly Mediates the Formation of Single-Chain Polymeric Nanoparticles. *ACS Macro Lett.* **2015**, *4* (10), 1184–1188.
49. (a) Mavila, S.; Diesendruck, C. E.; Linde, S.; Amir, L.; Shikler, R.; Lemcoff, N. G. Polycyclooctadiene Complexes of Rhodium(I): Direct Access to Organometallic Nanoparticles. *Angew. Chem. Int. Ed.* **2013**, *52* (22), 5767–5770. (b) Willenbacher, J.; Altintas, O.; Trouillet, V.; Knöfel, N.; Monteiro, M. J.; Roesky, P. W.; Barner-Kowollik, C. Pd-Complex Driven Formation of Single-Chain Nanoparticles. *Polym. Chem.* **2015**, *6* (24), 4358–4365. (c) Jeong, J.; Lee, Y. J.; Kim, B.; Kim, B.; Jung, K. S.; Paik, H. J. Colored Single-Chain Polymeric Nanoparticles via Intramolecular Copper Phthalocyanine Formation. *Polym. Chem.* **2015**, *6* (18), 3392–3397. (d) Wang, F.; Pu, H.; Jin, M.; Wan, D. Supramolecular Nanoparticles via Single-Chain Folding Driven by Ferrous Ions. *Macromol. Rapid Commun.* **2016**, *37* (4), 330–336.
50. (a) Foster, E. J.; Berda, E. B.; Meijer, E. W. Metastable Supramolecular Polymer Nanoparticles via Intramolecular Collapse of Single Polymer Chains. *J. Am. Chem. Soc.* **2009**, *131* (20), 6964–6966. (b) Berda, E. B.; Foster, E. J.; Meijer, E. W. Toward Controlling Folding in Synthetic Polymers: Fabricating and Characterizing Supramolecular Single-Chain Nanoparticles. *Macromolecules* **2010**, *43* (3), 1430–1437. (c) Foster, E. J.; Berda, E. B.; Meijer, E. W. Tuning the Size of Supramolecular Single-Chain Polymer Nanoparticles. *J. Polym. Sci. Part A Polym. Chem.* **2011**, *49* (1), 118–126. (d) Stals, P. J. M.; Gillissen, M. A. J.; Nicolaÿ, R.; Palmans, A. R. A.; Meijer, E. W. The Balance between Intramolecular Hydrogen Bonding, Polymer Solubility and Rigidity in Single-Chain Polymeric Nanoparticles. *Polym. Chem.* **2013**, *4* (8), 2584–2597. (e) Hosono, N.; Gillissen, M. A. J.; Li, Y.; Sheiko, S. S.; Palmans, A. R. A.; Meijer, E. W. Orthogonal Self-Assembly in Folding Block Copolymers. *J. Am. Chem. Soc.* **2013**, *135* (1), 501–510.
51. (a) Bai, Y.; Feng, X.; Xing, H.; Xu, Y.; Kim, B. K.; Baig, N.; Zhou, T.; Gewirth, A. A.; Lu, Y.; Oldfield, E.; Zimmerman, S. C. A Highly Efficient Single-Chain Metal-Organic Nanoparticle Catalyst for Alkyne-Azide "Click" Reactions in Water and in Cells. *J. Am. Chem. Soc.* **2016**, *138* (35), 11077–11080. (b) Liu, Y.; Pujals, S.; Stals, P. J. M.; Paulöhrl, T.; Presolski, S. I.; Meijer, E. W.; Albertazzi, L.; Palmans, A. R. A. Catalytically Active Single-Chain Polymeric Nanoparticles: Exploring Their Functions in Complex Biological Media. *J. Am. Chem. Soc.* **2018**, *140* (9), 3423–3433. (c) Rothfuss,

H.; Knöfel, N. D.; Roesky, P. W.; Barner-Kowollik, C. Single-Chain Nanoparticles as Catalytic Nanoreactors. *J. Am. Chem. Soc.* **2018**, *140* (18), 5875–5881.

52. (a) Heiler, C.; Bastian, S.; Lederhose, P.; Blinco, J. P.; Blasco, E.; Barner-Kowollik, C. Folding Polymer Chains with Visible Light. *Chem. Commun.* **2018**, *54* (28), 3476–3479. (b) Delafresnaye, L.; Zaquen, N.; Kuchel, R. P.; Blinco, J. P.; Zetterlund, P. B.; Barner-Kowollik, C. A Simple and Versatile Pathway for the Synthesis of Visible Light Photoreactive Nanoparticles. *Adv. Funct. Mater.* **2018**, *28* (23), 1800342.
53. Rubio-Cervilla, J.; Frisch, H.; Barner-Kowollik, C.; Pomposo, J. A. Synthesis of Single-Ring Nanoparticles Mimicking Natural Cyclotides by a Stepwise Folding-Activation-Collapse Process. *Macromol. Rapid Commun.* **2019**, *40* (1), 1800491.
54. (a) Dirlam, P. T.; Kim, H. J.; Arrington, K. J.; Chung, W. J.; Sahoo, R.; Hill, L. J.; Costanzo, P. J.; Theato, P.; Char, K.; Pyun, J. Single Chain Polymer Nanoparticles via Sequential ATRP and Oxidative Polymerization. *Polym. Chem.* **2013**, *4* (13), 3765. (b) Wen, J.; Yuan, L.; Yang, Y.; Liu, L.; Zhao, H. Self-Assembly of Monotethered Single-Chain Nanoparticle Shape Amphiphiles. *ACS Macro Lett.* **2013**, *2* (2), 100–106. (c) Roy, R. K.; Lutz, J. F. Compartmentalization of Single Polymer Chains by Stepwise Intramolecular Cross-Linking of Sequence-Controlled Macromolecules. *J. Am. Chem. Soc.* **2014**, *136* (37), 12888–12891. (d) Tanaka, R.; Watanabe, K.; Yamamoto, T.; Tajima, K.; Isono, T.; Satoh, T. A Facile Strategy for Manipulating Micellar Size and Morphology through Intramolecular Cross-Linking of Amphiphilic Block Copolymers. *Polym. Chem.* **2017**, *8* (23), 3647–3656. (e) Cui, Z.; Cao, H.; Ding, Y.; Gao, P.; Lu, X.; Cai, Y. Compartmentalization of an ABC Triblock Copolymer Single-Chain Nanoparticle: Via Coordination-Driven Orthogonal Self-Assembly. *Polym. Chem.* **2017**, *8* (24), 3755–3763.
55. Zhang, J.; Gody, G.; Hartlieb, M.; Catrouillet, S.; Moffat, J.; Perrier, S. Synthesis of Sequence-Controlled Multiblock Single Chain Nanoparticles by a Stepwise Folding-Chain Extension-Folding Process. *Macromolecules* **2016**, *49* (23), 8933–8942.
56. Harth, E.; Van Horn, B.; Lee, V. Y.; Germack, D. S.; Gonzales, C. P.; Miller, R. D.; Hawker, C. J. A Facile Approach to Architecturally Defined Nanoparticles via Intramolecular Chain Collapse. *J. Am. Chem. Soc.* **2002**, *124* (29), 8653–8660.
57. Zhou, F.; Xie, M.; Chen, D. Structure and Ultrasonic Sensitivity of the Superparticles Formed by Self-Assembly of Single Chain Janus Nanoparticles. *Macromolecules* **2014**, *47* (1), 365–372.
58. Wen, W.; Huang, T.; Guan, S.; Zhao, Y.; Chen, A. Self-Assembly of Single Chain Janus Nanoparticles with Tunable Liquid Crystalline Properties from Stilbene-Containing Block Copolymers. *Macromolecules* **2019**, *52* (8), 2956–2964.
59. Matsumoto, M.; Terashima, T.; Matsumoto, K.; Takenaka, M.; Sawamoto, M. Compartmentalization Technologies via Self-Assembly and Cross-Linking of

Amphiphilic Random Block Copolymers in Water. *J. Am. Chem. Soc.* **2017**, *139* (21), 7164–7167.

60. Jiang, L.; Xie, M.; Dou, J.; Li, H.; Huang, X.; Chen, D. Efficient Fabrication of Pure, Single-Chain Janus Particles through Their Exclusive Self-Assembly in Mixtures with Their Analogues. *ACS Macro Lett.* **2018**, *7* (11), 1278–1282.
61. (a) Astruc, D. The Metathesis Reactions: From a Historical Perspective to Recent Developments. *New J. Chem.* **2005**, *29* (1), 42–56. (b) Monsaert, S.; Lozano Vila, A.; Drozdzak, R.; Van Der Voort, P.; Verpoort, F. Latent Olefin Metathesis Catalysts. *Chem. Soc. Rev.* **2009**, *38* (12), 3360–3372.
62. (a) Olayo-Valles, R.; Guo, S.; Lund, M. S.; Leighton, C.; Hillmyer, M. A. Perpendicular Domain Orientation in Thin Films of Polystyrene-Polylactide Diblock Copolymers. *Macromolecules* **2005**, *38* (24), 10101–10108. (b) Keen, I.; Yu, A.; Cheng, H.; Jack, K. S.; Nicholson, T. M.; Whittaker, A. K.; Blakey, I. Control of the Orientation of Symmetric Poly(Styrene)-*block*-Poly(D,L-Lactide) Block Copolymers Using Statistical Copolymers of Dissimilar Composition. *Langmuir* **2012**, *28* (45), 15876–15888.
63. (a) Zalusky, A. S.; Olayo-Valles, R.; Taylor, C. J.; Hillmyer, M. A. Mesoporous Polystyrene Monoliths. *J. Am. Chem. Soc.* **2001**, *123* (7), 1519–1520. (b) Seo, M.; Amendt, M. A.; Hillmyer, M. A. Cross-Linked Nanoporous Materials from Reactive and Multifunctional Block Polymers. *Macromolecules* **2011**, *44* (23), 9310–9318.

Chapter 2

Intramolecular Olefin Methathesis for Synthesis of Single-Chain Nanoparticles in a Size-Controlled Manner

2.1 Introduction

The intramolecular crosslinking of a single polymer chain leading to single-chain nanoparticles (SCNPs) has rapidly emerged as a unique approach to lead the novel polymer architecture and the according properties.[1-4] A variety of highly efficient crosslinking chemistries have been applied to generate SCNPs from linear precursors possessing crosslinkable functionalities. For example, Hawker et al. synthesized a series of SCNPs via the intramolecular thermal dimerization of the benzocyclobuten (BCB) group.[5,6] In addition, the copper-mediated azide-alkyne click reaction,[7-10] Glaser-Hay coupling,[11-13] thiol-ene/thiol-yne click chemistry,[14,15] etc.,[16-18] have also been employed as a crosslinking reaction to construct SCNPs. On the other hand, the establishment of a simple, yet versatile intramolecular crosslinking protocol still remains challenging because the present approaches sometimes have the following problems: (1) the preparation of the precursor requires a complicated multistep synthesis, (2) the crosslinking reaction requires harsh reaction conditions, and (3) the polymer main chain is limited to hydrocarbons like styrenic and arylate polymers.

The other inherent problem of the reported intramolecular crosslinking is the difficulty in size control of the resultant SCNPs. Since the chain dimensions of SCNPs affects their properties as well as the self-assembling behavior when they are applied to the BCP system,[19,20] this particular aspect is quite crucial. Although several research groups succeeded in regulating the size of the SCNPs by varying the crosslinkable functionality content or the molecular weight of the precursor,[15,21-23] a systematic examination of the SCNP size control is still a remaining task. Hence, of particular importance is to identify the factors involving the primary structures of the linear precursor as well as the crosslinking reaction conditions.

Therefore, the aim of this study is to provide a general method to produce SCNPs in a size-controlled manner. Such a methodology has to meet the following criteria: (1) the linear precursor can be prepared in a simple manner, (2) the crosslinking can be implemented under mild reaction conditions, (3) various kinds of polymer main chains can be applied, and (4) the size of the resultant SCNPs can be precisely controlled. For achieving these requirements, one of the effective approaches should be the intramolecular olefin metathesis of the linear precursor possessing pendant olefin groups. In fact, Vandeveer et al. successfully applied the olefin metathesis approach to the dendrimers possessing multiple homoallyl end groups, which produced the well-defined organic nanoparticles.[24] The advantage of this approach is that the precursor possessing pendant olefin groups can be easily prepared because C=C double bonds are typically stable under a wide range of polymerization reaction conditions. When combined with the Grubbs' catalysts for the crosslinking reaction, it is highly expected that the crosslinking reaction can be implemented under a mild condition due to the high reactivity of the catalyst. Furthermore, the excellent functional group tolerance of Grubbs' catalysts could allow the application of a wide range of linear precursors possessing various functionalities on the side chain and main chain structures. Therefore, the ruthenium-catalyzed olefin metathesis holds a significant potential to establish a general method of the intramolecular crosslinking. Indeed, Coates et al.[25] studied the intramolecular olefin metathesis of the poly(carbonate) precursor and observed the size variation of the resultant SCNPs versus the reaction time. Meanwhile, poly(norbornene dicarboximide)-based SCNPs, whose diameter was varied depending on the molecular weight of the precursor, were recently fabricated using the intramolecular olefin metathesis.[26] While the ruthenium-catalyzed olefin metathesis has been utilized as a crosslinking reaction as mentioned above, the versatility of

this tool, nevertheless, has not been fully investigated. In addition, further investigation about the size of SCNPs should be carried out to achieve the size-controlled synthesis of SCNPs by the olefin metathesis approach.

In this chapter, the author reports the comprehensive investigation of the ruthenium-catalyzed intramolecular olefin metathesis of a variety of linear precursors possessing pendant olefin groups, leading to the SCNPs with a controllable size. First, the author employed the methacrylate copolymers of *n*-butyl methacrylate (BMA) and 3-butenyl methacrylate (3BMA), i.e., P(BMA-*co*-3BMA), with various molecular weights and olefin contents as a model precursor system and conducted a comprehensive examination on the effect of the structural factors as well as the reaction conditions on the SCNP formation. The intramolecular olefin metathesis of P(BMA-*co*-3BMA)s efficiently gave the SCNPs with controlled diameters by adjusting the primary structures of the precursors or the solvent quality of the reaction medium. Furthermore, the present approach was expanded to the poly(acrylate), poly(ester), and poly(styrene-*block*-methacrylate) precursors possessing pendant olefin groups in order to demonstrate the versatility of the intramolecular olefin metathesis.

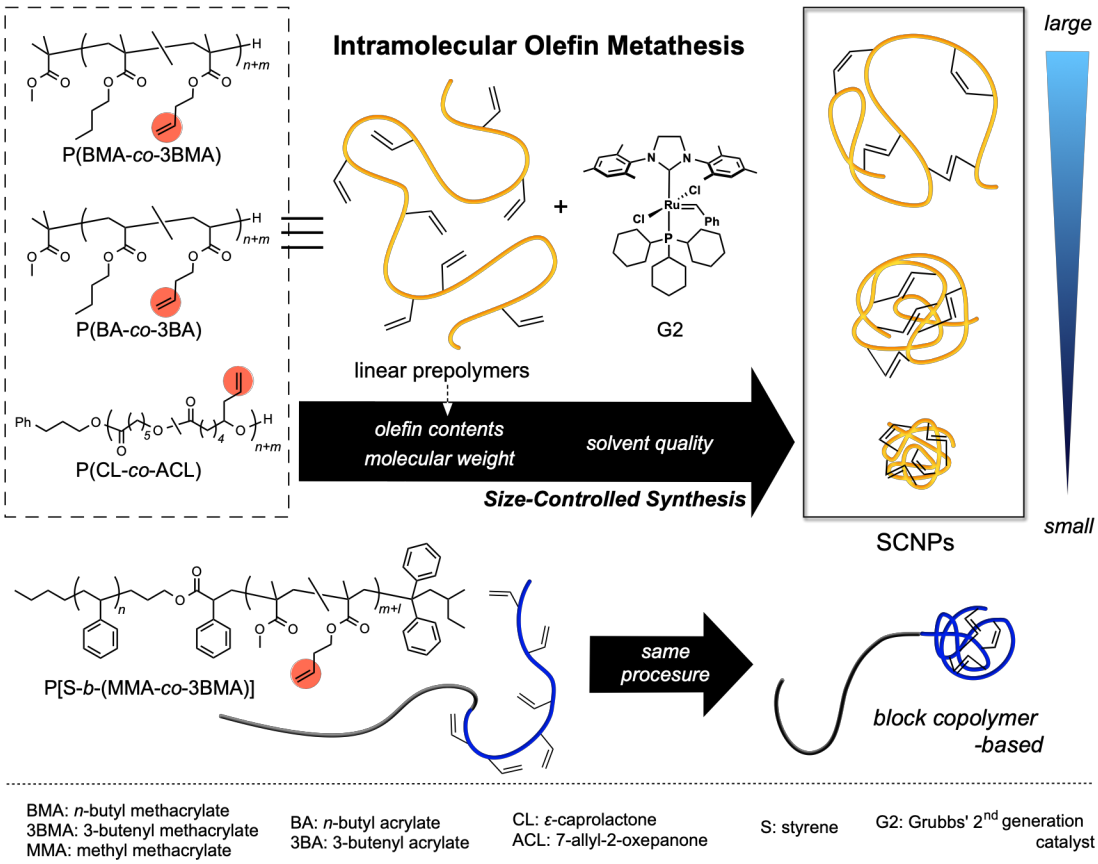

Scheme 2.1. Size-controlled synthesis of SCNPs from various linear prepolymers possessing pendant olefin groups via intramolecular olefin metathesis.

2.2 Experimental Section

2.2.1 Materials

1-*Tert*-butyl-4,4,4-tris(dimethylamino)-2,2-bis[tris(dimethylamino)phosphoranylide namino]-2Λ^5,4Λ^5,catenadi(phosphazene) (*t*-Bu-P$_4$; Sigma-Aldrich, 0.8 mol L^{-1} in *n*-hexane), benzoic acid (TCI, >99.0%), *N*-(trimethylsilyl)bis(trifluoromethanesulfonyl)imide (Me_3SiNTf_2; TCI, >95.0%), 1,1,4,7,10,10-hexamethyltriethylenetetramine (HMTETA; Sigma-Aldrich, 97.0%), *n*-butyllithium (*n*-BuLi; Kanto Chemical Co., Inc., 1.6 mol L^{-1} in *n*-hexane), diphenyl phosphate (DPP; TCI, >99.0%), Amberlyst® A21 (Organo), Grubbs 2nd generation catalyst (G2; Sigma-Aldrich), ethyl vinyl ether (TCI, >98.0%), and QuadraSil® AP (Sigma-Aldrich) were purchased and used as recieved. *n*-Butyl methacrylate (BMA; TCI, >99.0%), *n*-butyl acrylate (*n*BA; TCI, >99.0%), 1-methoxy-1-trimethylsiloxy-2-methyl-1-propene (Me-SKA; TCI, >95.0%), ε-caprolactone (CL, TCI, >99.0%), and 3-phenyl-1-propanol (PPA; TCI, >98.0%) were purchased and purified by distillation over CaH_2 under vacuum, then stored in a glovebox. 3-Butenyl methacrylate (3BMA)[27], 3-butenyl acrylate (3BA)[27], 7-allyl-2-oxcepanone (ACL)[28], and 1-methoxy-1-triisopropylsiloxy-2-methyl-1-propene (*i*Pr-SKA)[29] were prepared according to reported methods, then purified by distillation over CaH_2 under vacuum and stored under an argon atmosphere. Commercially available dry toluene (Kanto Chemical Co., Inc., >99.5%, water content, <0.001%), commercially-available dry CH_2Cl_2 (Kanto Chemical Co., Inc., >99.5%, water content, <0.001%), and commercially-available dry THF (Kanto Chemical Co., Inc., >99.5%, water content, <0.001%) were further purified using an MBRAUN MB-SPS Compact solvent purification system equipped with a MB-KOL-C column and a MB-KOL-A column (for dry toluene), a MB-KOL-A column and a MB-KOL-A column (for dry CH_2Cl_2),

or a MB-KOL-A column and a MB-KOL-M Type 1 column (for dry THF), which were then directly used for the polymerizations.

2.2.2 Instruments

The polymerization was carried out in an MBRAUN stainless steel glovebox equipped with a gas purification system (molecular sieves and copper catalyst) and a dry argon atmosphere (H_2O, O_2 <1 ppm). The moisture and oxygen contents in the glovebox were monitored by an MB-MO-SE 1 moisture sensor and an MB-OX-SE 1 oxygen sensor, respectively. The ^{1}H (400 MHz) and ^{13}C NMR (100 MHz) spectra were obtained using a JEOL JNM-ESC400 instrument at 25 °C. The size exclusion chromatography (SEC) was performed at 40 °C in THF (flow rate, 1.0 mL min^{-1}) using a Shodex GPC-101 gel permeation chromatography system (Shodex DU-2130 dual pump, Shodex RI-71 reflective index detector, and Shodex ERC-3125SN degasser) equipped with a Shodex KF-G guard column (4.6 mm × 10 mm; particle size, 8 μm) and two Shodex KF-804L columns (linear, 8.0 mm × 300 mm; particle size, 7 μm). The Fourier transform infrared spectroscopy (FT-IR) analysis was carried out using a PerkinElmer Frontier MIR spectrometer equipped with a single reflection diamond universal attenuated total refletion (ATR) accessory. The absolute molecular weight and intrinsic viscosity of the polymer samples were determined by triple detection SEC in THF (flow rate, 1.0 mL min^{-1}) at 40 °C using an Agilent 1100 series instrument equipped with two Shodex KF-805L columns (linear, 8.0 mm × 300 mm; particle size, 10 μm), a Shodex KF-800D column (linear, 8.0 mm × 100 mm; particle size, 10 μm), a DAWN 8+ multiangle laser light scattering detector (Wyatt Technology), an Optilab rEX refractive index detector (Wyatt Technology), and a ViscoStar viscosity detector (Wyatt Technology). The

hydrodynamic radius (R_h) of the polymers were determined by the dynamic light scattering (DLS) measurement in THF using an Otsuka Electronics FDLS-3000 light scattering spectrophotometer equipped with a solid state laser (λ = 532 nm; detection angle, 90 °; temp., 25 °C). Matrix-assisted laser desorption ionization time-of-flight mass spectrometry (MALDI−TOF MS) of the obtained polymers was performed using an AB SciEX TOF/TOF 5800 system equipped with a 349-nm Nd:YAG laser (3-ns pulse width). One thousand shots were accumulated for the spectra in the reflector mode and calibrated using polystyrene as the internal standard. Samples for the MALDI−TOF MS were prepared by mixing the polymer (1.0 mg), the matrix (dithranol, 2.0 mg), and the cationizing agent (silver trifluoroacetate, 1.0 mg) in THF (100 μL). A sample plate, Opti-TOF^{TM} 384-Well (123 × 81 mm), was used for the measurement.

2.2.3 Synthesis of statistical copolymer of BMA and 3BMA ($P(BMA_{0.70}$-co-$3BMA_{0.30})_{55k}$).

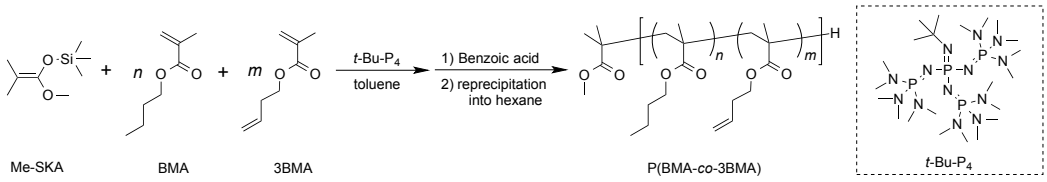

A typical copolymerization procedure of BMA and 3BMA is as follows (method A): In the glovebox, the mixture of BMA (861 mg, 6.05 mmol) and 3BMA (367 mg, 2.59 mmol) in toluene (6.30 mL) was dropwise added to a solution of Me-SKA (4.30 mg, 24.7 μmol) and *t*-Bu-P_4 (50.0 μL, 0.50 μmol, 0.010 mol L^{-1} in toluene) in toluene (1.00 mL) over 3 min at 27 °C. After stirring for 7 h, the polymerization was quenched by the addition of a small amount of benzoic acid. The crude product was purified by reprecipitation in *n*-hexane to give $P(BMA_{0.70}$-*co*-$3BMA_{0.30})_{55k}$ as a colorless viscous liquid. Yield: 1.00 g (81.3%). ^{1}H

NMR (400 MHz, $CDCl_3$): δ (ppm) 5.87−5.72 (m, 1H × *m*, −C*H*=CH_2), 5.20−5.05 (m, 2H × *m*, −CH=CH_2), 4.19−3.71 (m, 2H × (*m*+*n*), −OCH_2(CH_2)$_2$$CH_3$, −OC$H_2$$CH_2$CH=$CH_2$), 3.63 (s, 3H, −OC$H_3$), 2.45−2.30 (m, 2H × *m*, −OCH_2CH_2CH=CH_2), 2.13−1.31 (m, 2H × (*m*+*n*), −C$H_2$$CCH_3$($COO(CH_2)_3CH_3$)−, −C$H_2$$CCH_3$($COO(CH_2)_2CH=CH_2$)−), 1.70−1.51 (m, 2H × *n*, −OCH_2C$H_2$$CH_2CH_3$), 1.51−1.31 (m, 2H × *n*, −O(CH_2)$_2$C$H_2$$CH_3$), and 1.12-0.56 (m, 6H × *n* + 3H × *m*, −O(CH_2)$_3$CH_3, −CH_2CCH_3($COO(CH_2)_3CH_3$)−, −CH_2CCH_3($COO(CH_2)_2CH=CH_2$)−). $M_{n,SEC}$ = 55,400 g mol^{-1}, $Đ$ = 1.18 (THF), the mole fraction of 3BMA units in the copolymer (F_{3BMA}) = 0.30.

2.2.4 Synthesis of poly(methacrylate)-based SCNP from P(BMA$_{0.70}$-co-3BMA$_{0.30}$)$_{55k}$ (NP$_{BMA}$1).

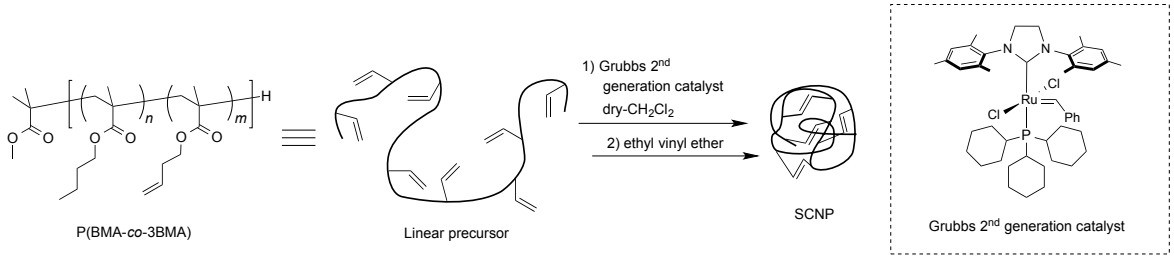

A typical intramolecular crosslinking procedure is as follows (method B): P($BMA_{0.70}$-*co*-$3BMA_{0.30}$)$_{55k}$ (104 mg, 0.221 mmol olefin-containing units) was dissolved in dry-CH_2Cl_2 (130 mL). After degassing by N_2 bubbling, Grubbs 2nd generation catalyst (G2; 3.8 mg, 4.5 μmol) was added to the mixture. After stirring for 10 h under an N_2 atmosphere at 30 °C, the reaction was quenched by the addition of ethyl vinyl ether. The solvent was removed by 2 evaporation, then the residue was dissolved in CH_2Cl_2 and treated with QuadraSil® AP to remove the residual G2. The obtained SCNP (NP_{BMA}1) was stored as a

stock solution in CH_2Cl_2. ^1H NMR (400 MHz, $CDCl_3$): δ (ppm) 5.87−5.72 (m, 1H × (*m*-s), −C*H*=CH_2), 5.72−5.25 (m, 1H × s, −C*H*=C*H*−), 5.20−5.05 (m, 2H × (*m*-s), −CH=CH_2), 4.54−3.33 (m, 2H × (*m*+*n*), −OC$H_2$$(CH_2)_2CH_3$, −OC$H_2$$CH_2CH$=$CH_2$, −OC$H_2$$CH_2CH$=CH−), 2.82−2.22 (m, 2H × *m*, −OCH_2CH_2CH=CH_2, −OCH_2CH_2CH=CH−), 2.22−1.16 (m, 2H × (*m*+*n*), −C$H_2$$CCH_3$(COO−)−), 1.71−1.51 (m, 2H × *n*, −OCH_2C$H_2$$CH_2CH_3$), 1.51−1.31 (m, 2H × *n*, −$O(CH_2)_2$C$H_2$$CH_3$), and 1.16-0.33 (m, 6H × *n* + 3H × *m*, −$O(CH_2)_3$CH_3, −CH_2CCH_3(COO−)−). $M_{n,SEC}$ = 48,200 g mol^{-1}, $Đ$ = 1.18 (THF), the conversion of the terminal olefins ($conv._{olefin}$) = 93%.

2.3 Results and Discussion

2.3.1 Synthesis of poly(methacrylate)-based SCNPs

2.3.1.1 Preparation of prepolymers possessing pendant olefin groups

In order to systematically investigate the SCNP formation through the intramolecular olefin metathesis reaction, a series of poly(methacrylate) possessing pendant olefin groups was employed as the linear prepolymer. The *n*-butyl methacrylate (BMA) and 3-butenyl methacrylate (3BMA) were chosen as the base monomer and crosslinkable monomer, respectively. For synthesizing such copolymers of BMA and 3BMA, i.e, P(BMA-*co*-3BMA)s, the group transfer polymerization (GTP), which is one of the living polymerization methods to produce poly[(meth)acrylate]s by the repetitive Michael addition, was employed because the side chain double bond of 3BMA is expected to remain intact under the GTP conditions.

Therefore, the initial effort was directed toward the establishment of a suitable GTP condition for the synthesis of P(BMA-*co*-3BMA)s with the desired total molecular weight and composition. After a thorough screening of the polymerization conditions, such as the choice of the initiator and catalyst as well as the catalyst loading, the author found that the combination of 1-methoxy-1-trimethylsiloxy-2-methyl-1-propene (Me-SKA) and 1-*tert*-butyl-4,4,4-tris(dimethylamino)-2,2-bis[tris(dimethylamino)phosphoranylidenamino]-2Λ^5,4Λ^5,catenadi(phosphazene) (*t*-Bu-P_4) as the initiator and catalyst, respectively, worked well to produce the well-defined P(BMA-*co*-3BMA)s.

For the GTP of BMA and 3BMA with the $[BMA]_0/[3BMA]_0/[t\text{-Bu-}P_4]_0/[Me\text{-}SKA]_0$ ratio of 245/105/0.02/1 (entry 1 in **Table 2.1**), the monomer conversions of both BMA and 3BMA reached >99% after 10 h. Given that BMA and 3BMA are similar in chemical

structure, the obtained copolymers should have a random monomer sequence. The ^{1}H NMR spectrum of the product (**Figure 2.1**(a)) was reasonably assigned to the expected structure of P(BMA-*co*-3BMA). The mole fraction of the 3BMA units in the copolymer (F_{3BMA}) was determined to be 0.30 by the ^{1}H NMR analysis. The IR spectrum of the product showed absorption bands at 643, 1642 and 3049 cm^{-1} due to the C=CH$_2$ (**Figure 2.2**(a), see also **Figure S2.5**), confirming that the resultant copolymer definitely possessed the terminal olefin group of the 3BMA units. The size exclusion chromatography (SEC) trace of the product exhibited a unimodal peak with a dispersity ($Đ$) of 1.18, thus confirming the absence of side reactions, such as crosslinking between the pendant olefin groups. The number-average molecular weight estimated by SEC ($M_{n,SEC}$) was calculated to be 55,400 g mol^{-1}, and thus the obtained product was denoted as P(BMA$_{0.70}$-*co*-3BMA$_{0.30}$)$_{55k}$. In a similar manner, the P(BMA-*co*-3BMA)s with the $M_{n,SEC}$ of ca. 50,000 g mol^{-1} possessing the varied F_{3BMA} of 0.60 and 1.00, i.e., P(BMA$_{0.40}$-*co*-3BMA$_{0.60}$)$_{49k}$ and P(3BMA)$_{50k}$, respectively, were prepared by applying the [BMA]$_0$/[3BMA]$_0$/[*t*-Bu-P$_4$]$_0$/[Me-SKA]$_0$ ratios of 140/210/0.02/1 and 0/355/0.02/1, respectively (entries 2 and 3). In addition, the P(BMA-*co*-3BMA)s with varied molecular weights at the fixed F_{3BMA} value of 0.60, i.e., P(BMA$_{0.40}$-*co*-3BMA$_{0.60}$)$_{24k}$ and P(BMA$_{0.40}$-*co*-3BMA$_{0.60}$)$_{80k}$, were also prepared in accordance with the established method using the [BMA]$_0$/[3BMA]$_0$/[*t*-Bu-P$_4$]$_0$/[Me-SKA]$_0$ ratios of 70/105/0.01/1 and 210/315/0.02/1, respectively (entries 4 and 5).

Table 2.1. GTPs of BMA and 3BMA catalyzed by *t*-Bu-P_4 using Me-SKA as the initiator[a]

entry	polymer sample	$[BMA]_0/[3BMA]_0/[t\text{-Bu-}P_4]_0/[Me\text{-}SKA]_0$	F_{3BMA}[b, c]	$M_{n,SEC}$[d] (g mol^{-1})	$Đ$[d]	yield (%)
1	$P(BMA_{0.70}\text{-}co\text{-}3BMA_{0.30})_{55k}$	245/105/0.02/1	0.30	55,400	1.18	81.3
2	$P(BMA_{0.40}\text{-}co\text{-}3BMA_{0.60})_{49k}$	140/210/0.02/1	0.60	49,000	1.14	86.1
3	$P(3BMA)_{50k}$	0/355/0.02/1	1.00	50,200	1.21	87.1
4	$P(BMA_{0.40}\text{-}co\text{-}3BMA_{0.60})_{24k}$	70/105/0.01/1	0.60	23,700	1.12	74.6
5	$P(BMA_{0.40}\text{-}co\text{-}3BMA_{0.60})_{80k}$	210/315/0.02/1	0.60	79,700	1.22	88.5

[a]Polymerization conditions: Ar atmosphere; solvent, toluene; temp., 27 °C; polymerization time, 10 h; $[BMA+3BMA]_0$ = 1.0 mol L^{-1}. Conversions of BMA and 3BMA in all entries were determined as >99% by ^1H NMR in $CDCl_3$. [b]Mole fraction of 3BMA units in the copolymer. [c]Determined by ^1H NMR in $CDCl_3$. [d]Determined by SEC in THF using poly(methyl methacrylate) standards.

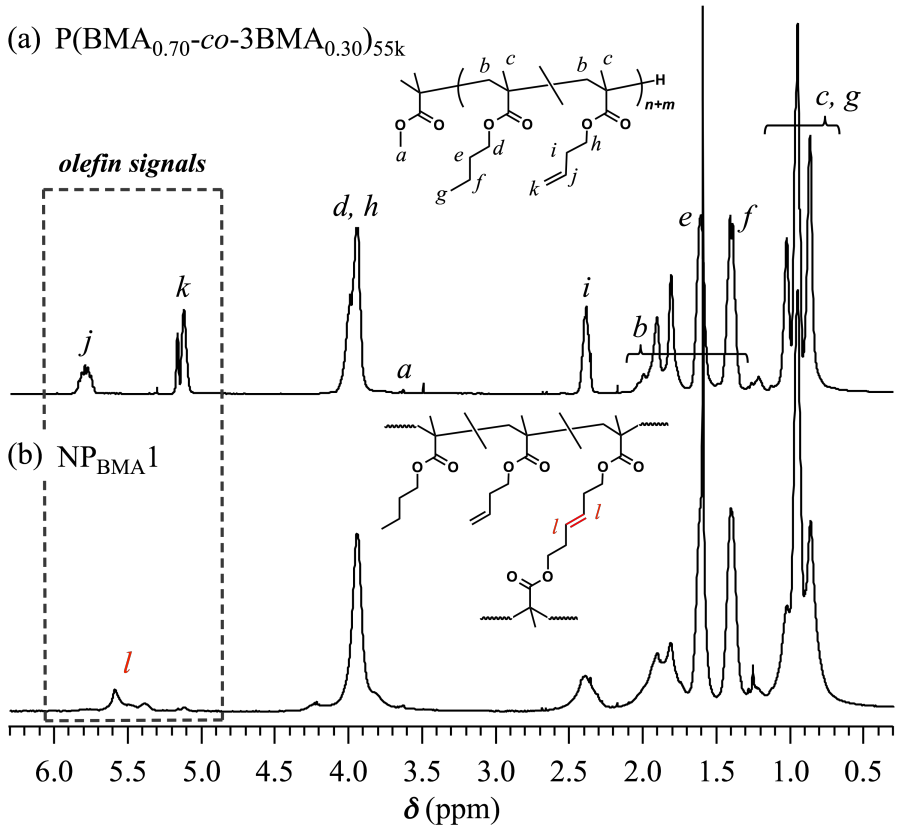

Figure 2.1. ^{1}H NMR spectra of (a) P(BMA$_{0.70}$-*co*-3BMA$_{0.30}$)$_{55k}$ and (b) NP$_{BMA}$1 in $CDCl_3$ (400 MHz).

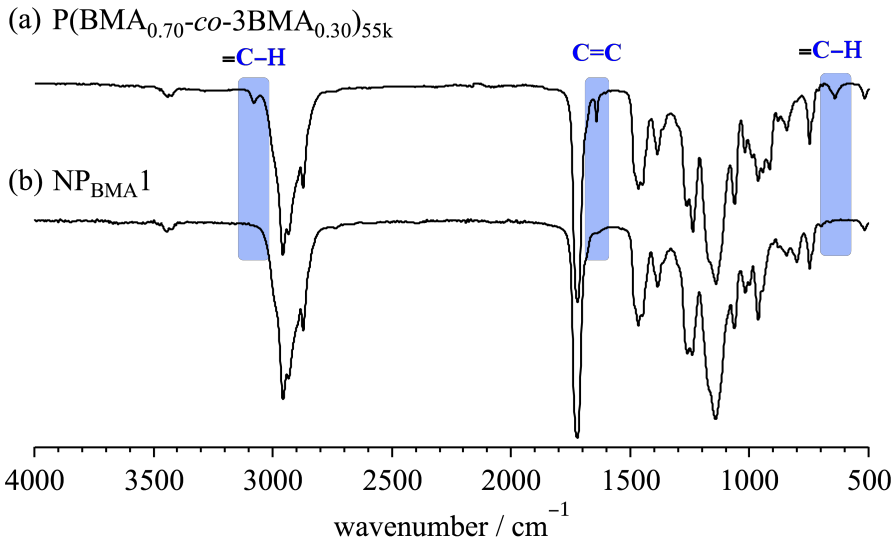

Figure 2.2. IR spectra of (a) P(BMA$_{0.70}$-*co*-3BMA$_{0.30}$)$_{55k}$ and (b) NP$_{BMA}$1.

2.3.1.2 Synthesis of SCNP via olefin metathesis

With a series of the P(BMA-*co*-3BMA)s in hand, the intramolecular olefin metathesis to produce the poly(methacrylate)-based SCNPs were investigated in the presence of Grubbs' 2nd generation catalyst (G2). First, the intramolecular olefin metathesis of $P(BMA_{0.70}\text{-}co\text{-}3BMA_{0.30})_{55k}$ was carried out under the highly diluted condition ($[P(BMA_{0.70}\text{-}co\text{-}3BMA_{0.30})_{55k}]_0$ = 0.80 g L^{-1}) in CH_2Cl_2 at 30 °C for 10 h in the presence of 2.0 mol % of G2 with respect to the pendant double bond (**Table 2.2**). As a result, the reaction homogeneously proceeded without gelation giving a soluble product after the treatment with ethyl vinyl ether followed by catalyst removal using a metal scavenger. In the ^{1}H NMR spectrum of the product, the intensity of the signals due to the terminal olefin protons (*j*, *k*) decreased and the new signals due to the internal olefin protons (*l*) appeared (**Figure 2.1**(b)). The conversion of the terminal olefins ($conv._{olefin}$) was calculated to be 93% by comparing the peak areas of the terminal and internal olefin signals. The IR spectrum of the product also supported the high olefin conversion. The characteristic absorption bands at 643, 1642 and 3049 cm^{-1} due to the terminal olefin were no longer observed in the IR spectrum of the resultant product (**Figure 2.2**(b)). Thus, the ^{1}H NMR and IR studies demonstrated the crosslink formation via the olefin metathesis reaction.

To ensure the intramolecular crosslink formation, SEC experiments were performed using the obtained product. As can be seen in **Figure 2.3**(a), the SEC trace of the crosslinked product exhibited a unimodal peak in the lower molecular weight region as compared to the linear prepolymer. The molecular weight at the peak top ($M_{p,SEC}$ = 58,600 g mol^{-1}) of the product is apparently lower than that of the linear prepolymer ($M_{p,SEC}$ = 67,400 g mol^{-1}), from which the shrinking factor, i.e., $\langle G \rangle = M_{p,SEC}(SCNP)/M_{p,SEC}(prepolymer)$, was calculated to be

0.87. These results implied a decrease in the hydrodynamic volume through the crosslinking reaction. In addition to the conventional SEC analysis, the absolute molecular weights ($M_{w,MALS}$s) were determined by the triple detection SEC consisting of multiangle light scattering (MALS), viscosity, and refractive index (RI) detectors. While the apparent hydrodynamic volume decreased by the crosslinking, the $M_{w,MALS}$ value of the product ($M_{w,MALS}$ = 83,400 g mol^{-1}) was found to be comparable to that of the linear prepolymer ($M_{w,MALS}$ = 81,600 g mol^{-1}). This guarantees the absence of undesired reactions, such as intermolecular coupling and main chain scission. Based on the ^{1}H NMR, IR, and SEC analyses, the author concluded that the crosslinking reaction via olefin metathesis proceeded in an intramolecular fashion, leading to the desired SCNP, $NP_{BMA}1$.

Table 2.2. Synthesis of SCNPs from various P(BMA-*co*-3BMA)s[a]

polymer sample	conv.$_{olefin}$[b] (%)	$M_{w,MALS}$[c] (g mol^{-1})	$M_{p,SEC}$[d] (g mol^{-1})	$Đ$[d]	$\langle G \rangle$[e]	$[\eta]$[c] (mL g^{-1})	$R_{h,DLS}$[f] (nm)	$R_{h,visc}$[g] (nm)
$P(BMA_{0.70}$-*co*-$3BMA_{0.30})_{55k}$	93	81,600	67,400	1.18	0.87	24.9	6.5	6.8
$NP_{BMA}1$		83,400	58,600	1.18		18.2	6.2	6.2
$P(BMA_{0.40}$-*co*-$3BMA_{0.60})_{49k}$	95	65,900	60,000	1.14	0.62	25.8	6.4	6.4
$NP_{BMA}2$		66,900	37,400	1.19		12.9	5.1	5.1
$P(3BMA)_{50k}$	94	74,700	65,600	1.21	0.46	27.0	6.0	6.8
$NP_{BMA}3$		84,200	30,500	1.19		9.5	4.8	4.9
$P(BMA_{0.40}$-*co*-$3BMA_{0.60})_{24k}$	97	33,100	24,200	1.11	0.71	13.5	4.6	4.0
$NP_{BMA}4$		34,800	17,100	1.10		8.3	3.5	3.6
$P(BMA_{0.40}$-*co*-$3BMA_{0.60})_{80k}$	95	95,000	91,500	1.22	0.58	33.3	6.9	7.8
$NP_{BMA}5$		90,900	52,800	1.23		15.9	6.0	6.1

[a]Reaction conditions: $[polymer]_0$ = 0.80 g L^{-1} in CH_2Cl_2; [3BMA units]/[G2] = 1/0.02; temp., 30 °C. [b]Determined by ^{1}H NMR in $CDCl_3$. [c]Determined by triple detection SEC in THF (0.30 mg mL^{-1}). [d]Determined by SEC in THF using poly(methyl methacrylate) standards. [e]Determined by $M_{p,SEC}$(SCNP)/$M_{p,SEC}$(linear). [f]Determined by DLS in THF (5.0 g L^{-1}, 25 °C). [g]$R_{h,visc.} = (3V_h/4\pi)^{1/3}$; V_h: hydrodynamic volume. V_h was calculated by Einstein-Simha equation ($V_h = M_{w,MALS}[\eta]/2.5N_A$; N_A: Avogadro's number).

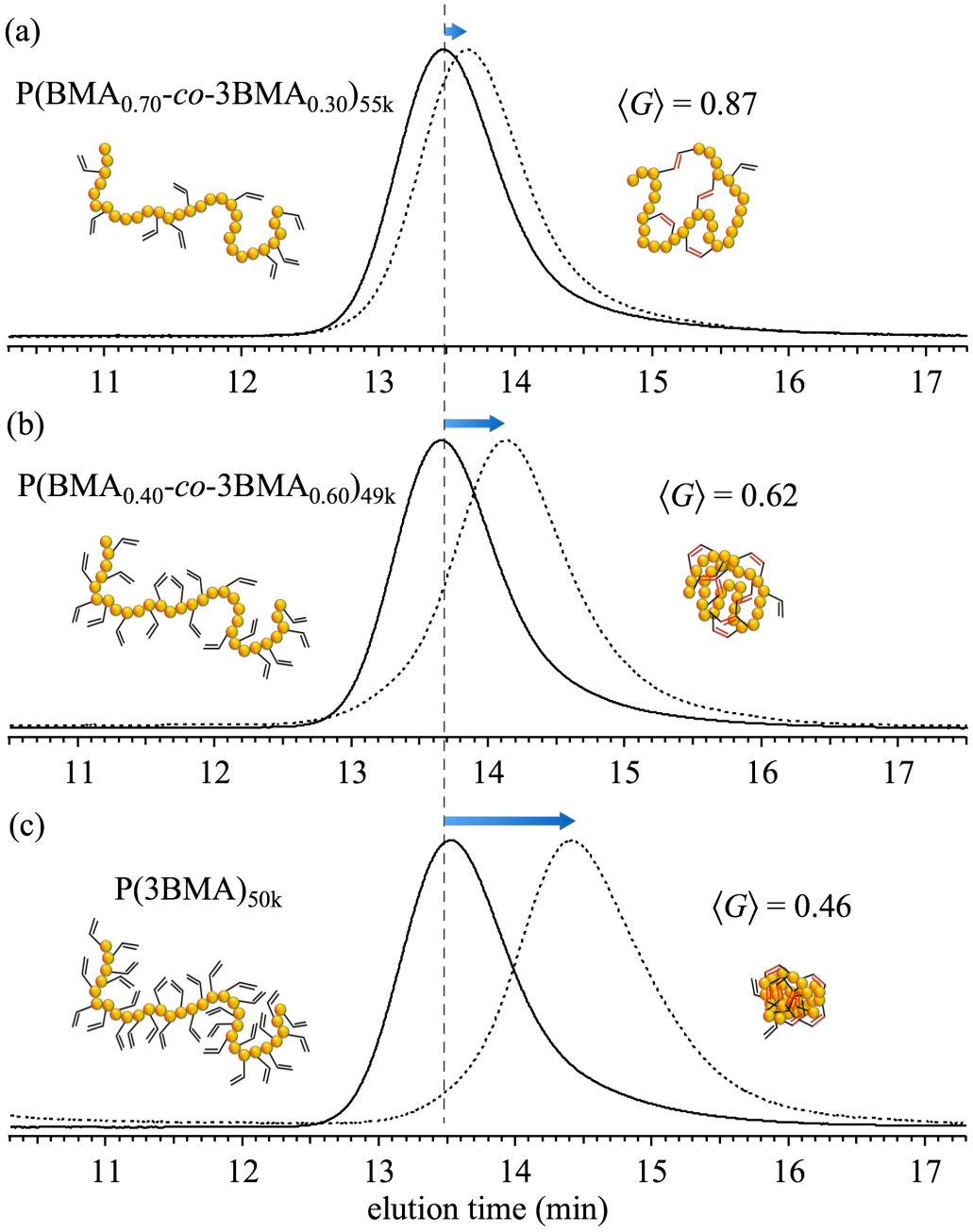

Figure 2.3. SEC traces of (a) $P(BMA_{0.70}\text{-}co\text{-}3BMA_{0.30})_{55k}$ and $NP_{BMA}1$, (b) $P(BMA_{0.40}\text{-}co\text{-}3BMA_{0.60})_{49k}$ and $NP_{BMA}2$, and (c) $P(3BMA)_{50k}$ and $NP_{BMA}3$ (eluent, THF; flow rate, 1.0 mL min^{-1}). Linear prepolymers and corresponding SCNPs are presented using solid and dashed lines, respectively.

The obtained $NP_{BMA}1$ was further characterized by viscometric and dynamic light scattering (DLS) measurements in order to gain information about its size in solution (**Table 2.2**). The intrinsic viscosity ([η]) of $NP_{BMA}1$ was determined to be 18.2 mL g^{-1} by the triple detection SEC in THF, which was apparently smaller than that of the linear prepolymer ([η] = 24.9 mL g^{-1}). This observation also supported the decrease in the hydrodynamic volume via the intramolecular olefin metathesis. The hydrodynamic radius ($R_{h,visc}$) of $NP_{BMA}1$ was calculated to be 6.2 nm based on the $M_{w,MALS}$ and [η] values. The DLS experiment using $NP_{BMA}1$ was also conducted in THF (5.0 g L^{-1}) at 25 °C (**Figure S2.6**), and the hydrodynamic radius ($R_{h,DLS}$ = 6.2 nm) well agreed with the $R_{h,visc}$ value. Notably, both the $R_{h,visc}$ and $R_{h,DLS}$ values for $NP_{BMA}1$ were smaller than those of $P(BMA_{0.70}\text{-}co\text{-}3BMA_{0.30})_{55k}$, which again confirmed that the linear prepolymer had indeed collapsed into an SCNP through the intramolecular olefin metathesis process. Thus, the author successfully established a general procedure to produce well-defined SCNPs via the intramolecular olefin metathesis.

2.3.1.3 Effect of olefin content on the SCNP formation

In order to probe the effect of the F_{3BMA} values on the SCNP formation, the SCNPs ($NP_{BMA}2$ and $NP_{BMA}3$ in **Table 2.2**) were synthesized using $P(BMA_{0.40}$-*co*-$3BMA_{0.60})_{49k}$ (F_{3BMA} = 0.60, $M_{n,SEC}$ = 49,000 g mol^{-1}, $Đ$ = 1.14) and $P(3BMA)_{50k}$ (F_{3BMA} = 1.00, $M_{n,SEC}$ = 50,200 g mol^{-1}, $Đ$ = 1.21), and compared to $NP_{BMA}1$ that had been prepared from $P(BMA_{0.70}$-*co*-$3BMA_{0.30})_{55k}$. The intramolecular olefin metathesis reactions of $P(BMA_{0.40}$-*co*-$3BMA_{0.60})_{49k}$ and $P(3BMA)_{50k}$ in CH_2Cl_2 also proceeded without gelation, which gave the corresponding SCNPs ($NP_{BMA}2$ and $NP_{BMA}3$, respectively) with the $conv._{olefin}$s of >90% (^{1}H NMR and IR spectra are shown in **Figures S2.7, S2.8, S2.10, and S2.11**). It is rather suprising that the intramolecular olefin metathesis of $P(3BMA)_{50k}$ proceeded up to a high $conv._{olefin}$ without intermolecular coupling even though the prepolymer consisted of 100 mol % 3BMA units.

As can be seen in **Figure 2.3**, the $\langle G \rangle$ value decreased with the increasing F_{3BMA} value of the linear prepolymer, i.e., 0.87 for $NP_{BMA}1$, 0.62 for $NP_{BMA}2$ and 0.46 for $NP_{BMA}3$, revealing that the higher crosslinking density resulted in the further reduction of the hydrodynamic volume. Indeed, all the $[\eta]$, $R_{h,visc}$, and $R_{h,DLS}$ values decreased in the following order: $NP_{BMA}1$ ($[\eta]$ = 18.2 mL g^{-1}, $R_{h,visc}$ = 6.2 nm and, $R_{h,DLS}$ = 6.2 nm) > $NP_{BMA}2$ ($[\eta]$ = 12.9 mL g^{-1}, $R_{h,visc}$ = 5.1 nm, and $R_{h,DLS}$ = 5.1 nm) > $NP_{BMA}3$ ($[\eta]$ = 9.5 mL g^{-1},$R_{h,visc}$ = 4.9 nm, and $R_{h,DLS}$ = 4.8 nm) (DLS results are shown in **Figures S2.9** and **S2.12**). Given that these linear prepolymers have similar $M_{n,SEC}$ values, the effect of the prepolymer molecular weight can be neglected. Thus, the author found that varying the olefin content of the linear prepolymer is an effective approach to control the SCNP size.

2.3.1.4 Effect of molecular weight on the SCNP formation

It is reasonably expected that the molecular weight of the linear prepolymer directly influences the size of the resultant SCNPs. To prove the effect of the prepolymer molecular weight on the SCNP size, we compared the SCNP formations using a set of linear P($BMA_{0.40}$-*co*-$3BMA_{0.60}$)s with varying molecular weights (P($BMA_{0.40}$-*co*-$3BMA_{0.60}$)$_{24k}$, P($BMA_{0.40}$-*co*-$3BMA_{0.60}$)$_{49k}$, and P($BMA_{0.40}$-*co*-$3BMA_{0.60}$)$_{80k}$), while fixing the F_{3BMA} value at 0.60. The intramolecular olefin metathesis of P($BMA_{0.40}$-*co*-$3BMA_{0.60}$)$_{24k}$ and P($BMA_{0.40}$-*co*-$3BMA_{0.60}$)$_{80k}$ in CH_2Cl_2 also proceeded without gelation as for the case of P($BMA_{0.40}$-*co*-$3BMA_{0.60}$)$_{49k}$, which gave the corresponding SCNPs ($NP_{BMA}4$ and $NP_{BMA}5$, respectively) with the conv.$_{olefin}$s of >90% (**Table 2.2**). The triple detection SEC analysis of the obtained $NP_{BMA}4$ and $NP_{BMA}5$ confirmed the absence of intermolecular coupling, demonstrating the success of the SCNP formation. The author found that the $\langle G \rangle$ value slightly decreased with the increasing prepolymer molecular weight (**Figures 2.3**(b), **S2.13**, and **S2.14**). More importantly, the [η] and R_h values of the SCNPs clearly decreased with the decreasing molecular weight of the prepolymer, i.e., $NP_{BMA}5$ ([η] = 15.9 mL g^{-1}, $R_{h,visc}$ = 6.1 nm, and $R_{h,DLS}$ = 6.0 nm) > $NP_{BMA}2$ ([η] = 12.9 mL g^{-1}, $R_{h,visc}$ = 5.1 nm, and $R_{h,DLS}$ = 5.1 nm) > $NP_{BMA}4$ ([η] = 8.3 mL g^{-1}, $R_{h,visc}$ = 3.6 nm, and $R_{h,DLS}$ = 3.5 nm) (DLS results are shown in **Figure S2.15** and **S2.16**). Hence, the author confirmed that varying the molecular weight of the linear prepolymer is one of the reasonable ways of controlling the size of the SCNPs via the olefin metathesis approach.

2.3.1.5 Effect of reaction medium on the SCNP formation

Finally, the author examined the effect of the reaction medium on the SCNP formation. It is presumed that the chain dimensions of the linear prepolymers are dependent on the solvent quality, which in turn should affect the size of the resultant SCNPs. Thus, the intramolecular olefin metathesis of $P(BMA_{0.70}\text{-}co\text{-}3BMA_{0.30})_{55k}$ was implemented in the mixture of CH_2Cl_2 (good solvent) and *n*-hexane (poor solvent) with the various *n*-hexane volume fractions (ϕ_{hexane}) of 0, 0.50, 0.75, and 0.83 to give the corresponding SCNPs, i.e., $NP_{BMA}1$, 6, 7, and 8, respectively (see **Tables 2.2** and **2.3**). Importantly, all the reactions homogeneously proceeded with the high $conv._{olefin}$ of >90% regardless of the reaction medium and produced the soluble products (see **Figure S2.17**). **Figure 2.4**(a) shows the comparison of the SEC traces of $P(BMA_{0.70}\text{-}co\text{-}3BMA_{0.30})_{55k}$ and the resultant SCNPs obtained after a 10 h reaction in each solvent. Interestingly, the $M_{p,SEC}$ value of the resultant SCNPs decreased with the increasing ϕ_{hexane} despite all the other reaction conditions being the same. Accordingly, the $\langle G \rangle$ value decreased with the increasing ϕ_{hexane}; $\langle G \rangle = 0.87$ for $\phi_{hexane} = 0$ ($NP_{BMA}1$), $\langle G \rangle = 0.68$ for $\phi_{hexane} = 0.50$ ($NP_{BMA}6$), $\langle G \rangle = 0.59$ for $\phi_{hexane} = 0.75$ ($NP_{BMA}7$), and $\langle G \rangle = 0.45$ for $\phi_{hexane} = 0.83$ ($NP_{BMA}8$). However, a high molecular weight shoulder was detected in the SEC trace of $NP_{BMA}8$, indicating that the high volume fraction of the poor solvent in the reaction medium led to forming the by-product due to the intermolecular coupling. Nevertheless, the SEC results clearly indicated that the addition of the poor solvent to the reaction medium resulted in forming SCNPs with a smaller size (**Figure 2.4**(b)). Besides the SEC analysis, the viscosity and DLS measurements also suggested the decrease in the SCNP size with the increasing ϕ_{hexane}. More interestingly, the double logarithmic plots for the $[\eta]$ vs $M_{w,MALS}$ (**Figure S2.18**), which were obtained by the triple detection SEC measurements of the

resultant SCNPs, proved the decrease in the slope of the plot with the increasing ϕ_{hexane}. Here, the slope is equal to parameter *a* of the Mark-Houwink-Sakurada equation ($[\eta] = KM^a$), which is correlated with the polymer morphology in the solution. It was found that the *a* values of the SCNPs decreased in the following order: 1.12 for $NP_{BMA}1$ > 0.66 for $NP_{BMA}6$ > 0.39 for $NP_{BMA}7$. This tendency clearly indicated that the SCNPs turned more globular when the crosslinking took place in the poorer solvent, which is highly interesting from the view point of synthesizing SCNPs with well-defined compact morphologies. Since the linear prepolymer took the shrunken state due to the effect of the poor solvent, the crosslinking reaction between the olefins separated by long counter distances easily occurred, leading to globule SCNPs. In fact, this result is consistent with the MD simulation result reported by Moreno et al.[30] Thus, the author now propose that the intramolecular olefin metathesis in a mixture of good and poor solvents is a rational approach to not only control the hydrodynamic volume of the SCNPs, but also bring the resultant SCNPs closer to globular state. It should be mentioned that the excellent tolerance of Grubbs' catalyst toward various solvents as well as the mild reaction conditions for implementing the olefin metathesis are both necessary to achieve the simultaneous control over the SCNP size and morphology.

Table 2.3. Synthesis of SCNPs from P($BMA_{0.7}$-*co*-$3BMA_{0.3}$)$_{55k}$ in CH_2Cl_2/*n*-hexane mixture with various ϕ_{hexane} value[a]

polymer sample	ϕ_{hexane}	conv.$_{olefin}$[b] (%)	$M_{w,MALS}$[c] (g mol^{-1})	$M_{p,SEC}$[d] (g mol^{-1})	$Đ$[d]	$\langle G \rangle$[e]	$[\eta]$[c] (mL g^{-1})	$R_{h,DLS}$[f] (nm)	$R_{h,visc}$[g] (nm)
$NP_{BMA}6$	0.50	96	79,700	45,700	1.20	0.68	13.7	5.6	5.4
$NP_{BMA}7$	0.75	97	83,600	39,800	1.19	0.59	13.5	5.0	5.6
$NP_{BMA}8$	0.83	96	103,000	30,500	1.21	0.45	9.0	5.3	5.4

[a]Reaction conditions: [polymer] = 0.80 g L^{-1}; [3BMA units]/[G2] = 1/0.02; temp., 30 °C. Linear prepolymer: P($BMA_{0.70}$-*co*-$3BMA_{0.30}$)$_{55k}$, $M_{w,MALS}$ = 81,600 g mol^{-1}, $M_{p,SEC}$ = 67,400 g mol^{-1}, $Đ$ = 1.18, $[\eta]$ = 24.9 mL g^{-1}, $R_{h,DLS}$ = 6.5 nm, $R_{h,calc}$ = 6.8 nm. [b]Determined by ^{1}H NMR in $CDCl_3$. [c]Determined by triple detection SEC in THF (0.30 mg ml^{-1}). [d]Determined by SEC in THF using poly(methyl methacrylate) standards. [e]Determined by $M_{p,SEC}$(SCNP)/$M_{p,SEC}$(linear). [f]Determined by DLS in THF (5.0 g L^{-1}, 25 °C). [g]$R_{h,visc} = (3V_h/4\pi)^{1/3}$; V_h: hydrodynamic volume. V_h was calculated by Einstein-Simha equation ($V_h = M_{w,MALS}[\eta]/2.5N_A$; N_A: Avogadro's number).

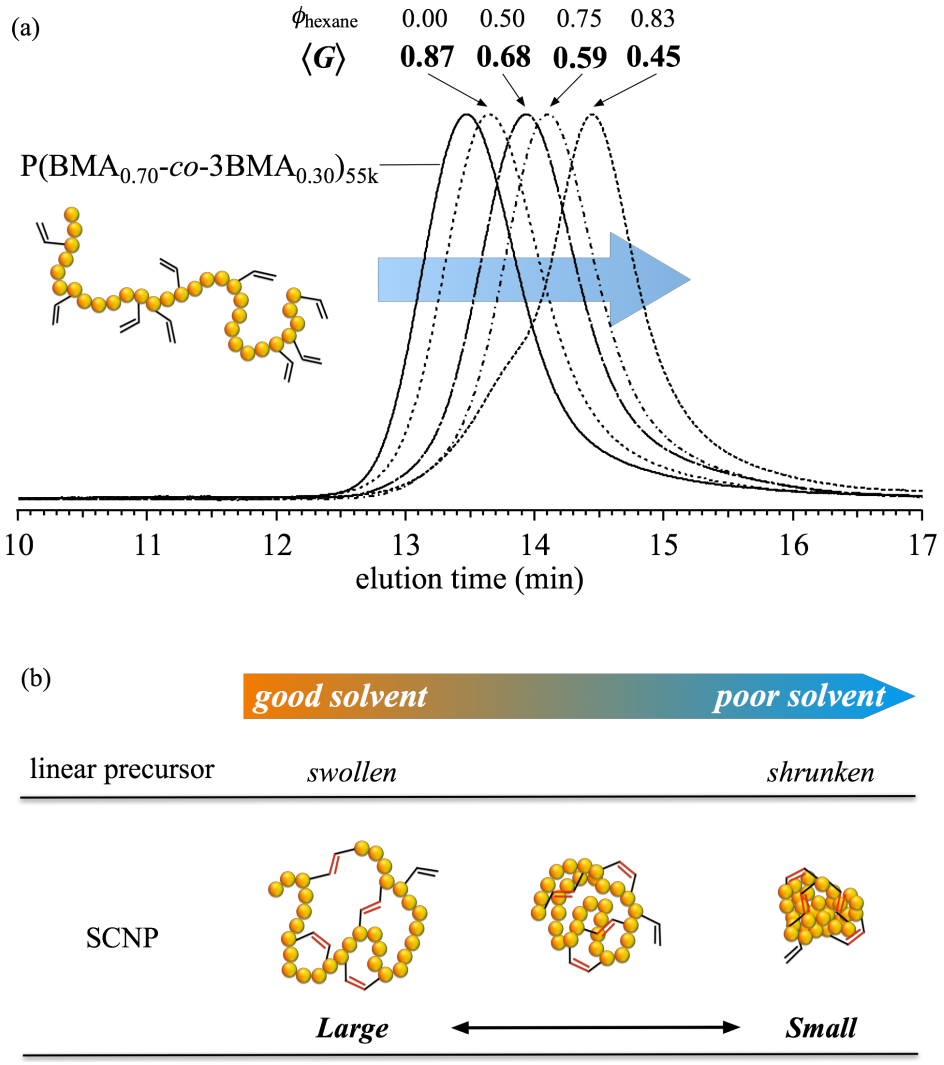

Figure 2.4. (a) SEC traces of $P(BMA_{0.70}\text{-}co\text{-}3BMA_{0.30})_{55k}$ (solid) and corresponding SCNPs ($NP_{BMA}1$, 6-8; dashed) (eluent, THF; flow rate, 1.0 mL min^{-1}). (b) Schematic representation of the correlation between the SCNP size/morphology and solvent quality of the reaction medium.

To summarize these results, the author have successfully synthesized a series of poly(methacrylate)-based SCNPs with diameters of sub-20 nm by the intramolecular olefin metathesis strategy under mild conditions. In addition, the author found that the size of the resultant SCNPs can be controlled by varying the following three factors: (1) the olefin content in the linear prepolymers, (2) molecular weight of the linear prepolymers, and (3) solvent quality of the reaction medium. Thus, the size-selective synthesis of SCNPs can be achieved by tuning these three factors. Moreover, adjusting the solvent quality to be poorer for the linear prepolymer was found to be a promising approach to produce globular SCNPs.

2.3.2 Synthesis of SCNPs from a variety of linear prepolymers

As already described, the author have demonstrated that the olefin metathesis is an effective way to produce SCNPs from poly(methacrylate) precursors. In order to expand the scope of the above-established procedure, the author next investigated the SCNP formation from a wide variety of linear prepolymers possessing pendant olefin groups, i.e., poly[(*n*-butyl acrylate)-*co*-(3-butenyl acrylate)], poly[styrene-*co*-(*p*-3-butenyl styrene)], poly[(ε-caprolactone)-*co*-(7-allyl-2-oxepanone)], and poly{styrene-*block*-[(methyl methacrylate)-*co*-(3-butenyl methacrylate)]}.

2.3.2.1 Synthesis of poly(acrylate)-based SCNPs

To evaluate the SCNP formation from the poly(acrylate) precursor possessing pendant olefin groups, a statistical copolymer of *n*-butyl acrylate (BA) and 3-butenyl acrylate (3BA) was prepared, wherein BA and 3BA were chosen as the base monomer and crosslinkable monomer, respectively. The *N*-(trimethylsilyl)bis(trifluoromethanesulfonyl)imide (Me_3SiNTf_2)-catalyzed GTP of *n*BA and 3BA in the presence of 1-methoxy-1-triisopropylsiloxy-2-methyl-1-propene (*i*Pr-SKA) as the initiator was carried out with the $[BA]_0/[3BA]_0/[Me_3SiNTf_2]_0/[i\text{Pr-SKA}]_0$ ratio of 200/200/0.15/1 (**Scheme 2.2**), which successfully gave a statistical copolymer of BA and 3BA with the mole fraction of 3BA (F_{3BA}) of 0.50, i.e., $P(BA_{0.50}\text{-}co\text{-}3BA_{0.50})_{120k}$ ($M_{n,SEC}$ = 120,000 g mol^{-1}, $Đ$ = 1.05, THF).

Scheme 2.2. Synthesis of statistical copolymer of *n*BA and 3BA

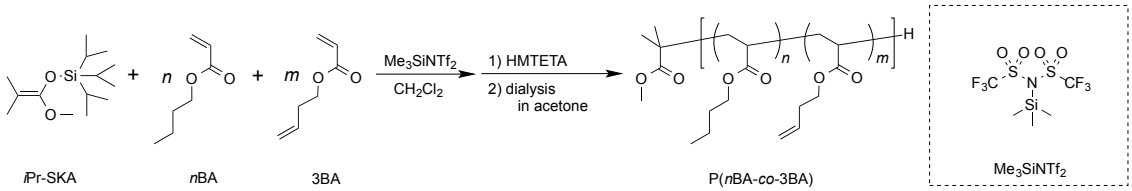

The intramolecular olefin metathesis of $P(BA_{0.50}\text{-}co\text{-}3BA_{0.50})_{120k}$ was performed in CH_2Cl_2 ($[P(BA_{0.50}\text{-}co\text{-}3BA_{0.50})_{120k}]_0$ = 0.80 g L^{-1}) for 10 h using the above-established procedure, giving $NP_{BA}1$ without gelation. The ^1H NMR analysis indicated the transformation of the terminal olefins into the internal olefins with the $conv._{olefin}$ of 54%. The SEC trace of $NP_{BA}1$ slightly shifted toward the lower molecular weight region as compared to that of $P(BA_{0.50}\text{-}co\text{-}3BA_{0.50})_{120k}$, and the $\langle G \rangle$ value was calculated to be 0.92 as summarized in **Figure 2.5** and **Table S2.1**. These results confirmed the SCNP formation from the poly(acrylate) precursor. However, the rate of the crosslinking formation seems to be slower than for the P(BMA-*co*-3BMA) precursor, which could be due to the difference in the main chain flexibility of the precursors.

As already mentioned, the intramolecular crosslinking in poor solvents is an effective approach to further minimize the size of the resultant SCNPs. Thus, the intramolecular olefin metathesis of $P(BA_{0.50}\text{-}co\text{-}3BA_{0.50})_{120k}$ was carried out in the mixture of *n*-hexane and CH_2Cl_2 with the varied ϕ_{hexane} values of 0.67, 0.75 or 0.83 to give $NP_{BA}2$, $NP_{BA}3$, and $NP_{BA}4$, respectively (**Table S2.1**). For each reaction, the SEC traces of the resultant SCNPs shifted toward the lower molecular weight region as compared to that of the prepolymer, and the $\langle G \rangle$ value for the obtained NP_{BA}s decreased when increasing the ϕ_{hexane} value of the reaction medium; $\langle G \rangle$ = 0.92 for $NP_{BA}1$, 0.66 for $NP_{BA}2$, 0.50 for $NP_{BA}3$, and

0.29 for $NP_{BA}4$ (**Figure 2.5**), which again confirmed the advantage of the present olefin metathesis approach. Importantly, the $conv._{olefin}$ for the resultant SCNPs increased with the increasing ϕ_{hexane} of the reaction medium (**Figure S2.19**), suggesting that the intramolecular crosslinking was promoted due to the shrunken state of the linear prepolymer. Thus, the author succeeded in the intramolecular olefin metathesis of the acrylate-based copolymer to produce SCNPs in a size-controlled manner.

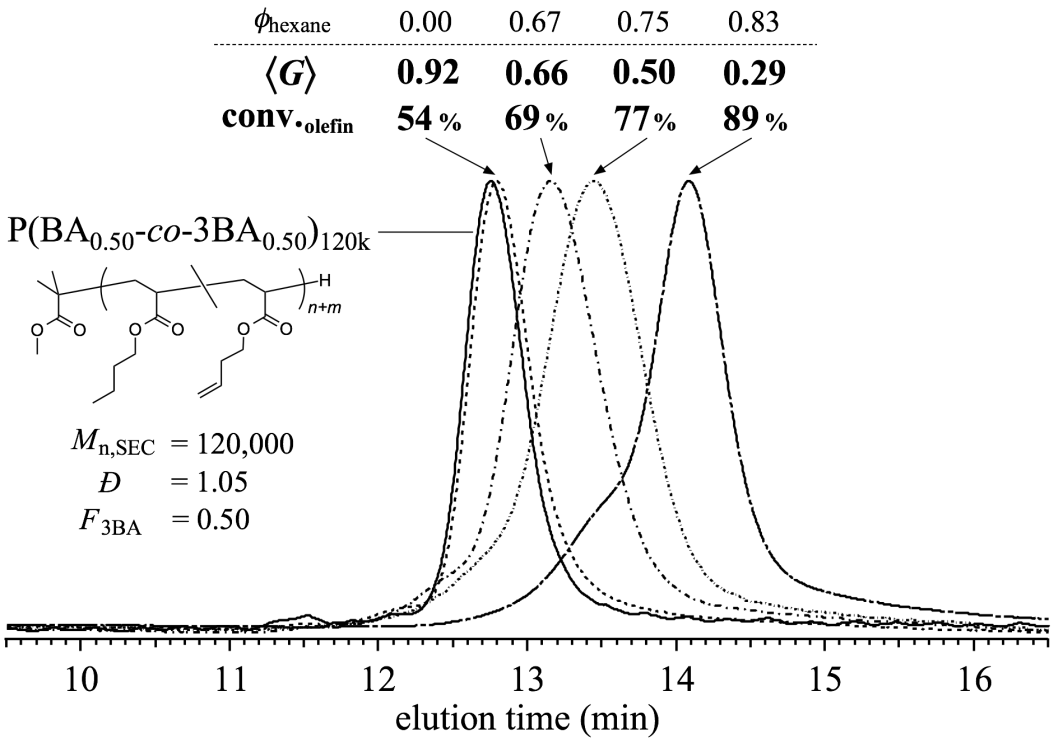

Figure 2.5. SEC traces of $P(BA_{0.50}\text{-}co\text{-}3BA_{0.50})_{120k}$ (solid) and corresponding SCNPs ($NP_{BA}1$-4; dashed) (eluent, THF; flow rate, 1.0 mL min^{-1}).

2.3.2.2 Synthesis of poly(ester)-based SCNPs

The author also examined the intramolecular olefin metathesis of an aliphatic poly(ester) precursor as a representative example of non-vinyl polymers. To obtain the aliphatic poly(ester) precursor, *ε*-caprolactone (CL) and 7-allyl-2-oxepanone (ACL) were copolymerized by the diphenyl phosphate(DPP)-catalyzed living ring-opening copolymerization in the presence of 3-phenyl-1-propanol (PPA) as the initiator with the $[CL]_0/[ACL]_0/[DPP]_0/[PPA]_0$ ratio of 70/70/1/1 (**Scheme 2.3**). The desired copolymer of CL and ACL, i.e., $P(CL_{0.64}\text{-}co\text{-}ACL_{0.36})_{13k}$, was obtained with the mole fraction of the ACL unit (F_{ACL}) value of 0.36 ($M_{n,SEC}$ = 12,900 g mol^{-1}, $Đ$ = 1.08, THF). It should be noted that the obtained copolymer might have a compositional drift with the ACL-rich segment near the *ω*-chain end because of the lower ACL reactivity.

Scheme 2.3. Synthesis of copolymer of CL and ACL

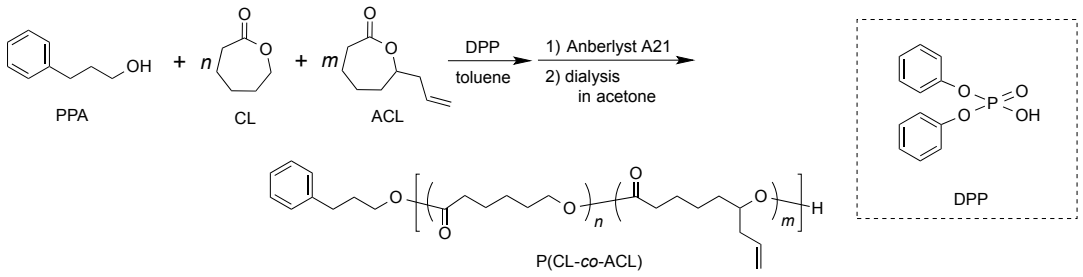

The intramolecular olefin metathesis of $P(CL_{0.64}\text{-}co\text{-}ACL_{0.36})_{13k}$ was conducted in CH_2Cl_2 ($NP_{CL}1$) or a CH_2Cl_2/*n*-hexane mixture with the ϕ_{hexane} of 0.67 ($NP_{CL}2$) using the same procedure as for P(BMA-*co*-3BMA) ($[P(CL_{0.64}\text{-}co\text{-}ACL_{0.36})_{13k}]_0$ = 0.80 g L^{-1}) (**Table S2.1**), which also gave soluble products. The ^{1}H NMR analysis of the products revealed that the metathesis reactions sufficiently proceeded with the $conv._{olefin}$ value of ca. 80% for each run

(**Figure S2.20**). More importantly, the SEC traces of the obtained products showed a unimodal peak in the lower molecular weight region as compared to that of $P(CL_{0.64}\text{-}co\text{-}ACL_{0.36})_{13k}$ (**Figure 2.6**). These results confirmed the successful formation of SCNP via the intramolecular olefin metathesis. Furthermore, the $\langle G \rangle$ values for $NP_{CL}1$ and $NP_{CL}2$ were calculated to be 0.82 and 0.62, respectively, supporting the possibility of the size-controllable SCNP synthesis from the aliphatic poly(ester) precursor.

The vast majority of the reported SCNP syntheses have focused on vinyl polymers, such as the acrylate-, methacrylate-, and styrene-based copolymers. On the other hand, the synthesis of aliphatic poly(ester)-based SCNPs has rarely been reported despite the apparent advantages of their biodegradability and biocompatibility. Above established procedure is thus highly interesting for the general route to create biodegradable and biocompatible SCNPs with the desired size.

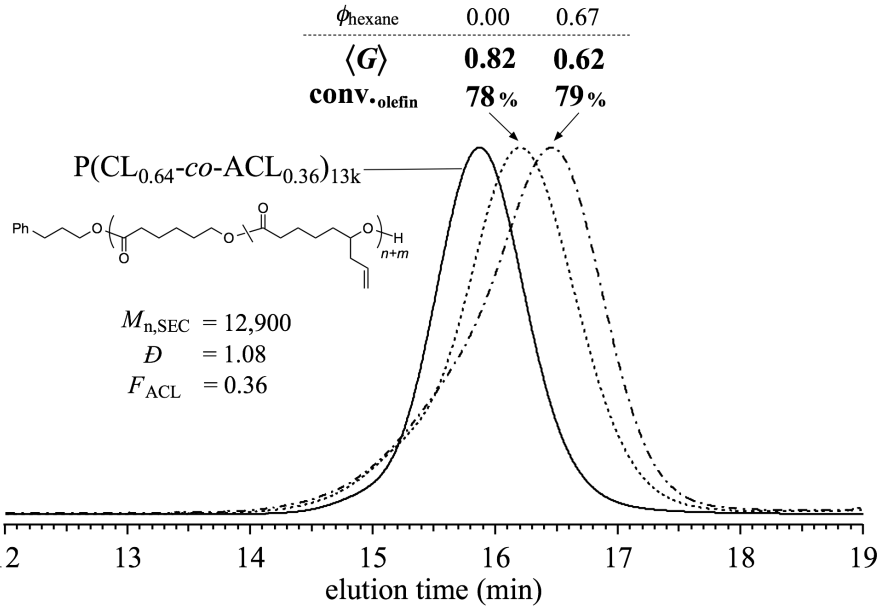

Figure 2.6. SEC traces of $P(CL_{0.64}\text{-}co\text{-}ACL_{0.36})_{13k}$ (solid) and corresponding SCNPs ($NP_{CL}1$, 2; dashed) (eluent, THF; flow rate, 1.0 mL min^{-1}).

2.3.2.3 Synthesis of poly(styrene-block-methacrylate)-based SCNPs

Finally, the intramolecular olefin metathesis was applied to the block copolymer (BCP) precursor consisting of styrene (S) homopolymer and methyl methacrylate (MMA)-3BMA statistical copolymer, i. e., P[S-*b*-(MMA-*co*-3BMA)]. Three steps are involved in the synthesis of P[S-*b*-(MMA-*co*-3BMA)]: (1) the living anionic polymerization of S followed by ω-end functionalization with α-phenylacrylate (PA) to give PS_{45k}–PA, (2) the living anionic copolymerization of MMA with 3BMA to give living $P(MMA_{0.70}\text{-}co\text{-}3BMA_{0.30})_{19k}$ anion, and (3) coupling of PS_{45k}–PA and living $P(MMA_{0.70}\text{-}co\text{-}3BMA_{0.30})_{19k}$ anion to produce $P[S_{45k}\text{-}b\text{-}(MMA_{0.70}\text{-}co\text{-}3BMA_{0.30})_{19k}]$ having F_{3BMA} value of 0.30 in the P(MMA-*co*-3BMA) segment (**Scheme 2.4** and **2.5** (see Supporting Information for detail); $M_{n,SEC}$ = 61,400 g mol^{-1}, $Đ$ = 1.06, THF).

Scheme 2.4. Synthesis of ω-end-PA functionalized polystyrene (PS–PA)

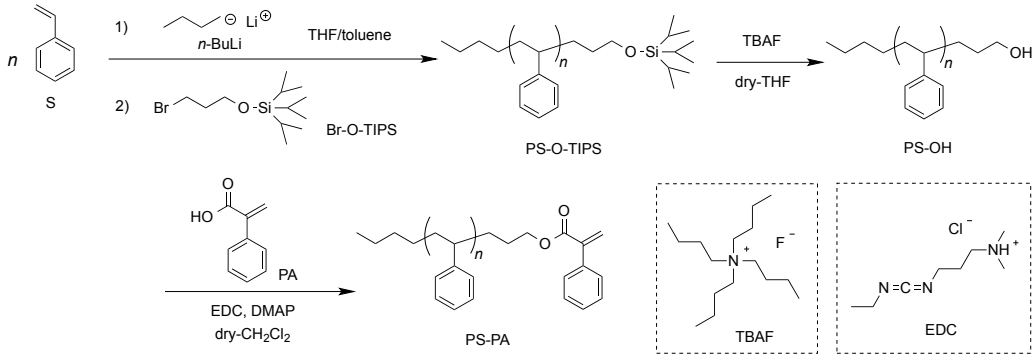

Scheme 2.5. Synthesis of BCP consisting of PS and P(MMA-*co*-3BMA)

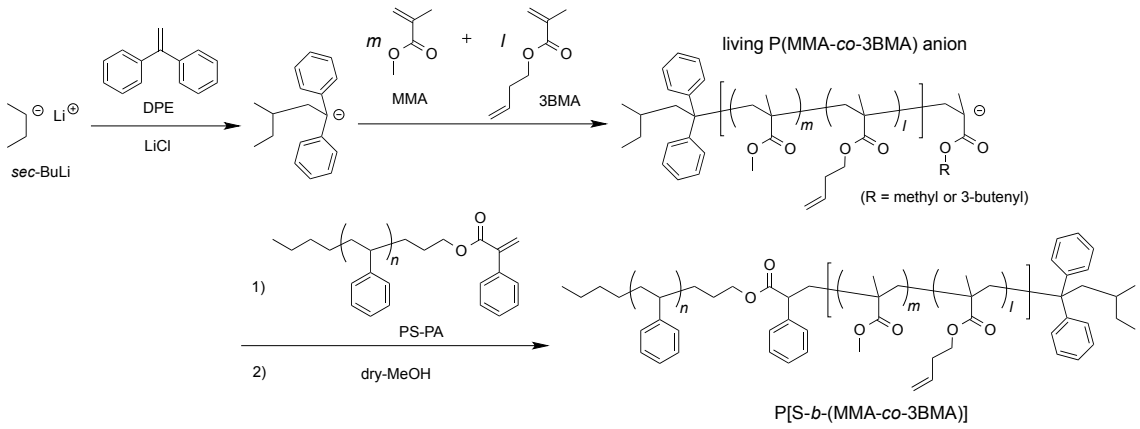

The intramolecular olefin metathesis of P[S_{45k}-*b*-($MMA_{0.70}$-*co*-$3BMA_{0.30}$)$_{19k}$] was carried out in CH_2Cl_2 (PS−NP_{MMA}1) or a CH_2Cl_2/*n*-hexane mixture with the ϕ_{hexane} of 0.50 (PS−NP_{MMA}2) using the same procedure as for P(BMA-*co*-3BMA) (**Table S2.1**), which also gave soluble products. The ^{1}H NMR analysis of the products revealed that the metathesis reactions sufficiently proceeded with the $conv._{olefin}$ value of ca. 90% for each run (**Figure S2.21**). The SEC traces of the obtained products shifted toward the lower molecular weight regions compared to that of P[S_{45k}-*b*-($MMA_{0.70}$-*co*-$3BMA_{0.30}$)$_{19k}$], showing the decrease in the hydrodynamic volume through the intramolecular crosslinking of the P(MMA-*co*-3BMA) segment (**Figure 2.7**). Although a high molecular weight shoulder was detected in the SEC trace of PSt−NP_{MMA}2, the $\langle G \rangle$ values clearly decreased with increasing ϕ_{hexane}; $\langle G \rangle$ = 0.96 for ϕ_{hexane} = 0 (PSt−NP_{MMA}1) > $\langle G \rangle$ = 0.88 for ϕ_{hexane} = 0.50 (PSt−NP_{MMA}2). From these results, the author confirmed that the presented intramolecular olefin metathesis approach can be successfully extended to the field of BCPs.

It is well-known that BCPs show various unique properties, such as self-assembly in solution (micelle formation) and bulk (microphase separation), due to their chemical structure

in which the chemically different polymers are tethered via a covalent bond. These properties would be adjusted by controlling the chain dimensions using the above established strategy, which is highly promising for the development of advanced applications based on BCPs.

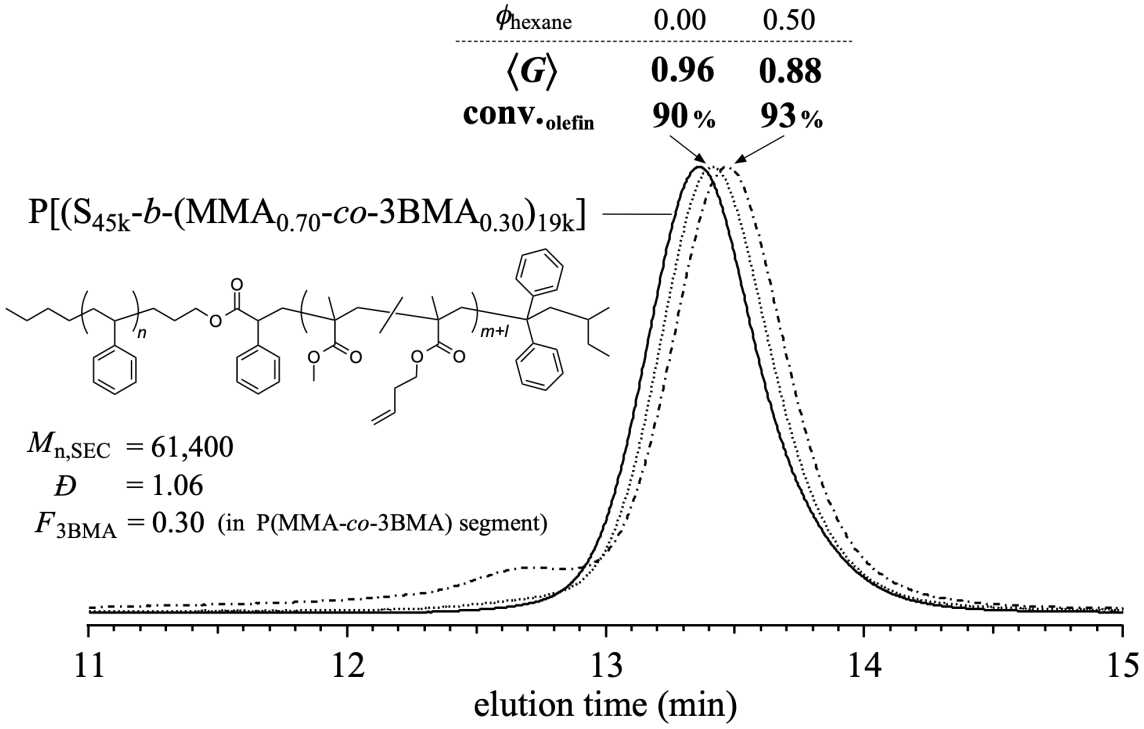

Figure 2.7. SEC traces of P[S_{45k}-*b*-($MMA_{0.70}$-*co*-$3BMA_{0.30}$)$_{19k}$] (solid) and corresponding SCNPs (PS−NP_{MMA}1, 2; dashed) (eluent, THF; flow rate, 1.0 mL min^{-1}).

2.4 Conclusion

The author has successfully synthesized a series of SCNPs via the intramolecular olefin metathesis of a series of linear prepolymers possessing pendant olefin groups prepared by simple copolymerization systems. The comprehensive investigation using P(BMA-*co*-3BMA)s as prepolymers revealed that the size of the resultant SCNP can be precisely controlled by adjusting the following three factors: (1) the olefin contents of the prepolymer (crosslinking density), (2) molecular weight of the prepolymer, and (3) the poor solvent content in the reaction medium (which eventually affected the conformation of the linear prepolymer in the solution). In addition, the author found that the solvent quality affected not only the SCNP size, but also the morphology of the SCNPs; the resultant SCNPs got closer to a globular morphology with the increasing poor solvent content in the reaction medium. Moreover, the established olefin metathesis approach was applicable to the poly(acrylate), poly(ester), and poly(styrene-*block*-methacrylate) precursors, giving the desired SCNPs with various main chain structures. Considering the excellent functional group tolerance and sufficient reactivity of the ruthenium-based metathesis catalysts, the intramolecular metathesis approach is applicable to a wide variety of polymers bearing olefin functionality.

2.5 References

1. Lyon, C. K.; Prasher, A.; Hanlon, A. M.; Tuten, B. T.; Tooley, C. A.; Frank, P. G.; Berda, E. B. A Brief User's Guide to Single-Chain Nanoparticles. *Polym. Chem.* **2015**, *6*, 181–197. C. K. Lyon, A. Prasher, A. M. Hanlon, B. T. Tuten, C. A. Tooley, P. G. Frank and E. B. Berda, *Polym. Chem.,* 2015, **6**, 181–197.
2. Gonzalez-Burgos, M.; Latorre-Sanchez, A.; Pomposo, J. A. Advances in Single Chain Technology. *Chem. Soc. Rev.* **2015**, *44* (17), 6122–6142.
3. Altintas, O.; Barner-Kowollik, C. Single-Chain Folding of Synthetic Polymers: A Critical Update. *Macromol. Rapid Commun.* **2016**, *37* (1), 29–46.
4. Mavila, S.; Eivgi, O.; Berkovich, I.; Lemcoff, N. G. Intramolecular Cross-Linking Methodologies for the Synthesis of Polymer Nanoparticles. *Chem. Rev.* **2016**, *116*, 878–961.
5. Harth, E.; Van Horn, B.; Lee, V. Y.; Germack, D. S.; Gonzales, C. P.; Miller, R. D.; Hawker, C. J. A Facile Approach to Architecturally Defined Nanoparticles via Intramolecular Chain Collapse. *J. Am. Chem. Soc.* **2002**, *124* (29), 8653–8660.
6. Dukette, T. E.; Mackay, M. E.; Van Horn, B.; Wooley, K. L.; Drockenmuller, E.; Malkoch, M.; Hawker, C. J. Conformation of Intramolecularly Cross-Linked Polymer Nanoparticles on Solid Substrates. *Nano Lett.* **2005**, *5* (9), 1704–1709.
7. De Luzuriaga, A. R.; Ormategui, N.; Grande, H. J.; Odriozola, I.; Pomposo, J. A.; Loinaz, I. Intramolecular Click Cycloaddition: An Efficient Room-Temperature Route towards Bioconjugable Polymeric Nanoparticles. *Macromol. Rapid Commun.* **2008**, *29* (12-13), 1156–1160.
8. Perez-Baena, I.; Loinaz, I.; Padro, D.; García, I.; Grande, H. J.; Odriozola, I. Single-Chain Polyacrylic Nanoparticles with Multiple Gd(Ⅲ) Centres as Potential MRI Contrast Agents. *J. Mater. Chem.* **2010**, *20* (33), 6916–6922.
9. De Luzuriaga, A. R.; Perez-Baena, I.; Montes, S.; Loinaz, I.; Odriozola, I.; García, I.; Pomposo, J. A. New Route to Polymeric Nanoparticles by Click Chemistry Using Bifunctional Cross-Linkers. *Macromol. Symp.* **2010**, *296* (1), 303–310.
10. Ormategui, N.; Garcia, I.; Padro, D.; Cabanero, G.; Grande, H. J.; Loinaz, I. Synthesis of Single Chain Thermoresponsive Polymer Nanoparticles. *Soft Matter* **2012**, *8* (3), 734–740.
11. Sanchez-Sanchez, A.; Asenjo-Sanz, I.; Buruaga, L.; Pomposo, J. A. Naked and Self-Clickable Propargylic-Decorated Single-Chain Nanoparticle Precursors via Redox-Initiated RAFT Polymerization. *Macromol. Rapid Commun.* **2012**, *33* (15), 1262–1267.
12. Roy, R. K.; Lutz, J. F. Compartmentalization of Single Polymer Chains by Stepwise Intramolecular Cross-Linking of Sequence-Controlled Macromolecules. *J. Am. Chem. Soc.* **2014**, *136* (37), 12888–12891.

13. Sanchez-Sanchez, A.; Arbe, A.; Colmenero, J.; Pomposo, J. A. Metallo-Folded Single-Chain Nanoparticles with Catalytic Selectivity. *ACS Macro Lett.* **2014**, *3* (5), 439–443.
14. Chao, D.; Jia, X.; Tuten, B.; Wang, C.; Berda, E. B. Controlled Folding of a Novel Electroactive Polyolefin via Multiple Sequential Orthogonal Intra-Chain Interactions. *Chem. Commun.* **2013**, *49* (39), 4178–4180.
15. Perez-Baena, I.; Asenjo-Sanz, I.; Arbe, A.; Moreno, A. J.; Lo Verso, F.; Colmenero, J.; Pomposo, J. A. Efficient Route to Compact Single-Chain Nanoparticles: Photoactivated Synthesis via Thiol-Yne Coupling Reaction. *Macromolecules* **2014**, *47* (23), 8270–8280.
16. Mecerreyes, B. D.; Lee, V.; Hawker, C. J.; Hedrick, J. L.; Wursch, A.; Volksen, W.; Magbitang, T.; Huang, E.; Miller, R. D. A Novel Approach to Functionalized Nanoparticles: Self-Crosslinking of Macromolecules in Ultradilute Solution. **2001**, *13* (3), 204–208.
17. Zhu, B.; Ma, J.; Li, Z.; Hou, J.; Cheng, X.; Qian, G.; Liu, P.; Hu, A. Formation of Polymeric Nanoparticles via Bergman Cyclization Mediated Intramolecular Chain Collapse. *J. Mater. Chem.* **2011**, *21* (8), 2679–2683.
18. Tuten, B. T.; Chao, D.; Lyon, C. K.; Berda, E. B. Single-Chain Polymer Nanoparticles via Reversible Disulfide Bridges. *Polym. Chem.* **2012**, *3* (11), 3068–3071.
19. Tanaka, R.; Watanabe, K.; Yamamoto, T.; Tajima, K.; Isono, T.; Satoh, T. A Facile Strategy for Manipulating Micellar Size and Morphology through Intramolecular Cross-Linking of Amphiphilic Block Copolymers. *Polym. Chem.* **2017**, *8* (23), 3647–3656.
20. Wen, W.; Huang, T.; Guan, S.; Zhao, Y.; Chen, A. Self-Assembly of Single Chain Janus Nanoparticles with Tunable Liquid Crystalline Properties from Stilbene-Containing Block Copolymers. *Macromolecules* **2019**, *52* (8), 2956–2964.
21. Altintas, O.; Willenbacher, J.; Wuest, K. N. R.; Oehlenschlaeger, K. K.; Krolla-Sidenstein, P.; Gliemann, H.; Barner-Kowollik, C. A Mild and Efficient Approach to Functional Single-Chain Polymeric Nanoparticles via Photoinduced Diels-Alder Ligation. *Macromolecules* **2013**, *46* (20), 8092–8101.
22. Hansell, C. F.; Lu, A.; Patterson, J. P.; O'Reilly, R. K. Exploiting the Tetrazine-Norbornene Reaction for Single Polymer Chain Collapse. *Nanoscale* **2014**, *6*, 4102–4107.
23. Willenbacher, J.; Wuest, K. N. R.; Mueller, J. O.; Kaupp, M.; Wagenknecht, H. A.; Barner-Kowollik, C. Photochemical Design of Functional Fluorescent Single-Chain Nanoparticles. *ACS Macro Lett.* **2014**, *3* (6), 574–579.
24. Lemcoff, N. G.; Spurlin, T. A.; Gewirth, A. A.; Zimmerman, S. C.; Beil, J. B.; Elmer, S. L.; Vandeveer, H. G. Organic Nanoparticles Whose Size and Rigidity Are Finely Tuned by Cross-Linking the End Groups of Dendrimers. *J. Am. Chem. Soc.* **2004**, *126* (37), 11420–11421.

25. Cherian, A. E.; Sun, F. C.; Sheiko, S. S.; Coates, G. W. Formation of Nanoparticles by Intramolecular Cross-Linking: Following the Reaction Progress of Single Polymer Chains by Atomic Force Microscopy. *J. Am. Chem. Soc.* **2007**, *129* (37), 11350–11351.
26. Bai, Y.; Xing, H.; Vincil, G. A.; Lee, J.; Henderson, E. J.; Lu, Y.; Lemcoff, N. G.; Zimmerman, S. C. Practical Synthesis of Water-Soluble Organic Nanoparticles with a Single Reactive Group and a Functional Carrier Scaffold. *Chem. Sci.* **2014**, *5* (7), 2862–2868.
27. Annibale, A. D.; Ciaralli, L.; Chimica, D.; Cnr, I.; Roma, S.; Uni, V. Synthesis of Alkyl-Substituted Six-Membered Lactones through Ring-Closing Metathesis of Homoallyl Acrylates. An Easy Route to Pyran-2-ones, Constituents of Tobacco Flavor. **2007**, *72* (16), 6067–6074.
28. Dyker, G.; Grundt, P. Construction of the Steroid Framework via a Functionalized Macrocyclic Compound. *European J. Org. Chem.* **1999**, *1999* (1), 323–327.
29. Liu, S. Y.; Hills, I. D.; Fu, G. C. Synthesis, Resolution, and Aldol Reactions of a Planar-Chiral Lewis Acid Complex. *J. Am. Chem. Soc.* **2005**, *127* (44), 15352–15353.
30. Lo Verso, F.; Pomposo, J. A.; Colmenero, J.; Moreno, A. J. Simulation Guided Design of Globular Single-Chain Nanoparticles by Tuning the Solvent Quality. *Soft Matter* **2015**, *11* (7), 1369–1375.

2.6 Supporting Information

2.6.1 Experimental

Synthesis of statistic copolymer of BMA and 3BMA ($P(BMA_{0.40}$-*co*-$3BMA_{0.60})_{49k}$). Method A was used for the GTP of BMA (492 mg, 3.46 mmol) and 3BMA (731 mg, 5.19 mmol) with Me-SKA (4.30 mg, 24.7 μmol) and *t*-Bu-P_4 (50.0 μL, 0.500 μmol, 0.0100 mol L^{-1} in toluene) in toluene (7.30 mL) for 6 h to give $P(BMA_{0.30}$-*co*-$3BMA_{0.60})_{49k}$. Yield: 1.05 g (86.1%). $M_{n,SEC}$ = 49,000 g mol^{-1}, $Đ$ = 1.14 (THF), F_{3BMA} = 0.60.

Synthesis of homopolymer of 3BMA ($P(3BMA)_{50k}$). Method A was used for the GTP of 3BMA (1.24 g, 8.77 mmol) with Me-SKA (4.30 mg, 24.7 μmol) and *t*-Bu-P_4 (50.0 μL, 0.500 μmol, 0.0100 mol L^{-1} in toluene) in toluene (7.4 mL) for 6 h to give $P(3BMA)_{50k}$. Yield: 1.08 g (87.1%). $M_{n,SEC}$ = 50,200 g mol^{-1}, $Đ$ = 1.21 (THF), F_{3BMA} = 1.00.

Synthesis of statistic copolymer of BMA and 3BMA ($P(BMA_{0.30}$-*co*-$3BMA_{0.60})_{24k}$). Method A was used for the GTP of BMA (495 mg, 3.48 mmol) and 3BMA (725 mg, 5.17 mmol) with Me-SKA (8.6 mg, 49.3 μmol) and *t*-Bu-P_4 (50.0 μL, 0.500 μmol, 0.0100 mol L^{-1} in toluene) in toluene (7.3 mL) for 17 h to give $P(BMA_{0.30}$-*co*-$3BMA_{0.60})_{26k}$. Yield: 0.91 g (74.6%). $M_{n,SEC}$ = 23,700 g mol^{-1}, $Đ$ = 1.11 (THF), F_{3BMA} = 0.60.

Synthesis of statistic copolymer of BMA and 3BMA ($P(BMA_{0.30}$-*co*-$3BMA_{0.60})_{80k}$). Method A was used for the GTP of BMA (740 mg, 5.20 mmol) and 3BMA (1.09 g, 7.78 mmol) with Me-SKA (4.30 mg, 24.7 μmol) and *t*-Bu-P_4 (50.0 μL, 0.500 μmol, 0.0100 mol L^{-1} in toluene) in toluene (11.0 mL) for 11 h to give

P($BMA_{0.30}$-*co*-$3BMA_{0.60}$)$_{86k}$. Yield: 1.62 g (88.5%). $M_{n,SEC}$ = 79,700 g mol^{-1}, $Đ$ = 1.22 (THF), F_{3BMA} = 0.60.

Synthesis of statistical copolymer of *n*BA and 3BA (P($BA_{0.50}$-*co*-$3BA_{0.50}$)$_{120k}$).

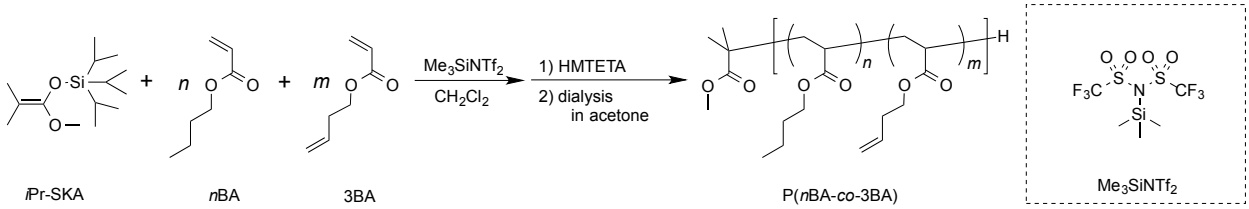

In the globebox, a stock solution of Me_3SiNTf_2 (120 μL, 12.0 μmol, 1.00 mol L^{-1} in toluene) was added to a solution of *n*BA (2.05 g, 16.0 mmol), 3BA (2.02 g, 16.0 mmol), and *i*Pr-SKA (20.7 μg, 80.0 μmol) in dry-CH_2Cl_2 (27.0 mL) at room temperature (27 °C). After stirring for 4.5 min, the polymerization was quenched by the addition of a small amount of HMTETA. The crude product was purified by dialysis in acetone to give the statistical copolymer of *n*BA and 3BA (P($BA_{0.50}$-*co*-$3BA_{0.50}$)$_{120k}$) as a colorless viscous liquid. Yield: 3.76 g (92.4%). ^{1}H NMR (400 MHz, $CDCl_3$): δ (ppm) 5.84−5.71 (m, 1H × *m*, −C*H*=CH_2), 5.16−5.04 (m, 2H × *m*, −CH=CH_2), 4.18−3.94 (m, 2H × (*m*+*n*), −OCH_2(CH_2)$_2$$CH_3$, −OC$H_2$$CH_2$CH=$CH_2$), 3.63 (s, 3H, −OC$H_3$), 2.44−2.19 (m, 3H × *m* + 1H × *n*, s−OCH_2CH_2CH=CH_2, −CH_2C*H*(COO(CH_2)$_3$$CH_3$)−, −$CH_2$C*H*(COO($CH_2$)$_2$CH=$CH_2$)−), 1.99−1.31 (m, 2H × (*m*+*n*), −CH_2CH(COO(CH_2)$_3$$CH_3$)−, −C$H_2$CH(COO($CH_2$)$_2$CH=$CH_2$)−), 1.74−1.53 (m, 2H × *n*, −OCH_2C$H_2$$CH_2$$CH_3$), 1.43−1.31 (m, 2H × *n*, −O(CH_2)$_2$C$H_2$$CH_3$), 1.14 (d, *J* = 11.4, 6H, −(CH_3OCO)C(CH_3)$_2$), and 0.93 (t, *J* = 15.1, 3H × *n*, −O(CH_2)$_3$CH_3). $M_{n,SEC}$ = 120,000 g mol^{-1}, $Đ$ = 1.05 (THF), F_{3BA} = 0.50.

Synthesis of copolymer of CL and ACL ($P(CL_{0.64}$-*co*-$ACL_{0.36})_{13k}$).

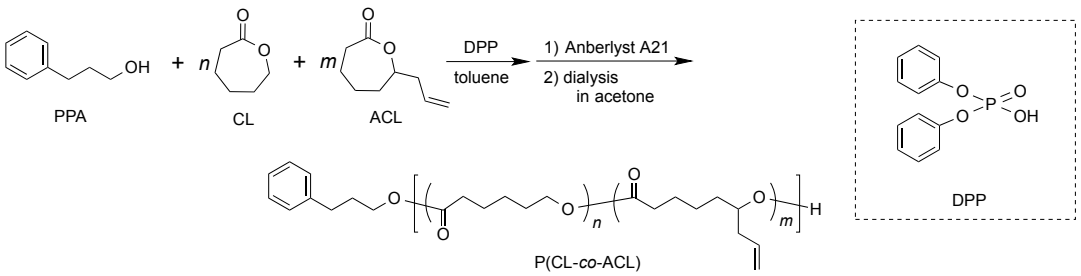

In the glovebox, a stock solution of PPA (40.0 μL, 40.0 μmol, 1.00 mol L^{-1} in toluene) was added to a solution of CL (320 mg, 2.80 mmol), ACL (432 mg, 2.80 mmol), and DPP (10.0 mg, 40.0 μmol) in dry-toluene (2.80 mL) at room temperature (27 °C) in a Shlenk flask. After sealing, the flask was taken out from the glovebox. After stirring for 30 h at 50 °C, the polymerization was quenched by the addition of an excessive amount of Amberlyst® A21. The crude product was purified by dialysis in acetone to give the copolymer of CL and ACL ($P(CL_{0.64}$-*co*-$ACL_{0.36})_{13k}$) as a colorless viscous liquid. Yield: 432 mg (57.6%). ^{1}H NMR (400 MHz, $CDCl_3$): δ (ppm) 7.13-7.31 (m, 5H, $-C_6H_5$), 5.63-5.79 (m, 1H × *m*, $-CH{=}CH_2$), 4.99-5.10 (m, 1H × *m*, $-CH{=}CH_2$), 4.86-4.96 (m, 1H × *m*, $-CH_2CH(CH_2-)O-$), 3.98-4.11 (m, 2H × *n*, $-CH_2OCO-$), 3.59-3.69 (m, 1H, $-CH(CH_2CH{=}CH_2)OH$), 2,69 (t, J = 8.4 Hz, 2H, $PhCH_2-$), 2.19-2.49 (m, 4H × (*n* + *m*) + 2H × *m*, $-COCH_2-$, $-CH_2CH(CH_2CH{=}CH_2)O-$), 1.90-2.00 (m, 2H, $PhCH_2CH_2-$), 1.43-1.83 (m, 4H × (*n* + *m*), $-COCH_2CH_2CH_2CH_2-$), and 1.20-1.43 (m, 2H × (*n* + *m*), $-COCH_2CH_2CH_2CH_2-$). $M_{n,SEC}$ = 12,900 g mol^{-1}, $Đ$ = 1.08 (THF), F_{ACL} = 0.36.

Synthesis of ω-end-(α-phenylacrylate) functionalized polystyrene (PS_{45k}−PA)

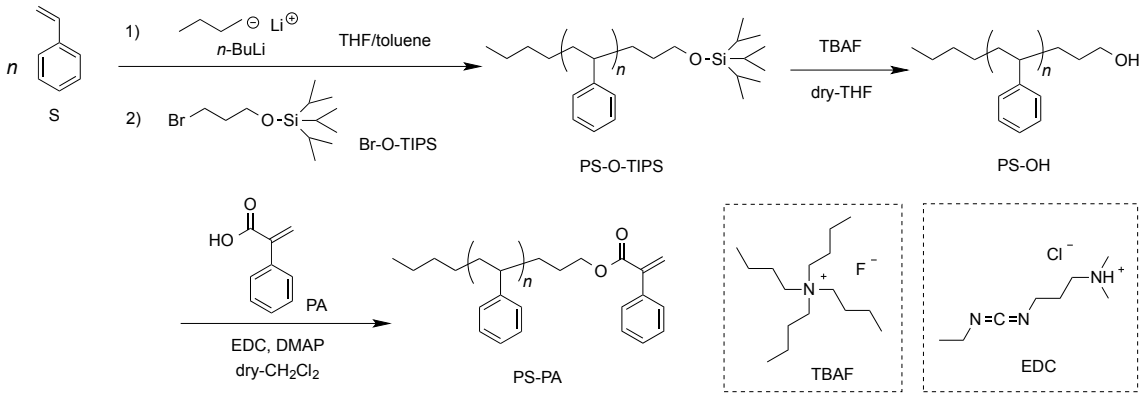

In the glovebox, dry-toluene (33.3 mL) and dry-THF (16.7 mL) were placed in a Shlenk flask. After sealing, the flask was taken out from the glovebox. After cooling to –78 °C, *n*-BuLi (100 μL, 71 μmol as a 0.71 mol L^{-1} stock solution in *n*-hexane) was added to the flask. S (3.2 g, 31 mmol) was then added at once to the initiator solution. After completing the monomer addition, the mixture was stirred at -78 °C for 2 h. Br–O–TIPS (88.4 mg. 299 mmol) was added to polymerization mixture at –78 °C, and was allowed to react for 0.5 h at –78 °C and additional 1 h at room temperature. The product was purified by dialysis using CH_2Cl_2 and reprecipitation from CH_2Cl_2 into MeOH to give PS_{45k}–O–TIPS as a white solid. Yield: 2.37 g (79.0 %). ^{1}H NMR (400 MHz, $CDCl_3$): δ (ppm) 7.37−6.25 (m, 5H × *n*, −C_6H_5), 3.55−3.37 (br, 2H, −CH_2−O−), 2.44−1.69 (m, 1H × *n*, −CHC_6H_5), 1.69−1.23 (m, 2H × *n*, −$CH_2CHC_6H_5$), and 1.06−0.90 (m, 21H, *triisopropyl*), 1.23−0.71 (m, 9H, *n-butyl*). $M_{n,SEC}$ = 44,700 g mol^{-1}, $Đ$ = 1.06 (THF).

TBAF (120 μL, 120 μmol in 1.0 mol L^{-1} stock solution in THF) was added to a solution of the obtaoined PS_{45k}–O–TIPS (1.70 mg, 38.0 μmol) in dry-THF (15 mL) at room temperature. After 15 h, the reaction mixture was purified by reprecipitation from CH_2Cl_2 into MeOH three times to give PS_{45k}–OH as a white solid. Yield: 1.45 g (85.3 %). ^{1}H NMR (400

MHz, $CDCl_3$): δ (ppm) 7.37−6.25 (m, 5H × n, −C_6H_5), 3.48−3.33 (br, 2H, −CH_2−OH), 2.44−1.69 (m, 1H × n, −$CH$$C_6H_5$), 1.69−1.23 (m, 2H × n, −$CH_2$$CHC_6H_5$), and 1.23−0.71 (m, 9H, *n-butyl*). $M_{n,SEC}$ = 44,700 g mol^{-1}, $Đ$ = 1.06 (THF).

The obtained PS_{45k}−OH (1.40 g. 31.3 μmol), PA (14.4 mg, 97.2 μmol), DMAP (18.1 mg, 148 μmol), and EDC (27.3 mg, 142 μmol) were dissolved in dry CH_2Cl_2 (30 mL) and the solution was stirred at room temperature for 36 h. The product was purified by reprecipitation from CH_2Cl_2 into MeOH three times to give PS_{45k}−PA as a white solid. PS_{45k}−PA was then freeze-dried from its absolute benzene solution three times. Yield: 1.20 g (85.7 %). ^{1}H NMR (400 MHz, $CDCl_3$): δ (ppm) 7.39−7.28 (m, 5H, −OCOC(=CH_2)C_6H_5), 7.37−6.25 (m, 5H × n, −CHC_6H_5), 4.07−3.91 (br, 2H, −CH_2−OCO−), 2.44−1.69 (m, 1H × n, −$CH$$C_6H_5$), 1.69−1.23 (m, 2H × n, −$CH_2$$CHC_6H_5$), and 1.23−0.71 (m, 9H, *n-butyl*). $M_{n,SEC}$ = 45,400 g mol^{-1}, $Đ$ = 1.06 (THF).

The author further confirmed the complete ω-end functionalization of PS by ^{1}H NMR and MALDI-TOF-MS measurement using a series of PS_{4k} synthesized via the same procedure as for a series of PS_{45k} (**Figure A6-1, A6-2**). PS_{4k}–O–TIPS ($M_{n,SEC}$ = 4,300 g mol^{-1}, $Đ$ = 1.08), PS_{4k}–OH ($M_{n,SEC}$ = 4,380 g mol^{-1}, $Đ$ = 1.06), PS_{4k}–PA ($M_{n,SEC}$ = 4,640 g mol^{-1}, $Đ$ = 1.06).

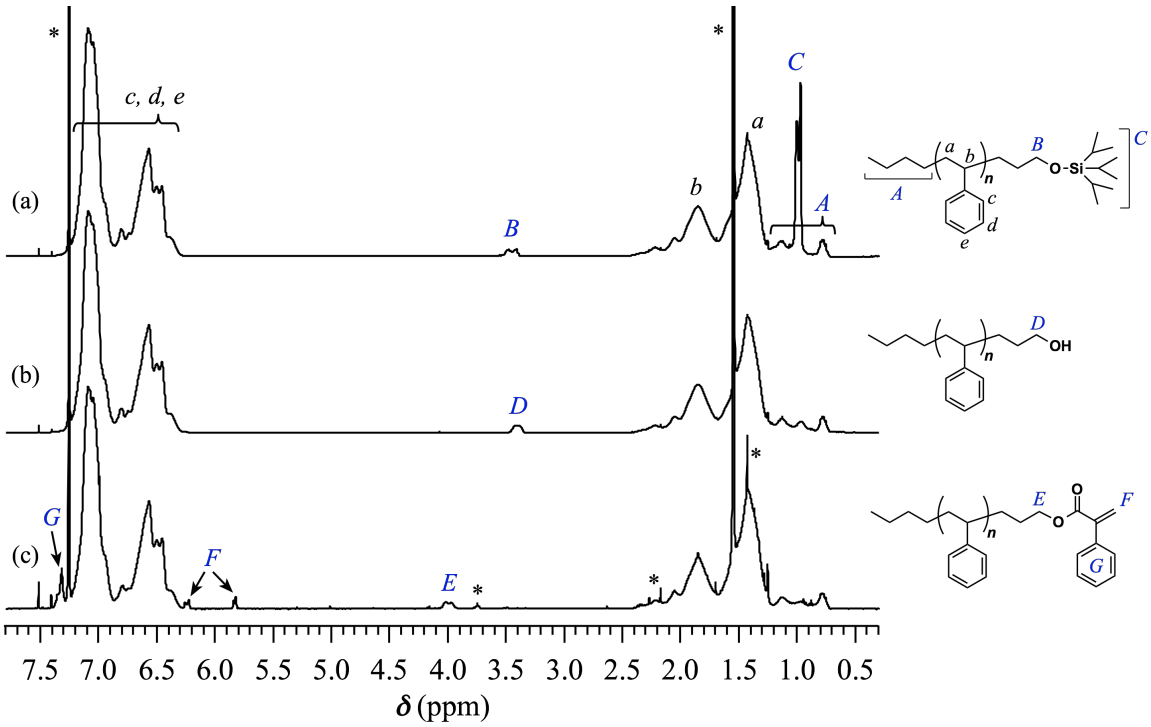

Figure S2.1. ^{1}H NMR spectra of (a) PS_{4k}–O–TIPS, (b) PS_{4k}–OH, and (c) PS_{4k}–PA.

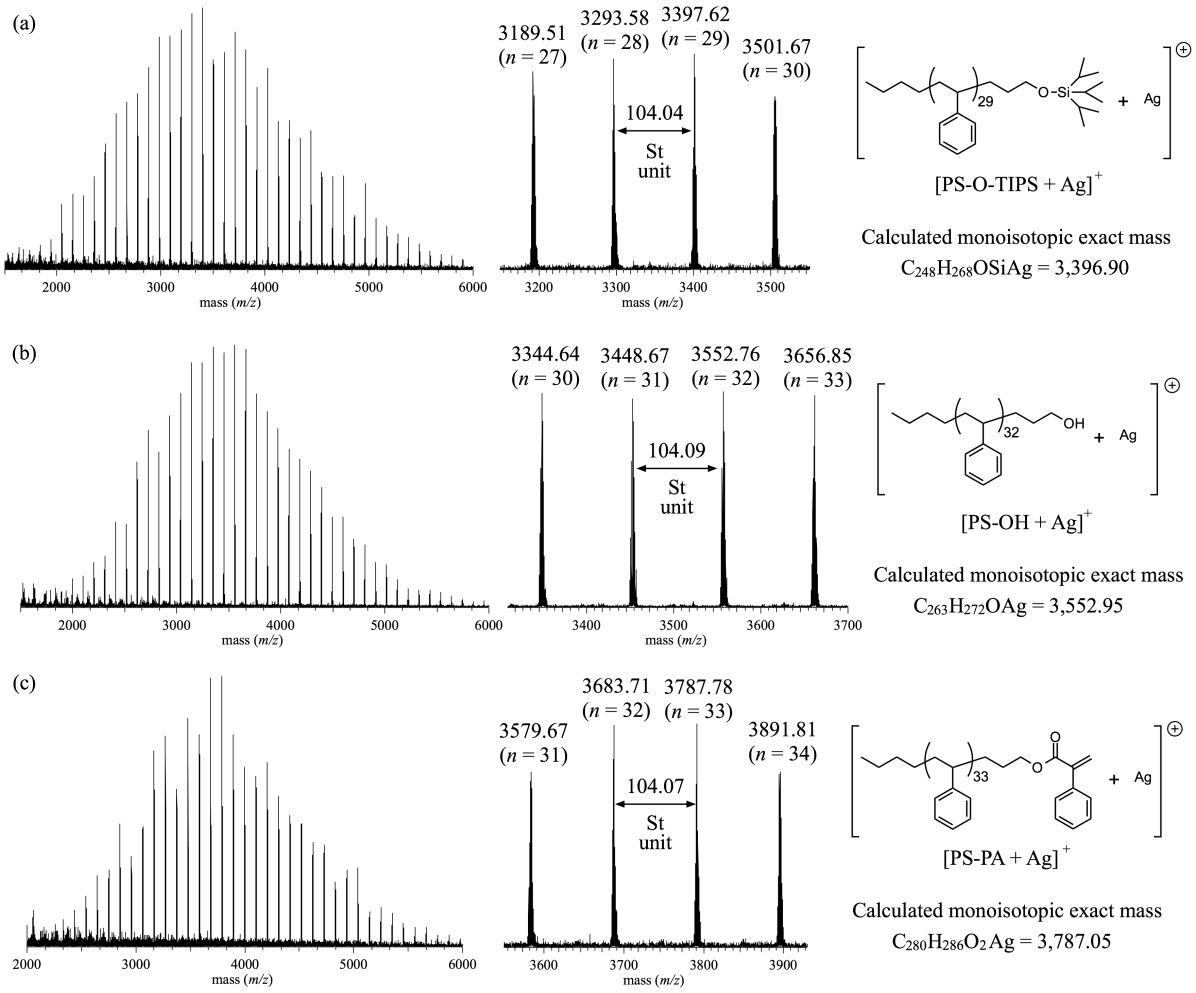

Figure S2.2. MALDI-TOF MS spectra of (a) PS_{4k}–O–TIPS, (b) PS_{4k}–OH, and (c) PS_{4k}–PA.

Synthesis of block copolymer consisting of PS and P(MMA-*co*-3BMA) (P[S_{45k}-*b*-($MMA_{0.70}$-*co*-$3BMA_{0.30}$)$_{18k}$]).

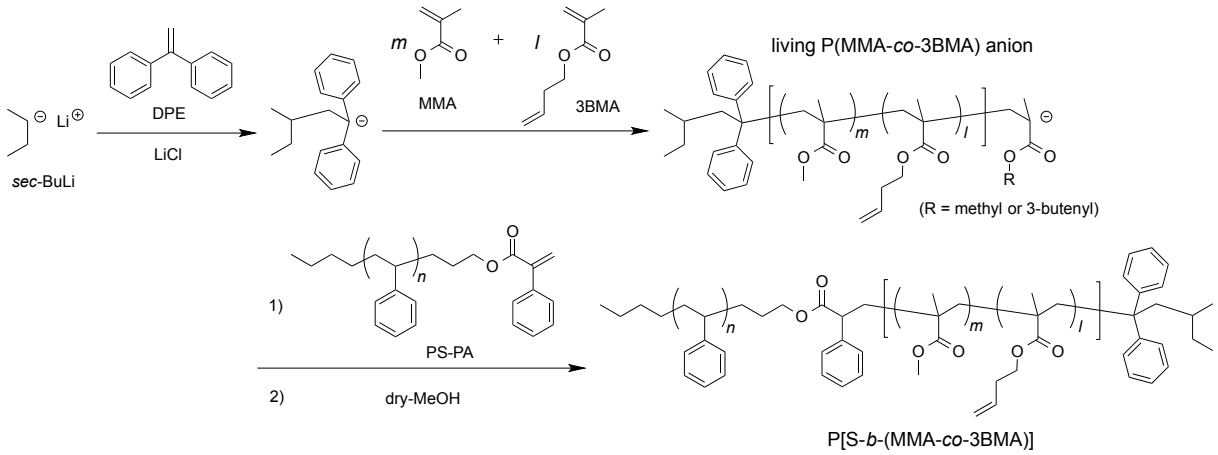

In the glovebox, dry-THF (10.0 mL) were placed in a Shlenk flask. After sealing, the flask was taken out from the glovebox. After cooling to -78 °C, *sec*-BuLi (24.0 μL, 24.0 μmol as a 1.0 mol L^{-1} stock solution in *n*-hexane) and DPE (9.3 mg, 51.6 μmol) was sequentially added to the flask. After 15 min, LiCl (120 μL, 120 μmol as a 1.0 mol L^{-1} stock solution in THF) was added to the solution. In a flame dried Shlenk flask, MMA (266 mg, 2.66 mmol) and 3BMA (160 mg, 1.14 mmol) were mixed together under an argon atmosphere. The mixture was added at once to the initiator solution. After stirring for 1 h at -78 °C, PS_{45k}-PA ($M_{n,SEC}$ = 45,400, 500 mg, 11.0 μmol) in THF (5.00 mL) was dropwise added to the solution of the resulting living P(MMA-*co*-3BMA) anion at -78 °C, and the reaction mixture was allowed to react at -40 °C for 48 h. After quenching the reaction with dry-MeOH, the resulting polymers were precipitated from CH_2Cl_2 into MeOH four times followed by preparative SEC, giving P[S_{45k}-*b*-($MMA_{0.70}$-*co*-$3BMA_{0.30}$)$_{19k}$] as a white solid. Yield: 277 mg (39.6 %). ^{1}H NMR (400 MHz, $CDCl_3$): δ (ppm) 7.34−6.26 (m, 5H × *n* + 15H, −C_6H_5), 5.86–5.71 (m, 1H × *l*, −C*H*=CH_2), 5.21–5.07 (m, 2H × *l*, −CH=CH_2), 4.09–3.93 (m, 2H × *l*,

−OCH_2CH$_2$CH = CH$_2$), 3.71–4.49 (m, 3H × *m*, −OCH_3), 2.46–2.31 (m, 2H × *l*, −OCH$_2$CH_2CH=CH$_2$), 2.30–1.67 (m, 1H × *n*, −CHC$_6$H$_5$), 2.09–1.12 (m, 2H × (*m* + *l*), −CH_2CCH$_3$(COOCH$_3$)−, −CH_2CCH$_3$(COO(CH$_2$)$_2$CH=CH$_2$)−), and 1.67–1.13 (m, 2H × *n*, −CH_2CHC$_6$H$_5$), 1.08–0.66 (m, 3H × (*m* + *l*), −CH$_2$CCH_3(COOCH$_3$)−, −CH$_2$CCH_3(COO(CH$_2$)$_2$CH=CH$_2$)−). $M_{n,SEC}$ = 61,400 g mol^{-1}, $Đ$ = 1.06 (THF), F_{3BMA} in the P(MMA-*co*-3BMA) segment = 0.30.

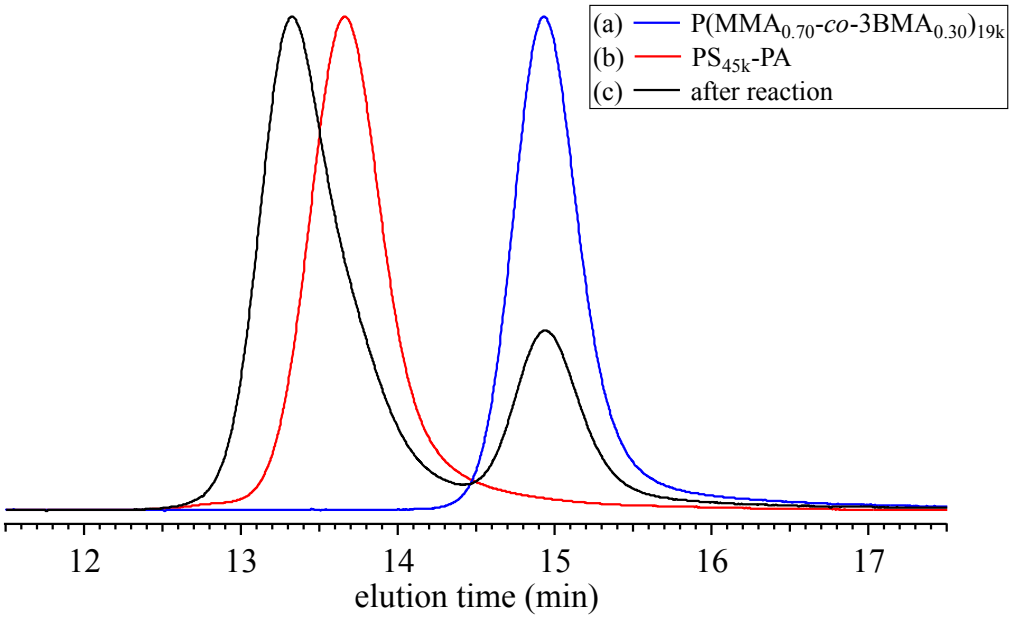

Figure S2.3. SEC traces of prepolymers ((a) P(MMA$_{0.70}$-*co*-3BMA$_{0.30}$)$_{19k}$; $M_{n,SEC}$ = 18,700 g mol^{-1}, $Đ$ = 1.03, (b) PS$_{45k}$-PA; $M_{n,SEC}$ = 45,400 g mol^{-1}, $Đ$ = 1.06) and (c) polymers obtained after the reaction (eluent, THF; flow rate, 1.0 mL min^{-1}). The SEC measurement of P(MMA-*co*-3BMA) were carried out after the termination of a portion of living polymer with dry-MeOH.

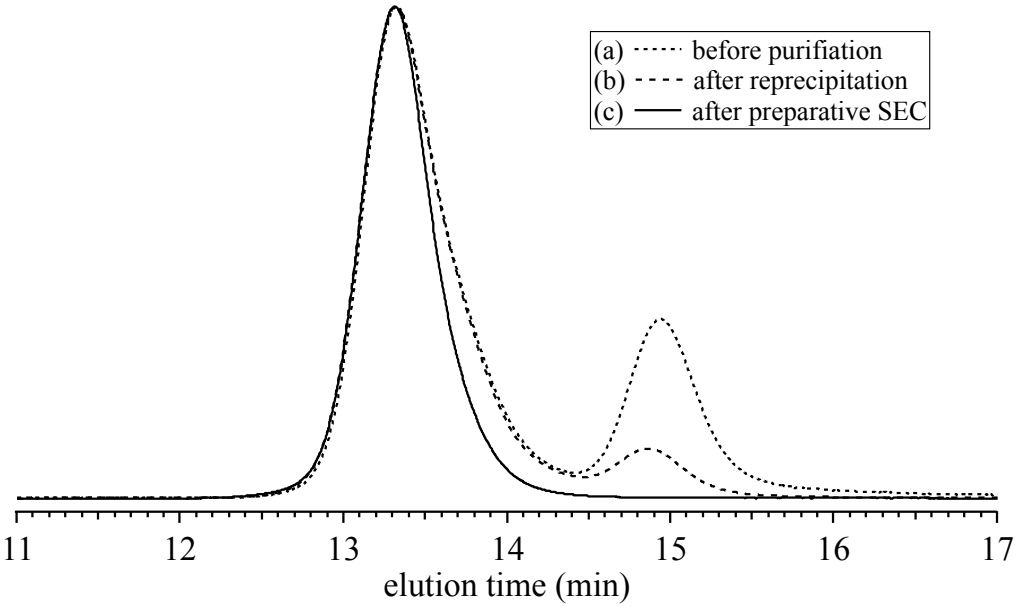

Figure S2.4. SEC traces obtained before and after the purifications (eluent, THF; flow rate, 1.0 mL min^{-1}).

Synthesis of poly(methacrylate)-based SCNP from P($BMA_{0.30}$-*co*-3$BMA_{0.60}$)$_{49k}$ (NP_{BMA}2). Method B was used for the intramolecular crosslinking of P($BMA_{0.30}$-*co*-3$BMA_{0.60}$)$_{49k}$ (117 mg, 0.496 mmol olefin-containing units) with G2 (7.8 mg, 9.2 μmol) in dry-CH_2Cl_2 (146 mL) for 10 h to give NP_{BMA}2. $M_{n,SEC}$ = 33,100 g mol^{-1}, $Đ$ = 1.19 (THF), conv.$_{olefin}$ = 95%.

Synthesis of poly(methacrylate)-based SCNP from P(3BMA)$_{50k}$ (NP_{BMA}3). Method B was used for the intramolecular crosslinking of P(3BMA)$_{50k}$ (96.8 mg, 0.691 mmol olefin-containing units) with G2 (11.7 mg, 13.8 μmol) in dry-CH_2Cl_2 (120mL) for 10 h to give NP_{BMA}3. $M_{n,SEC}$ = 25,700 g mol^{-1}, $Đ$ = 1.19 (THF), conv.$_{olefin}$ = 94%.

Synthesis of poly(methacrylate)-based SCNP from P($BMA_{0.40}$-*co*-3$BMA_{0.60}$)$_{24k}$ (NP_{BMA}4). Method B was used for the intramolecular crosslinking of P($BMA_{0.40}$-*co*-3$BMA_{0.60}$)$_{24k}$ (104 mg, 0.433 mmol olefin-containing units) with G2 (7.4 mg, 8.7 μmol) in mixture of dry-CH_2Cl_2 and *n*-hexane (dry-CH_2Cl_2/*n*-hexane = 1/1 (v/v)) (130 mL) for 10 h to give NP_{BMA}4. $M_{n,SEC}$ = 17,100 g mol^{-1}, $Đ$ = 1.10 (THF), conv.$_{olefin}$ = 97%

Synthesis of poly(methacrylate)-based SCNP from P($BMA_{0.40}$-*co*-3$BMA_{0.60}$)$_{80k}$ (NP_{BMA}5). Method B was used for the intramolecular crosslinking of P($BMA_{0.40}$-*co*-3$BMA_{0.60}$)$_{80k}$ (86.9 mg, 0.366 mmol olefin-containing units) with G2 (6.2 mg, 7.3 μmol) in mixture of dry-CH_2Cl_2 and *n*-hexane (dry-CH_2Cl_2/*n*-hexane = 1/1 (v/v)) (109 mL) for 10 h to give NP_{BMA}5. $M_{n,SEC}$ = 46,900 g mol^{-1}, $Đ$ = 1.23 (THF), conv.$_{olefin}$ = 95%.

Synthesis of poly(methacrylate)-based SCNP from P($BMA_{0.70}$-*co*-3$BMA_{0.30}$)$_{55k}$ (NP_{BMA}6). Method B was used for the intramolecular crosslinking of P($BMA_{0.70}$-*co*-3$BMA_{0.30}$)$_{55k}$ (56.1 mg, 0.119 mmol olefin-containing units) with G2 (2.0 mg,

2.4 μmol) in a mixture of dry-CH_2Cl_2 and *n*-hexane (dry-CH_2Cl_2/*n*-hexane = 1/1 (v/v)) for 10 h to give NP_{BMA}6. $M_{n,SEC}$ = 37,900 g mol^{-1}, $Đ$ = 1.20 (THF), conv.$_{olefin}$ = 96%.

Synthesis of poly(methacrylate)-based SCNP from P(BMA$_{0.70}$-*co*-3BMA$_{0.30}$)$_{55k}$ (NP_{BMA}7). Method B was used for the intramolecular crosslinking of P(BMA$_{0.70}$-*co*-3BMA$_{0.30}$)$_{55k}$ (61.6 mg, 0.131 mmol olefin-containing units) with G2 (2.2 mg, 2.6 μmol) in mixture of dry-CH_2Cl_2 and *n*-hexane (dry-CH_2Cl_2/*n*-hexane = 1/3 (v/v)) (77 mL) for 10 h to give NP_{BMA}7. $M_{n,SEC}$ = 33,600 g mol^{-1}, $Đ$ = 1.19 (THF), conv.$_{olefin}$ = 97%.

Synthesis of poly(methacrylate)-based SCNP from P(BMA$_{0.70}$-*co*-3BMA$_{0.30}$)$_{55k}$ (NP_{BMA}8). Method B was used for the intramolecular crosslinking of P(BMA$_{0.70}$-*co*-3BMA$_{0.30}$)$_{55k}$ (100 mg, 0.212 mmol olefin-containing units) with G2 (3.6 mg, 4.2 μmol) in mixture of dry-CH_2Cl_2 and *n*-hexane (dry-CH_2Cl_2/*n*-hexane = 1/5 (v/v)) (125 mL) for 10 h to give NP_{BMA}8. $M_{n,SEC}$ = 28,000 g mol^{-1}, $Đ$ = 1.21 (THF), conv.$_{olefin}$ = 96%.

Synthesis of poly(acrylate)-based SCNP from P(BA$_{0.50}$-*co*-3BA$_{0.50}$)$_{120k}$ (NP_{BA}1). Method B was used for the intramolecular crosslinking of P(BA$_{0.50}$-*co*-3BA$_{0.50}$)$_{120k}$ (40.4 mg, 0.152 mmol olefin-containing units) with G2 (2.6 mg, 3.1 μmol) in dry-CH_2Cl_2 (50 mL) for 10 h to give NP_{BA}1. $M_{n,SEC}$ = 106,000 g mol^{-1}, $Đ$ = 1.13 (THF), conv.$_{olefin}$ = 54%.

Synthesis of poly(acrylate)-based SCNP from P(BA$_{0.50}$-*co*-3BA$_{0.50}$)$_{120k}$ (NP_{BA}2). Method B was used for the intramolecular crosslinking of P(BA$_{0.50}$-*co*-3BA$_{0.50}$)$_{120k}$ (40.2 mg, 0.151 mmol olefin-containing units) with G2 (2.6 mg, 3.1 μmol) in mixture of dry-CH_2Cl_2 and *n*-hexane (dry-CH_2Cl_2/*n*-hexane = 1/2 (v/v)) (50 mL) for 10 h to give NP_{BA}2. $M_{n,SEC}$ = 73,000 g mol^{-1}, $Đ$ = 1.23 (THF), conv.$_{olefin}$ = 69%.

Synthesis of poly(acrylate)-based SCNP from P($BA_{0.50}$-*co*-$3BA_{0.50}$)$_{120k}$ (NP_{BA}3). Method B was used for the intramolecular crosslinking of P($BA_{0.50}$-*co*-$3BA_{0.50}$)$_{120k}$ (40.1 mg, 0.150 mmol olefin-containing units) with G2 (2.5 mg, 3.0 μmol) in mixture of dry-CH_2Cl_2 and *n*-hexane (dry-CH_2Cl_2/*n*-hexane = 1/3 (v/v)) (50 mL) for 10 h to give NP_{BA}3. $M_{n,SEC}$ = 56,100 g mol^{-1}, $Đ$ = 1.31 (THF), conv.$_{olefin}$ = 77%.

Synthesis of poly(acrylate)-based SCNP from P($BA_{0.50}$-*co*-$3BA_{0.50}$)$_{120k}$ (NP_{BA}4). Method B was used for the intramolecular crosslinking of P($BA_{0.50}$-*co*-$3BA_{0.50}$)$_{120k}$ (40.1 mg, 0.150 mmol olefin-containing units) with G2 (2.6 mg, 3.1 μmol) in mixture of dry-CH_2Cl_2 and *n*-hexane (dry-CH_2Cl_2/*n*-hexane = 1/5 (v/v)) (50 mL) for 10 h to give NP_{BA}4. $M_{n,SEC}$ = 36,000 g mol^{-1}, $Đ$ = 1.20 (THF), conv.$_{olefin}$ = 89%.

Synthesis of poly(ester)-based SCNP from P($CL_{0.64}$-*co*-$ACL_{0.36}$)$_{13k}$ (NP_{CL}1). Method B was used for the intramolecular crosslinking of P($CL_{0.64}$-*co*-$ACL_{0.36}$)$_{13k}$ (38.1 mg, 0.106 mmol olefin-containing units) with G2 (1.8 mg, 2.1 μmol) in dry-CH_2Cl_2 (47.6 mL) for 10 h to give NP_{CL}1. $M_{n,SEC}$ = 9,470 g mol^{-1}, $Đ$ = 1.15 (THF), conv.$_{olefin}$ = 78%.

Synthesis of poly(ester)-based SCNP from P($CL_{0.64}$-*co*-$ACL_{0.36}$)$_{13k}$ (NP_{CL}2). Method B was used for the intramolecular crosslinking of P($CL_{0.64}$-*co*-$ACL_{0.36}$)$_{13k}$ (33.0 mg, 0.0910 mmol olefin-containing units) with G2 (1.5 mg, 1.8 μmol) in mixture of dry-CH_2Cl_2 and *n*-hexane (dry-CH_2Cl_2/*n*-hexane = 1/2 (v/v)) (41.3 mL) for 10 h to give NP_{CL}2. $M_{n,SEC}$ = 8,640 g mol^{-1}, $Đ$ = 1.19 (THF), conv.$_{olefin}$ = 79%.

2.6.2 Additional data

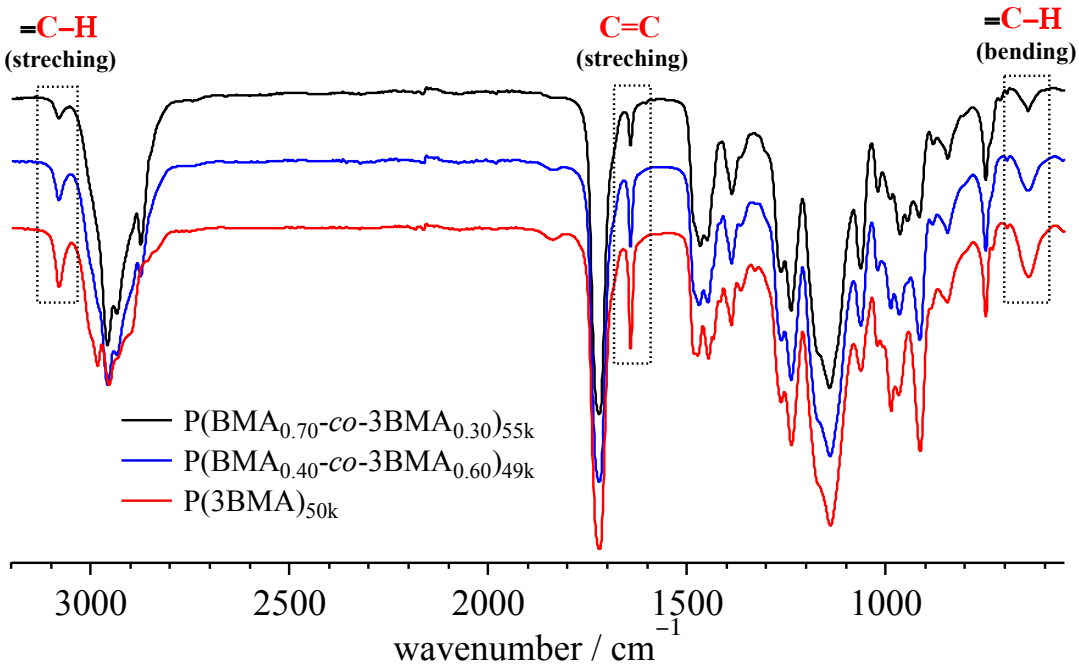

Figure S2.5. IR spectra of $P(BMA_{0.70}\text{-}co\text{-}3BMA_{0.30})_{55k}$ (black), $P(BMA_{0.40}\text{-}co\text{-}3BMA_{0.60})_{49k}$ (blue), and $P(3BMA)_{50k}$ (red).

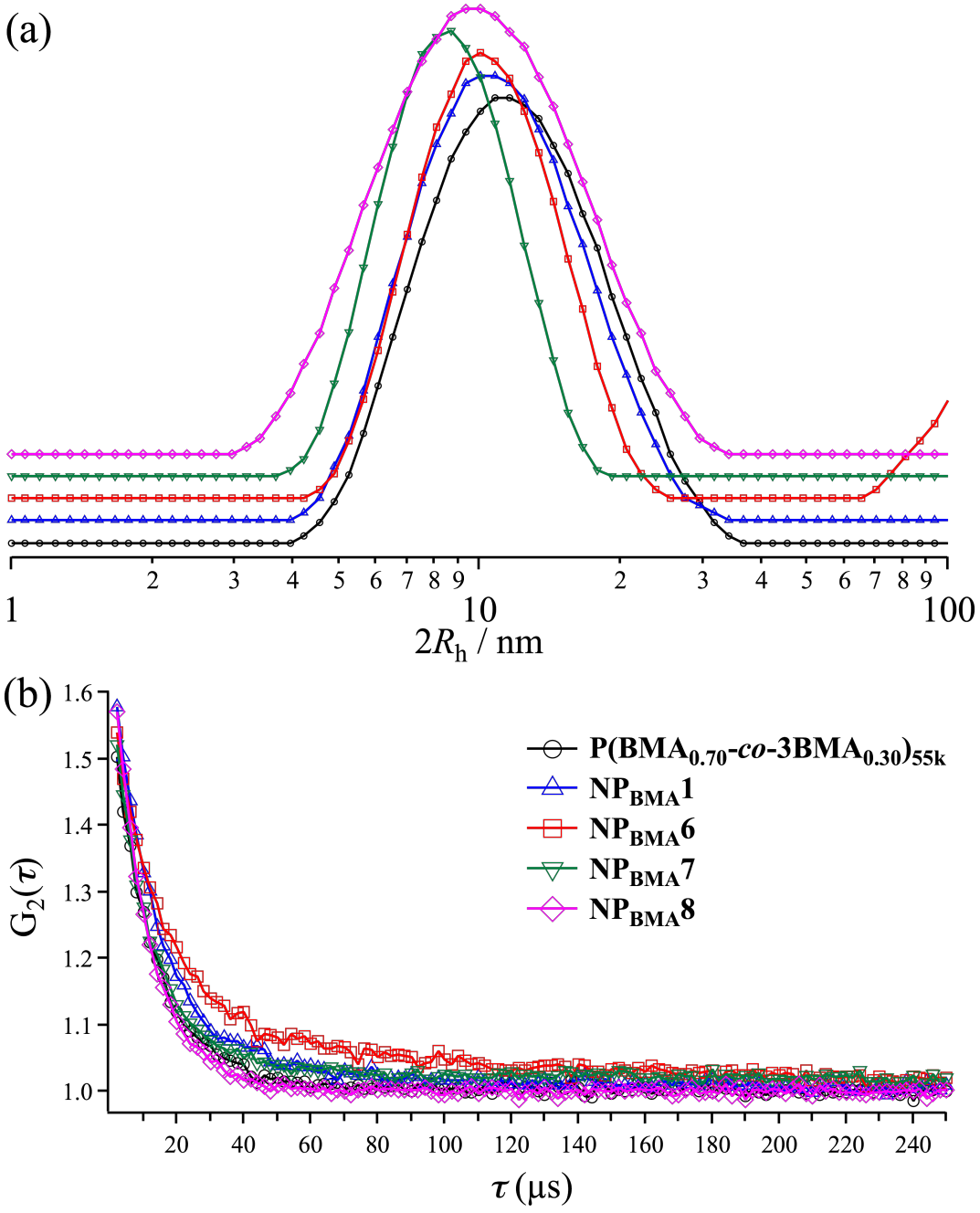

Figure S2.6. DLS results of P(BMA$_{0.70}$-*co*-3BMA$_{0.30}$)$_{55k}$ (black), NP$_{BMA}$1 (blue), NP$_{BMA}$6 (red), NP$_{BMA}$7 (green), and NP$_{BMA}$8 (pink). (a) Intensity-averaged size distributions and (b) autocorrelation functions measured at $\theta = 90°$ at 25 °C in THF ([polymer] = 5 mg mL^{-1}).

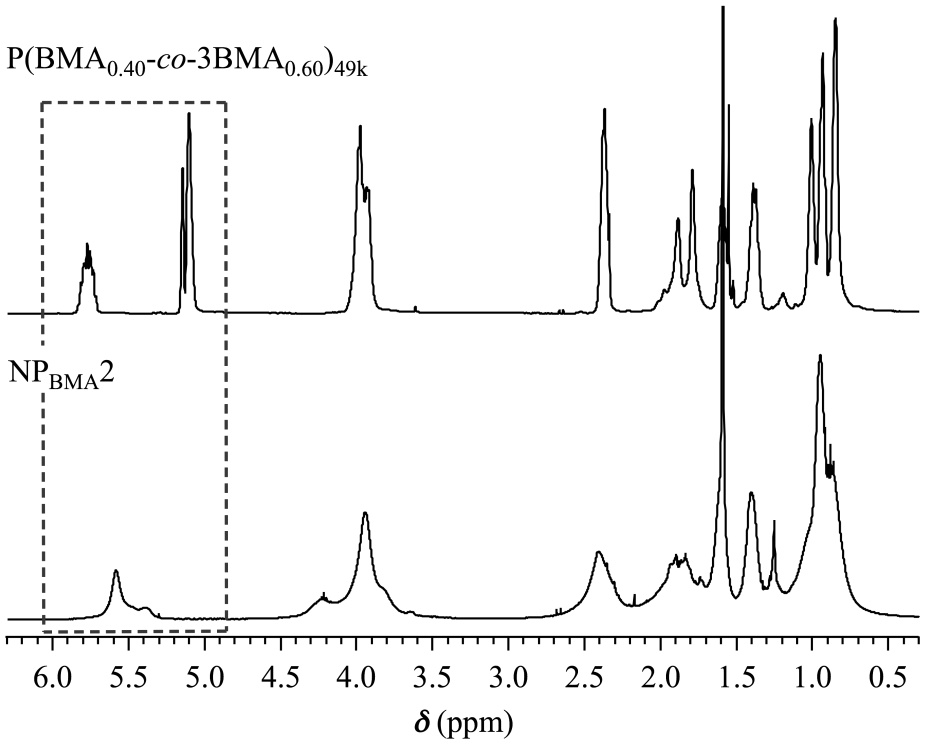

Figure S2.7. ^{1}H NMR spectra of P(BMA$_{0.40}$-*co*-3BMA$_{0.60}$)$_{49k}$ (upper) and NP$_{BMA}$2 (lower) in $CDCl_3$ (400 MHz).

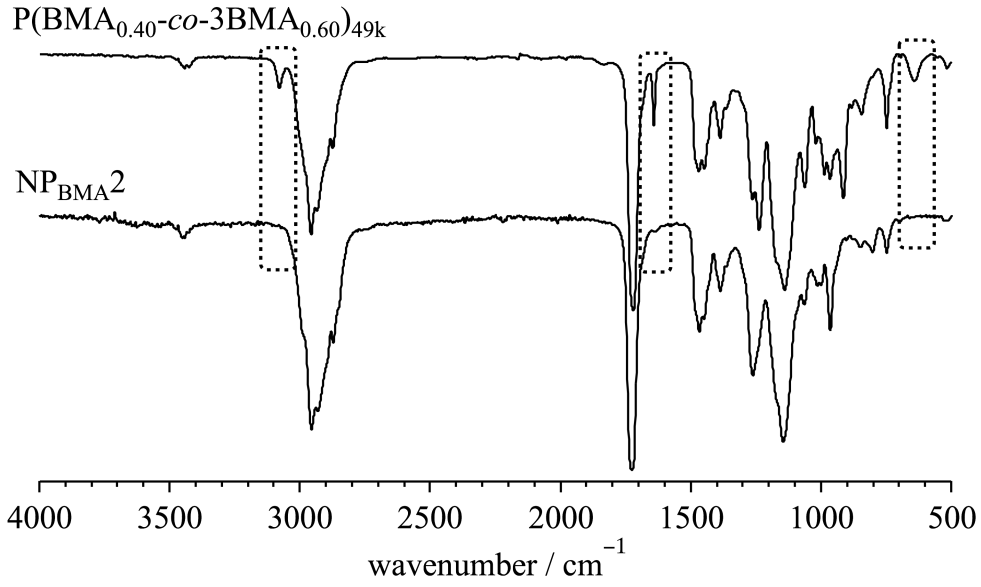

Figure S2.8. IR spectra of P(BMA$_{0.40}$-*co*-3BMA$_{0.60}$)$_{49k}$ (upper) and NP$_{BMA}$2 (lower).

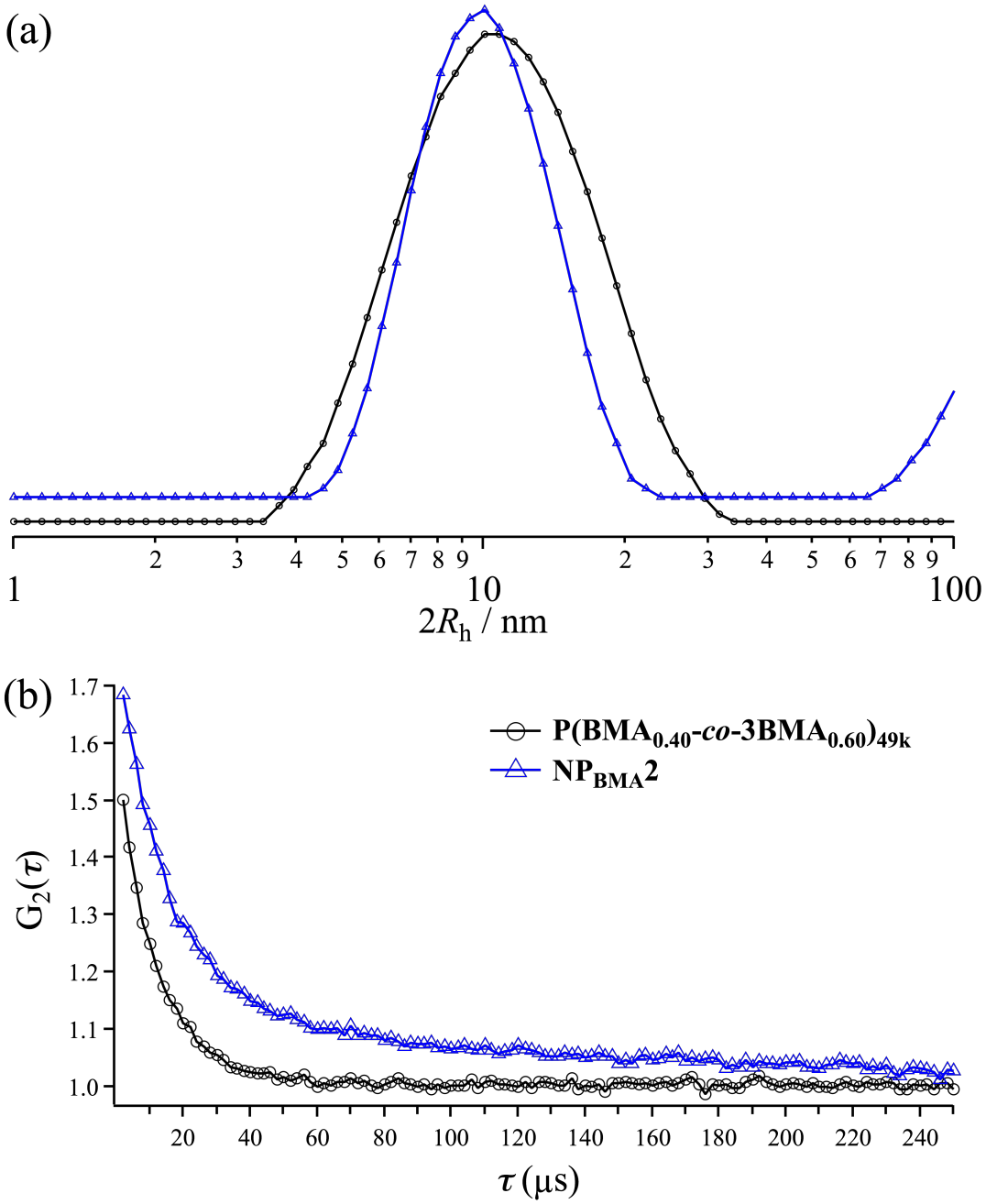

Figure S2.9. DLS results of P(BMA$_{0.40}$-*co*-3BMA$_{0.60}$)$_{49k}$ (black) and NP$_{BMA}$2 (blue). (a) Intensity-averaged size distributions and (b) autocorrelation functions measured at $\theta = 90°$ at 25 °C in THF ([polymer] = 5 mg mL^{-1}).

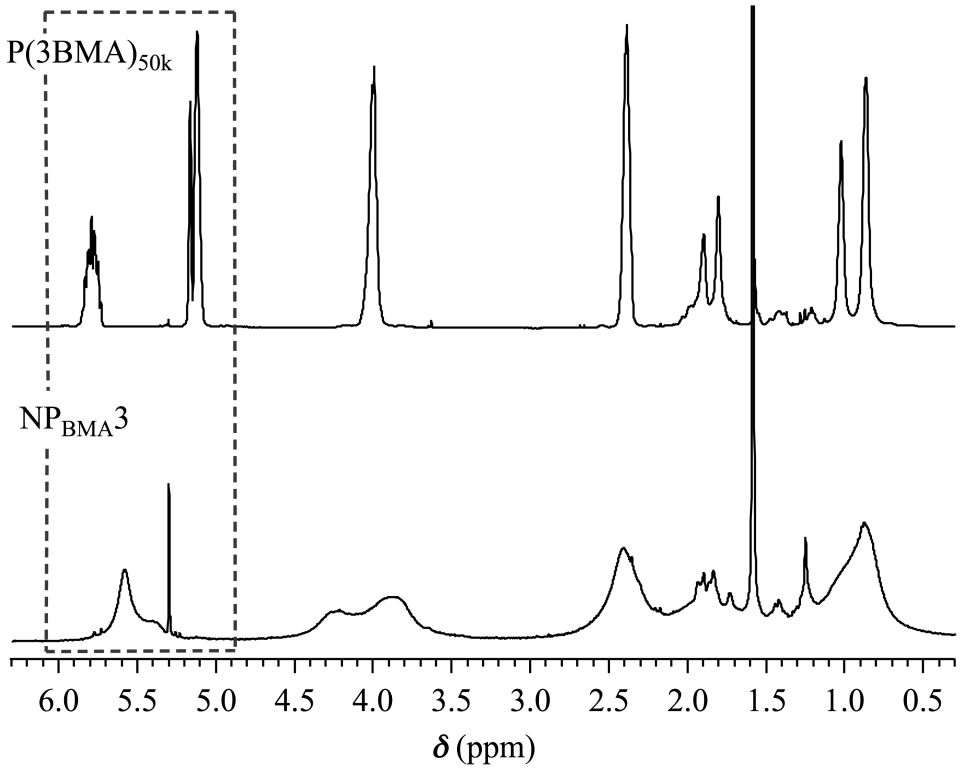

Figure S2.10. ^{1}H NMR spectra of $P(3BMA)_{55k}$ (upper) and $NP_{BMA}3$ (lower) in $CDCl_3$ (400 MHz).

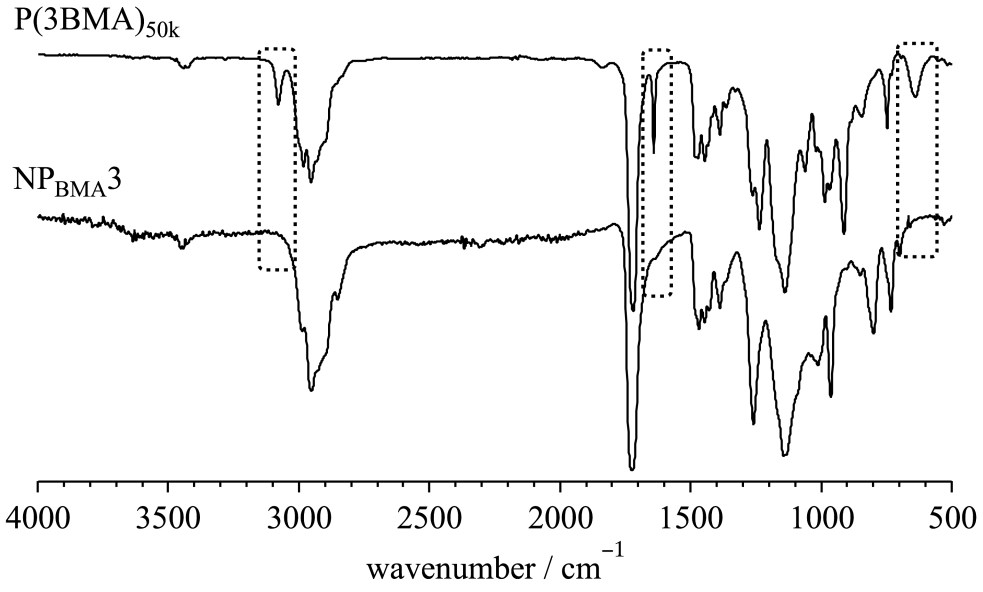

Figure S2.11. IR spectra of $P(3BMA)_{50k}$ (upper) and $NP_{BMA}3$ (lower).

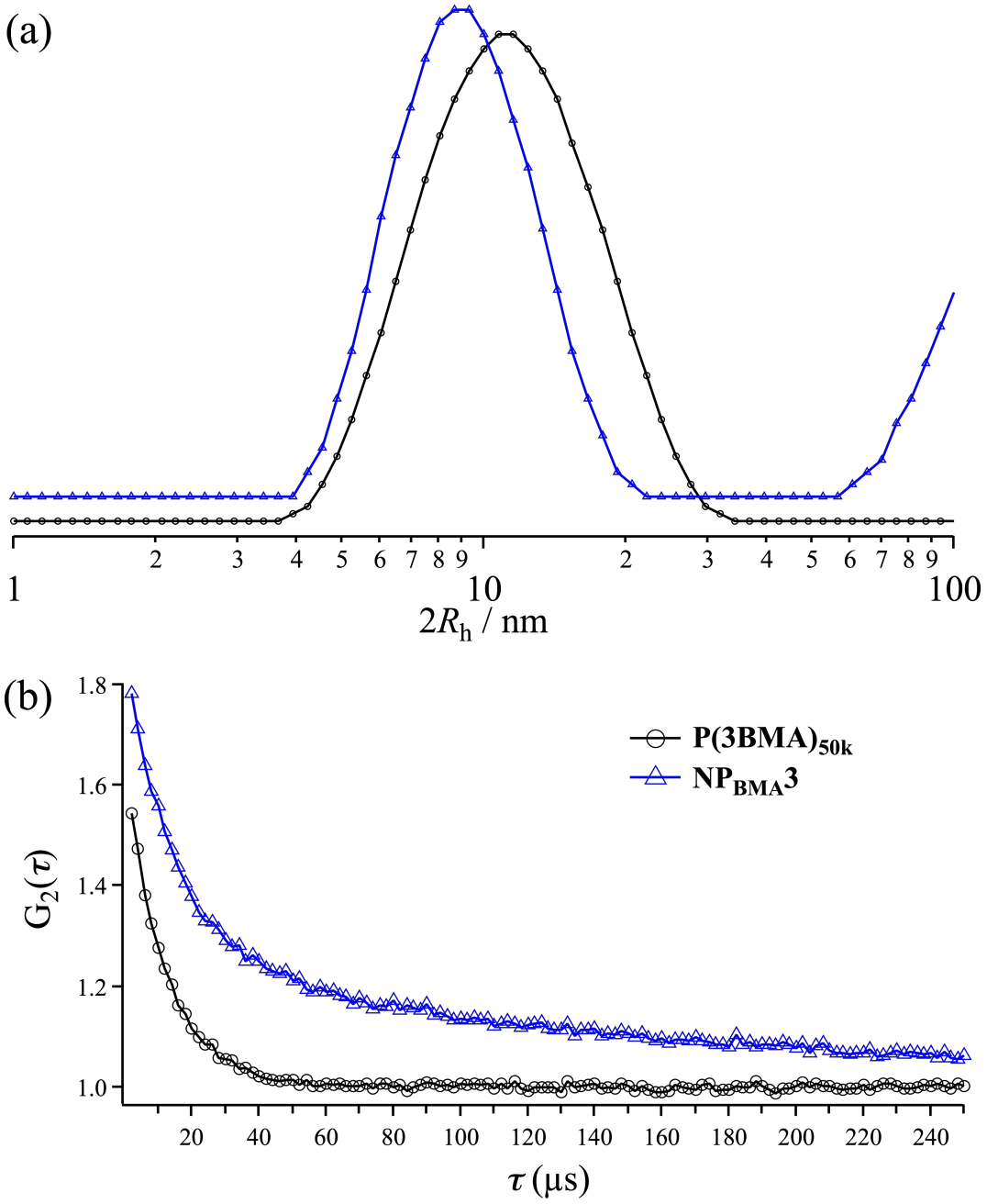

Figure S2.12. DLS results of P(3BMA)$_{50k}$ (black) and NP$_{BMA}$3 (blue). (a) Intensity-averaged size distributions and (b) autocorrelation functions measured at $\theta = 90°$ at 25 °C in THF ([polymer] = 5 mg mL^{-1}).

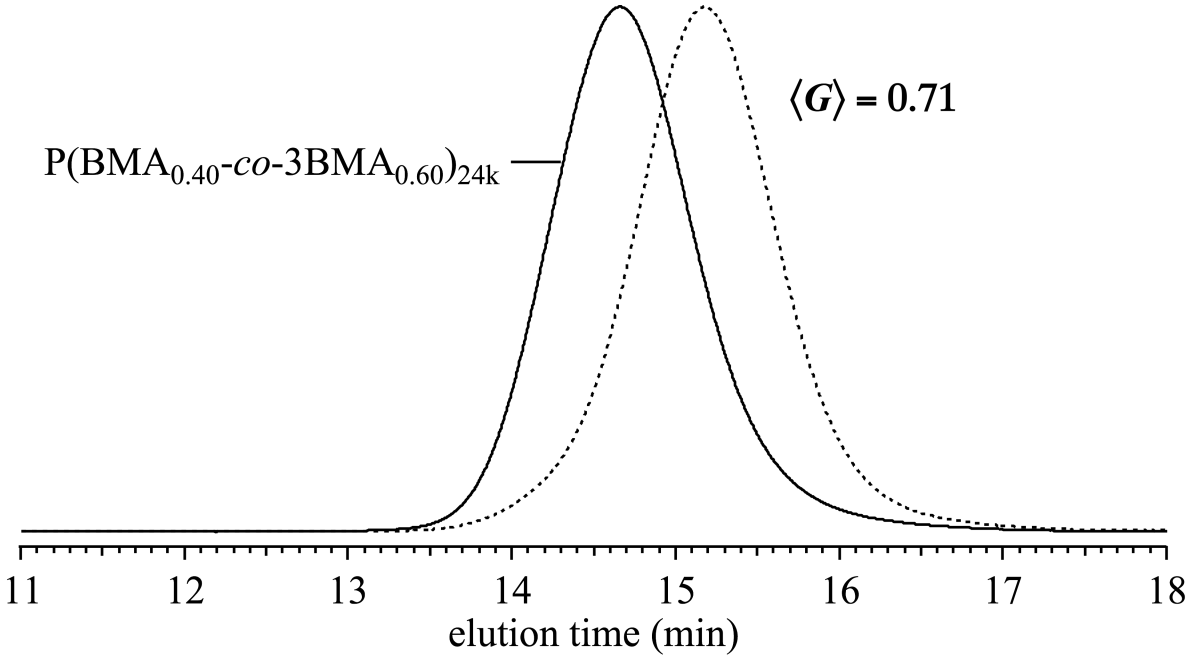

Figure S2.13. SEC traces of $P(BMA_{0.40}\text{-}co\text{-}3BMA_{0.60})_{24k}$ (solid) and $NP_{BMA}4$ (dashed) (eluent, THF; flow rate, 1.0 mL min^{-1}).

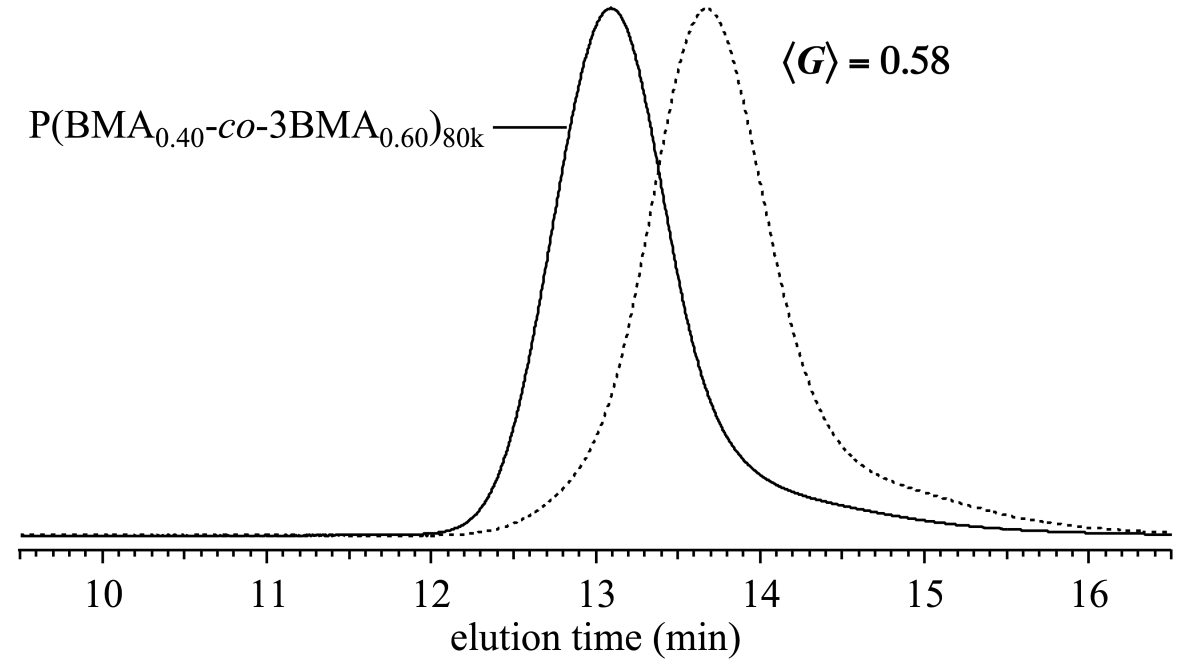

Figure S2.14. SEC traces of $P(BMA_{0.40}\text{-}co\text{-}3BMA_{0.60})_{80k}$ (solid) and $NP_{BMA}5$ (dashed) (eluent, THF; flow rate, 1.0 mL min^{-1}).

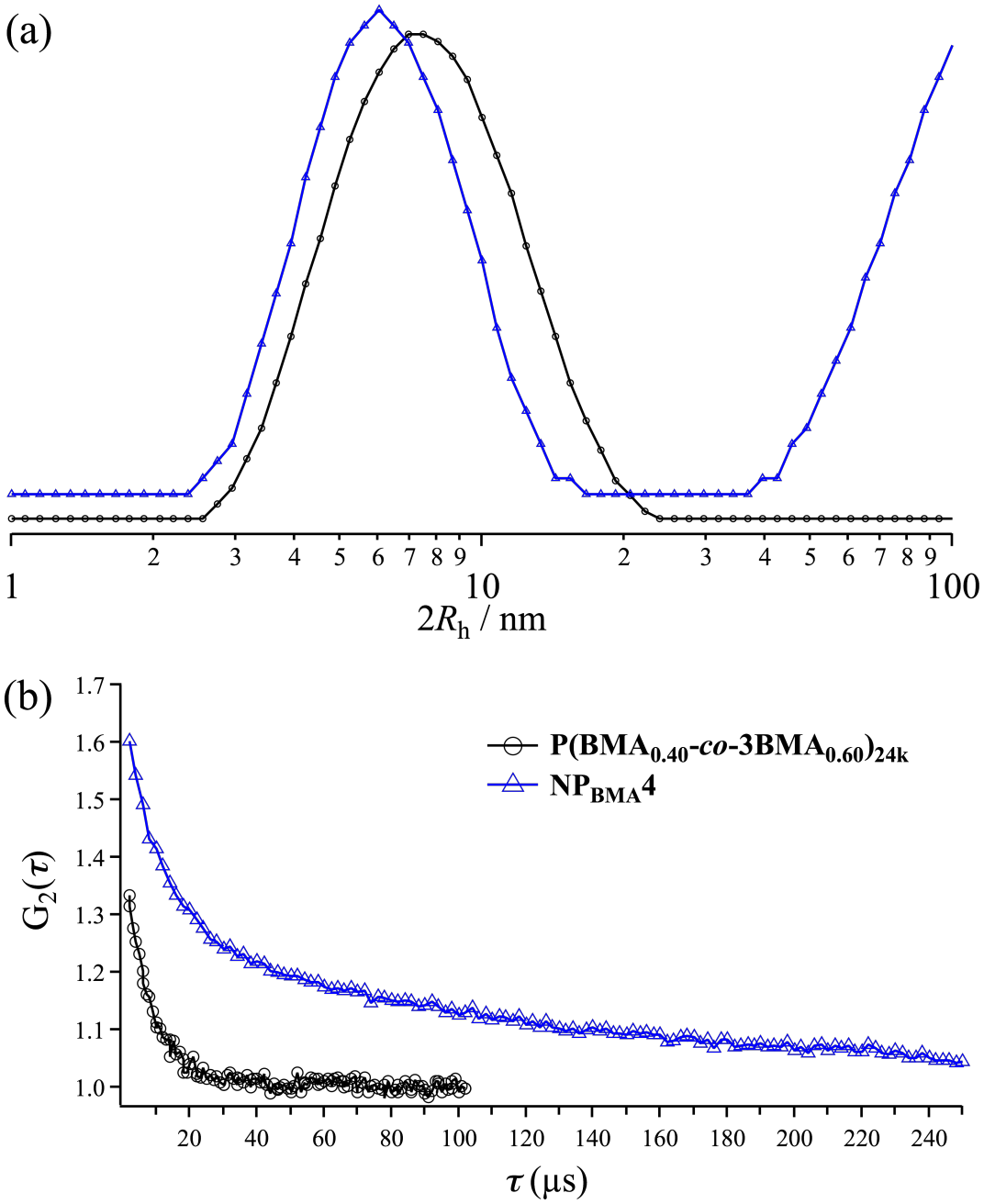

Figure S2.15. DLS results of P(BMA$_{0.40}$-*co*-3BMA$_{0.60}$)$_{24k}$ (black) and NP$_{BMA}$4 (blue). (a) Intensity-averaged size distributions and (b) autocorrelation functions measured at $\theta = 90°$ at 25 °C in THF ([polymer] = 5 mg mL^{-1}).

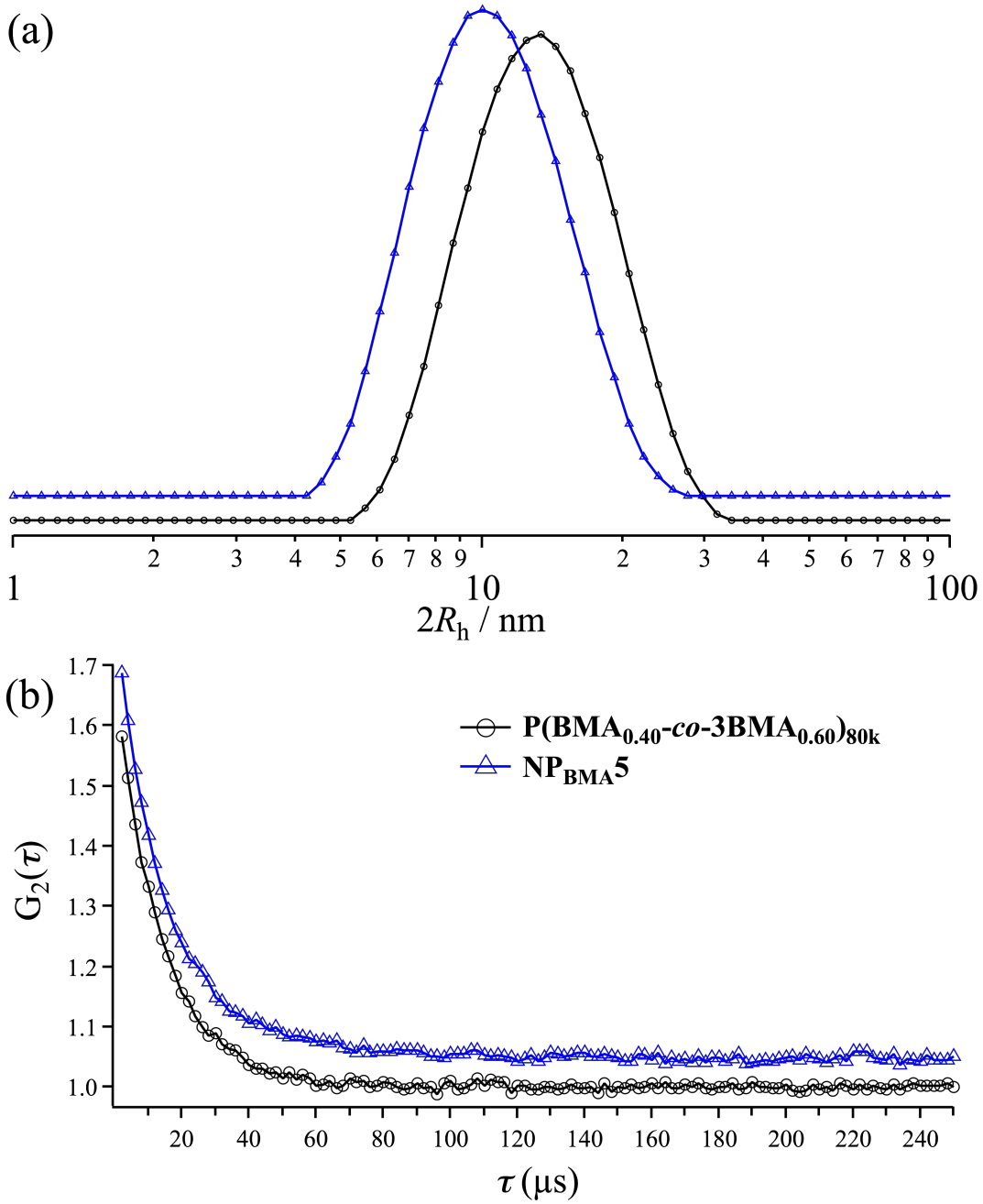

Figure S2.16. DLS results of P(BMA$_{0.40}$-*co*-3BMA$_{0.60}$)$_{80k}$ (black) and NP$_{BMA}$5 (blue). (a) Intensity-averaged size distributions and (b) autocorrelation functions measured at $\theta = 90°$ at 25 °C in THF ([polymer] = 5 mg mL^{-1}).

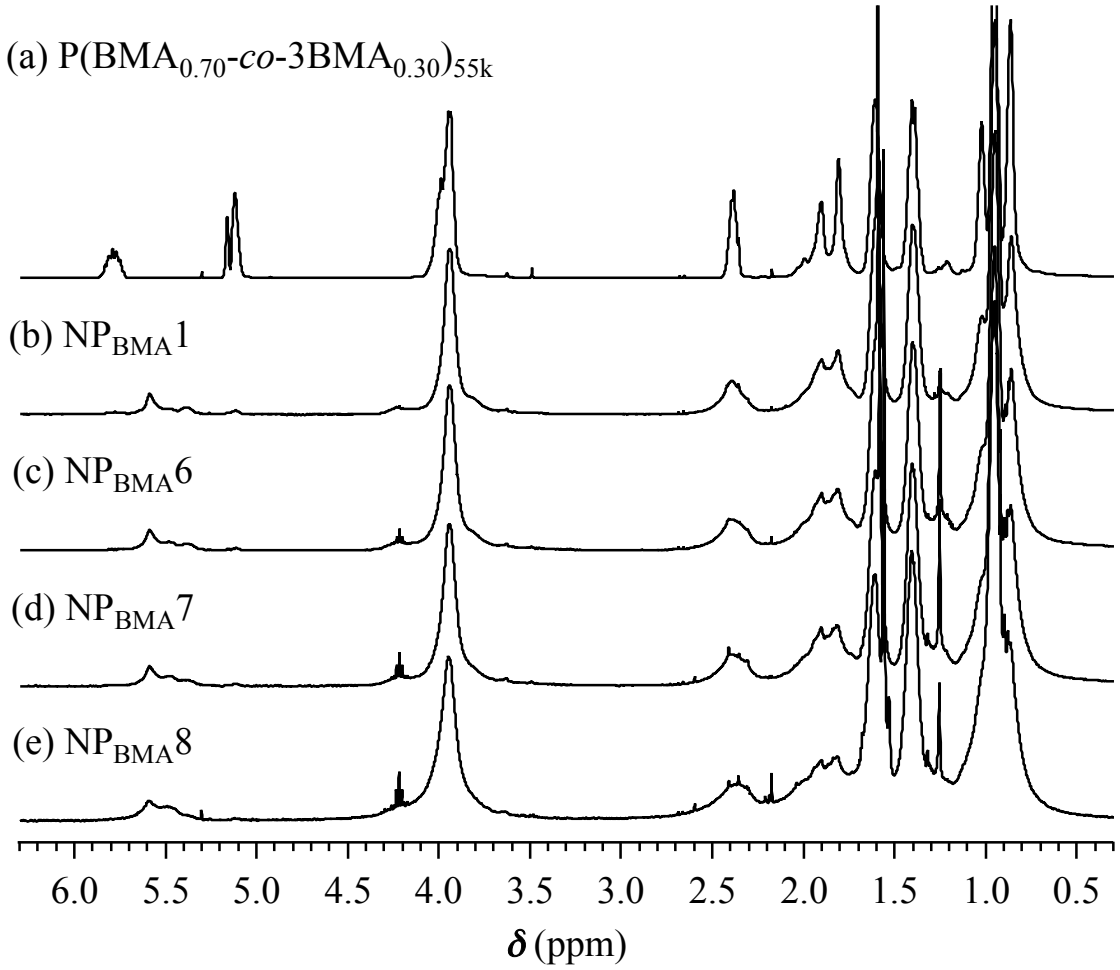

Figure S2.17. ^{1}H NMR spectra of (a) P(BMA$_{0.70}$-*co*-3BMA$_{0.30}$)$_{55k}$, (b) NP$_{BMA}$1, (c) NP$_{BMA}$6, (d) NP$_{BMA}$7, and (e) NP$_{BMA}$8 in $CDCl_3$ (400 MHz).

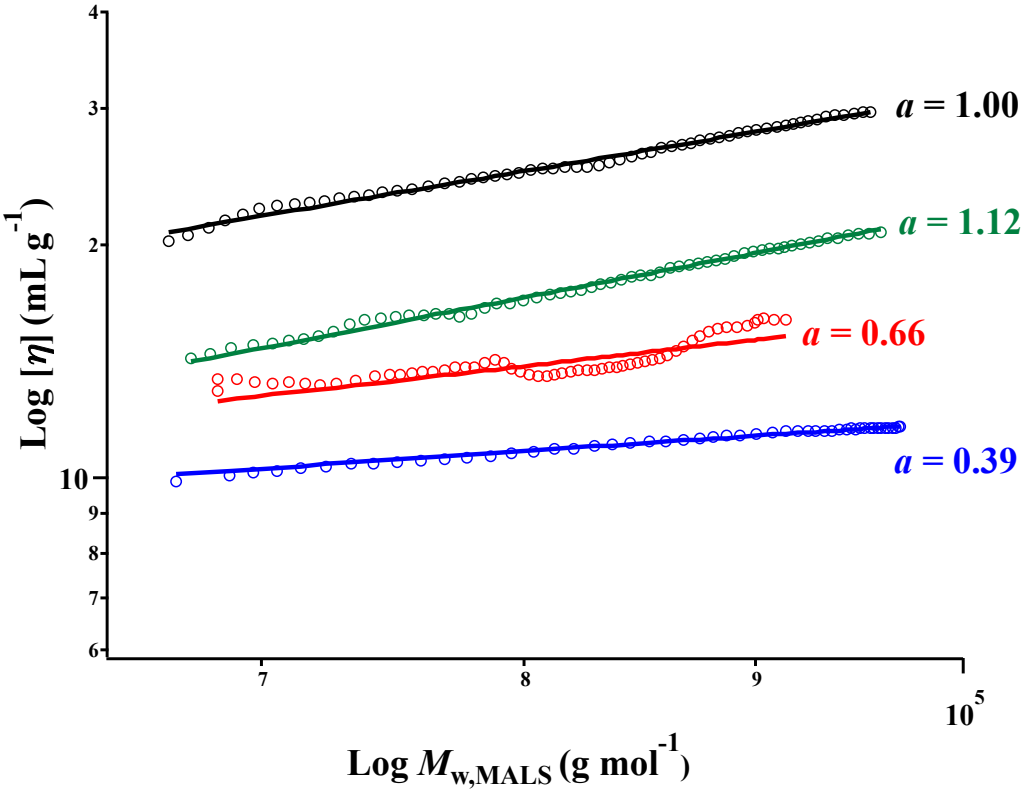

Figure S2.18. MHS plots for P($BMA_{0.70}$-*co*-3$BMA_{0.30}$)$_{55k}$ (black), $NP_{BMA}1$ (green), $NP_{BMA}6$ (red), and $NP_{BMA}7$ (blue). Values of *a* were calculated from MHS equation ($[\eta] = KM^a$).

Table S2.1. Synthesis of SCNPs from a variety of linear precursors[a]

polymer sample	linear precursor	ϕ_{hexane}	conv.$_{olefin}$[f] (%)	$M_{n,SEC}$[g] (g mol^{-1})	$M_{p,SEC}$[g] (g mol^{-1})	$Đ$[g]	$\langle G \rangle$[h]
$NP_{BA}1$	$P(BA_{0.50}$-*co*-$3BA_{0.50})_{120k}$[b]	0.00	54	106,000	119,000	1.13	0.92
$NP_{BA}2$		0.66	69	73,000	86,300	1.23	0.66
$NP_{BA}3$		0.75	77	56,100	64,400	1.31	0.50
$NP_{BA}4$		0.83	89	36,000	37,700	1.20	0.29
$NP_{CL}1$	$P(CL_{0.64}$-*co*-$ACL_{0.36})_{13k}$[d]	0.00	78	9,470	10,000	1.15	0.82
$NP_{CL}2$		0.67	79	8,640	7,630	1.19	0.62
PSt–$NP_{MMA}1$	$P[St_{45k}$-*b*-$(MMA_{0.70}$-*co*-$3BMA_{0.30})_{19k}]$[e]	0.00	90	59,900	62,500	1.06	0.96
PSt–$NP_{MMA}2$		0.50	93	59,700	57,900	1.26	0.88

[a]Reaction conditions: $[polymer]_0$ = 0.80 g L^{-1} in CH_2Cl_2; [3BMA units]/[G2] = 1/0.02; temp., 30 °C. [b]$M_{n,SEC}$ = 120,000 g mol^{-1}, $M_{p,SEC}$ = 130,000 g mol^{-1}, $Đ$ = 1.05. [c]$M_{n,SEC}$ = 19,800 g mol^{-1}, $M_{p,SEC}$ = 19,600 g mol^{-1}, $Đ$ = 1.04. [d]$M_{n,SEC}$ = 12,900 g mol^{-1}, $M_{p,SEC}$ = 12,300 g mol^{-1}, $Đ$ = 1.08. [e]$M_{n,SEC}$ = 61,400 g mol^{-1}, $M_{p,SEC}$ = 65,400 g mol^{-1}, $Đ$ = 1.06. [f]Determined by ^{1}H NMR in $CDCl_3$. [g]Determined by SEC in THF using poly(methyl methacrylate) (for NP_{BA}s) or poly(styrene) (for NP_{St}s, NP_{CL}s, and PSt–NP_{MMA}s) standards. [h]Determined by $M_{p,SEC}$(SCNP)/$M_{p,SEC}$(linear).

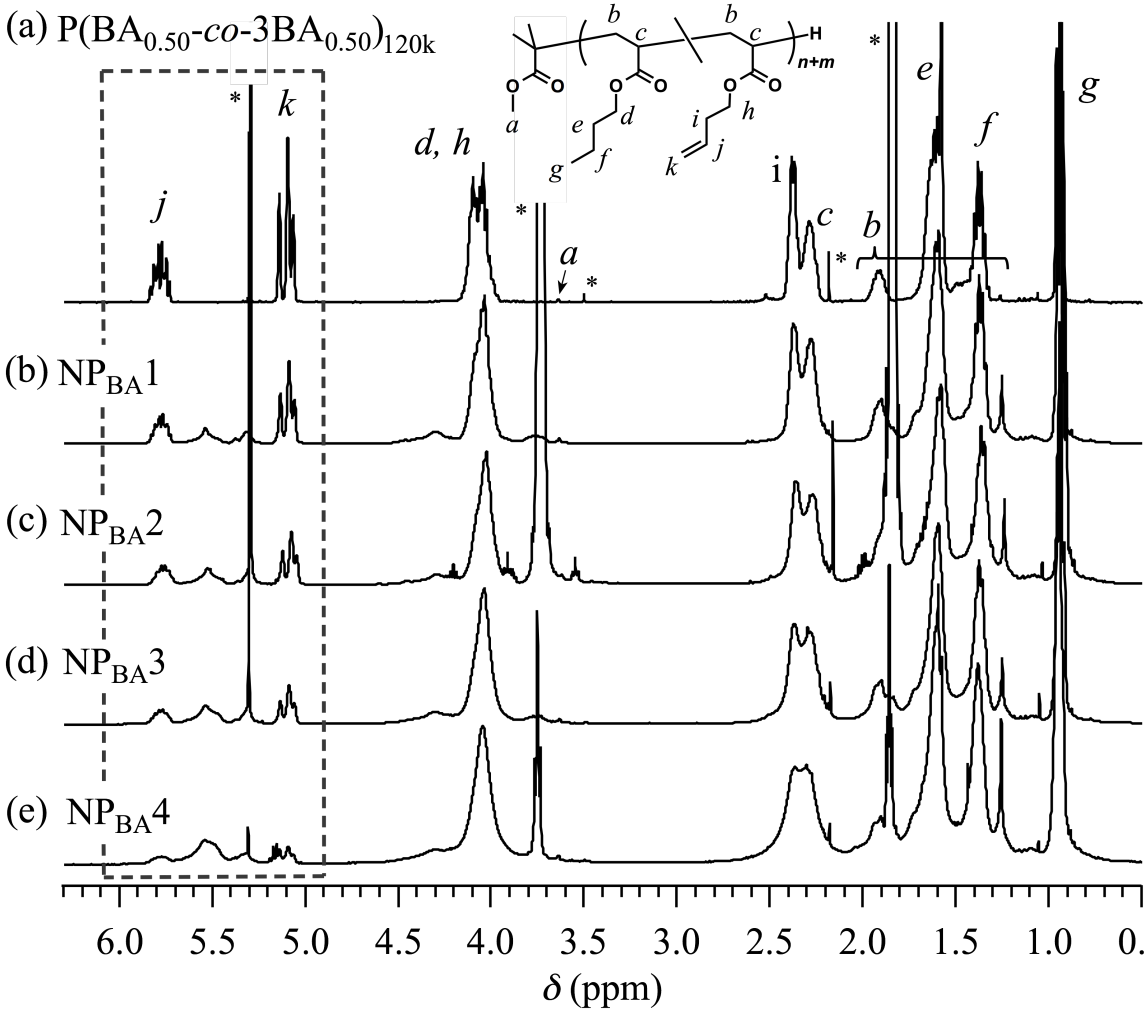

Figure S2.19. ^{1}H NMR spectra of (a) P($BA_{0.50}$-*co*-$3BA_{0.50}$)$_{120k}$, (b) $NP_{BA}1$, (c) $NP_{BA}2$, (d) $NP_{BA}3$, and (e) $NP_{BA}4$ in $CDCl_3$ (400 MHz).

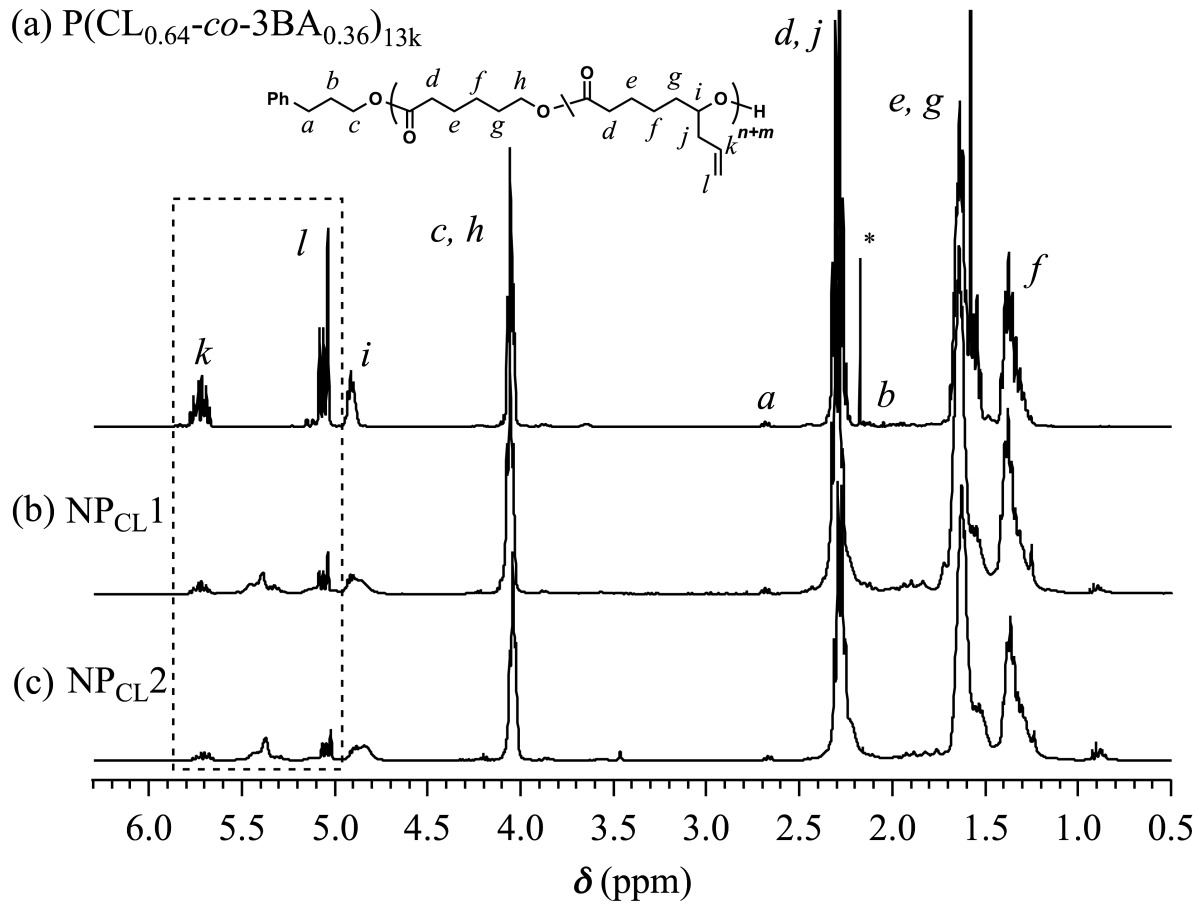

Figure S2.20. ^{1}H NMR spectra of (a) $P(CL_{0.64}\text{-}co\text{-}BSt_{0.36})_{13k}$, (b) $NP_{CL}1$, and (c) $NP_{CL}2$ in $CDCl_3$ (400 MHz).

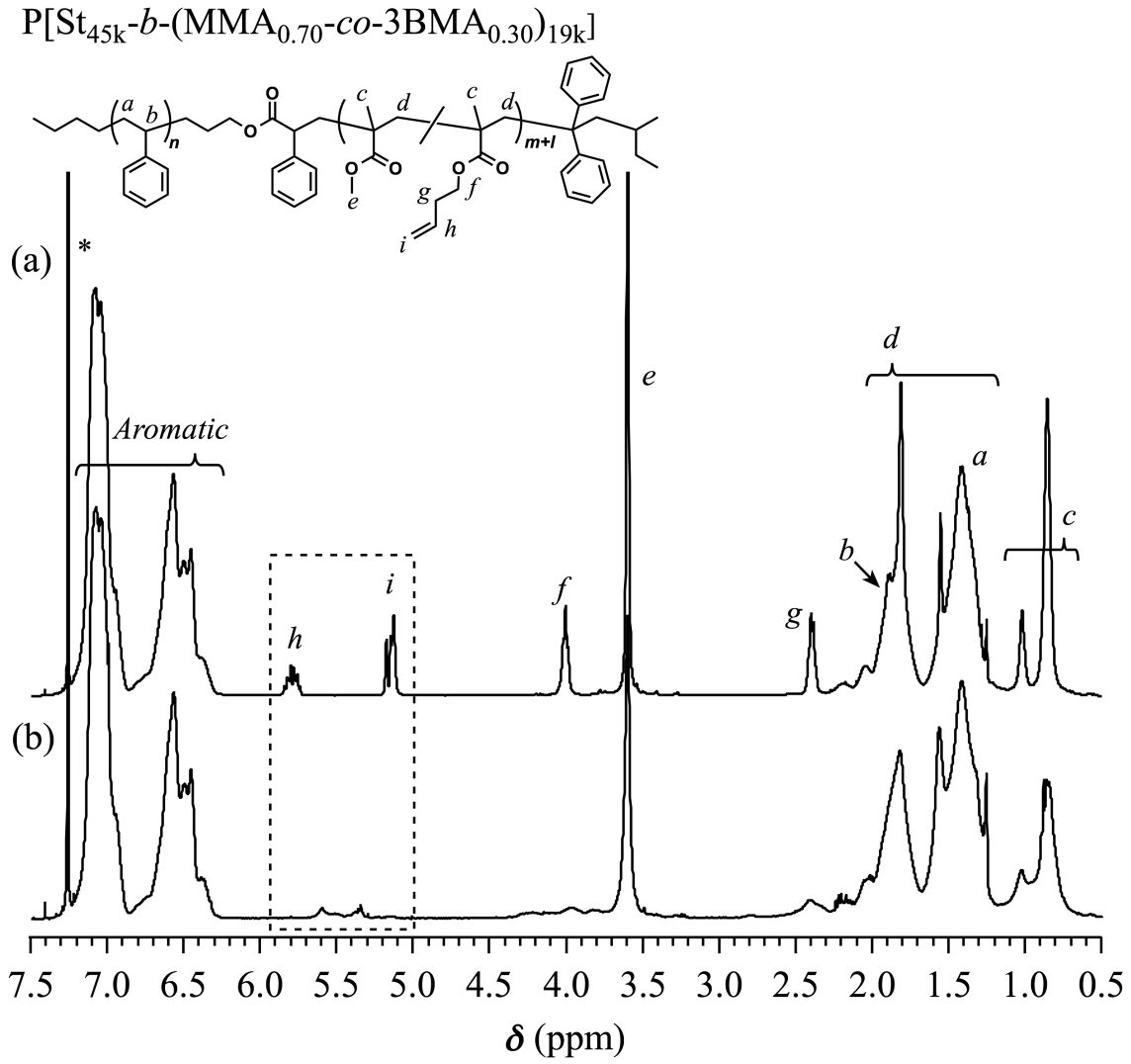

Figure S2.21. ^{1}H NMR spectra of (a) P[St_{45k}-*b*-($MMA_{0.70}$-*co*-$3BMA_{0.30}$)$_{19k}$] and (b) PSt-NP_{MMA}1 in $CDCl_3$ (400 MHz).

Chapter 3

Downsizing of Microphase-Separated Structures via Intramolecular Crosslinking of Block Copolymers with One Olefin-Containing-Block

3.1 Introduction

The self-assembly of block copolymers (BCPs) can produce various periodic nanostructures depending on the volume fraction of each block (*f*), such as lamellar, hexagonally close-packed cylinder, bicontinuous gyroid, and body-centered cubic structures. Therefore, it has attracted great interest in the nanomanufacturing fields.[1–8] In particular, "bottom-up" BCP lithography, in which line and dot patterns can be fabricated on the underlying substrate using microphase-separated thin film with ca. 10–100 nm features as a resist, has received substantial attention as a next-generation technology to replace the conventional "top-down" photolithography.[9–20] To further advance BCP lithography, a very important issue is to create nanostructures with shorter periodicity, i.e., smaller domain-spacing (*d*), and thus it is a current major focus in the field of BCP self-assembly. Since the feature size of the microphase-separated structures reflects the radius of gyration (R_g) of the BCP, the *d* value can be decreased by reducing the degree of polymerization (*N*). Yet, microphase separation requires the product of Flory–Huggins interaction parameter (χ) and *N* to exceed the critical value of $\chi N = 10.5$ for linear symmetric diblock copolymers ($f = 0.5$).[21,22]

A rational approach to achieve smaller *d* value is decreasing *N* value while increasing the χ value. Thus, a number of "high-χ BCPs", such as silicon-containing,[23–28] metal-doped,[29–31] and oligosaccharides-based BCPs[32–35] have been developed. However, only limited pairs of monomers are available for this approach. An alternative approach that is applicable to a wide range of polymers is reducing the R_g of BCP by varying the macromolecular architecture. In the pioneering work by Hawker et al., the macrocyclic BCP was found to exhibit a microphase-separated structure with smaller *d* value than the linear

counterpart.[36] Furthermore, the several groups reported that the miktoarm star architecture is also effective for decreasing the *d* value, by increasing the branching number while retaining the total molecular weight and *f*.[37–40] Thus, the preparation of BCPs with specific chain architectures is a promising way for shrinking the microphase-separated structures without decreasing the *N* value. Nevertheless, polymers with such architectures require elaborate synthesis consisting of multiple reaction steps. Therefore, a synthetically more accessible way to reduce the *d* value through regulating the polymer chain dimensions is of significant interest.

Here, the author highlight a crosslinking technique, which involves the intramolecular reaction of a crosslinkable precursor under highly diluted condition, as a novel approach for reducing the *d* value of microphase-separated structures. Several reports by Meijer et al.,[41–44] Pomposo et al.,[45–48] and Sawamoto et al.[49,50] clearly demonstrated the remarkable reduction in R_g as well as in the hydrodynamic radius of single polymer molecule in certain solvents due to the crosslink formation, presenting the potential of this approach for chain compaction even in the bulk. Importantly, the intramolecular crosslinking not only is a simple procedure itself, but also has the capability of controlling the chain dimensions by adjusting the crosslink density.[51–54] Barner-Kowollik et al. have indeed demonstrated size regulation of intramolecularly crosslinked polymers by varying the content of crosslinkable functionality or the amount of the crosslinking agent.[55–58] Thus, the intramolecular crosslinking of BCPs would allow fine tuning of the *d* value as well as modulating the phase structure. However, the microphase separation behavior of the intramolecularly crosslinked BCPs has not been investigated yet.

In this chapter, the author demonstrate shrinking the microphase-separated structures through restricting the BCP chain dimensions by the intramolecular crosslinking of linear BCPs. Polystyrene-*b*-poly(*rac*-lactide) (PS-*b*-PLA), which has been widely investigated by Hillmyer et al.,[59–65] was employed as a model system for examining the feasibility of this approach. The author designed poly{[styrene-*statistical*-(*p*-3-butenyl styrene)]-*block*-(*rac*-lactide)} polymers (P(S-*st*-BS)-*b*-PLA or SBS-LA), in which the SBS block can be intramolecularly crosslinked upon the olefin metathesis reaction to produce the crosslinked-linear BCPs, i.e., SBS(*cl*)–LAs (**Scheme 3.1**). Indeed, the SBS(*cl*)–LAs exhibited smaller *d* value in the microphase-separated structures as compared to the corresponding linear SBS–LA precursors. The minimum *d* values achieved in this study was 12.0 nm, corresponding to a sub-10 nm feature size. Furthermore, the author succeeded in reducing the domain size up to 22% by varying the crosslink density of the SBS block.

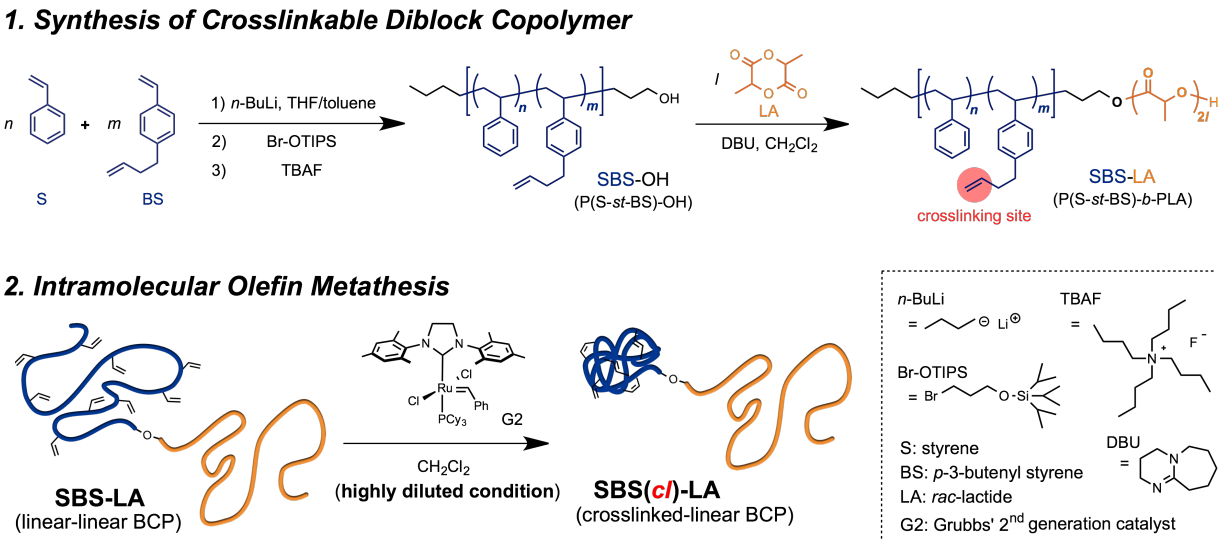

Scheme 3.1. Synthesis of the crosslinked–linear BCP via intramolecular olefin metathesis reaction of the linear–linear BCP possessing pendant double bonds as the crosslinking sites.

3.2 Experimental Section

3.2.1 Materials

sec-Butyllithium (*sec*-BuLi; Kanto Chemical Co., Inc. (Kanto), 1.05 mol L^{-1} in *n*-hexane), *n*-butyllithium (*n*-BuLi; Kanto, 1.01 mol L^{-1} in *n*-hexane), tetrabutylammonium fluoride (TBAF; Tokyo Chemical Industry Co., Ltd. (TCI), 1.0 mol L^{-1} in THF), absolute benzene (Wako Pure Chemical Industries, Ltd., super dehydrated, >99.5%), benzoic acid (TCI, >99.0%), Grubbs 2nd generation catalyst (G2; Sigma-Aldrich Chemicals Co.), and ethyl vinyl ether (TCI, >98.0%) were purchased and used as received. Styrene (S; TCI, >99.0%) and 1,8-diazabicyclo[5.4.0]-7-undecene (DBU; TCI, >98.0%) were purchased and purified by distillation over CaH_2 under vacuum. *rac*-Lactide (LA; TCI, >98.0%) was purchased and purified by recrystallization twice from dry toluene. *p*-3-Butenyl styrene (BS)[66] and (3-bromopropoxy)triisopropylsilane (Br–OTIPS)[67] were prepared according to the reported methods, then further purified by distillation over CaH_2 under vacuum. Commercially available dry THF (Kanto, >99.5%, water content, <0.001%), dry toluene (Kanto, >99.5%, water content, <0.001%), and dry CH_2Cl_2 (Kanto, >99.5%, water content, <0.001%) were further purified by an MBRAUN MB SPS Compact solvent purification system equipped with a MB-KOL-A and a MB-KOL-M Type 1 columns (for dry THF), a MB-KOL-C and a MB-KOL-A columns (for dry toluene), or two MB-KOL-A columns (for dry CH_2Cl_2) which were then directly used for the polymerizations.

3.2.2 Instruments

The ring-opening polymerization of *rac*-LA was carried out in an MBRAUN stainless steel glovebox equipped with a gas purification system (molecular sieves and copper catalyst) in a dry argon atmosphere (H_2O, O_2 <1 ppm). The moisture and oxygen contents in the glovebox were monitored by an MB-MO-SE 1 moisture sensor and an MB-OX-SE 1 oxygen sensor, respectively. The ^{1}H (400 MHz) and ^{13}C NMR (100 MHz) spectra were obtained using a JEOL JNM-ESC400 instrument at room temperature. The size exclusion chromatography (SEC) measurements were performed at 40 °C in THF (flow rate, 1.0 mL min^{-1}) using a Jasco high-performance liquid chromatography system (PU-980 Intelligent HPLC Pump, CO-2065 Plus Intelligent Column Oven, RI-2031 Plus Intelligent RI Detector, and DG-2080-53 Degasser) equipped with a Shodex KF-G guard column (4.6 mm × 10 mm; particle size, 8 μm) and two Shodex KF-804L columns (linear; particle size, 7 μm; 8.0 mm × 300 mm; exclusion limit, 4×10^4). Preparative SEC purification was performed in $CHCl_3$ (3.5 mL min^{-1}) at 23 °C using JAI LC-9201 equipped with a JAI JAIGEL-3H column (20 mm × 600 mm; exclusion limit, 7×10^4) and a JAI RI-50s refractive index detector. The Fourier transform infrared spectroscopy (FT-IR) analysis was carried out using a PerkinElmer Frontier MIR spectrometer equipped with a single reflection diamond universal attenuated total reflection (ATR) accessory. Differential scanning calorimetry (DSC) experiments were performed using a Bruker AXS DSC 3100 under a nitrogen atmosphere. All polymers for DSC measurement were heated to 150 or 200 °C, cooled to 10 °C, and heated to 150 or 200 °C again at the heating and cooling rate of 10 °C min^{-1} and 20 °C min^{-1}, respectively.

3.2.3 Synthesis of ω-end hydroxy-functionalized statistical copolymer of S and BS (SBS_{5k}–OH).

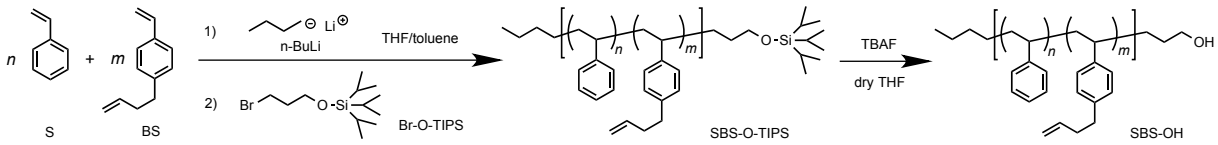

A typical procedure for the copolymerization of S and BS is as follows (method A). In the glovebox, dry toluene (47 mL) and dry THF (23 mL) were placed in a Schlenk flask. After sealing, the flask was taken out from the glovebox. *sec*-BuLi (100 μL, 105 μmol as a 1.05 mol L^{-1} stock solution in *n*-hexane) was added to the solvent under an Ar atmosphere to remove water completely. Then, the solvent was further purified by trap-to-trap distillation under high vacuum to transfer to another Schlenk flask for polymerization. After cooling to –78 °C, *n*-BuLi (900 μL, 909 μmol as a 1.01 mol L^{-1} stock solution in *n*-hexane) was added to the flask. In another flame-dried Schlenk flask, S (2.5 g, 24 mmol) and BS (1.6 g, 10 mmol) were mixed together under an Ar atmosphere. The mixture was added at once to the initiator solution using a syringe. After monomer addition, the mixture was stirred at −78 °C for 6 h. Br–O–TIPS (679 mg, 2.30 mmol) was added to the solution of living polymer anions at −78 °C, and the whole mixture was allowed to react for 0.5 h at −78 °C and an additional 1 h at room temperature. Afterwards, The solvent was removed from the polymerization mixture under reduced pressure. TBAF (6.89 mL, 6.89 mmol as a 1.0 mol L^{-1} stock solution in THF) and dry THF (20 mL) were added to the crude product at room temperature. After 15 h stirring, the reaction mixture was passed through a short silica-gel column, and the resulting residue was purified by repeated reprecipitation (at least twice) from the THF solution into MeOH to give SBS_{5k}–OH as a white solid. Yield: 3.76 g (86.4%). ^{1}H NMR (400 MHz,

$CDCl_3$): δ (ppm) 7.40−6.19 (m, 10H × n + 8H × m, −C_6H_{10}, −C_6H_8−), 5.97−5.74 (m, 1H × m, −CH=CH_2), 5.15−4.90 (m, 2H × m, −CH=CH_2), 3.47−3.33 (m, 2H, −CH_2OH), 2.85−2.45 (m, 2H × m, −C_6H_8CH_2−), 2.46−2.14 (m, 2H × m, −$C_6H_8CH_2$CH_2−), 2.15−1.62 (m, 1H × (n+m), −CH(C_6H_{10})−, −CH(C_6H_8−)−), 1.74−0.69 (m, 2H × (m+n) + 9H, −CH_2CH(C_6H_{10})−, −CH_2CH(C_6H_8−)−, C_4H_9−). $M_{n,NMR}$ = 4,670 ($CDCl_3$), the mole fraction of the BS units = 0.28, $M_{n,SEC}$ = 4,610 (THF), $Đ$ = 1.09 (THF).

3.2.4 Synthesis of block copolymer consisting of SBS and poly(rac-LA) (SBS_{5k}−LA_{7k}) via ring-opening polymerization of rac-LA using SBS_{5k}−OH as an initiator.

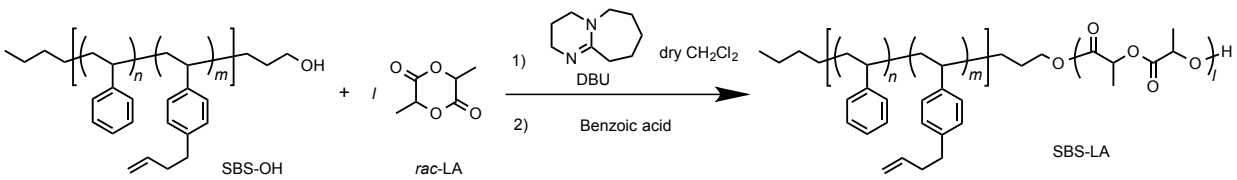

A typical procedure for the polymerization of *rac*-LA is as follows (method B). SBS_{5k}−OH was freeze-dried from its absolute benzene solution three times prior to the polymerization. In the glovebox, SBS_{5k}−OH ($M_{n,NMR}$ = 4,670, 1.04 g, 223 μmol) and *rac*-LA (1.50 g, 10.4 mmol) were dissolved in dry CH_2Cl_2 (20.8 mL). DBU (15.5 μL, 104 μmol) was then added to the CH_2Cl_2 solution to initiate the polymerization. After 18 min, the polymerization was quenched by the addition of benzoic acid. The mixture was purified by reprecipitation from the CH_2Cl_2 solution into MeOH to give SBS_{5k}−LA_{7k} as a white solid (2.21 g, 90.6%). The product was further purified by preparative SEC prior to the intramolecular crosslinking reaction and each measurement. ^{1}H NMR (400 MHz, $CDCl_3$): δ (ppm) 7.40−6.19 (m, 10H × n + 8H × m, −C_6H_{10}, −C_6H_8−), 5.97−5.74 (m, 1H × m, −CH=CH_2), 5.42−5.05 (m, 1H × (2l-1), −OCOCH(CH_3)−), 5.15−4.90 (m, 2H × m, −CH=CH_2),

4.43−4.31 (m, 1H, −C*H*(CH$_3$)OH), 4.00−3.76 (m, 2H, −C*H*$_2$O−), 2.85−2.45 (m, 2H × *m*, −C$_6$H$_8$C*H*$_2$−), 2.46−2.14 (m, 2H × *m*, −C$_6$H$_8$CH$_2$C*H*$_2$−), 2.15−1.62 (m, 1H × (*n*+*m*), −C*H*(C$_6$H$_{10}$)−, −C*H*(C$_6$H$_8$−)−), 1.77−0.69 (m, 3H × 2*l* + 2H × (*m*+*n*) + 9H, −C*H*$_2$CH(C$_6$H$_{10}$)−, −C*H*$_2$CH(C$_6$H$_8$−)−, C$_4$*H*$_9$−). Conversion = 93%, $M_{n,NMR}$ = 11,000 ($CDCl_3$), the weight fraction of SBS = 0.42, $M_{n,SEC}$ = 13,900 (THF), $Đ$ = 1.04 (THF).

3.2.5 Intramolecular crosslinking of SBS$_{5k}$−LA$_{7k}$ via olefin metathesis reaction.

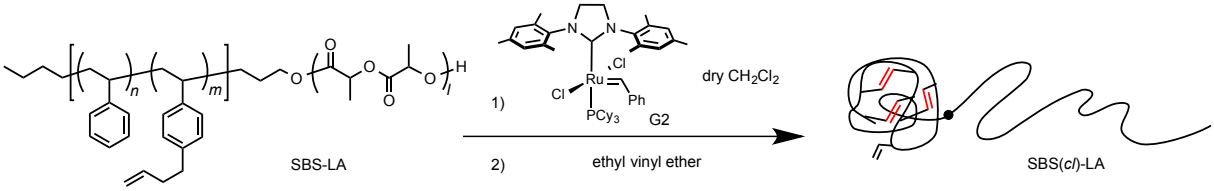

A typical procedure for the intramolecular crosslinking is as follows (method C). SBS$_{5k}$−LA$_{7k}$ ($M_{n,NMR}$ = 11,000, 403 mg, 471 μmol olefin-containing units) was dissolved in dry CH_2Cl_2 (1340 mL). After degassing by N_2 bubbling, G2 (4.0 mg, 4.7 μmol) was added to the mixture. After stirring for 3 h under an N_2 atmosphere at 30 °C, the reaction was quenched by the addition of ethyl vinyl ether. The solvent was removed by evaporation, then the residue was purified by reprecipitation from the CH_2Cl_2 solution into MeOH to givecrosslinked−linear diblock copolymer (SBS$_{5k}$(*cl*)−LA$_{6k}$) as a white solid (373 mg, 92.6%). The product was further purified by preparative SEC prior to each measurement. $M_{n,SEC}$ = 12,300 (THF), $Đ$ = 1.03 (THF), the conversion of the terminal olefins = 93%.

3.2.6 Bulk and thin film studies

Small angle X-ray scattering (SAXS). The morphologies and *d* values of samples in the bulk state were investigated using SAXS. The experiments were performed on the BL-6A beamline at the Photon Factory in the High Energy Accelerator Research Organization (KEK, Tsukuba, Japan) using X-ray beams with λ = 1.5 Å. The two-dimensional scattering patterns were collected by a PILATUS3 1M detector (Dectris Ltd.), where the sample-to-detector distance was set to 1.0 or 1.5 m. The scattering angle (θ) was calibrated using silver behenate (Nagara Science Co., Ltd.) as the standard and subsequently converted to the scattering vector (q) using Bragg's equation ($q = (4\pi/\lambda)\sin(\theta/2)$). The *d* values of the samples were calculated according to $d = 2\pi/q^*$, where q^* is the principal scattering peak position. The sample powder were annealed at 150 or 180 °C for 1 h under vacuum and then put into a glass capillary (Hilgenberg, Mark-tube, lindemann glass, 2.0 mm diameter).

Transmission electron microscopy (TEM). Bright-field TEM images of the thinly sliced bulk samples were obtained using a JEM-3200FS electron microscope (JEOL) with an accelerating voltage of 100 kV. Bulk film samples prepared by drop-cast from the toluene solutions were annealed at 150 °C for 1 h under vacuum and then embedded in a photocurable resin (Toagosei Co., Ltd., Alonix D-800). Sample slices with a thickness of 35−50 nm were obtained using a Leicca Ultracut S ultramicrotome equipped with a diamond knife (DiATOME, Ultra 35°) at room temperature, and a piece of slice was transferred to copper grids.

Atomic force microscopy (AFM). The AFM phase images were realized using a Molecular Imaging PicoPlus atomic force microscope operating in the tapping mode with a silicon cantilever (Nanoworld AG, NANOSENSORS^{TM} PPP-NCH) having a resonant

frequency and a force constant of 190 kHz and 48 N m^{-1}, respectively. The thin films for AFM experiments were prepared by spin-coating (2000 rpm for 1 min) the polymer solution in toluene (1.0 wt%) onto a Si substrate with a native oxide layer. The obtained thin film samples were annealed in the vapor of THF to induce the microphase separation. In a closed glass desiccator (ca. 3.0 L), the samples were positioned above the surface of THF (30 mL) placed in a reservoir for 4 h at 20 °C. The thin films were then taken out from the desiccator and allowed to dry at 20 °C. The film thickness was measured by ellipsometry (JASCO M-500S).

3.3 Results and Discussion

3.3.1 Intramolecular crosslinking of SBS−LAs

A series of poly[styrene-*block*-(*rac*-lactide)] possessing pendant olefin groups on the PS block (SBS−LA, **Table 3.1**) were successfully synthesized in two steps according to **Scheme 3.1**. First, the hydroxyl-terminated poly[styrene-*st*-(*p*-3-butenyl styrene)] (SBS−OH) was prepared via living anionic copolymerization of styrene (S) and *p*-3-butenyl styrene (BS) in a THF/toluene co-solvent (**Figure S3.1**, **Table S3.1**), under which the side chain double bond of BS remains intact due to the reduced polarity of the solvent.[66] This is followed by termination reaction with Br−OTIPS and the deprotection with tetrabutylammonium fluoride (TBAF). The subsequent ring-opening polymerization of *rac*-lactide (LA) using the obtained SBS−OH as the macroinitiator yielded the desired SBS−LAs. The total molecular weight ($M_{n,total}$) and the weight fraction of SBS block (F_{SBS}) were systematically varied to adjust the *d* values and morphologies of the microphase-separated structures. The mole fraction of BS units in the SBS block (f_{BS}) was fixed at around 0.3 or 0.5. (SBS−LAs with f_{BS} of ca. 0.5 have an asterisk in their sample names, i.e., SBS*−LAs.) Note that the SBS_{8k} and SBS^{*}_{9k} blocks were designed to be comparable in degree of polymerization (DP), in order to examine the effect of olefin contents on the chain compaction as well as on the microphase separation behavior.

Table 3.1. Molecular characteristics of SBS–LAs

polymer	$M_{n,SBS}$ (DP, f_{BS})[a]	$M_{n,LA}$ (DP)[a]	$M_{n,total}$	F_{SBS}[b]	$M_{n,SEC}$[c]	$Đ$[c]
SBS_{5k}–LA_{7k}	4,910 (40, 0.28)	6,750 (47)	11,700	0.42	13,700	1.03
SBS_{8k}–LA_{5k}	7,940 (65, 0.31)	4,680 (32)	12,600	0.63	12,500	1.03
SBS_{8k}–LA_{8k}	7,940 (65, 0.31)	8,250 (57)	16,200	0.49	16,500	1.03
SBS^{*}_{9k}–LA_{6k}	9,460 (71, 0.49)	6,420 (45)	15,900	0.60	16,800	1.03
SBS^{*}_{9k}–LA_{11k}	9,460 (71, 0.49)	11,400 (79)	20,900	0.45	23,300	1.03
SBS_{27k}–LA_{13k}	27,000 (224, 0.29)	13,400 (93)	40,400	0.67	36,600	1.03
SBS_{27k}–LA_{28k}	27,000 (224, 0.29)	27,900 (193)	54,900	0.49	54,400	1.03

[a]Determined by ^{1}H NMR in $CDCl_3$. [b]SBS weight fraction determined using $M_{n.SBS}$ and $M_{n,LA}$. [c]Determined by SEC in THF using polystyrene standards.

In chapter 2, the author has reported the intramolecular olefin metathesis of linear precursors possessing pendant olefins using Grubbs' 2nd generation catalyst (G2), whose high reactivity and excellent functional group tolerance enabled the crosslinking of a variety of polymers in mild conditions.[68,69] With a series of SBS–LAs in hand, the intramolecular olefin metathesis was conducted in the presence of G2 to produce the crosslinked–linear diblock copolymers (SBS(*cl*)–LAs). First, the intramolecular olefin metathesis of SBS_{5k}–LA_{7k} was carried out under highly diluted condition ($[SBS_{5k}–LA_{7k}]_0$ = 0.30 g L^{-1}) in CH_2Cl_2 at 30 °C for 3 h in the presence of 1.0 mol% of G2 with respect to the pendant double bond. The reaction proceeded homogeneously without gelation, giving a soluble product after the treatment with ethyl vinyl ether, followed by reprecipitation to remove the catalyst and the preparative SEC purification to isolate the main products from the minor byproducts with high molecular weights. In the ^{1}H NMR spectrum of the product, the intensity of the signals due to the terminal olefin protons (*e* and *f*) decreased, and those due to the internal olefin protons (*k*) newly appeared (**Figure 3.1**). The conversion of the terminal olefins ($conv._{olefin}$) was

calculated to be 93% by comparing the intensities of *e* signals before and after the crosslinking, after normalization with the intensity of signals derived from the aromatic protons. Notably, all signals from the SBS block were broadened after the crosslinking reaction although those from LA block remained unchanged, indicating that only the SBS block was intramolecularly crosslinked without unwanted reaction on the LA block. The IR spectrum of the product also supported the high olefin conversion ratio. The characteristic absorption band at 1642 cm^{-1} due to the terminal olefin was no longer observed in the spectrum of product (**Figure S3.2**). Thus, the ^{1}H NMR and IR studies confirmed the crosslink formation via the olefin metathesis reaction.

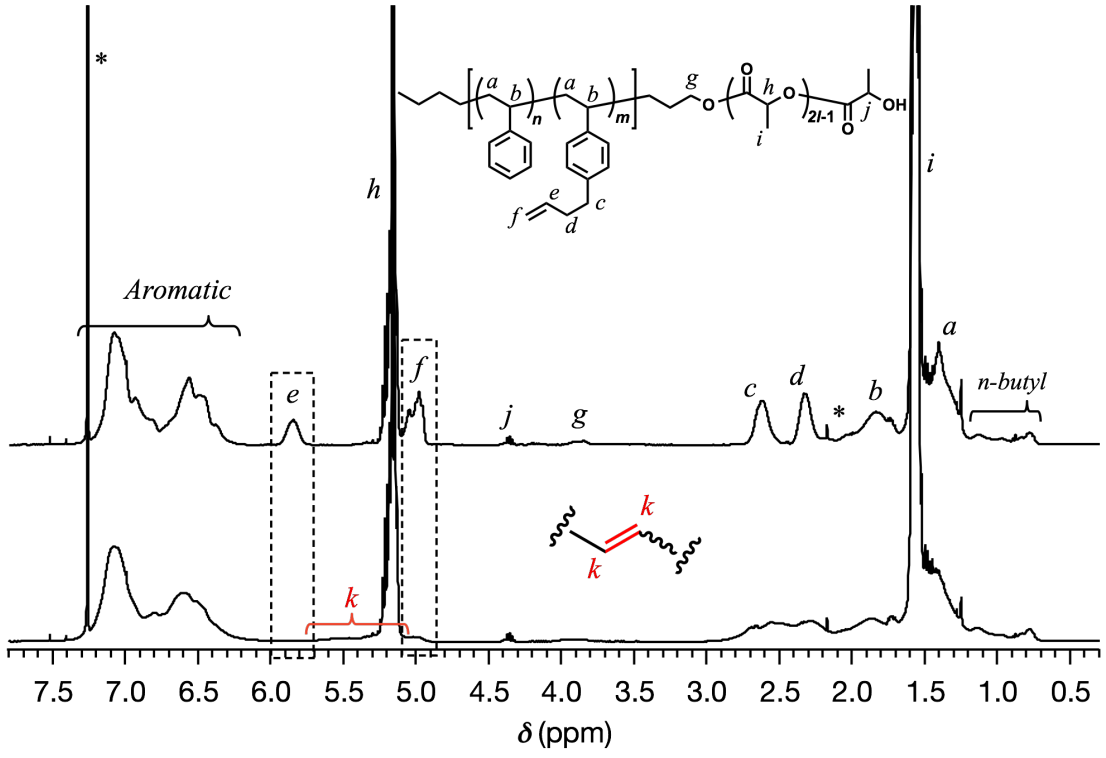

Figure 3.1. ^{1}H NMR spectra of SBS_{5k}–LA_{7k} (upper) and SBS_{5k}(*cl*)–LA_{7k} (lower) in $CDCl_3$ (400 MHz).

To further verify the intramolecular crosslink formation, SEC measurement was performed on SBS_{5k}–LA_{7k} and its reaction product. As can be seen in **Figure 3.2**(a), the SEC trace of the crosslinked product exhibited a monomodal peak in the lower molecular weight region as compared to that of SBS_{5k}–LA_{7k}, implying a decrease in the hydrodynamic volume through the crosslinking reaction. (The SEC trace of the product obtained before preparative SEC purification is shown in **Figure S3.3**.) Under the assumption that the LA block maintains its linear structure after intramolecular crosslinking, the shrinking factor of SBS block, $\langle G \rangle_{SBS}$, can be defined using the following equations:

$$\langle G \rangle_{SBS} = \frac{M_{p,SEC}[SBS(cl)\text{–}LA] - M_{p,SEC}[LA]}{M_{p,SEC}[SBS\text{–}OH]} \qquad (1)$$

$$M_{p,SEC}[LA] = M_{p,SEC}[SBS\text{–}LA] - M_{p,SEC}[SBS\text{–}OH] \qquad (2)$$

where $M_{p,SEC}$[SBS(*cl*)–LA], $M_{p,SEC}$[SBS–OH], and $M_{p,SEC}$[SBS–LA] stand for the molecular weights calculated from the peak top of the corresponding SEC traces. The $\langle G \rangle_{SBS}$ value in **Figure 3.2**(a) was 0.78, which was comparable to the $\langle G \rangle$ value (0.79) obtained from the intramolecular crosslinking of SBS_{5k}–OH (**Table S3.1**). Based on the ^{1}H NMR, IR, and SEC analyses, the author concluded that the crosslinked–linear diblock copolymer, i.e., SBS_{5k}(*cl*)–LA_{7k}, was successfully obtained. In a similar manner, SBS–LAs with different compositions and molecular weights were also successfully converted to the corresponding SBS(*cl*)–LAs with sufficient $conv._{olefin}$ values (**Table 3.2**, **Figures 3.2**(b)–(g), and **S3.3–S3.15**). It is worth noting that the $\langle G \rangle_{SBS}$ values for SBS^*_{9k}(*cl*)–LA_{6k} and SBS^*_{9k}(*cl*)–LA_{11k} (0.67 and 0.66) were apparently lower than those of SBS_{8k}(*cl*)–LA_{5k} and

$SBS_{8k}(cl)$–LA_{8k} (0.81 and 0.84) despite the comparable DP values of the SBS block, indicating that a higher crosslinking density led to further reduction in the chain dimensions.

Table 3.2. Characterization data for SBS–LAs and SBS(*cl*)–LAs

polymer	conv.$_{olefin}$ (%)[a]	$M_{p,SEC}$[b]	$Đ$[b]	$\langle G \rangle_{SBS}$[c]	$T_{g,SBS}$ (°C)[d]	$T_{g,LA}$ (°C)[d]
SBS_{5k}–LA_{7k}		13,400	1.03		59	51
$SBS_{5k}(cl)$–LA_{7k}	93	12,200	1.03	0.78	91	54
SBS_{8k}–LA_{5k}		12,500	1.03		60	49
$SBS_{8k}(cl)$–LA_{5k}	88	11,100	1.03	0.81	109	54
SBS_{8k}–LA_{8k}		16,500	1.03		63	52
$SBS_{8k}(cl)$–LA_{8k}	79	15,300	1.03	0.84	110	55
SBS^{*}_{9k}–LA_{6k}		16,900	1.03		–	49
$SBS^{*}_{9k}(cl)$–LA_{6k}	86	14,100	1.03	0.67	138	52
SBS^{*}_{9k}–LA_{11k}		23,600	1.03		–	51.1
$SBS^{*}_{9k}(cl)$–LA_{11k}	89	20,700	1.03	0.66	143	55
SBS_{27k}–LA_{13k}		39,300	1.03		76	52
$SBS_{27k}(cl)$–LA_{13k}	88	28,200	1.03	0.45	140	53
SBS_{27k}–LA_{28k}		54,400	1.03		80	55
$SBS_{27k}(cl)$–LA_{28k}	87	45,200	1.04	0.54	137	53

[a]Determined by ^{1}H NMR in $CDCl_3$. [b]Determined by SEC in THF using polystyrene standards. [c]Calculated using equations (1) and (2). $M_{p,SEC}[SBS_{5k}–OH]$ = 5,360, $M_{p,SEC}[SBS_{8k}–OH]$ = 7,290, $M_{p,SEC}[SBS^{*}_{9k}–OH]$ = 8,510, $M_{p,SEC}[SBS_{19k}–OH]$ = 20,100. [d]Determined by DSC at the heating rate of 10 °C min^{-1}.

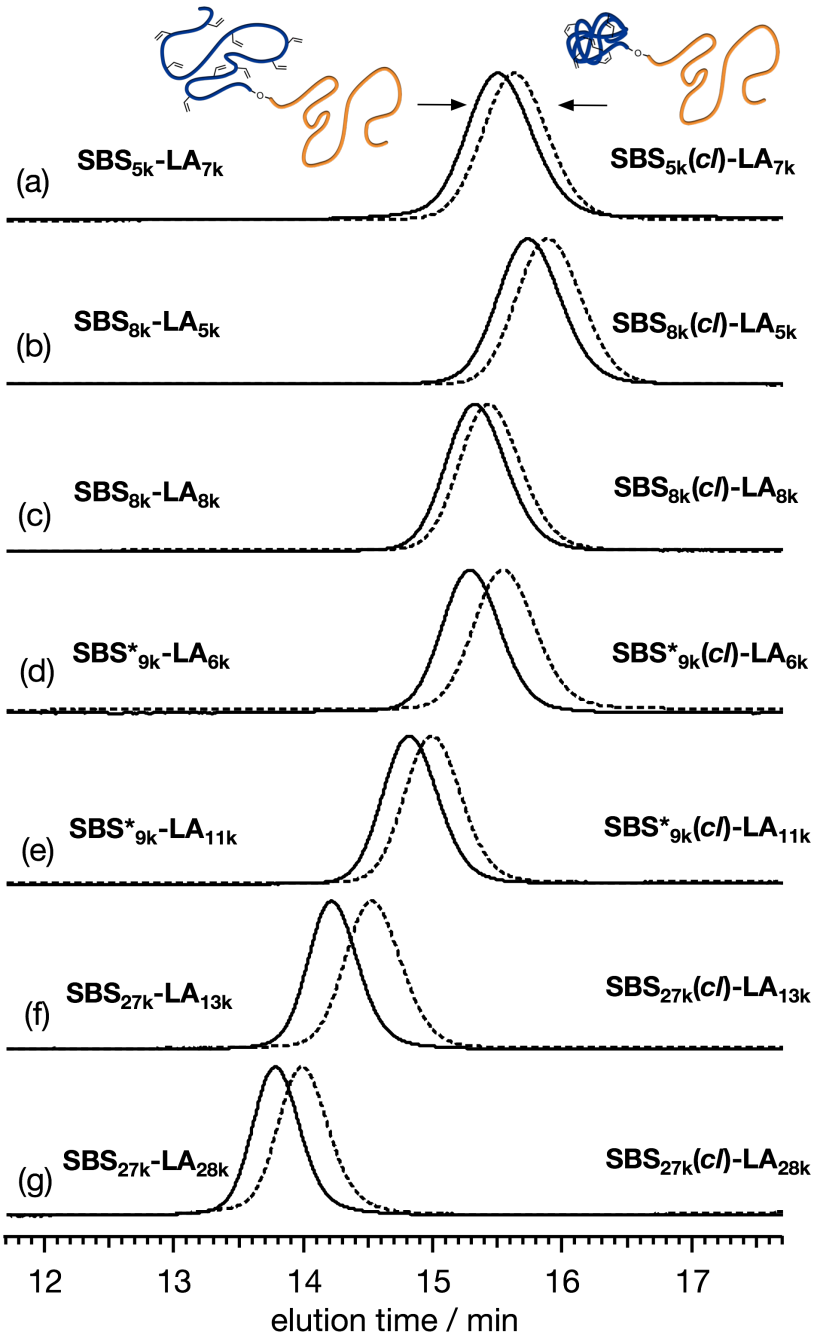

Figure 3.2. SEC traces of (a) SBS_{5k}–LA_{7k} and SBS_{5k}(*cl*)–LA_{7k}, (b) SBS_{8k}–LA_{5k} and SBS_{8k}(*cl*)–LA_{5k}, (c) SBS_{8k}–LA_{8k} and SBS_{8k}(*cl*)–LA_{8k}, (d) SBS^{*}_{9k}–LA_{6k} and SBS^{*}_{9k}(*cl*)–LA_{6k}, (e) SBS^{*}_{9k}–LA_{11k} and SBS^{*}_{9k}(*cl*)–LA_{11k}, (f) SBS_{27k}–LA_{13k} and SBS_{27k}(*cl*)–LA_{13k}, and (g) SBS_{27k}–LA_{28k} and SBS_{27k}(*cl*)–LA_{28k} (eluent, THF; flow rate, 1.0 mL min^{-1}). SBS–LAs and the corresponding SBS(*cl*)–LAs are presented using solid and dashed lines, respectively.

3.3.2 Thermal properties

Since the intramolecularly crosslinked polymers obviously differ in molecular mobility from typical polymers with random coils, their bulk thermal property is an important consideration when evaluating of the microphase separation behavior. Thus, the obtained SBS–LAs, SBS(*cl*)–LAs, as well as the corresponding homopolymers (SBS–OHs, SBS(*cl*)–OHs, and PLAs) were characterized by differential scanning calorimetry (DSC) to determine their glass transition temperature (T_g) (**Table 3.2** and **Table S3.1**). The DSC curves of SBS–LAs and SBS(*cl*)–LAs during the second heating process are shown in **Figure S3.16.** See also **Figure S3.17** for the DSC curves of SBS–OHs, SBS(*cl*)–OHs, and PLA.

For SBS_{5k}–LA_{7k} and SBS_{5k}(*cl*)–LA_{7k}, two sets of baseline shifts due to the separate glass transitions of SBS and LA blocks were observed, indicating the formation of microphase-separated structures (**Figure 3.3**). Importantly, the T_g of SBS_{5k}(*cl*) block was determined to be 91 °C, which was much higher than that of the SBS_{5k} block, i.e., 59 °C, while there was no significant difference in T_g for the LA blocks between SBS_{5k}–LA_{7k} (51 °C) and SBS_{5k}(*cl*)–LA_{7k} (54 °C). The increased T_g of the crosslinked SBS block compared to the linear counterparts strongly reflected a decrease in the segmental chain mobility, which again confirmed the formation of the intramolecularly crosslinked structure. A similar thermal behavior was observed for all other SBS(*cl*)–LAs (**Figure S3.16**). It should also be noted that the determined T_g values of SBS–LAs and SBS(*cl*)–LAs were comparable with those of the corresponding homopolymers (**Figure S3.17** and **Table S3.1**). The baseline shift of the SBS^*_{9k} block in SBS^*_{9k}–LA_{6k} and SBS^*_{9k}–LA_{11k} could not be detected (**Figure S3.16**(d)(e)). Considering that T_g value of SBS^*_{9k}–OH was 46 °C (**Table S3.1**), the baseline shift due to the

SBS*$_{9k}$ block seems to overlap with that of the LA blocks at around 50 °C. Surprisingly, the T_g values of the SBS*$_{9k}$(*cl*) block (138 °C for SBS*$_{9k}$(*cl*)–LA$_{6k}$ and 143 °C for SBS*$_{9k}$(*cl*)–LA$_{11k}$) were considerably higher than that of the corresponding linear SBS*$_{9k}$ block (around 50 °C). To the best of author's knowledge, such a dramatic increase in the T_g values has not been reported for intramolecularly crosslinked polymers to date.[54,68–74] This is probably due to the substantial incorporation of the crosslinkable units into the precursor (50 mol%) and the high conversion ratio to the crosslinkages (conv.$_{olefin}$ = ca. 90%). The T_g values of SBS$_{27k}$(*cl*) blocks in SBS$_{27k}$(*cl*)–LA$_{10k}$ (140 °C) and SBS$_{27k}$(*cl*)–LA$_{28k}$ (137 °C) were also very high, which is surely due to their high molecular weights.

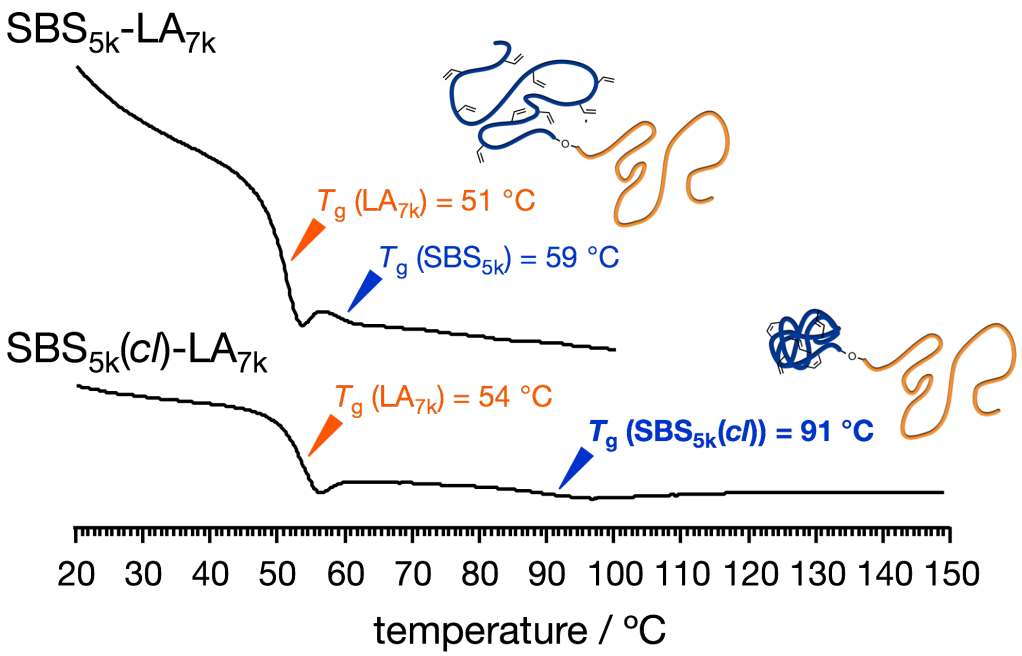

Figure 3.3. DSC curves during the 2nd heating process of SBS$_{5k}$–LA$_{7k}$ (upper) and SBS$_{5k}$(*cl*)–LA$_{7k}$ (lower).

3.3.3 Microphase separation behavior in the bulk state

To investigate the microphase-separated structures of SBS–LAs and SBS(*cl*)–LAs, small-angle X-ray scattering (SAXS) study was carried out on their bulk samples. Prior to SAXS experiments, the samples were thermally annealed for 1 h under vacuum at temperatures higher than their measured T_g values. The resulting morphological characteristics of all samples are summarized in **Table 3.3**. The SAXS profile of SBS_{8k}–LA_{8k} (F_{SBS} = 0.49) showed a primary scattering peak at q^* = 0.413 nm^{-1} with higher-ordered scattering peaks at 2q^*, 3q^*, and 4q^* positions, indicative of a well-ordered lamellar (LAM) morphology (**Figure 3.4**(a), upper). The d value of the LAM structure was determined to be 15.2 nm based on the relationship of $d = 2\pi/q^*$. The SAXS profile of SBS_{8k}(*cl*)–LA_{8k} also exhibited scattering peaks (q^* = 0.469 nm^{-1}, 2q^*, and 3q^*) corresponding to the LAM morphology with the d value of 13.4 nm (**Figure 3.4**(a), lower). Importantly, these results clearly demonstrated a decrease in the d value by 12% after the intramolecular crosslinking process, indicating the compact chain dimensions of the resultant polymers in bulk state. Because the chain dimensions of the LA block are presumed to be almost unchanged even after the intramolecular crosslinking process, the decrease in d should be attributed to a reduction in the chain volume of the SBS block. Transmission electron microscopy (TEM) observation of the microtomed samples was performed to further confirm the above hypothesis. TEM images of SBS_{8k}–LA_{8k} and SBS_{8k}(*cl*)–LA_{8k} exhibited the line patterns corresponding to the LAM morphology without any staining, in which dark and bright parts were assigned to the SBS (SBS(*cl*)) block and the LA block, respectively (**Figure 3.4**(b)(c)). The large wrinkles in the horizontal direction are defects that occurred during ultra-microtome cutting. The estimated d value of 15.5–16.0 nm for SBS_{8k}–LA_{8k} is in good agreement with that determined from the

SAXS profile (d = 15.2 nm). In the case of $SBS_{8k}(cl)$–LA_{8k}, the d value was estimated to be 14.0–14.5 nm from the TEM image, which is slightly different from the SAXS result (d = 13.4 nm). Nevertheless, the LAM period of $SBS_{8k}(cl)$–LA_{8k} was found to be smaller than that of SBS_{8k}–LA_{8k}, according to both the real space TEM image and the SAXS results in the reciprocal space.

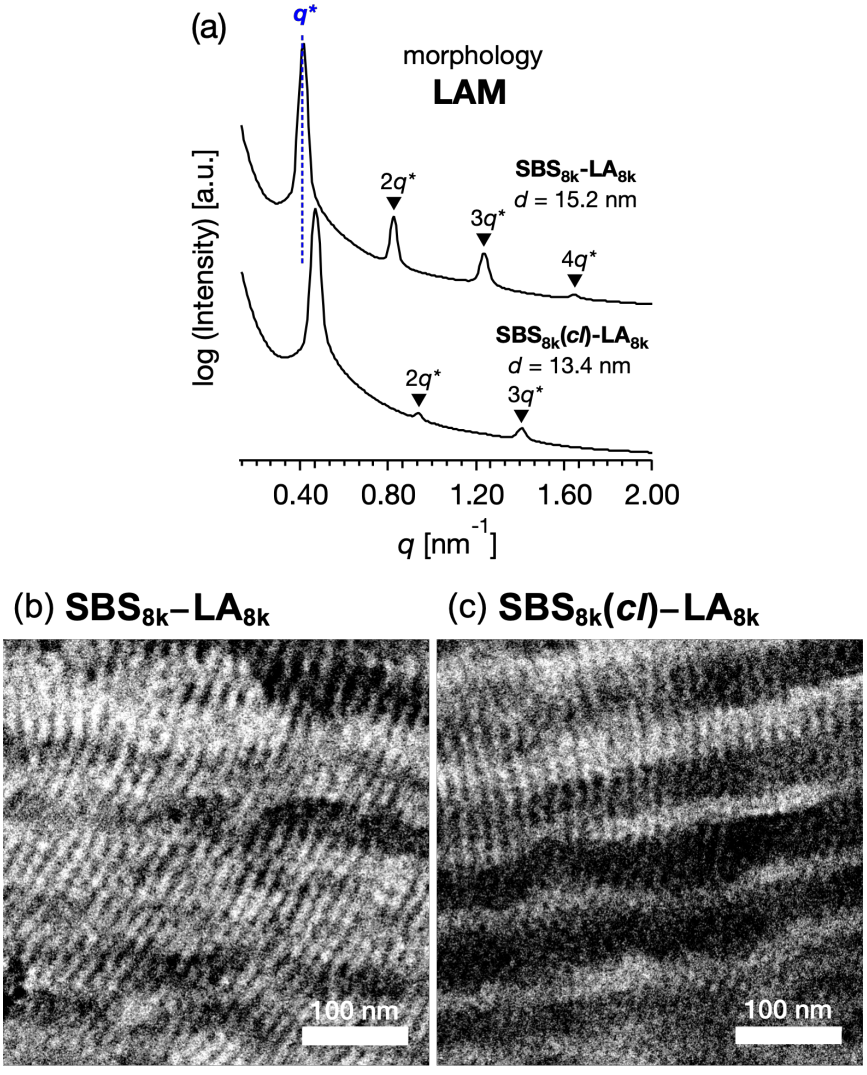

Figure 3.4. (a) SAXS profiles of SBS_{8k}–LA_{8k} (upper) and $SBS_{8k}(cl)$–LA_{8k} (lower). Cross-sectional TEM images of (b) SBS_{8k}–LA_{8k} and (c) $SBS_{8k}(cl)$–LA_{8k}. The scale bar is 100 nm.

Table 3.3. Morphological characteristics of SBS–LAs and SBS(*cl*)–LAs in the bulk

linear–linear			crosslinked–linear			
name	morphology	d (nm)[d]	name	morphology	d (nm)[d]	% decrease[f]
SBS_{5k}–LA_{7k}	LAM	13.4	SBS_{5k}(*cl*)–LA_{7k}	LAM	12.0	10
SBS_{8k}–LA_{5k}	HEX	14.5[e]	SBS_{8k}(*cl*)–LA_{5k}	HEX	12.9[e]	11
SBS_{8k}–LA_{8k}	LAM	15.2	SBS_{8k}(*cl*)–LA_{8k}	LAM	13.4	12
SBS^{*}_{9k}–LA_{6k}	HEX	18.1[e]	SBS^{*}_{9k}(*cl*)–LA_{6k}	HEX	15.0[e]	17
SBS^{*}_{9k}–LA_{11k}	LAM	19.8	SBS^{*}_{9k}(*cl*)–LA_{11k}	LAM	15.5	22
SBS_{27k}–LA_{13k}	HEX	29.4[e]	SBS_{27k}(*cl*)–LA_{13k}	HEX	22.9[e]	22
SBS_{27k}–LA_{28k}	LAM	34.9	SBS_{27k}(*cl*)–LA_{28k}	HEX	31.9[e]	(9)

[a]Total molecular weight of SBS–LA determined by ^{1}H NMR. [b]Determined by SEC in THF using polystyrene standards. [c]SBS volume fraction. [d]Determined by SAXS. [e]*d* Value was converted to the center-to-center distance of cylinder ($d_{C\text{-}C}$).[f]Decreasing ratio of the *d* ($d_{C\text{-}C}$) value.

SBS_{5k}–LA_{7k} (F_{SBS} = 0.42), SBS^{*}_{9k}–LA_{11k} (F_{SBS} = 0.45), and the corresponding SBS(*cl*)–LAs also exhibited the LAM morphology, as expected from their F_{SBS} values (**Figure 3.5**(a) and (b)). From the SAXS results of the polymers with the lowest molecular weights (SBS_{5k}–LA_{7k} and SBS_{5k}(*cl*)–LA_{7k}), the *d* value was reduced from 13.4 to 12.0 nm after the intramolecular crosslinking. These *d* values equal to sub-10 nm half-pitch, demonstrating that the presented approach can be applied at such small size scales. Remarkably, SBS^{*}_{9k}(*cl*)–LA_{11k} exhibited the maximum downsizing in *d* in this work, being 22% smaller compared to the corresponding linear SBS^{*}_{9k}–LA_{11k} (*d* = 15.5 vs. 19.8 nm). As described above, the SBS_{8k} and SBS^{*}_{9k} blocks were designed to be different in f_{BS} but with the comparable DP values, which enabled us to examine the effect of olefin contents on the size of the microphase-separated structures. As expected, the decrease ratio in *d* is greater for SBS^{*}_{9k}(*cl*)–LA_{11k} than for SBS_{8k}(*cl*)–LA_{8k} (22% vs. 12%), in spite of their comparable DPs in the crosslinkable SBS block. This result clearly demonstrates that increasing the crosslinking

density of BCP is an effective approach to further reduce feature sizes of the microphase-separated structures.

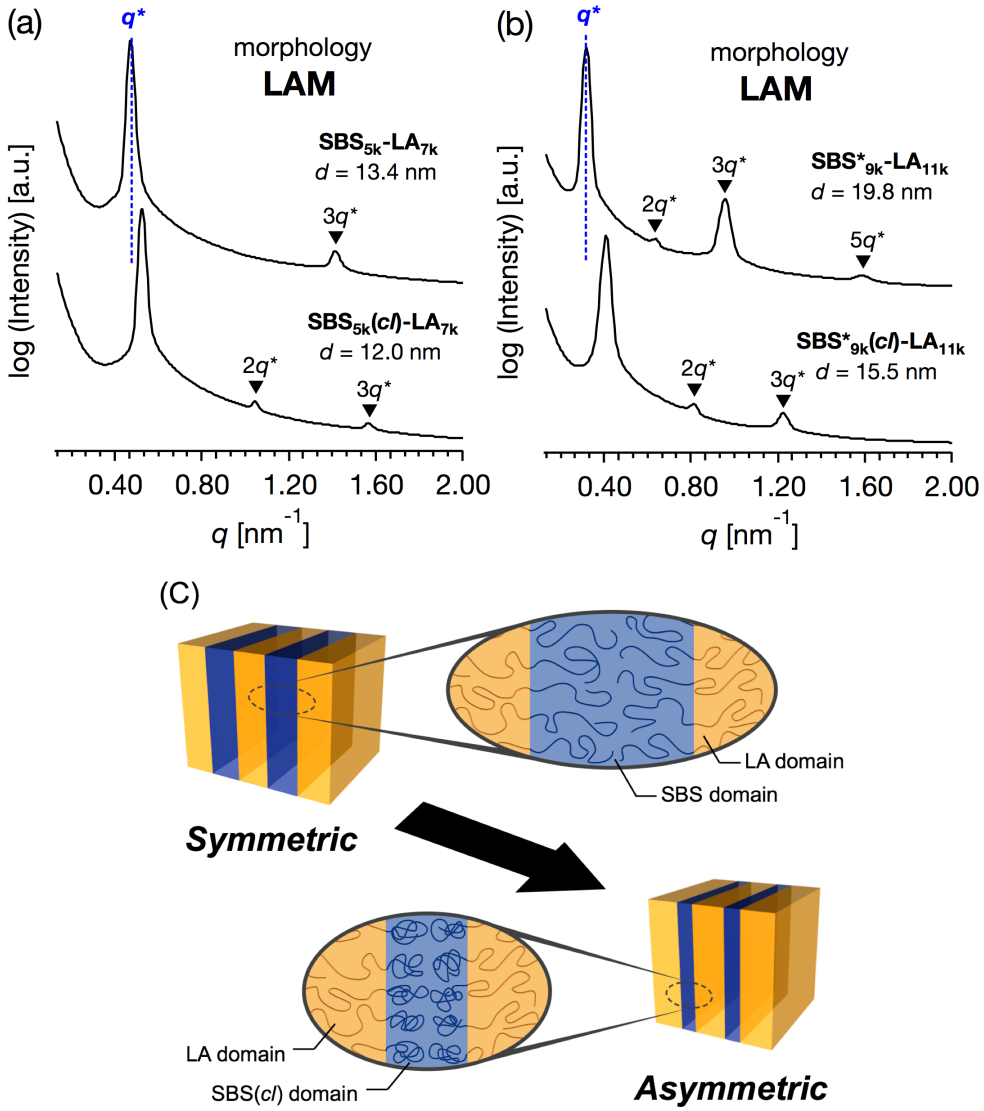

Figure 3.5. SAXS profiles for the bulk samples of (a) SBS_{5k}–LA_{7k} and $SBS_{5k}(cl)$–LA_{7k} annealed at 150 °C and (b) SBS^{*}_{9k}–LA_{11k} and $SBS^{*}_{9k}(cl)$–LA_{11k} annealed at 180°C. (c) Schematic illustration of the structural transition in LAM morphology via the intramolecular cross-linking. SBS domains and LA domains are shown in blue and yellow, respectively.

Notably, the even-ordered peaks in the SAXS profiles of SBS_{5k}–LA_{7k} and SBS^{*}_{9k}–LA_{11k} were absent (or suppressed) (**Figure 3.5**(a) and (b), upper), indicating that the two phases of the LAM morphology were highly symmetric.[75] On the otherhand, the SAXS profiles of intramolecularly crosslinked products, *i.e.*, SBS_{5k}(*cl*)–LA_{7k} and SBS^{*}_{9k}(*cl*)–LA_{11k}, clearly exhibited a scattering peak at 2*q** position with intensity similar to those at 3*q** position (**Figure 3.5**(a)(b), lower), indicative of the transition from the symmetric LAM to an asymmetric one (**Figure 3.5**(c)). These results support the assumption that the major reason for the decrease in *d* is reduction of feature sizes of the SBS phase.

The SAXS profile of SBS_{8k}–LA_{5k} (F_{SBS} = 0.63) showed a primary scattering peak at q^* = 0.500 nm^{-1} and higher-ordered ones at $\sqrt{3}q^*$, $2q^*$, $\sqrt{7}q^*$, and $3q^*$ positions, which correspond to the hexagonally close-packed cylinder (HEX) morphology with d = 12.6 nm (**Figure 3.6**(a), upper). For the HEX, the d value was converted to the center-to-center distance between cylinders ($d_{C\text{-}C} = 2d/\sqrt{3}$) to be 14.5 nm. The SAXS profile of SBS_{8k}(*cl*)–LA_{5k} also suggested the HEX morphology with $d_{C\text{-}C}$ = 12.9 nm, as revealed by the scattering peaks observed at q^* (0.563 nm^{-1}), $2q^*$, and $\sqrt{7}q^*$ (**Figure 3.6**(a), lower), representing a 11% decrease in the $d_{C\text{-}C}$ value compared with the corresponding linear SBS_{8k}–LA_{5k}. Since the HEX-forming SBS–LAs were designed to have longer SBS blocks (matrix) and shorter LA blocks (cylinder domain), the structure transition model in **Figure** 3.**6**(b) is assumed. In this model, the volume of SBS matrix is reduced after the intramolecular crosslinking to decrease the $d_{C\text{-}C}$ while the LA cylinder diameter is maintained. Thus, the author successfully reduced the feature size in both the LAM and HEX morphologies.

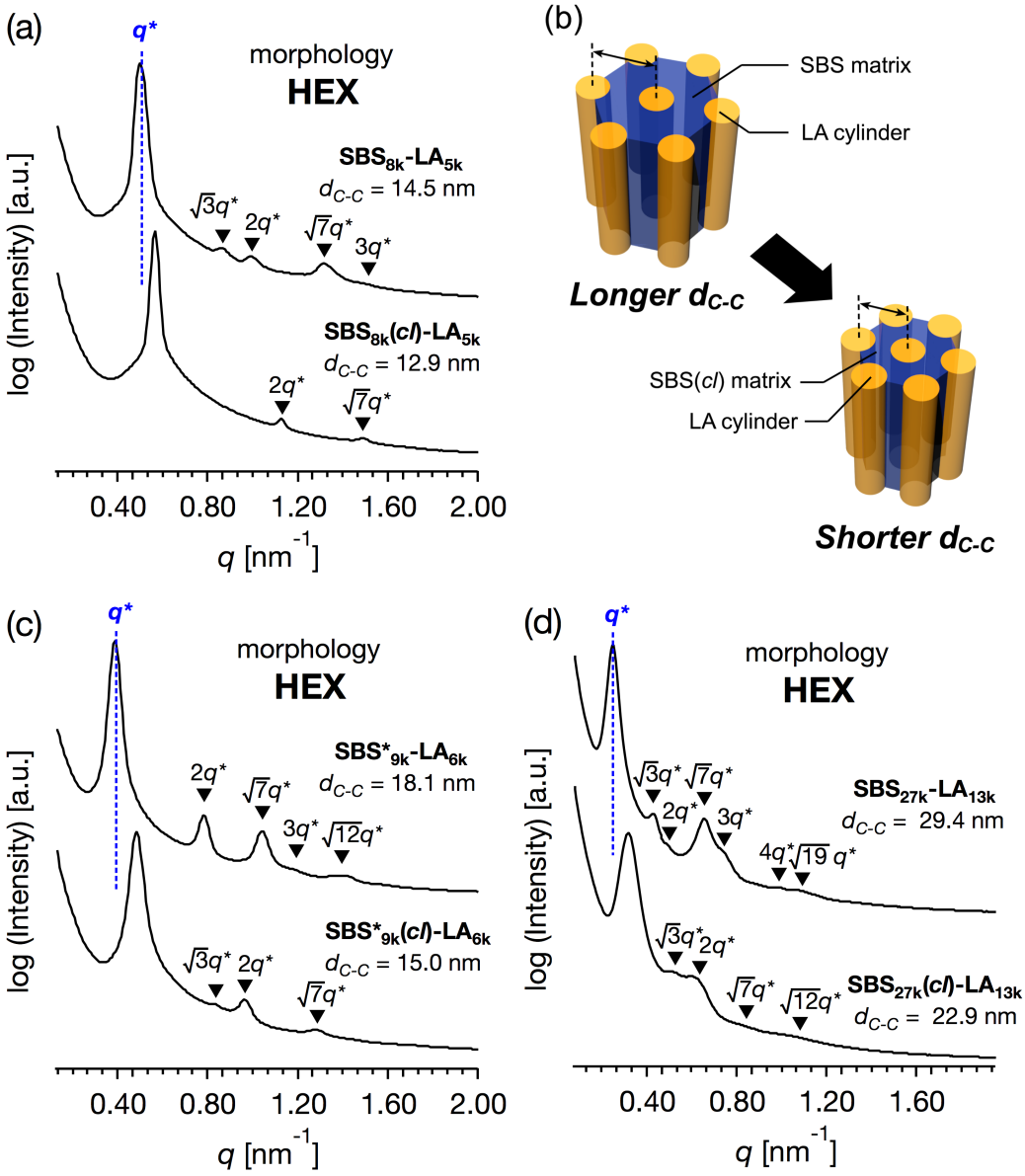

Figure 3.6. SAXS profiles for the bulk samples of (a) SBS_{8k}–LA_{5k} and SBS_{8k}(*cl*)–LA_{5k} annealed at 150 °C, (c) SBS^{*}_{9k}–LA_{6k} and SBS^{*}_{9k}(*cl*)–LA_{6k} annealed at 180 °C and (d) SBS_{27k}–LA_{13k} and SBS_{27k}(*cl*)–LA_{13k} annealed at 180 °C. (b) Schematic illustration of the structural transition in HEX morphology via the intramolecular cross-linking. SBS domains and LA domains are shown in blue and yellow, respectively.

SBS^{*}_{9k}–LA_{6k} (F_{SBS} = 0.60), SBS_{19k}–LA_{10k} (F_{SBS} = 0.65), and the corresponding SBS(*cl*)–LAs also exhibited the HEX morphology as expected from their F_{SBS} value. A similar result was obtained for the case of SBS^{*}_{9k}–LA_{6k} and SBS^{*}_{9k}–LA_{11k}: SBS^{*}_{9k}(*cl*)–LA_{6k} has a $d_{C\text{-}C}$ value 17% smaller (15.0 nm) compared to the linear SBS^{*}_{9k}–LA_{6k} (18.1 nm, **Figure 3.6**(c)), representing a larger decrease ratio than that for SBS_{8k}(*cl*)–LA_{5k} (11%, **Figure 3.6**(a)) because of the higher crosslink density. In the case of the high-molecular-weight SBS_{27k}–LA_{13k}, a larger volume reduction of SBS block is expected after the crosslinking reaction as indicated by the $\langle G \rangle_{SBS}$ values. Indeed, SBS_{27k}(*cl*)–LA_{13k} exhibited a 22% reduction in $d_{C\text{-}C}$ (22.9 nm) compared to that of the corresponding linear SBS_{27k}–LA_{13k} (29.4 nm, **Figure 3.6**(d)).

While SBS_{27k}–LA_{28k} (F_{SBS} = 0.49) exhibited a well-ordered LAM morphology, the SAXS profile of SBS_{27k}(*cl*)–LA_{28k} showed scattering peaks (q^*, $\sqrt{3}q^*$, $2q^*$, and $\sqrt{13}q^*$) corresponding to the HEX morphology (**Figure 3.7**). Such a change in phase was only observed in this BCP with the highest molecular weight, and it should also be attributed to a significant change in the effective volume fraction of SBS block due to the intramolecular crosslinking. Therefore, the presented methodology can be applied for not only downsizing the feature but also varying the morphology in the microphase-separated structures.

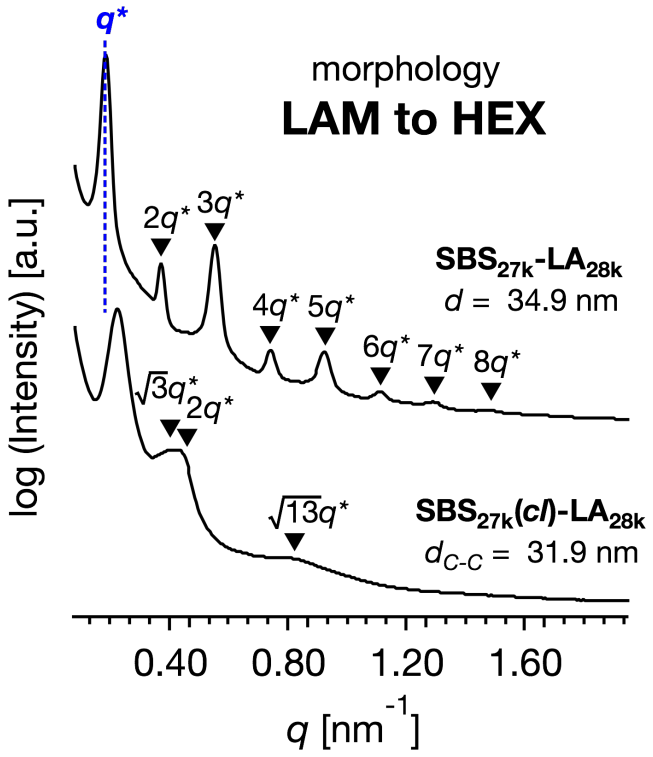

Figure 3.7. SAXS profiles for the bulk samples of SBS_{27k}–LA_{28k} and SBS_{27k}(*cl*)–LA_{28k}. annealed at 180 °C.

3.3.4 Microphase separation behavior in the thin film state

For the lithographic application, microphase separation in the thin film state is of particular importance. The author therefore finally investigated the thin film morphologies of the HEX-forming SBS_{27k}–LA_{13k} and SBS_{27k}(*cl*)–LA_{13k} via atomic force microscopy (AFM) observation. To obtain vertically oriented microphase-separated structures, thin films ca. 50 nm in thickness were prepared by spin-coating onto Si substrates, and THF vapor annealing was applied to the films.[76,77] The AFM height images of SBS_{27k}–LA_{28k} and SBS_{27k}(*cl*)–LA_{13k} thin films are shown in **Figures 3.8**(a) and (b), respectively, where the dot patterns corresponding to the HEX structural oriented perpendicular to the film surface were observed. The insets show the 2D fast Fourier transform (FFT) profiles obtained from each height image. As expected, the LA cylinders embedded within the SBS matrix were more tightly packed in the SBS_{27k}(*cl*)–LA_{13k} thin film than in the SBS_{27k}–LA_{13k} thin film (**Figure 3.8**(c)), strongly supporting the above assumption about the structure change in HEX morphology after crosslinking (**Figure 3.6**(b)). The $d_{C\text{-}C}$ values extracted from the 2D FFT profiles indeed decreased from 27.9 nm (SBS_{27k}–LA_{13k}) to 24.5 nm (SBS_{27k}(*cl*)–LA_{13k}) due to the intramolecular crosslinking. Thus, the author confirmed the downsizing of the microphase-separated structures in the thin film state as well as in the bulk state. It is worth noting that a uniformly packed structure was observed in the thin film even after the intramolecular crosslinking (**Figure 3.8**(b)) despite the decreased molecular mobility, as indicated by the ^{1}H NMR and DSC results. Overall, the author successfully demonstrated feature size reduction as well as nanoscale organization of the crosslinked–linear BCPs into a well-ordered morphology in the thin film state, supporting the applicability of the presented approach to lithographic technology.

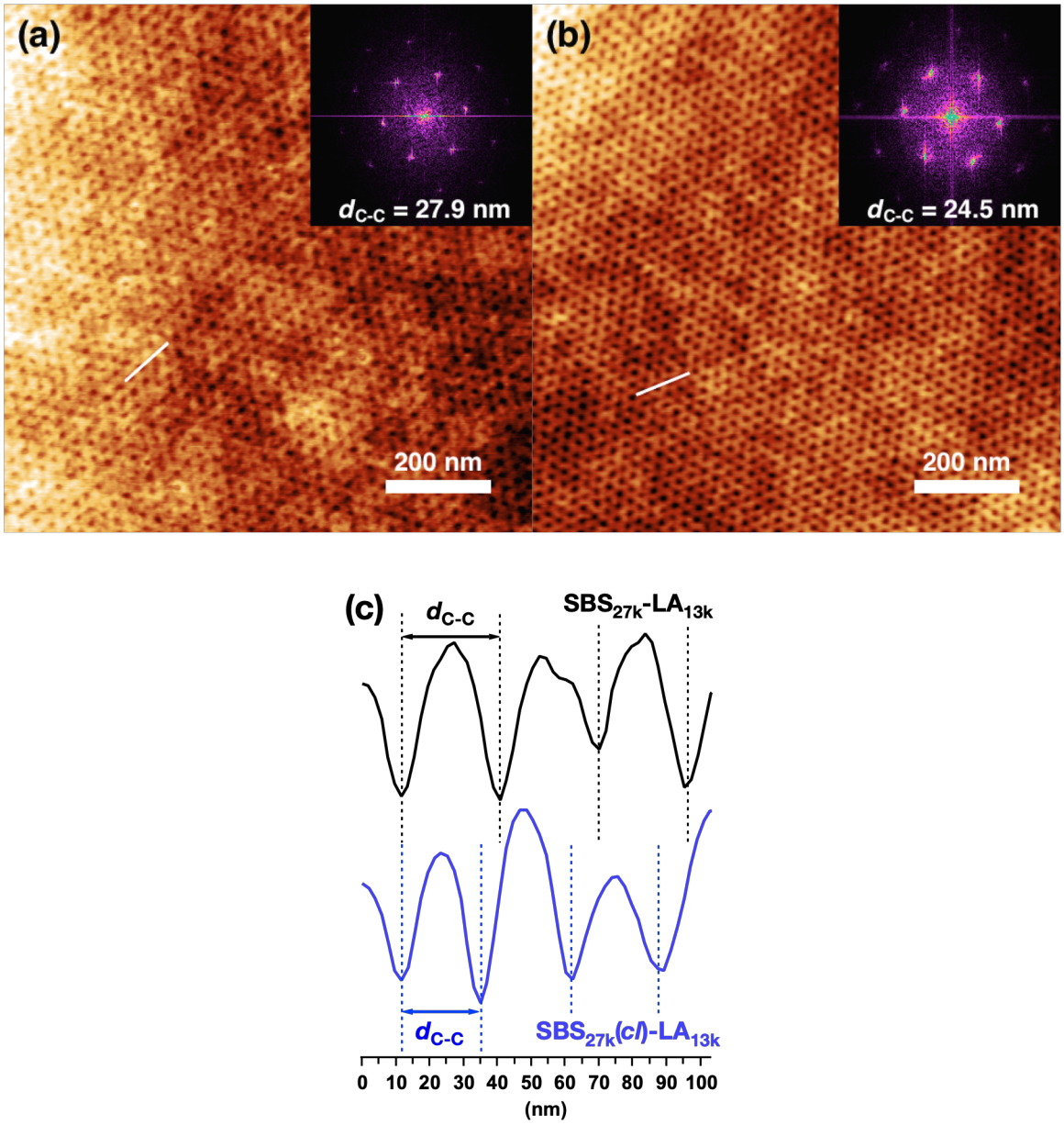

Figure 3.8. AFM height images of (a) SBS_{27k}–LA_{13k} and (b) SBS_{27k}(*cl*)–LA_{13k} thin films with the thickness of 56 and 42 nm, respectively. Insets show the 2D FFTs obtained from the height images. Scale bars are 200 nm. (c) AFM height cross sectional images along the white lines in (a) (upper) and (b) (lower).

3.4 Conclusion

The author have successfully synthesized crosslinked–linear BCPs (SBS(*cl*)–LAs) from the linear–linear BCPs consisting of the crosslinkable SBS segment possessing pendant double bonds and the LA segment (SBS–LA), via intramolecular olefin metathesis under the highly diluted condition. Morphological analyses of the obtained BCPs in the bulk state by SAXS measurement clearly revealed that the SBS(*cl*)–LAs had a smaller *d* values in their LAM and HEX morphologies as compared to the corresponding SBS–LAs, due to the restricted chain dimensions of the SBS(*cl*) segments. Importantly, the amount of *d* decrease was controllable by varying content of the crosslinking sites, where the largest decrease (22%) was achieved in LAM morphology with ca. 50% of the crosslinkable BS unit incorporated into the SBS block. Although the macrocyclic or miktoarm architectures can effectively reduce the size of microphase-separated structures to some extent, further reduction in the *d* value requires increasing the number of the cyclic units or the branching, which presents synthetic challenge and practical limitations. In contrast, the currently reported intramolecular crosslinking approach could easily reduce the *d* value further by simply controlling the crosslink density. The author also confirmed the downsizing of the HEX morphology in the thin film state by AFM observation, and the uniformly packed structures were present even after the intramolecular crosslinking that reduced chain mobility of the crosslinked segment. Considering the fact that the sub-10 nm scale nanostructure was successfully downsized here and the crosslinked–linear BCP could form well-ordered structure in thin film, the current approach is highly promising for the development of next-generation lithography.

3.5 References

1. Park, C.; Yoon, J.; Thomas, E. L. Enabling Nanotechnology with Self Assembled Block Copolymer Patterns. *Polymer* **2003**, *44* (22), 6725–6760.
2. Kim, H. C.; Park, S. M.; Hinsberg, W. D.; Division, I. R. Block Copolymer Based Nanostructures: Materials, Processes, and Applications to Electronics. *Chem. Rev.* **2010**, *110* (1), 146–177.
3. Kim, J. K.; Yang, S. Y.; Lee, Y.; Kim, Y. Functional Nanomaterials Based on Block Copolymer Self-Assembly. *Prog. Polym. Sci.* **2010**, *35* (11), 1325–1349.
4. Horechyy, A.; Nandan, B.; Zafeiropoulos, N. E.; Formanek, P.; Oertel, U.; Bigall, N. C.; Eychmüller, A.; Stamm, M. A Step-Wise Approach for Dual Nanoparticle Patterning via Block Copolymer Self-Assembly. *Adv. Funct. Mater.* **2013**, *23* (4), 483–490.
5. Hsueh, H. Y.; Yao, C. T.; Ho, R. M. Well-Ordered Nanohybrids and Nanoporous Materials from Gyroid Block Copolymer Templates. *Chem. Soc. Rev.* **2015**, *44* (7), 1974–2018.
6. Stefik, M.; Guldin, S.; Vignolini, S.; Wiesner, U.; Steiner, U. Block Copolymer Self-Assembly for Nanophotonics. *Chem. Soc. Rev.* **2015**, *44* (15), 5076–5091.
7. Bates, C. M.; Bates, F. S. 50th Anniversary Perspective: Block Polymers-Pure Potential. *Macromolecules* **2017**, *50* (1), 3–22.
8. Hung, C. C.; Chiu, Y. C.; Wu, H. C.; Lu, C.; Bouilhac, C.; Otsuka, I.; Halila, S.; Borsali, R.; Tung, S. H.; Chen, W. C. Conception of Stretchable Resistive Memory Devices Based on Nanostructure-Controlled Carbohydrate-Block-Polyisoprene Block Copolymers. *Adv. Funct. Mater.* **2017**, *27* (13), 1606161.
9. Stoykovich, M. P.; Müller, M.; Kim, S. O.; Solak, H. H.; Edwards, E. W.; de Pablo, J. J.; Nealey, P. F. Directed Assembly of Block Copolymer Blends into Nonregular Device-Oriented Structures. *Science* **2005**, *308* (5727), 1442–1446.
10. Stoykovich, M. P.; Nealey, P. F. Block Copolymers and Conventional Lithography. *Mater. Today* **2006**, *9* (9), 20–29.
11. Li, M.; Ober, C. K. Block Copolymer Patterns and Templates. *Mater. Today* **2006**, *9* (9), 30–39.
12. Ruiz, R.; Kang, H.; Detcheverry, F. A.; Dobisz, E.; Kercher, D. S.; Albrecht, T. R.; de Pablo, J. J.; Nealey, P. F. Density Multiplication and Improved Lithography by Directed Block Copolymer Assembly. *Science* **2008**, *321* (5891), 936–939.
13. Bang, J.; Jeong, U.; Ryu, D. Y.; Russell, T. P.; J Hawker, C. Block Copolymer Nanolithography: Translation of Molecular Level Control to Nanoscale Patterns. *Adv. Mater.* **2009**, *21* (47), 4769–4792.
14. Bates, C. M.; Maher, M. J.; Janes, D. W.; Ellison, C. J.; Willson, C. G. Block Copolymer Lithography. *Macromolecules* **2014**, *47* (1), 2–12.
15. Nunns, A.; Gwyther, J.; Manners, I. Inorganic Block Copolymer Lithography. *Polymer* **2013**, *54* (4), 1269–1284.

16. Jeong, S. J.; Kim, J. Y.; Kim, B. H.; Moon, H. S.; Kim, S. O. Directed Self-Assembly of Block Copolymers for next Generation Nanolithography. *Mater. Today* **2013**, *16* (12), 468–476.
17. Liu, C. C.; Han, E.; Onses, M. S.; Thode, C. J.; Ji, S.; Gopalan, P.; Nealey, P. F. Fabrication of Lithographically Defined Chemically Patterned Polymer Brushes and Mats. *Macromolecules* **2011**, *44* (7), 1876–1885.
18. Kwak, J.; Mishra, A. K.; Lee, J.; Lee, K. S.; Choi, C.; Maiti, S.; Kim, M.; Kim, J. K. Fabrication of Sub-3 Nm Feature Size Based on Block Copolymer Self-Assembly for Next-Generation Nanolithography. *Macromolecules* **2017**, *50* (17), 6813–6818.
19. Nakatani, R.; Takano, H.; Chandra, A.; Yoshimura, Y.; Wang, L.; Suzuki, Y.; Tanaka, Y.; Maeda, R.; Kihara, N.; Minegishi, S.; et al. Perpendicular Orientation Control without Interfacial Treatment of RAFT-Synthesized High-χ Block Copolymer Thin Films with Sub-10 Nm Features Prepared via Thermal Annealing. *ACS Appl. Mater. Interfaces* **2017**, *9* (37), 31266–31278.
20. Legrain, A.; Fleury, G.; Mumtaz, M.; Navarro, C.; Arias-Zapata, J.; Chevalier, X.; Cayrefourcq, I.; Zelsmann, M. Straightforward Integration Flow of a Silicon-Containing Block Copolymer for Line-Space Patterning. *ACS Appl. Mater. Interfaces* **2017**, *9* (49), 43043–43050.
21. Leibler, L. Theory of Microphase Separation in Block Copolymers. *Macromolecules* **1980**, *13* (10), 1602–1617.
22. Bates, F. S.; Fredrickson, G. H. Block Copolymer Thermodynamics: Theory and Experiment. *Annu. Rev. Phys. Chem.* **1990**, *41* (1), 525–557.
23. Lo, T. Y.; Krishnan, M. R.; Lu, K. Y.; Ho, R. M. Silicon-Containing Block Copolymers for Lithographic Applications. *Prog. Polym. Sci.* **2018**, *77*, 19–68.
24. Rodwogin, M. D.; Spanjers, C. S.; Leighton, C.; Hillmyer, M. A. Polylactide–Poly(dimethylsiloxane)–Polylactide Triblock Copolymers as Multifunctional Materials for Nanolithographic Applications. *ACS Nano* **2010**, *4* (2), 725–732.
25. Cushen, J. D.; Bates, C. M.; Rausch, E. L.; Dean, L. M.; Zhou, S. X.; Willson, C. G.; Ellison, C. J. Thin Film Self-Assembly of Poly(trimethylsilylstyrene-*b*-D,L-lactide) with Sub-10 nm Domains. *Macromolecules* **2012**, *45* (21), 8722–8728.
26. Maher, M. J.; Rettner, C. T.; Bates, C. M.; Blachut, G.; Carlson, M. C.; Durand, W. J.; Ellison, C. J.; Sanders, D. P.; Cheng, J. Y.; Willson, C. G. Directed Self-Assembly of Silicon-Containing Block Copolymer Thin Films. *ACS Appl. Mater. Interfaces* **2015**, *7* (5), 3323–3328.
27. Aissou, K.; Mumtaz, M.; Fleury, G.; Portale, G.; Navarro, C.; Cloutet, E.; Brochon, C.; Ross, C. A.; Hadziioannou, G. Sub-10 Nm Features Obtained from Directed Self-Assembly of Semicrystalline Polycarbosilane-Based Block Copolymer Thin Films. *Adv. Mater.* **2015**, *27* (2), 261–265.

28. Luo, Y.; Montarnal, D.; Kim, S.; Shi, W.; Barteau, K. P.; Pester, C. W.; Hustad, P. D.; Christianson, M. D.; Fredrickson, G. H.; Kramer, E. J.; et al. Poly(dimethylsiloxane-*b*-Methyl Methacrylate): A Promising Candidate for Sub-10 nm Patterning. *Macromolecules* **2015**, *48* (11), 3422–3430.
29. Young, W. S.; Epps, T. H. Salt Doping in PEO-Containing Block Copolymers: Counterion and Concentration Effects. *Macromolecules* **2009**, *42* (7), 2672–2678.
30. Park, S.; Lee, D. H.; Xu, J.; Kim, B.; Hong, S. W.; Jeong, U.; Russell, T. P. Macroscopic 10-Terabit−per−Sqsre-Inch Arrays from Block Copolymers with Lateral Order Supplemental Information. *Science* **2009**, *323* (2009), 1030.
31. Sun, Z.; Chen, Z.; Zhang, W.; Choi, J.; Huang, C.; Jeong, G.; Coughlin, E. B.; Hsu, Y.; Yang, X.; Lee, K. Y.; et al. Directed Self-Assembly of Poly(2-Vinylpyridine)-*b*-Polystyrene-*b*-poly(2-Vinylpyridine) Triblock Copolymer with Sub-15 nm Spacing Line Patterns Using a Nanoimprinted Photoresist Template. *Adv. Mater.* **2015**, *27* (29), 4364–4370.
32. Cushen, J. D.; Otsuka, I.; Bates, C. M.; Halila, S.; Fort, S.; Rochas, C.; Easley, J. A.; Rausch, E. L.; Thio, A.; Borsali, R.; et al. Oligosaccharide/Silicon-Containing Block Copolymers with 5 nm Features for Lithographic Applications. *ACS Nano* **2012**, *6* (4), 3424–3433.
33. Otsuka, I.; Tallegas, S.; Sakai, Y.; Rochas, C.; Halila, S.; Fort, S.; Bsiesy, A.; Baron, T.; Borsali, R. Control of 10 nm Scale Cylinder Orientation in Self-Organized Sugar-Based Block Copolymer Thin Films. *Nanoscale* **2013**, *5* (7), 2637–2641.
34. Sakai-Otsuka, Y.; Zaioncz, S.; Otsuka, I.; Halila, S.; Rannou, P.; Borsali, R. Self-Assembly of Carbohydrate-*block*-Poly(3-Hexylthiophene) Diblock Copolymers into Sub-10 nm Scale Lamellar Structures. *Macromolecules* **2017**, *50* (8), 3365–3376.
35. Isono, T.; Ree, B. J.; Tajima, K.; Borsali, R.; Satoh, T. Highly Ordered Cylinder Morphologies with 10 nm Scale Periodicity in Biomass-Based Block Copolymers. *Macromolecules* **2018**, *51* (2), 428–437.
36. Poelma, J. E.; Ono, K.; Miyajima, D.; Aida, T.; Satoh, K.; Hawker, C. J. Cyclic Block Copolymers for Controlling Feature Sizes in Block Copolymer Lithography. *ACS Nano* **2012**, *6* (12), 10845–10854.
37. Isono, T.; Otsuka, I.; Kondo, Y.; Halila, S.; Fort, S.; Rochas, C.; Satoh, T.; Borsali, R.; Kakuchi, T. Sub-10 nm Nano-Organization in AB_2- and AB_3-Type Miktoarm Star Copolymers Consisting of Maltoheptaose and Polycaprolactone. *Macromolecules* **2013**, *46* (4), 1461–1469.
38. Shi, W.; Tateishi, Y.; Li, W.; Hawker, C. J.; Fredrickson, G. H.; Kramer, E. J. Producing Small Domain Features Using Miktoarm Block Copolymers with Large Interaction Parameters. *ACS Macro Lett.* **2015**, *4* (11), 1287–1292.
39. Minehara, H.; Pitet, L. M.; Kim, S.; Zha, R. H.; Meijer, E. W.; Hawker, C. J. Branched Block Copolymers for Tuning of Morphology and Feature Size in Thin Film Nanolithography. *Macromolecules* **2016**, *49* (6), 2318–2326.

40. Yue, K.; Liu, C.; Huang, M.; Huang, J.; Zhou, Z.; Wu, K.; Liu, H.; Lin, Z.; Shi, A. C.; Zhang, W. Bin; et al. Self-Assembled Structures of Giant Surfactants Exhibit a Remarkable Sensitivity on Chemical Compositions and Topologies for Tailoring Sub-10 nm Nanostructures. *Macromolecules* **2017**, *50* (1), 303–314.
41. Hosono, N.; Gillissen, M. A. J.; Li, Y.; Sheiko, S. S.; Palmans, A. R. A.; Meijer, E. W. Orthogonal Self-Assembly in Folding Block Copolymers. *J. Am. Chem. Soc.* **2013**, *135* (1), 501–510.
42. ter Huurne, G. M.; Gillissen, M. A. J.; Palmans, A. R. A.; Voets, I. K.; Meijer, E. W. The Coil-to-Globule Transition of Single-Chain Polymeric Nanoparticles with a Chiral Internal Secondary Structure. *Macromolecules* **2015**, *48* (12), 3949–3956.
43. Liu, Y.; Pauloehrl, T.; Presolski, S. I.; Albertazzi, L.; Palmans, A. R. A.; Meijer, E. W. Modular Synthetic Platform for the Construction of Functional Single-Chain Polymeric Nanoparticles: From Aqueous Catalysis to Photosensitization. *J. Am. Chem. Soc.* **2015**, *137* (40), 13096–13106.
44. Altintas, O.; Artar, M.; Ter Huurne, G.; Voets, I. K.; Palmans, A. R. A.; Barner-Kowollik, C.; Meijer, E. W. Design and Synthesis of Triblock Copolymers for Creating Complex Secondary Structures by Orthogonal Self-Assembly. *Macromolecules* **2015**, *48* (24), 8921–8932.
45. Sanchez-Sanchez, A.; Akbari, S.; Moreno, A. J.; Verso, F. Lo; Arbe, A.; Colmenero, J.; Pomposo, J. A. Design and Preparation of Single-Chain Nanocarriers Mimicking Disordered Proteins for Combined Delivery of Dermal Bioactive Cargos. *Macromol. Rapid Commun.* **2013**, *34* (21), 1681–1686.
46. Perez-Baena, I.; Asenjo-Sanz, I.; Arbe, A.; Moreno, A. J.; Lo Verso, F.; Colmenero, J.; Pomposo, J. A. Efficient Route to Compact Single-Chain Nanoparticles: Photoactivated Synthesis via Thiol-Yne Coupling Reaction. *Macromolecules* **2014**, *47* (23), 8270–8280.
47. Sanchez-Sanchez, A.; Fulton, D. A.; Pomposo, J. A. pH-Responsive Single-Chain Polymer Nanoparticles Utilizing Dynamic Covalent Enamine Bonds. *Chem Commun* **2014**, *50* (15), 1871–1874.
48. Nanoparticles, S.; Basasoro, S.; Gonzalez-burgos, M.; Moreno, A. J.; Verso, F. Lo; Arbe, A.; Colmenero, J.; Pomposo, J. A. Basasoro, A Solvent-Based Strategy for Tuning the Internal Structure of Metallo-Folded Single-Chain Nanoparticles. *Macromol. Rapid. Commun.* **2016**, *37* (13), 1060–1065.
49. Terashima, T.; Sugita, T.; Fukae, K.; Sawamoto, M. Synthesis and Single-Chain Folding of Amphiphilic Random Copolymers in Water. *Macromolecules* **2014**, *47* (2), 589–600.
50. Matsumoto, K.; Terashima, T.; Sugita, T.; Takenaka, M.; Sawamoto, M. Amphiphilic Random Copolymers with Hydrophobic/Hydrogen-Bonding Urea Pendants: Self-Folding Polymers in Aqueous and Organic Media. *Macromolecules* **2016**, *49* (20), 7917–7927.
51. Harth, E.; Van Horn, B.; Lee, V. Y.; Germack, D. S.; Gonzales, C. P.; Miller, R. D.; Hawker, C. J. A Facile Approach to Architecturally Defined Nanoparticles via Intramolecular Chain Collapse. *J. Am. Chem. Soc.* **2002**, *124* (29), 8653–8660.

52. Hansell, C. F.; Lu, A.; Patterson, J. P.; O'Reilly, R. K. Exploiting the Tetrazine-Norbornene Reaction for Single Polymer Chain Collapse. *Nanoscale* **2014**, *6*, 4102–4107.
53. Beck, J. B.; Killops, K. L.; Kang, T.; Sivanandan, K.; Bayles, A.; Mackay, M. E.; Wooley, K. L.; Hawker, C. J. Facile Preparation of Nanoparticles by Intramolecular Cross-Linking of Isocyanate Functionalized Copolymers. *Macromolecules* **2009**, *42* (15), 5629–5635.
54. Song, C.; Li, L.; Dai, L.; Thayumanavan, S. Responsive Single-Chain Polymer Nanoparticles with Host-Guest Features. *Polym. Chem.* **2015**, *6* (26), 4828–4834.
55. Altintas, O.; Willenbacher, J.; Wuest, K. N. R.; Oehlenschlaeger, K. K.; Krolla-Sidenstein, P.; Gliemann, H.; Barner-Kowollik, C. A Mild and Efficient Approach to Functional Single-Chain Polymeric Nanoparticles via Photoinduced Diels-Alder Ligation. *Macromolecules* **2013**, *46* (20), 8092–8101.
56. Willenbacher, J.; Wuest, K. N. R.; Mueller, J. O.; Kaupp, M.; Wagenknecht, H. A.; Barner-Kowollik, C. Photochemical Design of Functional Fluorescent Single-Chain Nanoparticles. *ACS Macro Lett.* **2014**, *3* (6), 574–579.
57. Wuest, K. N. R.; Lu, H.; Thomas, D. S.; Goldmann, A. S.; Stenzel, M. H.; Barner-Kowollik, C. Fluorescent Glyco Single-Chain Nanoparticle-Decorated Nanodiamonds. *ACS Macro Lett.* **2017**, *6* (10), 1168–1174.
58. Fischer, T. S.; Spann, S.; An, Q.; Luy, B.; Tsotsalas, M.; Blinco, J. P.; Mutlu, H.; Barner-Kowollik, C. Self-Reporting and Refoldable Profluorescent Single-Chain Nanoparticles. *Chem. Sci.* **2018**, *9* (20), 4696–4702.
59. Zalusky, A. S.; Olayo-Valles, R.; Taylor, C. J.; Hillmyer, M. A. Mesoporous Polystyrene Monoliths. *J. Am. Chem. Soc.* **2001**, *123* (7), 1519–1520.
60. Zalusky, A. S.; Olayo-Valles, R.; Wolf, J. H.; Hillmyer, M. A. Ordered Nanoporous Polymers from Polystyrene-Polylactide Block Copolymers. *J. Am. Chem. Soc.* **2002**, *124* (43), 12761–12773.
61. Olayo-Valles, R.; Lund, M. S.; Leighton, C.; Hillmyer, M. A. Large Area Nanolithographic Templates by Selective Etching of Chemically Stained Block Copolymer Thin Films. *J. Mater. Chem.* **2004**, *14* (18), 2729–2731.
62. Olayo-Valles, R.; Guo, S.; Lund, M. S.; Leighton, C.; Hillmyer, M. A. Perpendicular Domain Orientation in Thin Films of Polystyrene-Polylactide Diblock Copolymers. *Macromolecules* **2005**, *38* (24), 10101–10108.
63. Baruth, A.; Rodwogin, M.; Shankar, A.; Torija, M. A.; Erickson, M. J.; Hillmyer, M. A.; Leighton, C. Non-Liftoff Block Copolymer Nanolithography of Magnetic Nanodot Arrays. *ACS Appl. Mater. Interfaces* **2011**, 3472–3481.
64. Baruth, A.; Seo, M.; Lin, C. H.; Walster, K.; Shankar, A.; Hillmyer, M. A.; Leighton, C. Optimization of Long-Range Order in Solvent Vapor Annealed Poly(styrene)-*block*-Poly(lactide) Thin Films for Nanolithography. *ACS Appl. Mater. Interfaces* **2014**, *6* (16), 13770–13781.

65. Vanderlaan, M. E.; Hillmyer, M. A. "Uncontrolled" Preparation of Disperse Poly(lactide)-Block-Poly(styrene)-*block*-Poly(lactide) for Nanopatterning Applications. *Macromolecules* **2016**, *49* (21), 8031–8040.
66. Zhang, H.; Ruckenstein, E. Selective Living Anionic Polymerization of a Novel Bifunctional Monomer 4-(vinylphenyl)-1-Butene and the Preparation of Uniform Size Functional Polymers and Amphiphilic Block Copolymers. *Macromolecules* **1999**, *32* (17), 5495–5500.
67. Burdyńska, J.; Li, Y.; Aggarwal, A. V.; Höger, S.; Sheiko, S. S.; Matyjaszewski, K. Synthesis and Arm Dissociation in Molecular Stars with a Spoked Wheel Core and Bottlebrush Arms. *J. Am. Chem. Soc.* **2014**, *136* (36), 12762–12770.
68. Watanabe, K.; Tanaka, R.; Takada, K.; Kim, M. J.; Lee, J. S.; Tajima, K.; Isono, T.; Satoh, T. Intramolecular Olefin Metathesis as a Robust Tool to Synthesize Single-Chain Nanoparticles in a Size-Controlled Manner. *Polym. Chem.* **2016**, *7* (29), 4782–4792.
69. Tanaka, R.; Watanabe, K.; Yamamoto, T.; Tajima, K.; Isono, T.; Satoh, T. A Facile Strategy for Manipulating Micellar Size and Morphology through Intramolecular Cross-Linking of Amphiphilic Block Copolymers. *Polym. Chem.* **2017**, *8* (23), 3647–3656.
70. Mecerreyes, D.; Lee, V.; Hawker, C. J.; Hedrick, J. L.; Wursch, A.; Volksen, W.; Magbitang, T.; Huang, E.; Miller, R. D. Novel Approach to Functionalized Nanoparticles: Self-Crosslinking of Macromolecules in Ultradilute Solution. *Adv. Mater.* **2001**, *13* (3), 204–208.
71. He, J.; Tremblay, L.; Lacelle, S.; Zhao, Y. Preparation of Polymer Single Chain Nanoparticles Using Intramolecular Photodimerization of Coumarin. *Soft Matter* **2011**, *7* (6), 2380–2386.
72. Rubio-Cervilla, J.; Barroso-Bujans, F.; Pomposo, J. A. Merging of Zwitterionic ROP and Photoactivated Thiol–Yne Coupling for the Synthesis of Polyether Single-Chain Nanoparticles. *Macromolecules* **2016**, *49* (1), 90–97.
73. Wang, F.; Pu, H.; Jin, M.; Wan, D. Supramolecular Nanoparticles via Single-Chain Folding Driven by Ferrous Ions. *Macromol. Rapid Commun.* **2016**, *37* (4), 330–336.
74. Zhang, J.; Gody, G.; Hartlieb, M.; Catrouillet, S.; Moffat, J.; Perrier, S. Synthesis of Sequence-Controlled Multiblock Single Chain Nanoparticles by a Stepwise Folding-Chain Extension-Folding Process. *Macromolecules* **2016**, *49* (23), 8933–8942.
75. Hashimoto, T.; Tanaka, H.; Hasegawa, H. Uniformity of Microdomain Size of Block Polymers As Compared with Uniformity of Their Molecular Weights. *Macromolecules* **1985**, *18* (10), 1864c1868.
76. Vayer, M.; Hillmyer, M. A.; Dirany, M.; Thevenin, G.; Erre, R.; Sinturel, C. Perpendicular orientation of cylindrical domains upon solvent annealing thin films of polystyrene-*b*-polylactide. *Thin Solid Films* **2010**, *518* (14), 3710–3715.
77. Dirany,M.; Lacroix-Desmazes, P.; Vayer, M.; Erre, R.; Boutevin, B.; Sinturel, C. Polystyrene-*b*-Polylactide Obtained by the Combination of Atom Transfer Radical

Polymerization and Ring-Opening Polymerization with a Commercial Dual Initiator. J. *Appl. polym. Sci.* **2011**, *122* (5), 2944–2951.

3.6 Supporting Information

3.6.1 Experimental

Synthesis of *ω*-end hydroxy-functionalized statistical copolymer of S and BS (SBS_{8k}–OH). Method A was used for the living anionic copolymerization of S (2.5 g, 24 mmol) and BS (1.6 g, 10 mmol) with *n*-BuLi (560 μL, 598 μmol as a 1.07 mol L^{-1} stock solution in *n*-hexane) and Br–O–TIPS (620 mg, 2.10 mmol) in mixture solvent of dry toluene (47 mL) and dry THF (23 mL) for 6 h followed by the deprotection with TBAF (6.30 mL, 6.30 mmol as a 1.0 mol L^{-1} stock solution in THF) in dry THF (20 mL) to give SBS_{8k}–OH. Yield: 3.25 g (76.3 %). $M_{n,NMR}$ = 7,940 ($CDCl_3$), f_{BS} = 0.31, $M_{n,SEC}$ = 4,730 (THF), $Đ$ = 1.04 (THF).

Synthesis of *ω*-end hydroxy-functionalized statistical copolymer of S and BS (SBS^*_{9k}–OH). Method A was used for the living anionic copolymerization of S (1.8 g, 17 mmol) and BS (2.7 g, 17 mmol) with *n*-BuLi (640 μL, 493 μmol as a 0.77 mol L^{-1} stock solution in *n*-hexane) and Br–O–TIPS (508 mg, 1.72 mmol) in mixture solvent of dry toluene (47 mL) and dry THF (23 mL) for 6 h followed by the deprotection with TBAF (5.17 mL, 5.17 mmol as a 1.0 mol L^{-1} stock solution in THF) in dry THF (20 mL) to give SBS^*_{9k}–OH. Yield: 4.33 g (93.5 %). $M_{n,NMR}$ = 9,460 ($CDCl_3$), f_{BS} = 0.49, $M_{n,SEC}$ = 8,250 (THF), $Đ$ = 1.04 (THF).

Synthesis of *ω*-end hydroxy-functionalized statistical copolymer of S and BS (SBS_{27k}–OH). Method A was used for the living anionic copolymerization of S (2.5 g, 24 mmol) and BS (1.6 g, 10 mmol) with *n*-BuLi (280 μL, 155 μmol as a 0.55 mol L^{-1} stock solution in *n*-hexane) and Br–O–TIPS (298 mg, 1.01 mmol) in mixture solvent of dry toluene

(47 mL) and dry THF (23 mL) for 6 h followed by the deprotection with TBAF (3.03 mL, 3.03 mmol as a 1.0 mol L^{-1} stock solution in THF) in dry THF (20 mL) to give SBS_{27k}–OH. Yield: 4.11 g (99.5 %). $M_{n,NMR}$ = 27,000 ($CDCl_3$), f_{BS} = 0.29, $M_{n,SEC}$ = 19,600 (THF), $Đ$ = 1.02 (THF).

Synthesis of block copolymer consisting of SBS and poly(*rac*-LA) (SBS_{8k}–LA_{5k}) via ring-opening polymerization of *rac*-LA using SBS_{8k}–OH as an initiator. Method B was used for the ring-opening polymerization of *rac*-LA (532 mg, 36.9 μmol) with SBS_{8k}–OH ($M_{n,NMR}$ = 7,940, 736 mg, 92.2 μmol) and DBU (5.5 μL, 36.8 μmol) in dry CH_2Cl_2 (7.4 mL) for 10 min to give SBS_{5k}–LA_{6k} as a white solid (1.11 g, 87.5%)). The product was further purified by preparative SEC prior to the intramolecular crosslinking reaction and each measurement. Conversion = 81%, $M_{n,NMR}$ = 12,600 ($CDCl_3$), F_{SBS} = 0.63, $M_{n,SEC}$ = 12,500 (THF), $Đ$ = 1.03 (THF).

Synthesis of block copolymer consisting of SBS and poly(*rac*-LA) (SBS_{8k}–LA_{8k}) via ring-opening polymerization of *rac*-LA using SBS_{8k}–OH as an initiator. Method B was used for the ring-opening polymerization of *rac*-LA (1.26 g, 8.71 mmol) with SBS_{8k}–OH ($M_{n,NMR}$ = 7,940, 1.25 g, 157 μmol) and DBU (13.0 μL, 87.1 μmol) in dry CH_2Cl_2 (17.4 mL) for 35 min to give SBS_{8k}–LA_{8k} as a white solid. Yield: 2.36 g, 87.5%). Conversion = 96%, $M_{n,NMR}$ = 16,200 ($CDCl_3$), F_{SBS} = 0.49, $M_{n,SEC}$ = 16,500 (THF), $Đ$ = 1.03 (THF).

Synthesis of block copolymer consisting of SBS and poly(*rac*-LA) (SBS^*_{9k}–LA_{6k}) via ring-opening polymerization of *rac*-LA using SBS^*_{9k}–OH as an initiator. Method B was used for the ring-opening polymerization of *rac*-LA (439 mg, 3.05 mmol) with SBS^*_{9k}–OH ($M_{n,NMR}$ = 9,460, 604 mg, 67.6 μmol) and DBU (5.0 μL, 33.5 μmol)

in dry CH_2Cl_2 (6.1 mL) for 13 min to give SBS^*_{9k}–LA_{6k} as a white solid (930 mg, 89.2%)). The product was further purified by preparative SEC prior to the intramolecular crosslinking reaction and each measurement. Conversion = 89%, $M_{n,NMR}$ = 15,900 ($CDCl_3$), F_{SBS} = 0.60, $M_{n,SEC}$ = 16,800 (THF), $Đ$ = 1.03 (THF).

Synthesis of block copolymer consisting of SBS and poly(*rac*-LA) (SBS^*_{9k}–LA_{11k}) via ring-opening polymerization of *rac*-LA using SBS^*_{9k}–OH as an initiator. Method B was used for the ring-opening polymerization of *rac*-LA (1.46 g, 10.1 mmol) with SBS^*_{9k}–OH ($M_{n,NMR}$ = 9,460, 999 mg, 112 μmol) and DBU (15.0 μL, 100 μmol) in dry CH_2Cl_2 (6.1 mL) for 20.2 min to give SBS^*_{9k}–LA_{11k} as a white solid (2.06 g, 83.8%)). The product was further purified by preparative SEC prior to the intramolecular crosslinking reaction and each measurement. Conversion = 85%, $M_{n,NMR}$ = 20,900 ($CDCl_3$), F_{LA} = 0.45, $M_{n,SEC}$ = 23,300 (THF), $Đ$ = 1.03 (THF).

Synthesis of block copolymer consisting of SBS and poly(*rac*-LA) (SBS_{27k}–LA_{13k}) via ring-opening polymerization of *rac*-LA using SBS_{27k}–OH as an initiator. Method B was used for the ring-opening polymerization of *rac*-LA (729 mg, 5.06 mmol) with SBS_{27k}–OH ($M_{n,NMR}$ = 27,000, 1.00 g, 37.0 μmol) and DBU (7.6 μL, 50.6 μmol) in dry CH_2Cl_2 (10.0 mL) for 35 min to give SBS_{27k}–LA_{13k} as a white solid (1.37 g, 79.2%)). The product was further purified by preparative SEC prior to the intramolecular crosslinking reaction and each measurement. Conversion = 75%, $M_{n,NMR}$ = 40,400 ($CDCl_3$), F_{SBS} = 0.67, $M_{n,SEC}$ = 16,500 (THF), $Đ$ = 1.03 (THF).

Synthesis of block copolymer consisting of SBS and poly(*rac*-LA) (SBS_{27k}–LA_{28k}) via ring-opening polymerization of *rac*-LA using SBS_{27k}–OH as an

initiator. Method B was used for the ring-opening polymerization of *rac*-LA (1.37 g, 9.52 mmol) with SBS_{27k}–OH ($M_{n,NMR}$ = 27,000, 1.00 g, 37.0 μmol) and DBU (14.1 μL, 94.7 μmol) in dry CH_2Cl_2 (18.9 mL) for 45 min to give SBS_{27k}–LA_{13k} as a white solid (1.96 g, 82.5%)). The product was further purified by preparative SEC prior to the intramolecular crosslinking reaction and each measurement. Conversion = 81%, $M_{n,NMR}$ = 54,900 ($CDCl_3$), F_{SBS} = 0.49, $M_{n,SEC}$ = 54,400 (THF), $Đ$ = 1.03 (THF).

Intramolecular crosslinking of SBS_{8k}–LA_{5k} via olefin metathesis reaction. Method C was used for the intramolecular crosslinking of SBS_{8k}–LA_{5k} ($M_{n,NMR}$ = 12,600, 400 mg, 614 μmol olefin-containing units) with G2 (5.3 mg, 6.2 μmol) in dry CH_2Cl_2 (1340 mL) for 3 h to give SBS_{8k}(*cl*)–LA_{5k} as a white solid (377 mg, 94.2 %)). The product was further purified by preparative SEC prior to each measurement. $M_{n,SEC}$ = 11,200 (THF), $Đ$ = 1.03 (THF), $conv._{olefin}$ = 88%.

Intramolecular crosslinking of SBS_{8k}–LA_{8k} via olefin metathesis reaction. Method C was used for the intramolecular crosslinking of SBS_{8k}–LA_{8k} ($M_{n,NMR}$ = 16,200, 309 mg, 410 μmol olefin-containing units) with G2 (3.5 mg, 4.1 μmol) in dry CH_2Cl_2 (1030 mL) for 3 h to give SBS_{8k}(*cl*)–LA_{5k} as a white solid (260 mg, 84.1 %)). The product was further purified by preparative SEC prior to each measurement. $M_{n,SEC}$ = 15,300 (THF), $Đ$ = 1.03 (THF), $conv._{olefin}$ = 79%.

Intramolecular crosslinking of SBS^*_{9k}–LA_{6k} via olefin metathesis reaction. Method C was used for the intramolecular crosslinking of SBS^*_{9k}–LA_{6k} ($M_{n,NMR}$ = 15,900, 341 mg, 510 μmol olefin-containing units) with G2 (4.3 mg, 5.1 μmol) in dry CH_2Cl_2 (1030 mL) for 3 h to give SBS^*_{9k}(*cl*)–LA_{6k} as a white solid (260 mg, 76.2 %)). The product was

further purified by preparative SEC prior to each measurement. $M_{n,SEC}$ = 13,900 (THF), $Đ$ = 1.03 (THF), $conv._{olefin}$ = 86%.

Intramolecular crosslinking of SBS^{*}_{9k}–LA_{11k} via olefin metathesis reaction. Method C was used for the intramolecular crosslinking of SBS^{*}_{9k}–LA_{11k} ($M_{n,NMR}$ = 20,900, 362 mg, 612 μmol olefin-containing units) with G2 (5.2 mg, 6.1 μmol) in dry CH_2Cl_2 (1200 mL) for 3 h to give SBS^{*}_{9k}(*cl*)–LA_{11k} as a white solid (262 mg, 72.4 %)). The product was further purified by preparative SEC prior to each measurement. $M_{n,SEC}$ = 20,600 (THF), $Đ$ = 1.03 (THF), $conv._{olefin}$ = 89%.

Intramolecular crosslinking of SBS_{27k}–LA_{13k} via olefin metathesis reaction. Method C was used for the intramolecular crosslinking of SBS_{27k}–LA_{13k} ($M_{n,NMR}$ = 40,400, 130 mg, 212 μmol olefin-containing units) with G2 (1.8 mg, 2.1 μmol) in dry CH_2Cl_2 (430 mL) for 3 h to give SBS_{27k}(*cl*)–LA_{13k} as a white solid (100 mg, 76.9 %)). The product was further purified by preparative SEC prior to each measurement. $M_{n,SEC}$ = 28,900 (THF), $Đ$ = 1.03 (THF), $conv._{olefin}$ = 88%.

Intramolecular crosslinking of SBS_{27k}–LA_{28k} via olefin metathesis reaction. Method C was used for the intramolecular crosslinking of SBS_{27k}–LA_{28k} ($M_{n,NMR}$ = 54,900, 253 mg, 307 μmol olefin-containing units) with G2 (2.9 mg, 3.4 μmol) in dry CH_2Cl_2 (840 mL) for 3 h to give SBS_{27k}(*cl*)–LA_{28k} as a white solid (158 mg, 62.5 %)). The product was further purified by preparative SEC prior to each measurement. $M_{n,SEC}$ = 45,400 (THF), $Đ$ = 1.04 (THF), $conv._{olefin}$ = 87%.

3.6.2 Additional data

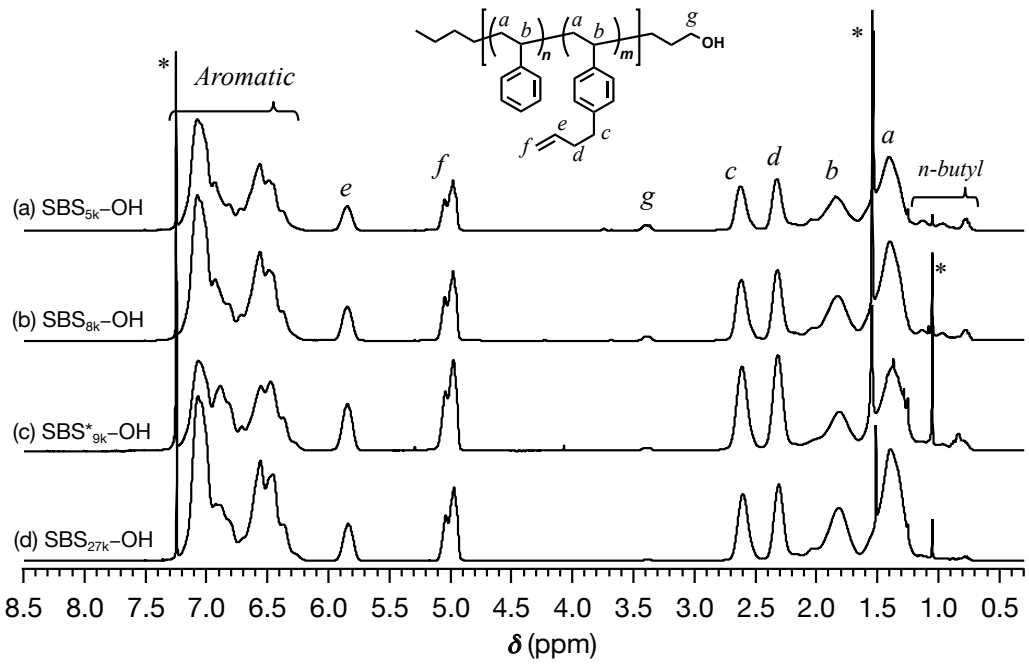

Figure S3.1. ^{1}H NMR spectra of (a) SBS_{5k}–OH, (b) SBS_{8k}–OH, (c) SBS^{*}_{9k}–OH, and (d) SBS_{27k}–OH in $CDCl_3$ (400 MHz).

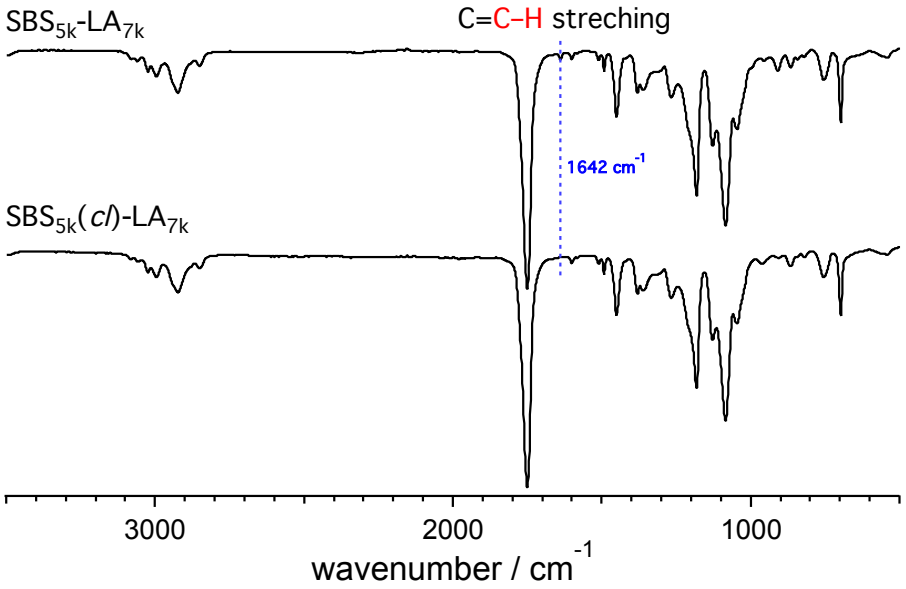

Figure S3.2. IR spectra of SBS_{5k}–LA_{7k} (upper) and SBS_{5k}(*cl*)–LA_{7k} (lower).

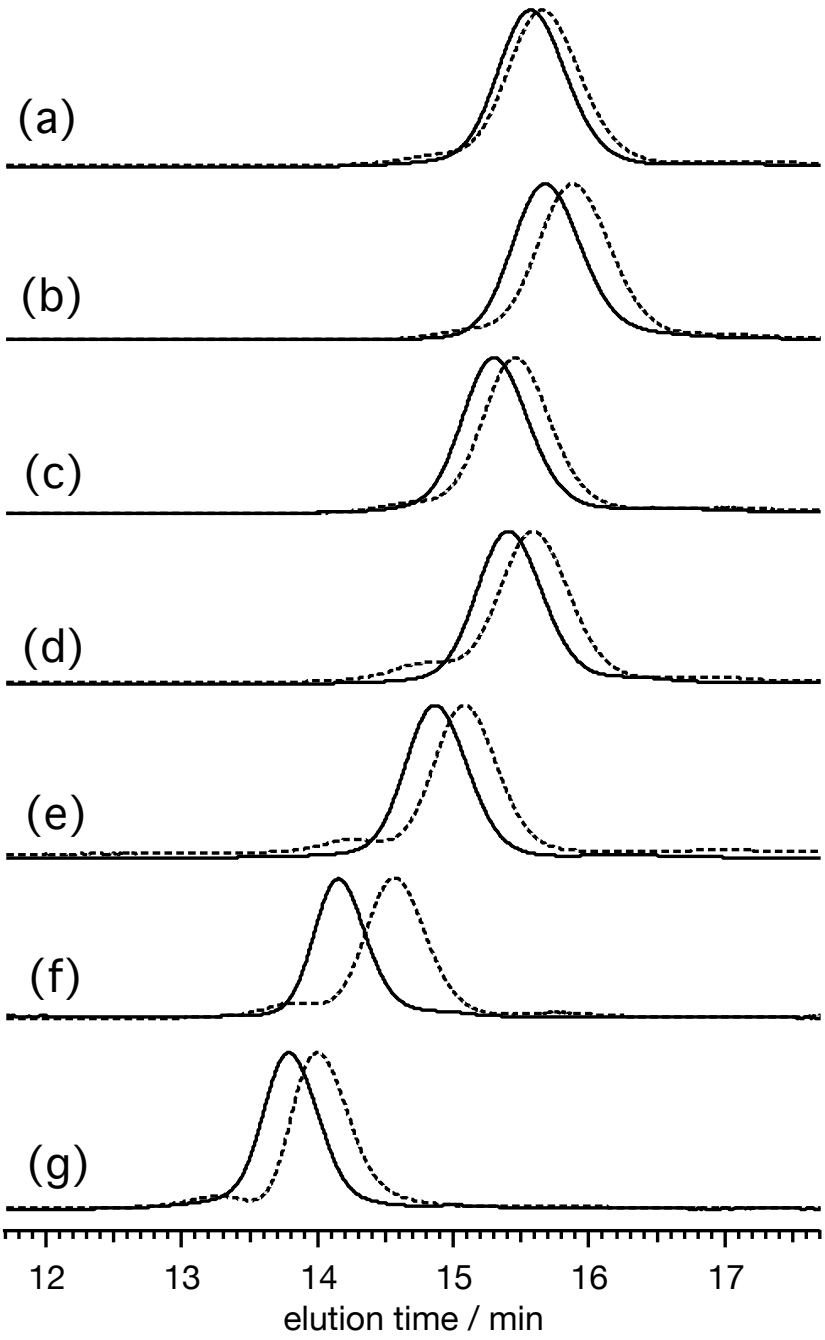

Figure S3.3. SEC traces of (a) SBS_{5k}–LA_{7k} and SBS_{5k}(*cl*)–LA_{7k}, (b) SBS_{8k}–LA_{5k} and SBS_{8k}(*cl*)–LA_{5k}, (c) SBS_{8k}–LA_{8k} and SBS_{8k}(*cl*)–LA_{8k}, (d) SBS^{*}_{9k}–LA_{6k} and SBS^{*}_{9k}(*cl*)–LA_{6k}, (e) SBS^{*}_{9k}–LA_{11k} and SBS^{*}_{9k}(*cl*)–LA_{11k}, (f) SBS_{27k}–LA_{13k} and SBS_{27k}(*cl*)–LA_{13k}, and (g) SBS_{27k}–LA_{28k} and SBS_{27k}(*cl*)–LA_{28k} (eluent, THF; flow rate, 1.0 mL min^{-1}). SBS–LAs and the corresponding SBS(*cl*)–LAs are presented using solid and dashed lines, respectively. SEC traces for SBS(*cl*)–LAs were obtained before preparative SEC purification.

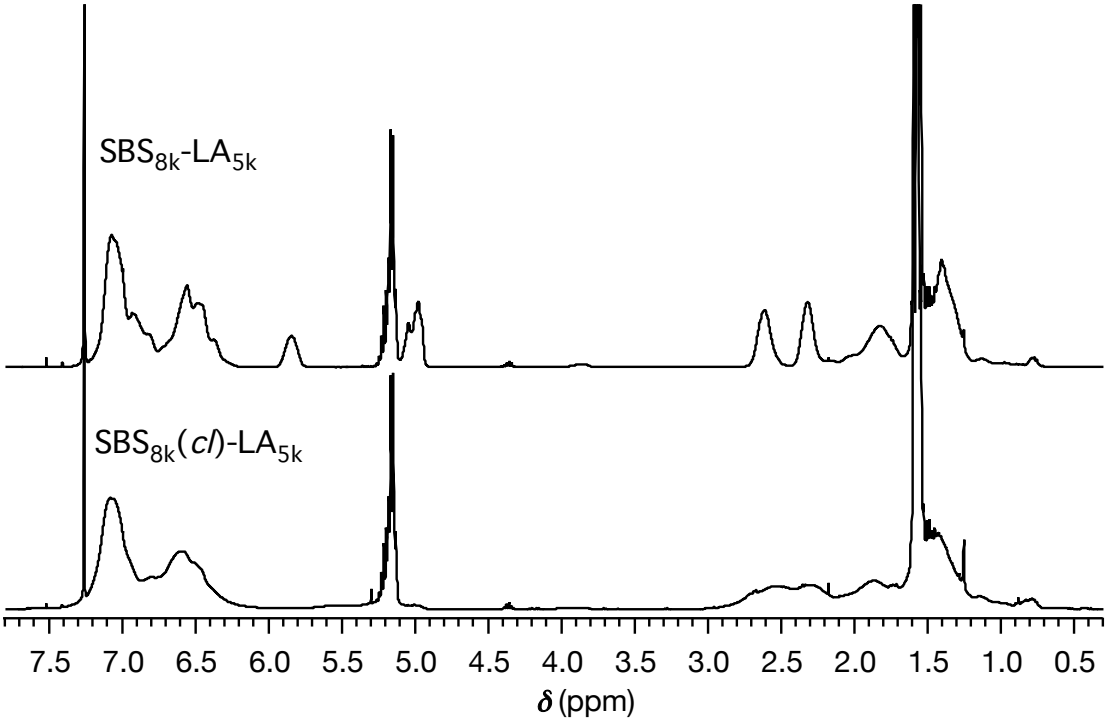

Figure S3.4. ^{1}H NMR spectra of SBS_{8k}–LA_{5k} (upper) and SBS_{8k}(*cl*)–LA_{5k} (lower) in $CDCl_3$ (400 MHz).

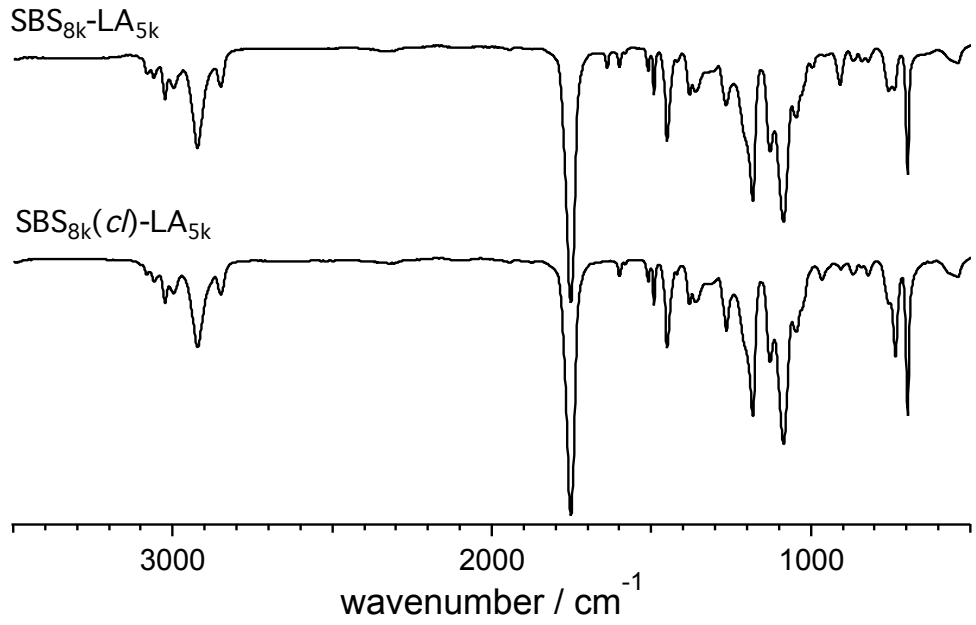

Figure S3.5. IR spectra of SBS_{8k}–LA_{5k} (upper) and SBS_{8k}(*cl*)–LA_{5k} (lower).

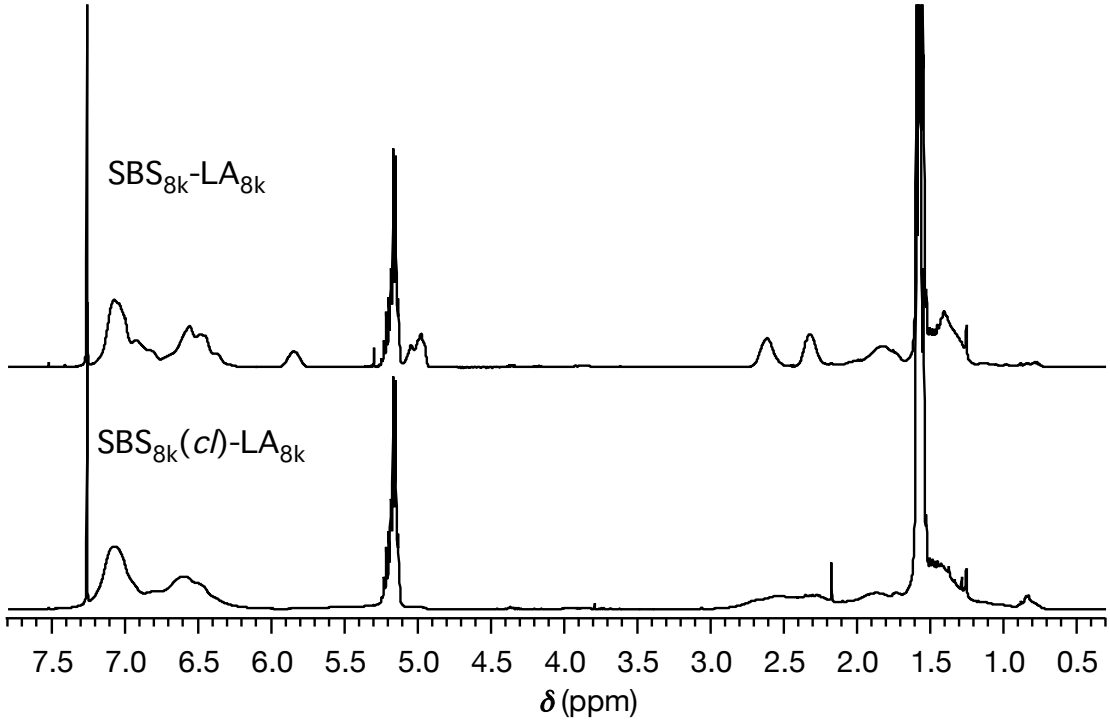

Figure S3.6. ^{1}H NMR spectra of SBS_{8k}–LA_{8k} (upper) and SBS_{8k}(*cl*)–LA_{8k} (lower) in $CDCl_3$ (400 MHz).

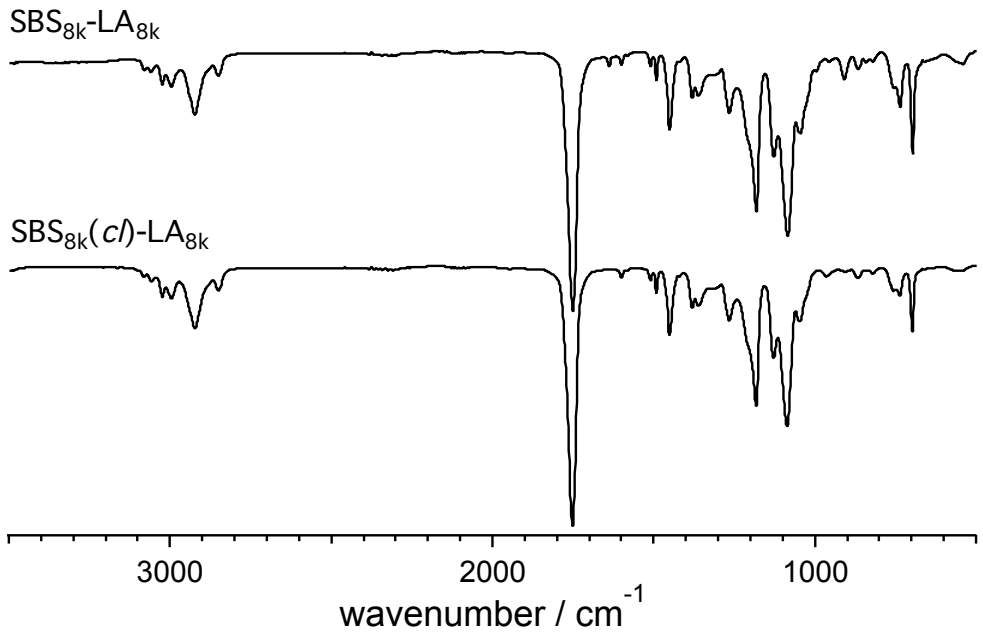

Figure S3.7. IR spectra of SBS_{8k}–LA_{8k} (upper) and SBS_{8k}(*cl*)–LA_{8k} (lower).

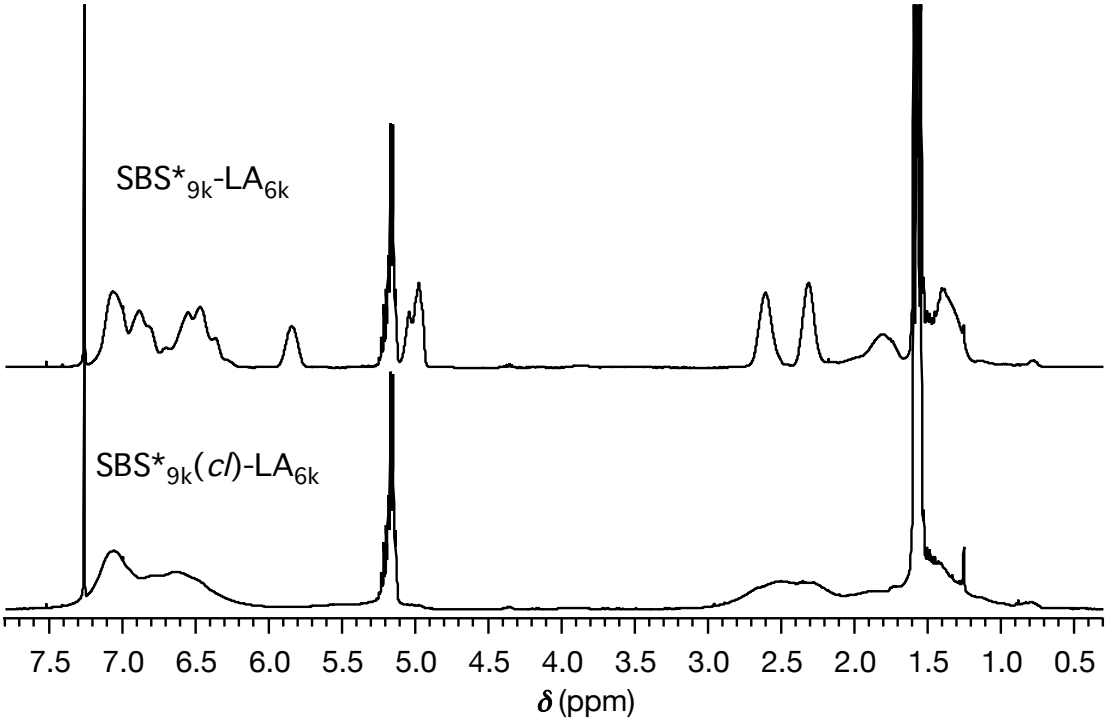

Figure S3.8. ^{1}H NMR spectra of SBS$^{*}_{9k}$–LA$_{6k}$ (upper) and SBS$^{*}_{9k}$(*cl*)–LA$_{6k}$ (lower) in $CDCl_3$ (400 MHz).

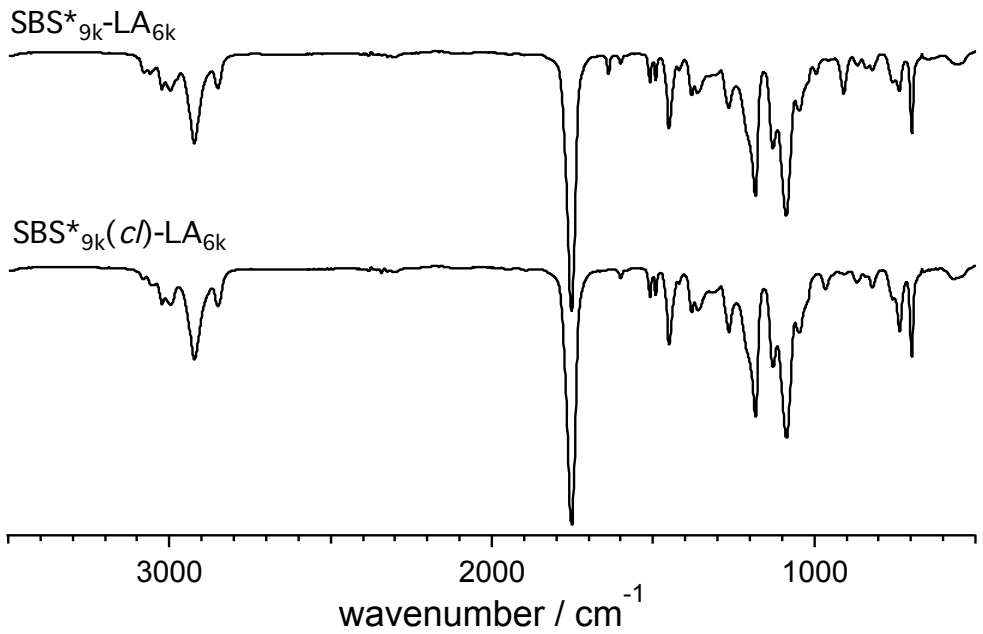

Figure S3.9. IR spectra of SBS$^{*}_{9k}$–LA$_{6k}$ (upper) and SBS$^{*}_{9k}$(*cl*)–LA$_{6k}$ (lower).

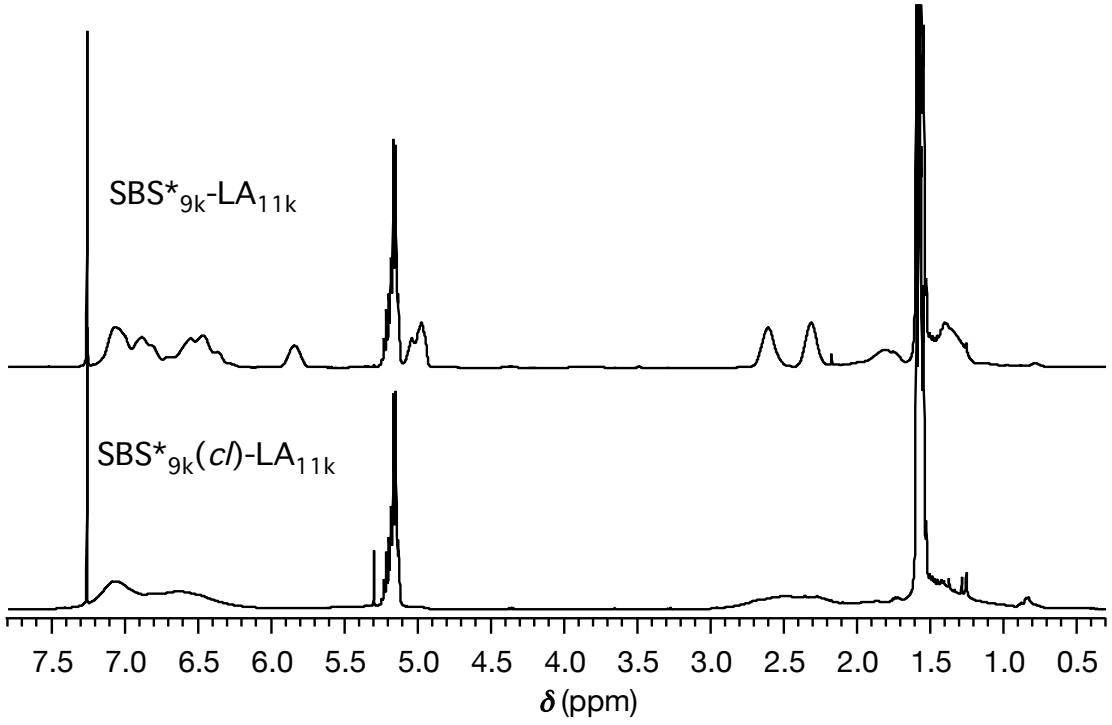

Figure S3.10. ^{1}H NMR spectra of SBS$^{*}_{9k}$–LA$_{11k}$ (upper) and SBS$^{*}_{9k}$(*cl*)–LA$_{11k}$ (lower) in $CDCl_3$ (400 MHz).

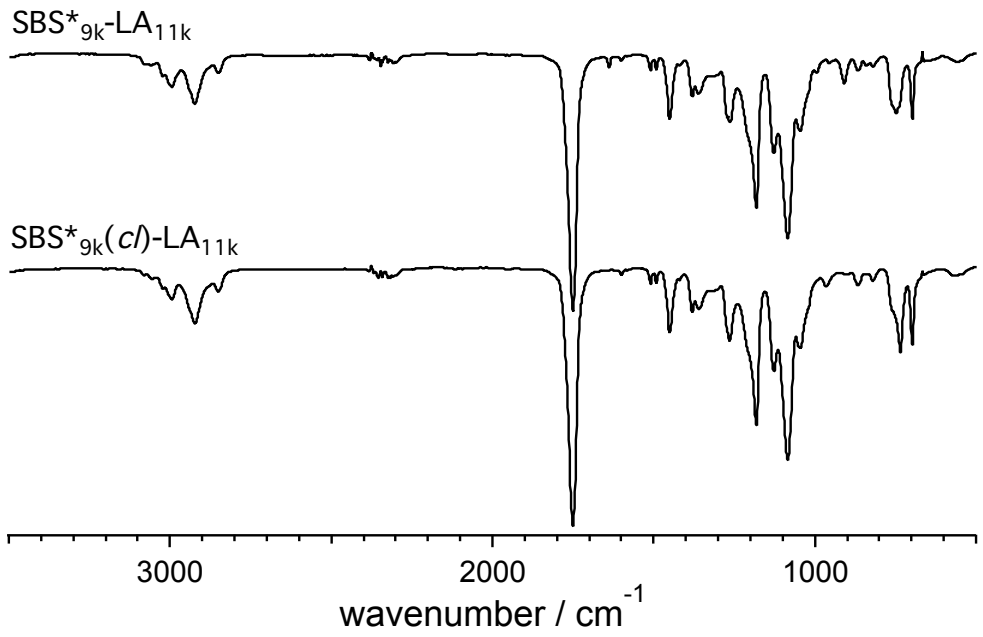

Figure S3.11. IR spectra of SBS$^{*}_{9k}$–LA$_{11k}$ (upper) and SBS$^{*}_{9k}$(*cl*)–LA$_{11k}$ (lower).

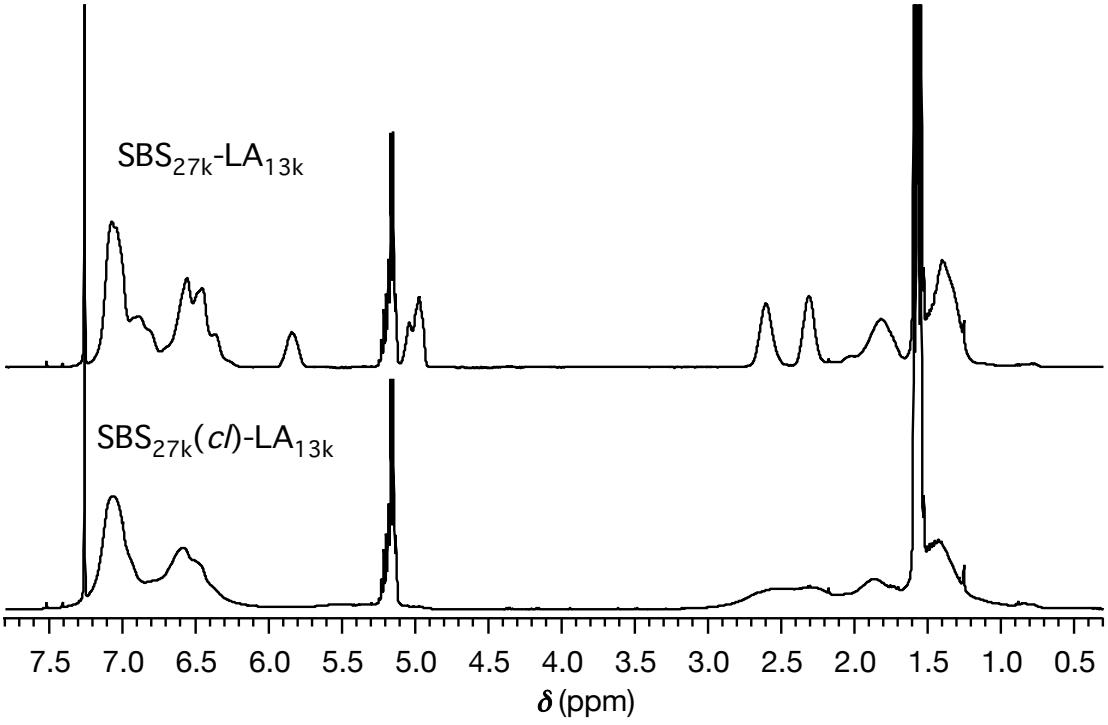

Figure S3.12. ^{1}H NMR spectra of SBS_{27k}–LA_{13k} (upper) and SBS_{27k}(*cl*)–LA_{13k} (lower) in $CDCl_3$ (400 MHz).

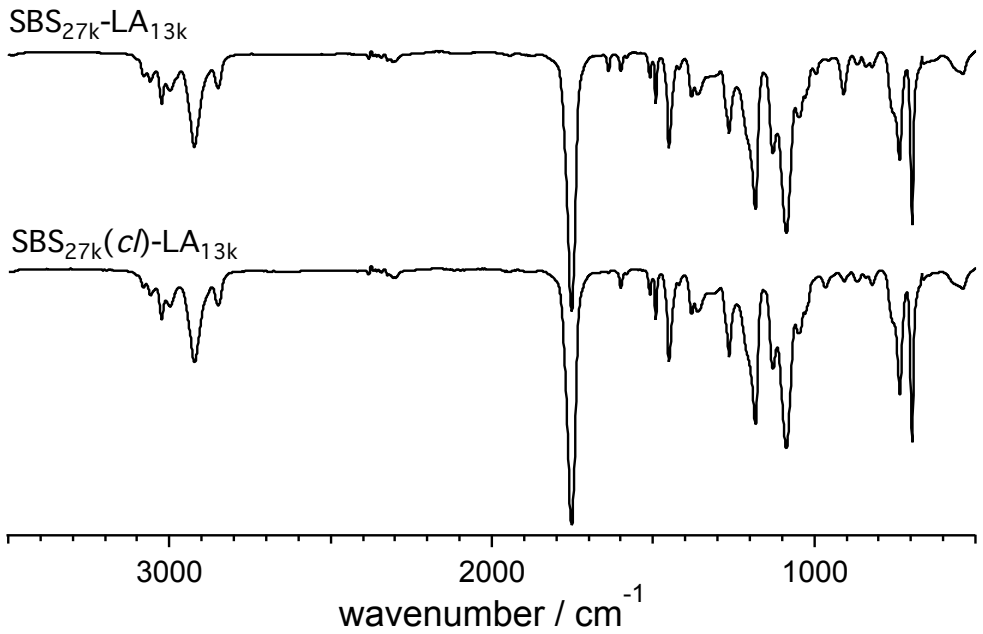

Figure S3.13. IR spectra of SBS_{27k}–LA_{13k} (upper) and SBS_{27k}(*cl*)–LA_{13k} (lower).

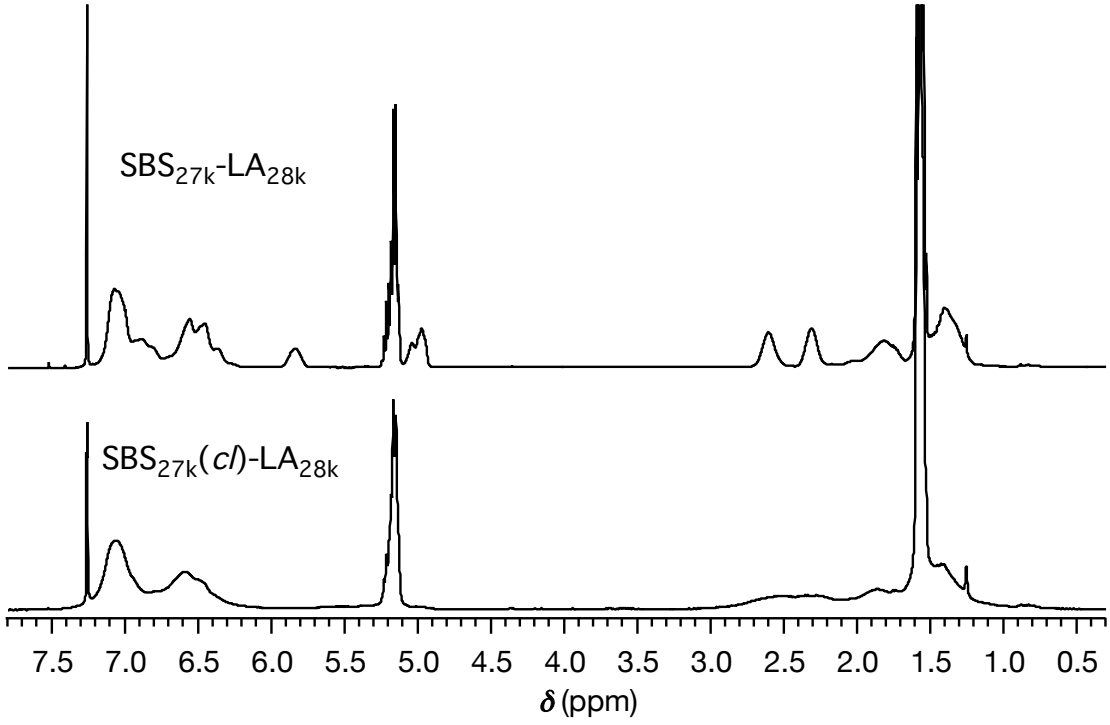

Figure S3.14. ^{1}H NMR spectra of SBS_{27k}–LA_{28k} (upper) and SBS_{27k}(*cl*)–LA_{28k} (lower) in $CDCl_3$ (400 MHz).

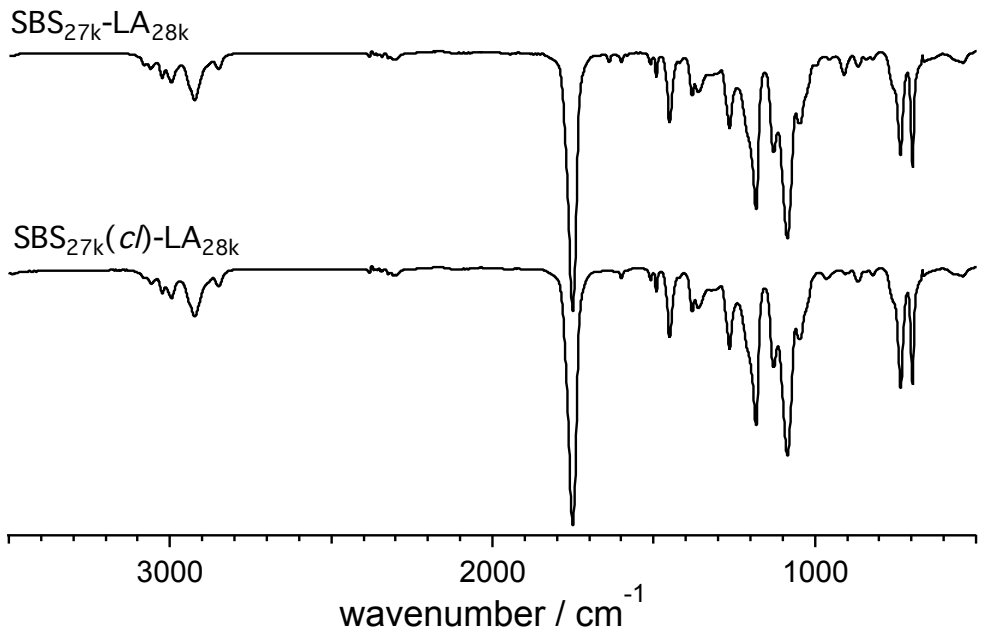

Figure S3.15. IR spectra of SBS_{27k}–LA_{28k} (upper) and SBS_{27k}(*cl*)–LA_{28k} (lower).

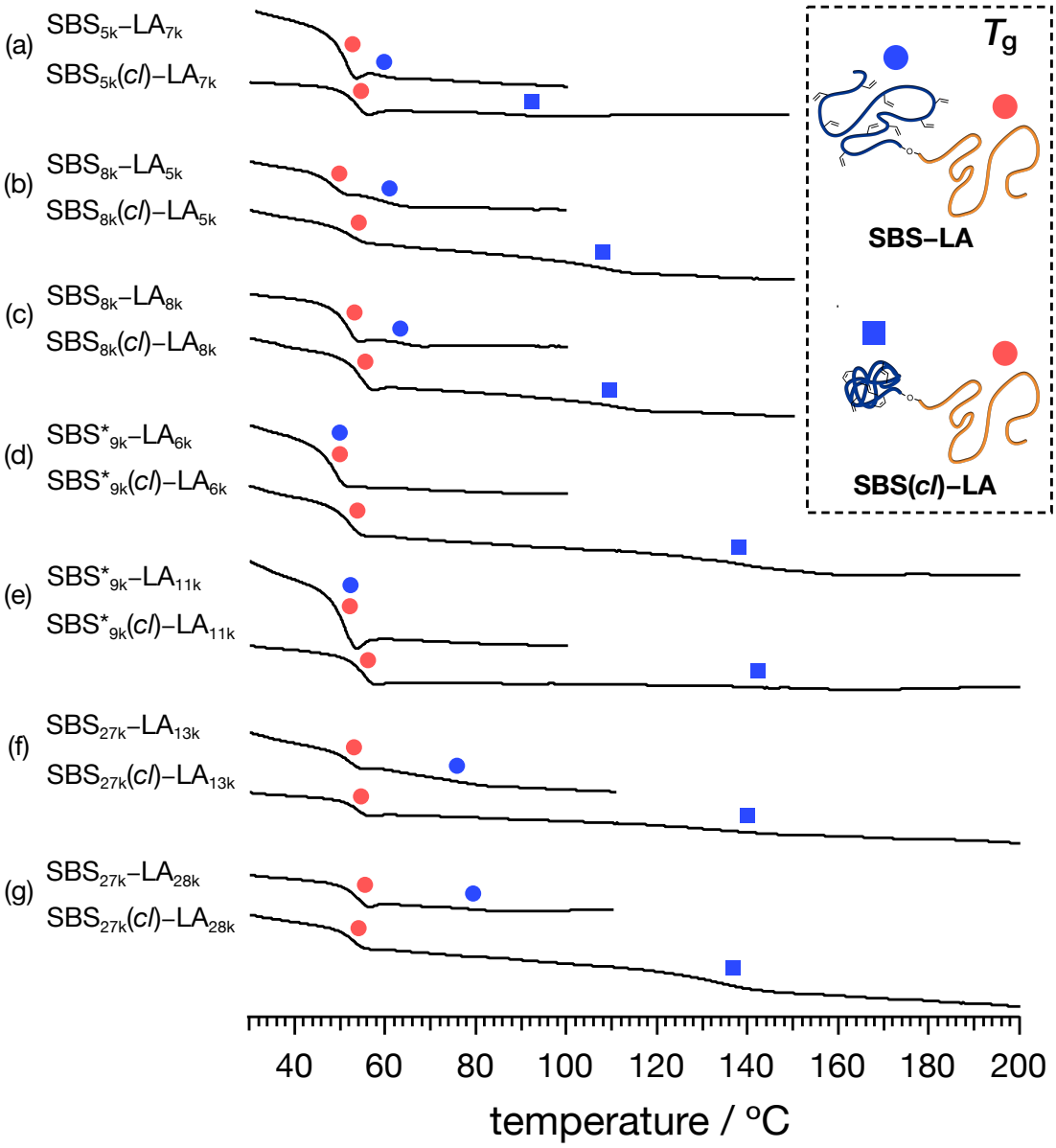

Figure S3.16. DSC curves during the 2nd heating process of (a) SBS_{5k}–LA_{7k} and $SBS_{5k}(cl)$–LA_{7k}, (b) SBS_{8k}–LA_{5k} and $SBS_{8k}(cl)$–LA_{5k}, (c) SBS_{8k}–LA_{8k} and $SBS_{8k}(cl)$–LA_{8k}, (d) SBS^{*}_{9k}–LA_{6k} and $SBS^{*}_{9k}(cl)$–LA_{6k}, (e) SBS^{*}_{9k}–LA_{11k} and $SBS^{*}_{9k}(cl)$–LA_{11k}, (f) SBS_{27k}–LA_{13k} and $SBS_{27k}(cl)$–LA_{13k}, and (g) SBS_{27k}–LA_{28k} and $SBS_{27k}(cl)$–LA_{28k}. The red circle, blue circle, and blue square denote the T_g of LA, SBS, and SBS(*cl*) blocks, respectively.

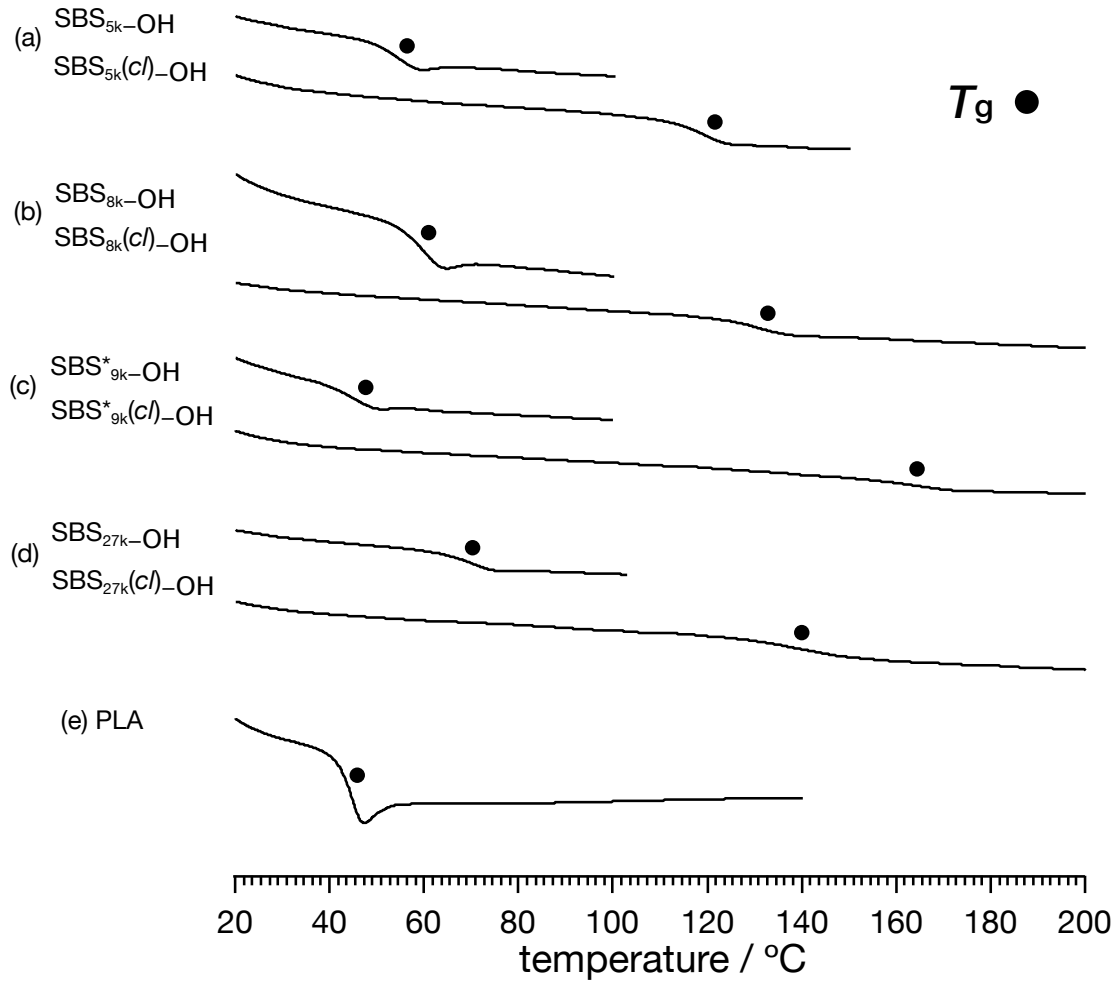

Figure S3.17. DSC curves during the 2nd heating process of (a) SBS_{5k}–OH and SBS_{5k}(*cl*)–OH, (b) SBS_{8k}–OH and SBS_{8k}(*cl*)–OH, (c) SBS^{*}_{9k}–OH and SBS^{*}_{9k}(*cl*)–OH, (d) SBS_{27k}–OH and SBS_{27k}(*cl*)–OH, and (g) PLA. The black circle denotes the T_g of each polymer.

Table S3.1 Characterization data for SBS−OHs, SBS(*cl*)−OHs, and PLA

sample name	conv.$_{olefin}$ (%)[a]	$M_{n,SEC}$[b]	$M_{p,SEC}$[b]	$Đ$[b]	$\langle G \rangle$[c]	T_g (°C)[d]
SBS_{5k}−OH		4,730	5,360	1.08		55
SBS_{5k}(*cl*)−OH	92	4,050	4,250	1.10	0.79	119
SBS_{8k}−OH		6,910	7,290	1.04		60
SBS_{8k}(*cl*)−OH	87	5,300	5,480	1.05	0.75	130
SBS^{*}_{9k}−OH		8,250	8,510	1.04		46
SBS^{*}_{9k}(*cl*)−OH	83	5,740	5,700	1.05	0.70	167
SBS_{27k}−OH		19,600	20,100	1.02		71
SBS_{27k}(*cl*)−OH	91	11,700	11,600	1.04	0.58	142
PLA		10,700		1.04		45

[a]Determined by ^{1}H NMR in $CDCl_3$. [b]Determined by SEC in THF using polystyrene standards. [c]Calculated by $M_{p,SEC}$(SBS(*cl*)−OH)/$M_{p,SEC}$(SBS−OH). [d]Determined by DSC at the heating rate of 10 °C min^{-1}.

3.6.3. References

1. H. Zhang and E. Ruckenstein, *Macromolecules*, 1999, **32**, 5495–5500.

2. J. Burdyńska, Y. Li, A. V. Aggarwal, S. Höger, S. S. Sheiko and K. Matyjaszewski, *J. Am. Chem. Soc.*, 2014, **136**, 12762–12770.

Chapter 4

Further Downsizing of Microphase-Separated Structures via One-Shot Intramolecular Crosslinking of Olefin-Containing Block Copolymer

4.1 Introduction

Microphase separation of block copolymers (BCPs) is of significant importance in the context of an application for the bottom-up BCP lithography technology.[1-5] Since the required size scale of a lithographic process is continuously miniaturized for the next-generation microelectronics industry, the realization of the BCP microphase-separated structures with an ultra-small domain-spacing (*d*) has been considered as one of the most crucial efforts.[6-10] A rational approach to minimize the *d* is reducing the BCP chain dimensions by applying the non-linear macromolecular architectures, such as branched[11-14] and cyclic ones[15-16], so that the resulting nanostructure could be essentially downsized without lowering the BCP molecular weight. For instance, Kakuchi et al. demonstrated that the much lower *d* value of the AB_3-type miktoarm BCP as compared to that of the linear AB diblock copolymer with the comparable molecular weight and block composition, i.e., $d(AB_3)$ = 9.8 nm and d(AB) = 14.0 nm, where the degree of downsizing ($1-d(AB_3)/d(AB)$) was estimated to be 30%.[11] Meanwhile, although the cyclization of the BCP molecule is also an effective strategy to reduce the BCP chain dimension, a recent simulation study suggested that the degree of downsizing is limited up to ca. 35%.[17]

In the previous chapter, the author successfully demonstrated an alternative and novel methodology to reduce the BCP chain dimension, that is, the intramolecular crosslinking of the BCPs.[18] Application of the intramolecular olefin metathesis to polystyrene-*block*-poly(*rac*-lactide)s (PS-*b*-PLAs) having the olefin side-chains in the PS block readily gave the crosslinked–linear BCP, by which the microphase-separated structures were downsized with the degree of downsizing up to 22%. For achieving a further downscaling, the dumbbell-like crosslinked–crosslinked BCPs, wherein the two distinct

blocks are separately crosslinked, should be highly promising. Indeed, Sawamoto et al.[19] and Chen et al.[20] have recently reported the "double crosslinking" protocols to realize these unique crosslinked–crosslinked architectures. However, since such protocols cause significant synthetic complications, including the selection of the two disparate crosslinking chemistries and/or the iterative crosslinking reactions, the synthesis of the crosslinked–crosslinked BCPs may not be feasible for practical applications. The author, thus, now highlights the "one-shot" intramolecular crosslinking of the BCP bearing one particular crosslinkable functionality along the whole chain, leading to a rapid and facile access to crosslinked–crosslinked BCPs. A very important hypothesis is that the spatially closer crosslinkable sites would preferentially react than farther ones even when the polymer chain behaves as a random coil. Under such a condition, the implementation of the one-shot crosslinking should result in the intramolecularly crosslinked product with two chemically compartmentalized spaces due to the preferential intrablock crosslinking, thus enabling the microphase-separated structures with a significantly smaller domain size as compared to that of the linear prepolymer.

In this study, the author designed the polystyrene-*block*-poly(glycolic acid), whose χ-value is slightly higher than that of PS-*b*-PLA, with the olefin side-chains distributed in both of the blocks (**Scheme 4.1**). The subsequent one-shot crosslinking of the linear BCP via the olefin metathesis reaction readily gave the corresponding crosslinked product with considerably small chain dimensions. Importantly, the block localization in the resultant molecule was successfully investigated by ^{1}H nuclear Overhauer effect difference spectroscopy in the solution state. The microphase separation behaviors of the obtained samples were finally explored using differential scanning calorimetry and small angle X-ray scattering analysis in the bulk state.

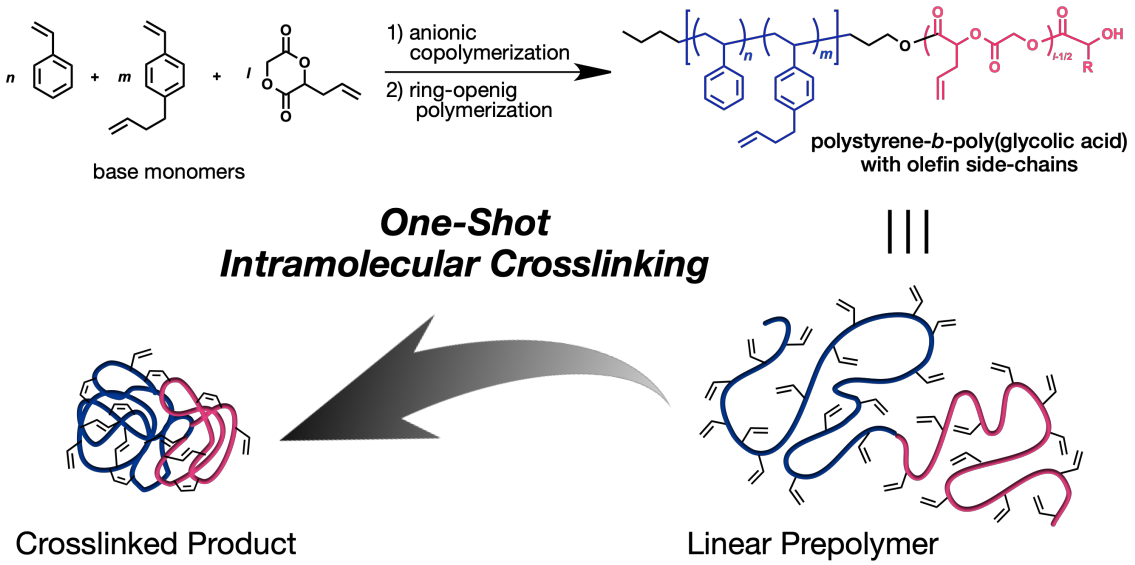

Scheme 4.1. Synthesis of polystyrene-*block*-poly(glycolic acid) with olefin side-chains in both of the blocks and subsequent "one-shot" intramolecular crosslinking.

4.2 Experimental Section

4.2.1 Materials

sec-Butyllithium (*sec*-BuLi; Kanto Chemical Co., Inc. (Kanto), 1.05 mol L^{-1} in *n*-hexane), *n*-butyllithium (*n*-BuLi; Kanto, 1.01 mol L^{-1} in *n*-hexane), tetrabutylammonium fluoride (TBAF; Tokyo Chemical Industry Co., Ltd. (TCI), 1.0 mol L^{-1} in THF), absolute benzene (Wako Pure Chemical Industries, Ltd., super dehydrated, >99.5%), benzoic acid (TCI, >99.0%), Grubbs 2nd generation catalyst (G2; Sigma-Aldrich Chemicals Co.), ethyl vinyl ether (TCI, >98.0%), glyoxylic acid (Sigma-Aldrich Chemicals Co., 50 wt% in H_2O), allyltributyltin (TCI, ca. 9 mol L^{-1} in water), bromoacetyl bromide (Sigma-Aldrich Chemicals Co., >98.0%), triethylamine (TEA; Kanto, >99.0%), *N,N*-dimethyl-4-aminopyridine (DMAP; TCI, >99.0%), sodium carbonate (Na_2CO_3; Kanto, >99.0%), acetonitrile (Kanto, >99.5%), and dry *N,N*-dimethylformamide (dry DMF; Kanto, >99.5%, water content, <0.001%) were purchased and used as received. Styrene (S; TCI, >99.0%) and 1,8-diazabicyclo[5.4.0]-7-undecene (DBU; TCI, >98.0%) were purchased and purified by distillation over CaH_2 under vacuum. *p*-3-Butenyl styrene (BS)[21] and (3-bromopropoxy)triisopropylsilane (Br–OTIPS)[22] was prepared according to the reported methods, then further purified by distillation over CaH_2 under vacuum. Commercially available dry THF (Kanto, >99.5%, water content, <0.001%), dry toluene (Kanto, >99.5%, water content, <0.001%), and dry CH_2Cl_2 (Kanto, >99.5%, water content, <0.001%) were further purified by an MBRAUN MB SPS Compact solvent purification system equipped with a MB-KOL-A and a MB-KOL-M Type 1 columns (for dry THF), a MB-KOL-C and a MB-KOL-A columns (for dry toluene), or two MB-KOL-A columns (for dry CH_2Cl_2) which were then directly used for the polymerizations.

4.2.2 Instruments

The ring-opening polymerization of 1,4-dioxane-2,5-dione (allylglycolide, AG) was carried out in an MBRAUN stainless steel glovebox equipped with a gas purification system (molecular sieves and copper catalyst) in a dry argon atmosphere (H_2O, O_2 <1 ppm). The moisture and oxygen contents in the glovebox were monitored by an MB-MO-SE 1 moisture sensor and an MB-OX-SE 1 oxygen sensor, respectively. The ^{1}H (400 MHz) and ^{13}C NMR (100 MHz) spectra were obtained using a JEOL JNM-ESC400 instrument at room temperature. ^{1}H nuclear Overhauser effect (NOE) difference spectra were obtained by irradiating the aromatic protons of polystyrene blocks (7.03 ppm) or α-methylene protons of polyglycolide blocks (4.77 ppm) in $CDCl_3$ at 50 °C. The number of scans was set at 256 (spectral width = 15 ppm). Other parameters for pulse were as follows: 90° pulse width = 6.6 μs; irradiation position (on-resonance) = 7.03 or 4.77 ppm; off-resonance = −10 ppm; irradiation time (NOE-building up) = 5 s; attenuator = 80 dB; data points = 16384; Relaxation delay = 7 s. The size exclusion chromatography (SEC) measurements were performed at 40 °C in THF (flow rate, 1.0 mL min^{-1}) using a Jasco high-performance liquid chromatography system (PU-980 Intelligent HPLC Pump, CO-2065 Plus Intelligent Column Oven, RI-2031 Plus Intelligent RI Detector, and DG-2080-53 Degasser) equipped with a Shodex KF-G guard column (4.6 mm × 10 mm; particle size, 8 μm) and two Shodex KF-804L columns (linear; particle size, 7 μm; 8.0 mm × 300 mm; exclusion limit, 4×10^4). Preparative SEC purification was performed in $CHCl_3$ (3.5 mL min^{-1}) at 23 °C using JAI LC-9201 equipped with a JAI JAIGEL-3H column (20 mm × 600 mm; exclusion limit, 7×10^4) and a JAI RI-50s refractive index detector. The Fourier transform infrared spectroscopy (FT-IR) analysis was carried out using a PerkinElmer Frontier MIR spectrometer equipped with a

single reflection diamond universal attenuated total reflection (ATR) accessory. Differential scanning calorimetry (DSC) experiments were performed using a Hitachi High-Technologies DSC7000X under a nitrogen atmosphere. All polymers for DSC measurement were heated to 200 °C, cooled to –50 °C, and heated to 200 °C again at the heating and cooling rate of 10 °C min^{-1} and 20 °C min^{-1}, respectively.

4.2.3 Synthesis of ω-end hydroxy-functionalized statistical copolymer of S and BS (SBS–OH).

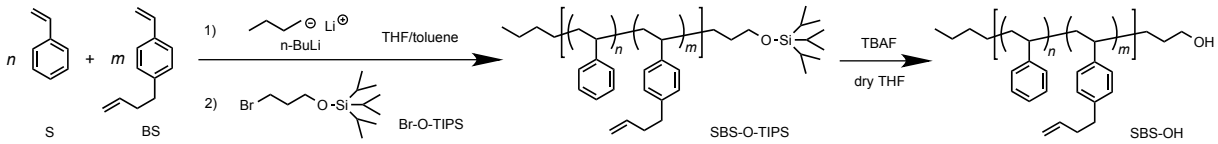

In the glovebox, dry toluene (100 mL) and dry THF (50 mL) were placed in a Schlenk flask. After sealing, the flask was taken out from the glovebox. *sec*-BuLi (100 μL, 105 μmol as a 1.05 mol L^{-1} stock solution in *n*-hexane) was added to the solvent under an Ar atmosphere to remove water completely. Then, the solvent was further purified by trap-to-trap distillation under high vacuum to transfer to another Schlenk flask for polymerization. After cooling to –78 °C, *n*-BuLi (920 μL, 787 μmol as a 0.86 mol L^{-1} stock solution in *n*-hexane) was added to the flask. In another flame-dried Schlenk flask, S (3.9 g, 37 mmol) and BS (5.9 g, 37 mmol) were mixed together under an Ar atmosphere. The mixture was added at once to the initiator solution using a syringe. After monomer addition, the mixture was stirred at −78 °C for 6 h. Br−O−TIPS (1.99 g, 6.73 mmol) was added to the solution of living polymer anions at −78 °C, and the whole mixture was allowed to react for 0.5 h at −78 °C and an additional 1 h at room temperature. Afterwards, the solvent was removed from the polymerization mixture

under reduced pressure. TBAF (20.2 mL, 20.2 mmol as a 1.0 mol L^{-1} stock solution in THF) and dry THF (30 mL) were added to the crude product at room temperature. After 15 h stirring, the reaction mixture was passed through a short silica-gel column, and the resulting residue was purified by repeated reprecipitation (at least twice) from the THF solution into MeOH to give SBS−OH as a white solid. Yield: 8.69 g (88.7%). ^{1}H NMR (400 MHz, $CDCl_3$): δ (ppm) 7.40−6.19 (m, 10H × n + 8H × m, −C_6H_{10}, −C_6H_8−), 5.97−5.74 (m, 1H × m, −CH= CH_2), 5.15−4.90 (m, 2H × m, −CH=CH_2), 3.47−3.33 (m, 2H, −CH_2OH), 2.85−2.45 (m, 2H × m, −C_6H_8CH_2−), 2.46−2.14 (m, 2H × m, −$C_6H_8CH_2CH_2$−), 2.15−1.62 (m, 1H × (n+m), −CH(C_6H_{10})−, −CH(C_6H_8−)−), 1.74−0.69 (m, 2H × (m+n) + 9H, −CH_2CH(C_6H_{10})−, −CH_2CH(C_6H_8−)−, n-butyl). $M_{n,NMR}$ = 12,400 ($CDCl_3$), the mole fraction of the BS units = 0.50, $M_{n,SEC}$ = 12,200 (THF), $Đ$ = 1.06 (THF).

4.2.4 Synthesis of block copolymer consisting of SBS and polyAG (SBS−AG) via ring-opening polymerization of AG using SBS−OH as an initiator.

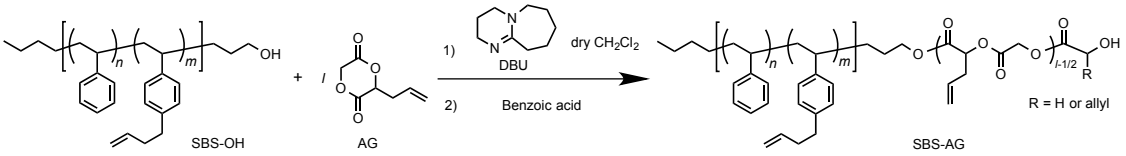

SBS−OH was freeze-dried from its absolute benzene solution three times prior to the polymerization. In the glovebox, SBS−OH ($M_{n,NMR}$ = 12,400, 600 mg, 48.4 μmol) and AG 877 mg, 5.61 mmol) were dissolved in dry CH_2Cl_2 (20.8 mL). DBU (1.12 μL, 112 μmol as 0.1 mol L^{-1} stock solution in CH_2Cl_2) was then added to the CH_2Cl_2 solution to initiate the polymerization. After 28 s, the polymerization was quenched by the addition of benzoic acid. The mixture was purified by reprecipitation from the CH_2Cl_2 solution into MeOH to give

SBS–AG as a white solid. The product was further purified by preparative SEC (Yield: 490 mg, 36.0%). ^{1}H NMR (400 MHz, $CDCl_3$): δ (ppm) 7.37–6.18 (m, 5H × n + 4H × m, –C_6H_5, –C_6H_4–), 6.02–5.69 (m, 1H × l + 1H × m, –$CHCH_2CH{=}CH_2$, –$C_6H_4CH_2CH_2CH{=}CH_2$), 5.48–5.08 (m, 3H × l, –$CHCH_2CH{=}CH_2$, –$CHCH_2CH{=}CH_2$), 5.12–4.88 (m, 2H × m, –$CHCH_2CH{=}CH_2$), 4.94–4.61 (m, 2H × l, –$OCOCH_2O$–), 3.50–3.39 (br, 2H, –CH_2OH), 2.92–2.43 (m, 2H × (l + m), –$CHCH_2CH{=}CH_2$, –$C_6H_4CH_2$–), 2.43–2.19 (m, 2H × m, –$C_6H_4CH_2CH_2$–), 2.13–1.64 (m, 1H × (n + m), –CHC_6H_5, –$CHC_6H_4CH_2$–), 1.64–0.70 (m, 2H × (n + m) + 9H, –$CH_2CHC_6H_5$, –$CH_2CHC_6H_4CH_2$–, n-butyl). Conversion = 87%, $M_{n,NMR}$ = 11,000 ($CDCl_3$), the weight fraction of SBS = 0.59, $M_{n,SEC}$ = 24,900 (THF), $Đ$ = 1.08 (THF).

4.2.5 Intramolecular crosslinking of SBS–AG via olefin metathesis reaction.

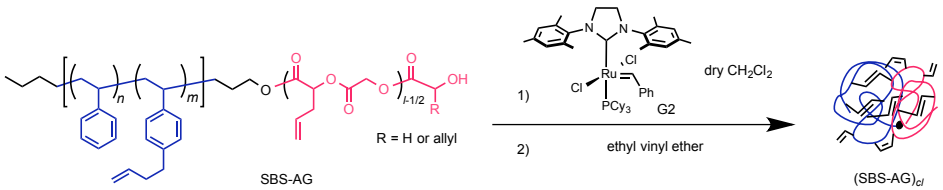

SBS–AG ($M_{n,NMR}$ = 21,100, 320 mg, 1.44 mmol olefin-containing units) was dissolved in dry CH_2Cl_2 (1,000 mL). After degassing by Ar bubbling, G2 (13.5 mg, 15.8 μmol) was added to the mixture. After stirring for 2 h under an Ar atmosphere at room temperature, the reaction was quenched by the addition of ethyl vinyl ether. The solvent was removed by evaporation, then the residue was purified by reprecipitation from the CH_2Cl_2 solution into MeOH to give intramolecularly crosslinked SBS–AG ($(SBS–AG)_{cl}$) as a white solid (177 mg, 78.7%). $M_{n,SEC}$ = 12,300 (THF), $Đ$ = 1.07 (THF), the conversion of the terminal olefins = 85% (^{1}H NMR in $CDCl_3$).

4.2.6 Small angle X-ray scattering (SAXS) experiments in solution and bulk state

SAXS experiments in solution state. The solution SAXS experiments were performed on the 4C beamline at the Pohang Accelerator Laboratory (PAL) in the Pohang University of Science and Technology (POSTECH, Pohang, Korea) at room temperature using X-ray beams (λ = 0.0756 nm) with an exposure time of 60 s. The two-dimensional scattering patterns were collected by a Rayonix 2D Mar (Rayonix L.L.C.), where the sample-to-detector distance was set to 4 m and 1 m. The scattering angle (θ) was calibrated using silver behenate (Tokyo Chemical Industry Co., Ltd.) as the standard. The 2D scattering data were circularly averaged with respect to the beam center and normalized to the intensity of the transmitted X-ray beam monitored via a scintillation counter positioned behind the sample. The scattering data were further corrected for the scattering due to the solvent. The sample solutions were loaded into a glass capillary (Hampton Research, quartz capillary tube, 1.0 mm diameter).

SAXS experiments in bulk state. The morphologies and *d* values of samples in the bulk state were investigated using SAXS in bulk state. The experiments were performed on the 4C beamline at the PAL using X-ray beams with λ = 0.00756 nm. The two-dimensional scattering patterns were collected by a Rayonix 2D Mar (Rayonix L.L.C.), where the sample-to-detector distance was set to 4 m. The scattering angle (θ) was calibrated using silver behenate (Tokyo Chemical Industry Co., Ltd.) as the standard and subsequently converted to the scattering vector (q) using Bragg's equation ($q = (4\pi/\lambda)\sin(\theta/2)$). The *d* values of the samples were calculated according to $d = 2\pi/q^*$, where q^* is the principal scattering peak position. The sample powders were annealed in the vapor of THF to induce the microphase separation. In a closed glass desiccator (ca. 3.0 L), the samples were positioned above the

surface of THF (30 mL) placed in a reservoir for 4 h at 20 °C. The samples taken out from the desiccator were allowed to dry at 20 °C and then put into a glass capillary (Hilgenberg, Mark-tube, lindemann glass, 2.0 mm diameter).

4.3 Results and Discussion

4.3.1 One-shot crosslinking of BCP bearing olefins in both blocks

The author has synthesized the linear BCP bearing the crosslinkable olefins (accounting for 50% of the monomer units) along both the block segments, *i.e.*, poly[styrene-*st*-(*p*-3-butenyl styrene)]-*b*-poly(allylglycolide), abbreviated as SBS−AG ($M_{n,SBS}$ = 12,400, $M_{n,AG}$ = 8,700, weight fraction of SBS block (F_{SBS}) = 0.59). Subsequently, the obtained BCP was subjected to the intramolecular olefin metathesis reaction using Grubbs' 2nd generation catalyst (G2) ($[SBS-AG]_0$ = 0.30 g L^{-1}, $[G2]_0/[BS\ unit]_0$ = 0.01), giving the corresponding intramolecularly crosslinked product, *i.e.*, $(SBS-AG)_{cl}$, with the olefin conversion of 85%, as revealed by ^{1}H nuclear magnetic resonance (NMR) and infrared (IR) spectroscopies (**Figures 4.4**(a) and **4.1**). A size exclusion chromatography (SEC) study confirmed that the peak-top molecular weight of $(SBS-AG)_{cl}$ ($M_{p,SEC}$ = 11,700) was much lower than that of the linear prepolymer ($M_{p,SEC}$ = 23,800), indicative of the remarkable reduction in the hydrodynamic volume (**Figure 4.2**). Surprisingly, the SEC trace of $(SBS-AG)_{cl}$ exhibited the monomodal peak without broadening of the $Đ$ value. Considering that an increase in the $Đ$ value is commonly observed upon intramolecular crosslinking, the successful result of the above reaction seems to be highly exceptional.

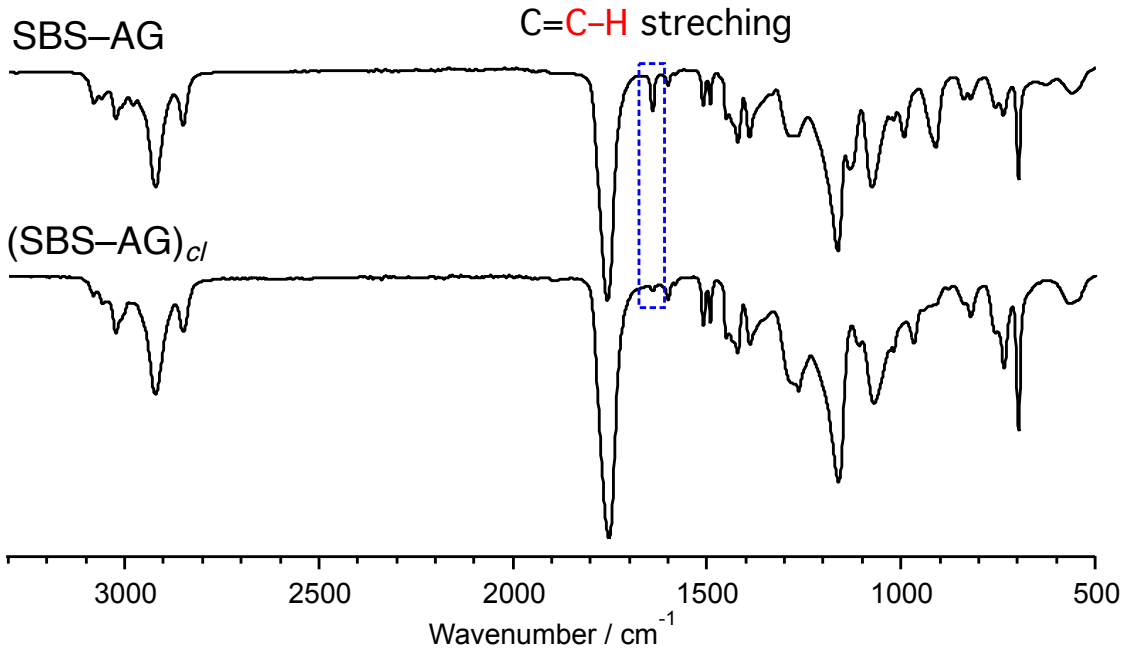

Figure 4.1. IR spectra of SBS–AG (upper) and $(SBS–AG)_{cl}$ (lower).

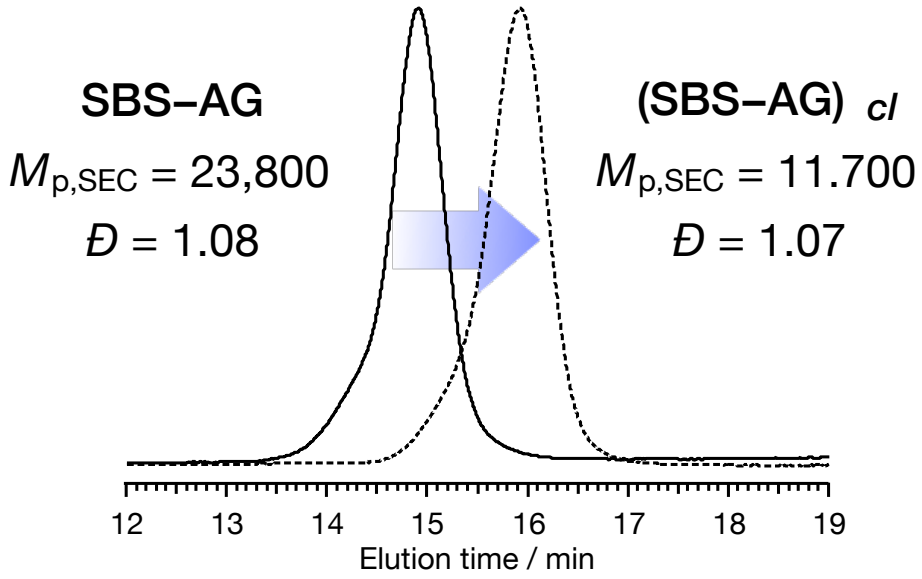

Figure 4.2. SEC traces of SBS–AG (solid line) and $(SBS–AG)_{cl}$ (dashed line) (eluent, THF; flow rate, 1.0 mL min^{-1}).

4.3.2 Characterization in solution state

In order to deeply evaluate the compactness of the obtained (SBS−AG)$_{cl}$, a transmission small-angle X-ray scattering (SAXS) measurement was carried out on the diluted DMF solution (3 wt%) at room temperature using synchrotron radiation. The obtained solution SAXS profile of (SBS−AG)$_{cl}$ exhibited a steeper decay of the scattering intensity ($I(q)$) in the middle-q region as compared to that of SBS−AG (**Figure 4.3**(a)), which is clearly emphasized by the Kratky plot analysis (**Figure 4.3**(b), see Supporting Information for detail). The Kratky plot of the linear SBS−AG exhibited a plateau-like region at 0.10 Å^{-1} < q < 0.20 Å^{-1}, which is indicative of the unfolded chain with a Gaussian random coil conformation. The increase in $q^2I(q)$ in the high-q regime presumably arose from the insufficient background subtraction from the original SAXS data and/or the additional scattering in the Porod regime. For (SBS−AG)$_{cl}$, on the other hand, a characteristic peak obviously appeared at around q = 0.1 Å^{-1}, although the $q^2I(q)$ increasing in the high-q region was observed due to the same reason. The shape of the Kratky plot strongly suggests that (SBS−AG)$_{cl}$ possesses the compact and folded chain conformation. Moreover, by Guinier analysis of the SAXS data (Guinier's low: ln $I(q) \sim -(R_g^2/3)q^2$, **Figure 4.3**(c), see Supporting Information for detail), the radius of gyrations (R_gs) of SBS−AG and (SBS−AG)$_{cl}$ were estimated to be 3.1 and 2.2 nm, respectively, which again confirmed the remarkable reduction in the hydrodynamic volume. These explained results, thus, clearly suggests the significantly compact chain state of the intramolecularly crosslinked (SBS−AG)$_{cl}$.

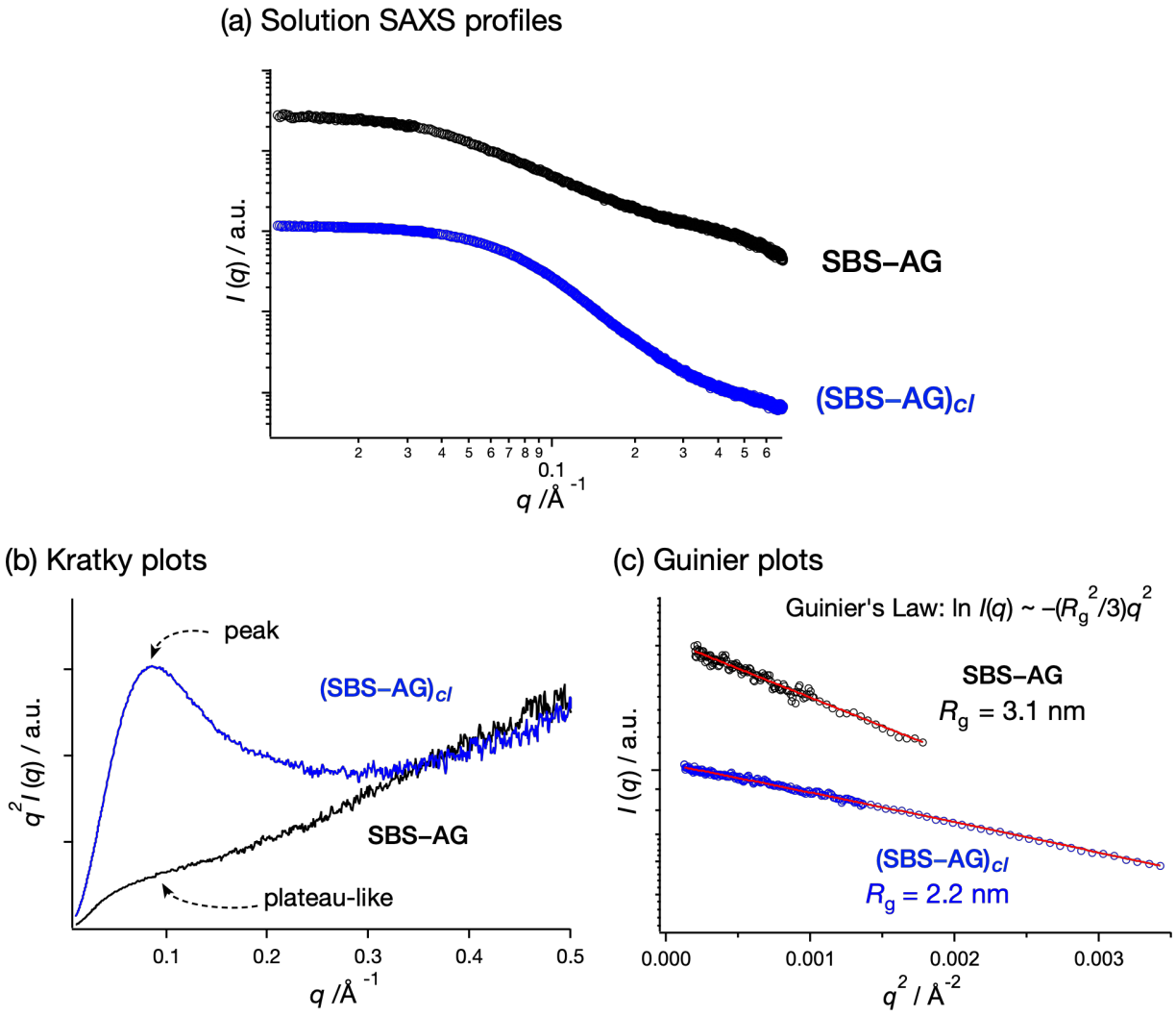

Figure 4.3. (a) Solution SAXS profiles of SBS–AG (black) and $(SBS–AG)_{cl}$ (blue). (b) Kratky and (c) Guinier plots were obtained from the corresponding SAXS profiles. The *I*(q) data in (a) and (c) were vertically shifted by multiplying arbitrary constants.

The importance here is to understand the localization of each segment in such a tightly crosslinked and compactly folded BCP molecule in order to evaluate the validity of the author's hypothesis; i.e., the two block segments should be compartmentalized in the obtained product. In order to access this issue, the author employed ^{1}H nuclear Overhauer effect (NOE) difference spectroscopy, which provides information about the average local distance between

the certain protons. **Figure 4.4** shows the ^{1}H NOE difference spectra obtained by irradiating the *d,e* and *p* protons in the SBS and AG blocks, respectively, and the corresponding ^{1}H NMR spectra of SBS–AG and $(SBS–AG)_{cl}$. Generally, the intensity of the ^{1}H NOE signals reflects the distance between a proton and the irradiated proton.[23] No significant enhancement in the ^{1}H NOE signals was confirmed for the linear SBS–AG in both of the irradiation cases, which is typical for the linear random coil polymers.[19] On the contrary, the ^{1}H NOE difference spectra of $(SBS–AG)_{cl}$ clearly exhibited strong signals (see colored squares in **Figure 4.4**(b)(c)); the NOE signals were distinctly enhanced in the SBS and AG blocks upon irradiating the *d,e* and *p* protons, respectively. This result clearly suggests that the local distance of the protons within each block turned out to be much closer upon the intramolecular crosslinking, which again confirms the highly compact chain conformation of $(SBS–AG)_{cl}$. Strikingly, in both of the irradiation cases, there is no observable ^{1}H NOE signals corresponding to the interaction of the protons between the block segments, which is clear evidence that the SBS and AG blocks were localized in the separated compartments in the intramolecularly crosslinked product. Given that the olefin metathesis reaction randomly occurred along the BCP molecule, the ^{1}H NOE signals should be observed for all the protons in the BCP molecule irrespective to the block segment. This discovery, thus, strongly suggests that the crosslinking reaction took place from the spatially close olefin pairs; in other words, it predominantly occurred within each block, and eventually resulted in the block compartmentalization. This assumption is definitely supported by a recent report by Tezuka et al., in which the reactivity of the identical crosslinkers periodically positioned along the polymer chain was extensively examined.[24] Since the architecture of $(SBS–AG)_{cl}$, including the folded, compact, and chemically compartmentalized structure, is reminiscent of the Janus

particles consisting of two disparate components,[25,26] the author labeled this unique nano-object as the "Janus BCP particle".

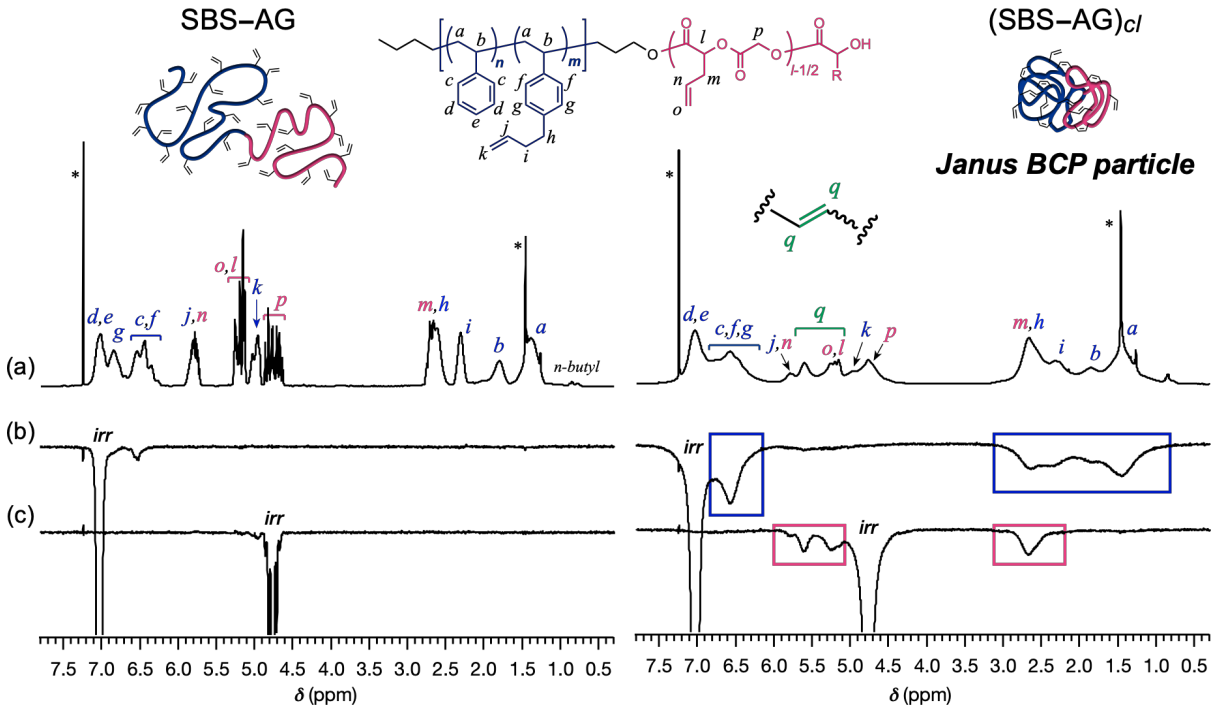

Figure 4.4. (a) ^{1}H NMR and (b)(c) ^{1}H NOE difference spectra of SBS–AG (left) and $(SBS–AG)_{cl}$ (right) in $CDCl_3$ at 50°C (400 MHz). ^{1}H NOE difference spectra were obtained by irradiating the (b) *d,e* and (c) *p* protons. Colored squares indicate the ^{1}H NOE signals.

4.3.3 Microphase separation in bulk

As the generation of a unique Janus BCP particle (Janus (SBS–AG)$_{cl}$) was successfully revealed by all the studies in the solution state as already described, the author then focused on their self-assembly behaviors in the bulk state. First, a differential scanning calorimetry (DSC) study was carried out to capture the thermal properties of the samples. Two different baseline shifts corresponding to the glass transition of each block were observed in both the DSC curves of the linear SBS–AG and Janus (SBS–AG)$_{cl}$, indicative of the microphase separation (**Figure 4.5**). Remarkably, the glass transition temperatures (T_gs) increased more than 100 °C after the intramolecular crosslinking ($T_{g,SBS}$: 64→177°C, $T_{g,AG}$: 18→144°C), revealing the tightly constrained chain nature of Janus (SBS–AG)$_{cl}$. The high T_g provides a material with an excellent thermal stability, which is essential for the lithographic process at high temperature.

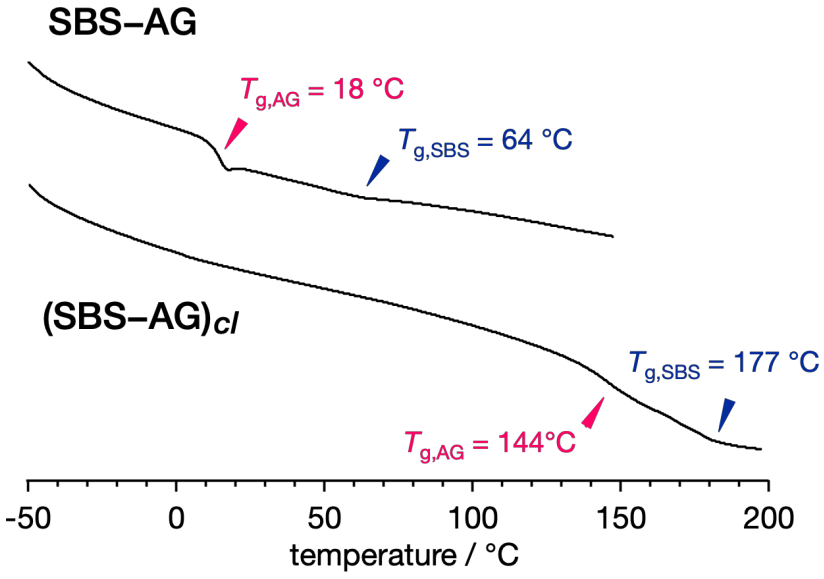

Figure 4.5. DSC curves during the 2nd heating process of SBS–AG (upper) and (SBS–AG)$_{cl}$ (lower).

The author finally investigated the bulk state morphology by the SAXS analysis of the bulk samples. Since the T_gs of (SBS–AG)$_{cl}$ were found to be considerably high ($T_{g,SBS}$ = 177 °C, $T_{g,AG}$ = 144 °C), the solvent vapor annealing using THF was employed for both of the samples to avoid any unwanted side reactions by the common thermal annealing. As can be seen in **Figure 4.6**(a), the SAXS profile of the linear SBS–AG exhibited a principal scattering peak at q^* of 0.262 nm^{-1} as well as the higher-ordered scattering peaks at the relative q-values of 2: √7, indicative of a hexagonally close-packed cylinder (HEX) structure. The domain-spacing (d) value was calculated to be 24.0 nm based on the relationship of $d = 2\pi/q^*$. For Janus (SBS–AG)$_{cl}$, although the scattering peaks are broad compared to the linear one, two scattering peaks at the relative q-values of 1: 2 were observed in the SAXS profile, indicating the formation of a microphase-separated structure (**Figure 4.6**(b)). Considering no difference in the block composition before and after the intramolecular crosslinking, this SAXS pattern should be assigned to the HEX. The ability of Janus (SBS–AG)$_{cl}$ to produce an ordered nanostructure again demonstrated the separated localization of the two block segments in the BCP molecule. Noteworthy is the remarkable shift in the principal scattering peak position toward the higher q region (q^* = 0.493 nm^{-1}, d = 12.7 nm) upon the crosslinking, which coincides with the 47% downsizing in the d value from the linear precursor. The author previously investigated the intramolecular crosslinking of the BCPs consisting of SBS and poly(*rac*-lactide)s (SBS–LAs) bearing the olefins only in the SBS block (similar olefin incorporation and total molecular weight with SBS–AG).[18] Considering that these SBS–LAs exhibited ca. 20% reductions in both the LAM and HEX structures upon the crosslinking, the presented degree of downsizing (47%) is quite reasonable. Such an extraordinary downscaling of the microphse-separated structure has never been accomplished to date by the architectural

control approaches, such as branching[11-14] and macrocyclization[15-17]. It is worth mentioning that the total molecular weight of $(SBS–AG)_{cl}$ was virtually identical with that of its prepolymer SBS–AG, even though the molecular volume reduced to nearly one-half upon the intramolecular crosslinking. Therefore, the author successfully demonstrated that the "one-shot crosslinking" of the BCPs is the unprecedented effective way to downsize the microphase-separated structures without changing the molecular weight.

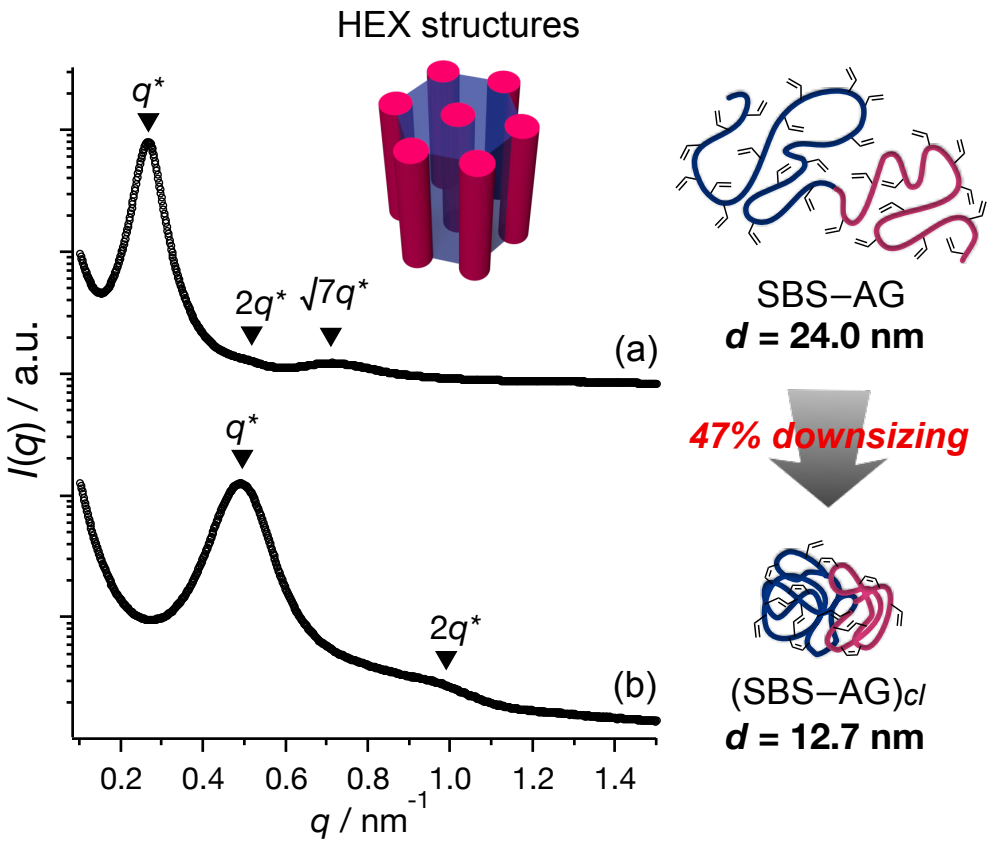

Figure 4.6. Bulk SAXS profiles of (a) SBS–AG and (b) $(SBS–AG)_{cl}$. The *I*(q) data were vertically shifted by multiplying arbitrary constants.

4.4 Conclusion

In summary, the author has successfully demonstrated the one-shot intramolecular crosslinking of the linear BCP bearing the crosslinkable olefins along the whole chain (SBS−AG) via olefin metathesis reaction, giving a Janus BCP particle ($(SBS-AG)_{cl}$). The intensive solution studies clearly revealed not only the folded and compact conformation, but also the compartmentalized block localization of the Janus $(SBS-AG)_{cl}$. The generation of this unique product was presumably related to the higher reactivity of the spatially closer olefin pairs compared to the farther ones. Most significantly, the bulk microphase-separated structure of the Janus $(SBS-AG)_{cl}$ was found to be 47% smaller as compared to that of the linear SBS−AG prepolymer, representing the unprecedented degree of downsizing among the BCP architectural control approach. The presented "one-shot crosslinking" of the BCP, therefore, is a remarkably robust methodology to downsize the microphase-separated structures, surely contributing to the advancement of the next-generation BCP lithography technology.

4.5 References

1. Stoykovich, M. P.; Nealey, P. F. Block Copolymers and Conventional Lithography. *Mater. Today* **2006**, *9* (9), 20–29.
2. Li, M.; Ober, C. K. Block Copolymer Patterns and Templates. *Mater. Today* **2006**, *9* (9), 30–39.
3. Jeong, S. J.; Kim, J. Y.; Kim, B. H.; Moon, H. S.; Kim, S. O. Directed Self-Assembly of Block Copolymers for Next Generation Nanolithography. *Mater. Today* **2013**, *16* (12), 468–476.
4. Koo, K.; Ahn, H.; Kim, S. W.; Ryu, D. Y.; Russell, T. P. Directed Self-Assembly of Block Copolymers in the Extreme: Guiding Microdomains from the Small to the Large. *Soft Matter* **2013**, *9* (38), 9059–9071.
5. Bates, C. M.; Maher, M. J.; Janes, D. W.; Ellison, C. J.; Willson, C. G. Block Copolymer Lithography. *Macromolecules* **2014**, *47* (1), 2–12.
6. Rodwogin, M. D.; Spanjers, C. S.; Leighton, C.; Hillmyer, M. A. Polylactide–Poly(dimethylsiloxane)–Polylactide Triblock Copolymers as Multifunctional Materials for Nanolithographic Applications. *ACS Nano* **2010**, *4* (2), 725–732.
7. Luo, Y.; Montarnal, D.; Kim, S.; Shi, W.; Barteau, K. P.; Pester, C. W.; Hustad, P. D.; Christianson, M. D.; Fredrickson, G. H.; Kramer, E. J.; Hawker, C. J. Poly(dimethylsiloxane-*b*-methyl methacrylate): A Promising Candidate for Sub-10 nm Patterning. *Macromolecules* **2015**, *48* (11), 3422–3430.
8. Cushen, J. D.; Otsuka, I.; Bates, C. M.; Halila, S.; Fort, S.; Rochas, C.; Easley, J. A.; Rausch, E. L.; Thio, A.; Borsali, R.; Willson, C. G.; Ellison, C. J. Oligosaccharide/Silicon-Containing Block Copolymers with 5 nm Features for Lithographic Applications. *ACS Nano* **2012**, *6* (4), 3424–3433.
9. Kwak, J.; Mishra, A. K.; Lee, J.; Lee, K. S.; Choi, C.; Maiti, S.; Kim, M.; Kim, J. K. Fabrication of Sub-3 nm Feature Size Based on Block Copolymer Self-Assembly for Next-Generation Nanolithography. *Macromolecules* **2017**, *50* (17), 6813–6818.
10. Zhang, W.; Huang, M.; Abdullatif, S. Al; Chen, M.; Shao-Horn, Y.; Johnson, J. A. Reduction of (Meth)acrylate-Based Block Copolymers Provides Access to Self-Assembled Materials with Ultrasmall Domains. *Macromolecules* **2018**, *51* (17), 6757–6763.
11. Isono, T.; Otsuka, I.; Kondo, Y.; Halila, S.; Fort, S.; Rochas, C.; Satoh, T.; Borsali, R.; Kakuchi, T. Sub-10 nm Nano-Organization in AB_2- and AB_3-Type Miktoarm Star Copolymers Consisting of Maltoheptaose and Polycaprolactone. *Macromolecules* **2013**, *46* (4), 1461–1469.
12. Shi, W.; Tateishi, Y.; Li, W.; Hawker, C. J.; Fredrickson, G. H.; Kramer, E. J. Producing Small Domain Features Using Miktoarm Block Copolymers with Large Interaction Parameters. *ACS Macro Lett.* **2015**, *4* (11), 1287–1292.

13. Minehara, H.; Pitet, L. M.; Kim, S.; Zha, R. H.; Meijer, E. W.; Hawker, C. J. Branched Block Copolymers for Tuning of Morphology and Feature Size in Thin Film Nanolithography. *Macromolecules* **2016**, *49* (6), 2318–2326.
14. Yue, K.; Liu, C.; Huang, M.; Huang, J.; Zhou, Z.; Wu, K.; Liu, H.; Lin, Z.; Shi, A. C.; Zhang, W. Bin; Cheng, S. Z. D. Self-Assembled Structures of Giant Surfactants Exhibit a Remarkable Sensitivity on Chemical Compositions and Topologies for Tailoring Sub-10 nm Nanostructures. *Macromolecules* **2017**, *50* (1), 303–314.
15. Poelma, J. E.; Ono, K.; Miyajima, D.; Aida, T.; Satoh, K.; Hawker, C. J. Cyclic Block Copolymers for Controlling Feature Sizes in Block Copolymer Lithography. *ACS Nano* **2012**, *6* (12), 10845–10854.
16. Gartner, T. E.; Kubo, T.; Seo, Y.; Tansky, M.; Hall, L. M.; Sumerlin, B. S.; Epps, T. H. Domain Spacing and Composition Profile Behavior in Salt-Doped Cyclic vs Linear Block Polymer Thin Films: A Joint Experimental and Simulation Study. *Macromolecules* **2017**, *50* (18), 7169–7176.
17. Goodson, A. D.; Troxler, J. E.; Rick, M. S.; Ashbaugh, H. S.; Albert, J. N. L. Impact of Cyclic Block Copolymer Chain Architecture and Degree of Polymerization on Nanoscale Domain Spacing : A Simulation and Scaling Theory Analysis. *Macromolecules* **2019**, *52* (23), 9389–9397.
18. Watanabe, K.; Katsuhara, S.; Mamiya, H.; Yamamoto, T.; Tajima, K.; Isono, T.; Satoh, T. Downsizing Feature of Microphase-Separated Structures via Intramolecular Crosslinking of Block Copolymers . *Chem. Sci.* **2019**, *10* (11), 3330–3339.
19. Matsumoto, M.; Terashima, T.; Matsumoto, K.; Takenaka, M.; Sawamoto, M. Compartmentalization Technologies via Self-Assembly and Cross-Linking of Amphiphilic Random Block Copolymers in Water. *J. Am. Chem. Soc.* **2017**, *139* (21), 7164–7167.
20. Jiang, L.; Xie, M.; Dou, J.; Li, H.; Huang, X.; Chen, D. Efficient Fabrication of Pure, Single-Chain Janus Particles through Their Exclusive Self-Assembly in Mixtures with Their Analogues. *ACS Macro Lett.* **2018**, *7* (11), 1278–1282.
21. Zhang, H.; Ruckenstein, E. Selective Living Anionic Polymerization of a Novel Bifunctional Monomer 4-(vinylphenyl)-1-Butene and the Preparation of Uniform Size Functional Polymers and Amphiphilic Block Copolymers. *Macromolecules* **1999**, *32* (17), 5495–5500.
22. Burdyńska, J.; Li, Y.; Aggarwal, A. V.; Höger, S.; Sheiko, S. S.; Matyjaszewski, K. Synthesis and Arm Dissociation in Molecular Stars with a Spoked Wheel Core and Bottlebrush Arms. *J. Am. Chem. Soc.* **2014**, *136* (36), 12762–12770.
23. Cheng, Y.; Li, Y.; Wu, Q.; Xu, T. New Insights into the Interactions between Dendrimers and Surfactants by Two Dimensional NOE NMR Spectroscopy. *J. Phys. Chem. B* **2008**, *112* (40), 12674–12680.

24. Kyoda, K.; Yamamoto, T.; Tezuka, Y. Programmed Polymer Folding with Periodically Positioned Tetrafunctional Telechelic Precursors by Cyclic Ammonium Salt Units as Nodal Points. *J. Am. Chem. Soc.* **2019**, *141* (18), 7526–7536.
25. Jiang, S.; Chen, Q.; Tripathy, M.; Luijten, E.; Schweizer, K. S.; Granick, S. Janus Particle Synthesis and Assembly. *Adv. Mater.* **2010**, *22* (10), 1060–1071.
26. Walther, A.; Müller, A. H. E. Janus Particles: Synthesis, Self-Assembly, Physical Properties, and Applications. *Chem. Rev.* **2013**, *113* (7), 5194–5261.

4.6 Supporting Information

Synthesis of 1,4-dioxane-2,5-dione (allylglycolide, AG)

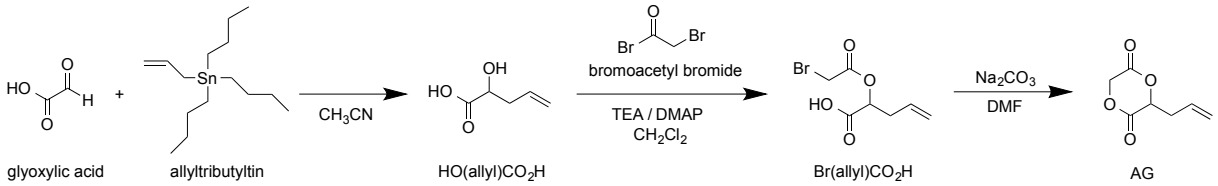

To a round bottom flask, glyoxylic acid (6.98 mL, 62.8 mmol; as 9.0 mol L^{-1} stock solution in H_2O), allyltributyltin (25.0 g, 75.4 mmol), and acetonitrile (170 mL) were added at room temperature. After stirring for 23 h, the reaction was quenched with HCl (4 mol L^{-1}, 110 mL), then the aqueous phase was washed with *n*-hexane (60 mL × 10) to remove tributyltin compounds. The product was extracted from the aqueous phase with diethyl ether (100 mL × 20). The combined organic layer was dried over Na_2SO_4 and concentrated under reduced pressure to give 2-hydroxy-4-pentenoic acid (HO(allyl)CO_2H) as a transparent oil (6.41 g, 82.3%).

In a 3-necked round-bottom flask, bromoacetyl bromide (4.13 g, 20.5 mmol) was dissolved in dry-CH_2Cl_2 (75 mL) under Ar atmosphere. After cooling to 0 °C, a solution of HO(allyl)CO_2H (2.50 mg, 21.7 mmol), TEA (2.18 g, 21.7 mmol), and DMAP (260 mg, 2.20 mmol) in CH_2Cl_2 (35 mL) was added drop wise and the reaction solution was stirred at room temperature for 17 h. The organic phase was washed with 1N HCl (85 mL × 1), distilled water (85 mL × 3), and brine (85 mL × 1), dried over Na_2SO_4, and concentrated under reduced pressure. The residue was purified by Kugelrohr distillation (b.p. = 110 °C /5 Pa) to give 2-(2-bromopropanoyloxy)-4-pentenoic acid (Br(allyl)CO_2H) as a transparent oil (1.66 g, 52.3%).

A solution of Br(allyl)CO_2H (1.56 g, 10.0 mmol) in dry-DMF (160 mL) was added drop wise over 3 h to a slurry of sodium carbonate (482 mg, 4.55 mmol) in dry-DMF (620 mL) in a 3-neck round bottom flask at 0 °C under N_2 atmosphere. The reaction slurry was stirred at room temperature for 4 h and turned clear after completion. The solution was concentrated (not completely) and distilled water (100 mL) was added. The product was extracted with CH_2Cl_2 (100 mL × 2) and purified by silicagel column chromatography (CH_2Cl_2, R_f = 0.25) to give AG as a transparent oil. Yield: 640 g (62.3%). ^{1}H NMR (400 MHz, $CDCl_3$): δ (ppm)

5.93-5.80 (m, 1H, –C*H*=CH_2), 5.35-5.25 (m, 2H, –CH=C*H*$_2$), 5.01-4.96 (m, 1H, –C*H*$CH_2CH=CH_2$), 4.93 (s, 2H, –C*H*$_2$COO–), 2.90-2.73 (m, 2H, –C*H*$_2$CH=CH_2). ^{13}C NMR (100 MHz, $CDCl_3$): δ (ppm) 165.4 (–CH_2O*C*O–), 164.3 (–CH_2*C*OO–), 130.3 (–*C*H=CH_2), 121.5 (–CH=*C*H_2), 75.4 (–*C*H$CH_2CH=CH_2$), 65.7 (–*C*H_2COO–), 35.6 (–*C*H_2CH=CH_2).

Kratky Plot Analysis of SAXS Data

The chain conformation of the samples was examined by Kratky plot analysis of the scattering data (**Figure 4.3**(a)). It is known that $I(q)$ at high q region reflects the chain conformation of an individual polymer being dependent on $q^{-1/v}$, where v is the Flory exponent. Depending on this decay of $I(q)$, the Kratky plot ($q^2I(q)$ *vs.* q, **Figure 4.3**(b)) exhibits the characteristic shape, by which the information about the conformation (degree of folding) of the polymer can be obtained as follows:

- The relationship of $I(q) \sim q^{-2}$ ($v = 0.5$) results in a plateau of the Kratky plot, corresponding to the Gaussian random coil chain (unfolded).
- The steeper $I(q)$ decay than q^{-2} ($v < 0.5$) results in a distinct peak of the Kratky plot, corresponding to the compact and folded chain.

Guinier Analysis of SAXS Data

The radius of gyration (R_g) of the samples in the bulk was approximated by the Guinier analysis of the scattering data (**Figure 4.3**(a)) at the low q region according to the following equation (Guinier's low):

$$\ln I(q) = \ln I_0(q) - \frac{q^2 {R_g}^2}{3}$$

where $I_0(q)$ is the incident beam intensity. This approximation must satisfy the maximum qR_g of less than 1.33 (1.32 and 1.30 for SBS–AG and $(SBS–AG)_{cl}$, respectively). Within this condition, the obtained scattering data can be plotted into a $\log I(q)$ *vs.* q^2 curve (**Figure 4.3**(c)), wherein the resulting slope of the curve m is used to give the approximate R_g values by the following equation:

$$R_g = \sqrt{-3m}$$

Chapter 5

Fabrication of Asymmetric Lamellar Structures by Intramolecularly Crosslinked Block Copolymers with Highly-Asymmetric Composition

5.1 Introduction

The block copolymer (BCP) lithography is a next generation technology to fabricate integrated circuits (ICs), which is considered as the alternative to the conventional photolithography.[1-5] In order to satisfy the ever-increasing demands on miniaturization and integration of IC chips, numerous efforts have been dedicated to create smaller and smaller microphase-separated structures by developing high-χ BCPs[6-10] or by adjusting the BCP architectures[11-15]. In addition, since the lamellar (LAM) morphology has to be oriented perpendicular with respect to the substrate in the thin film to fabricate the line and space (L/S) structure on the underlying substrate, the methodologies to control the structural orientation have also been extensively studied.[16-20]

Although recent research focuses are mainly addressing the above-mentioned studies, achieving the nonclassical microphase-separated morphologies should also be the key challenge to diversify the accessible pattern geometry in the BCP lithography. One of the important geometries, especially for logic IC design, is the asymmetric L/S wherein the space width is much larger than the line width, which could potentially be achieved with the aid of the highly-asymmetric LAM (A-LAM) nanostructure. Since the morphology of the microphase-separated structures is mainly governed by the volume fractions of the two blocks (f), the formation of the LAM morphology occurs only near the symmetric block composition ($f \approx 0.5$). This makes it quite challenging to achieve the A-LAM morphology with two phases of significantly different widths. A few pioneering studies of the fabrication of the A-LAM have recently been reported, in which specific molecular design or polymer blending technique was employed. Kim *et al*. demonstrated the A-LAM formation by the binary

blending of compositionally asymmetric A–B and A–C BCPs in which the minority blocks (B and C) strongly interacted with each other through the hydrogen-bonding.[21] Lynd *et al*. found that the $A(BA)_3$ miktoarm star BCP produced the A-LAM morphologies by blending with the A homopolymer even up to an extremely high degree of asymmetry.[22] These approaches, however, are not versatile enough to be applied to the other BCP systems because they are based on a specific non-covalent interaction or the time-consuming elaborate synthesis. On the other hand, Cheng *et al*. designed the BCPs that consisted of multiple polyhedral oligomeric silsesquioxane (POSS) derivatives and a long linear coil polymer.[23] Although they successfully obtained the A-LAM morphologies because of the bulkiness of the POSS block, it should be very difficult to achieve the perpendicular orientation in the thin film by this class of BCPs due to the remarkably lower surface free energy of the Si-containing segment when compared to the organic ones.[24,25] In order to further advance this particular technology, therefore, the development of a novel strategy to achieve an A-LAM morphology while fulfilling the following requirements is quite essential: the perpendicular orientation in the thin film state and versatility to be applied to various kinds of BCPs.

Considering the previous work on the previously mentioned POSS-containing BCP, one of the key parameters by which the A-LAM morphology is stabilized should be the bulkiness of the minority block at the interface. Indeed, it is known that the LAM region in the phase diagram of the AB_n-type miktoarm star BCPs is shifted toward the higher A-block composition due to the bulky B_n-block, resulting in the A-LAM morphologies.[26,27] As an alternative method to generate the bulky architecture, the author herein highlights the intramolecular crosslinking technique. This simple and unique reaction successfully gives the globule-like nano-objects,[28,29] which strongly indicates the promising potential of the

intramolecularly crosslinked polymer as a minority block of the BCPs to achieve the A-LAM morphologies. According to such a hypothesis, the author conceived the compositionally-high asymmetric BCPs consisting of an intramolecularly crosslinked segment as the minority block and longer linear one as the majority block, abbreviated as the asymmetric crosslinked–linear BCPs. The idea, thus, is fulfilling the requirements discussed above while achieving the highly A-LAM morphologies by applying the intramolecular olefin metathesis approach to a perpendicular LAM-forming BCP. As such a conventional BCP system, polystyrene-*b*-poly(*rac*-lactide) (PS-*b*-PLA) is employed because it provides some important advantages, including the large segregation strength between the two blocks to achieve small domain sizes[30] and the ability to form a perpendicularly-oriented LAM in the thin film using the appropriate underlayer.[31] In this study, the BCPs consisting of the intramolecularly crosslinked poly[styrene-*st*-(*p*-3-butenyl styrene)] and the linear poly(*rac*-lactide), *i.e.*, SBS(*cl*)–LAs, were synthesized with not only the asymmetric composition but also the symmetric one to elucidate the whole picture of the self-assembling behavior of the crosslinked–linear BCPs. The microphase separation behaviors of the obtained BCPs were then analyzed in the bulk state using SAXS and transmission electron microscopy, revealing the unusual phase behavior of the crosslinked–linear BCPs. Finally, the author carried out a thin film study of the A-LAM-forming crosslinked–linear BCPs by grazing incidence SAXS and atomic force microscopy to prove the perpendicularly-orientated A-LAM.

5.2 Experimental Section

5.2.1 Materials

sec-Butyllithium (*sec*-BuLi; Kanto Chemical Co., Inc. (Kanto), 1.05 mol L^{-1} in *n*-hexane), *n*-butyllithium (*n*-BuLi; Kanto, 1.01 mol L^{-1} in *n*-hexane), tetrabutylammonium fluoride (TBAF; Tokyo Chemical Industry Co., Ltd. (TCI), 1.0 mol L^{-1} in THF), absolute benzene (Wako Pure Chemical Industries, Ltd., super dehydrated, >99.5%), benzoic acid (TCI, >99.0%), Grubbs 2nd generation catalyst (G2; Sigma-Aldrich Chemicals Co.), and ethyl vinyl ether (TCI, >98.0%) re purchased and used as received. Styrene (S; TCI, >99.0%) and 1,8-diazabicyclo[5.4.0]-7-undecene (DBU; TCI, >98.0%) were purchased and purified by distillation over CaH_2 under vacuum. *rac*-Lactide (LA; TCI, >98.0%) was purchased and purified by recrystallization twice from dry toluene. *p*-3-Butenyl styrene (BS)[32] and (3-bromopropoxy)triisopropylsilane (Br–OTIPS)[33] were prepared according to the reported methods, then further purified by distillation over CaH_2 under vacuum. Commercially available dry THF (Kanto, >99.5%, water content, <0.001%), dry toluene (Kanto, >99.5%, water content, <0.001%), and dry CH_2Cl_2 (Kanto, >99.5%, water content, <0.001%) were further purified by an MBRAUN MB SPS Compact solvent purification system equipped with a MB-KOL-A and a MB-KOL-M Type 1 columns (for dry THF), a MB-KOL-C and a MB-KOL-A columns (for dry toluene), or two MB-KOL-A columns (for dry CH_2Cl_2) which were then directly used for the polymerizations.

5.2.2 Instruments

The ring-opening polymerization of *rac*-LA was carried out in an MBRAUN stainless steel glovebox equipped with a gas purification system (molecular sieves and copper catalyst) in a dry argon atmosphere (H_2O, O_2 <1 ppm). The moisture and oxygen contents in the glovebox were monitored by an MB-MO-SE 1 moisture sensor and an MB-OX-SE 1 oxygen sensor, respectively. The ^{1}H (400 MHz) and ^{13}C NMR (100 MHz) spectra were obtained using a JEOL JNM-ESC400 instrument at room temperature. The size exclusion chromatography (SEC) measurements were performed at 40 °C in THF (flow rate, 1.0 mL min^{-1}) using a Jasco high-performance liquid chromatography system (PU-980 Intelligent HPLC Pump, CO-2065 Plus Intelligent Column Oven, RI-2031 Plus Intelligent RI Detector, and DG-2080-53 Degasser) equipped with a Shodex KF-G guard column (4.6 mm × 10 mm; particle size, 8 μm) and two Shodex KF-804L columns (linear; particle size, 7 μm; 8.0 mm × 300 mm; exclusion limit, 4×10^4). Preparative SEC purification was performed in $CHCl_3$ (3.5 mL min^{-1}) at 23 °C using JAI LC-9201 equipped with a JAI JAIGEL-3H column (20 mm × 600 mm; exclusion limit, 7×10^4) and a JAI RI-50s refractive index detector. The Fourier transform infrared spectroscopy (FT-IR) analysis was carried out using a PerkinElmer Frontier MIR spectrometer equipped with a single reflection diamond universal attenuated total reflection (ATR) accessory. Differential scanning calorimetry (DSC) experiments were performed using a Hitachi High-Technologies DSC7000X under a nitrogen atmosphere. All polymers for DSC measurement were heated to 200 °C, cooled to 20 °C, and heated to 200 °C again at the heating and cooling rate of 10 °C min^{-1} and 20 °C min^{-1}, respectively.

5.2.3 Synthesis of ω-end hydroxy-functionalized statistical copolymer of S and BS ($S_{21}BS_8$–OH).

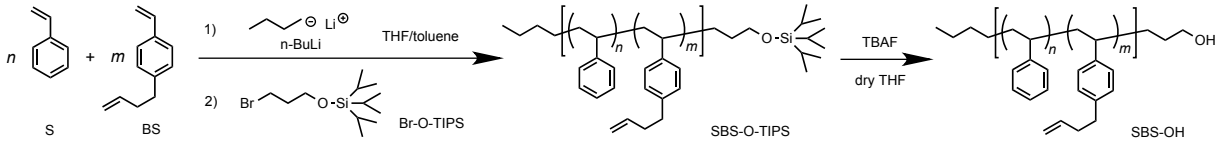

A typical procedure for the synthesis of SBS–OH is as follows (method A). In the glovebox, dry toluene (50 mL) and dry THF (100 mL) were placed in a Schlenk flask. After sealing, the flask was taken out from the glovebox. *sec*-BuLi (100 μL, 105 μmol as a 1.05 mol L^{-1} stock solution in *n*-hexane) was added to the solvent under an Ar atmosphere to remove water completely. Then, the solvent was further purified by trap-to-trap distillation under high vacuum to transfer to another Schlenk flask for polymerization. After cooling to –78 °C, *n*-BuLi (1.97 μmL, 2.39 mmol as a 1.21 mol L^{-1} stock solution in *n*-hexane) was added to the flask. In another flame-dried Schlenk flask, S (5.5 g, 53 mmol) and BS (3.6 g, 23 mmol) were mixed together under an Ar atmosphere. The mixture was added at once to the initiator solution using a syringe. After monomer addition, the mixture was stirred at −78 °C for 6 h. Br–O–TIPS (3.57 g, 9.30 mmol) was added to the solution of living polymer anions at −78 °C, and the whole mixture was allowed to react for 1 h at −78 °C and then overnight at room temperature. Afterwards, The solvent was removed from the polymerization mixture under reduced pressure. TBAF (8.35 mL, 8.35 mmol as a 1.0 mol L^{-1} stock solution in THF) and dry THF (20 mL) were added to the crude product at room temperature. After 15 h stirring, the reaction mixture was passed through a short silica-gel column, and the resulting residue was purified by repeated reprecipitation twice from the THF solution into MeOH to give $S_{21}BS_8$–OH as a white solid. Yield: 7.28 g (80%). ^{1}H NMR (400 MHz, $CDCl_3$): δ (ppm)

7.40−6.19 (m, 5H × *n* + 4H × *m*, −C_6H_5, −C_6H_4−), 5.97−5.74 (m, 1H × *m*, −C*H*=CH_2), 5.15−4.90 (m, 2H × *m*, −CH=CH_2), 3.47−3.33 (m, 2H, −CH_2OH), 2.85−2.45 (m, 2H × *m*, −C_6H_4CH_2−), 2.46−2.14 (m, 2H × *m*, −$C_6H_4CH_2$CH_2−), 2.15−1.62 (m, 1H × (*n*+*m*), −C*H*(C_6H_5)−, −C*H*(C_6H_4−)−), 1.74−0.69 (m, 2H × (*m*+*n*) + 9H, −CH_2CH(C_6H_5)−, −CH_2CH(C_6H_4−)−, C_4H_9−). $M_{n,NMR}$ = 3,600 ($CDCl_3$), the mole fraction of the BS units = 0.29, $M_{n,SEC}$ = 3,920 (THF), $Đ$ = 1.08 (THF).

5.2.4 Intramolecular crosslinking of $S_{21}BS_8$−OH via olefin metathesis reaction.

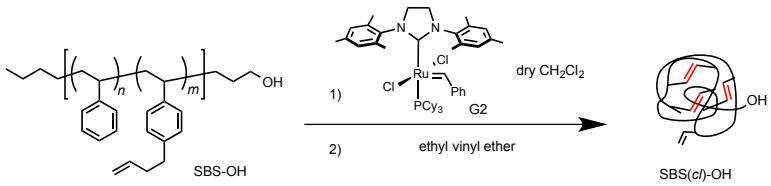

A typical procedure for the intramolecular crosslinking of SBS−OH is as follows (method B). $S_{65}BS_{28}$−OH ($M_{n,NMR}$ = 3,600, 1.50 g, 3.74 mmol olefin-containing units) was dissolved in dry CH_2Cl_2 (3000 mL). After degassing by N_2 bubbling, G2 (31.7 mg, 37.4 μmol) was added to the mixture. After stirring for 3 h under an N_2 atmosphere at 30 °C, the reaction was quenched by the addition of ethyl vinyl ether. The solvent was removed by evaporation, then the residue was purified by reprecipitation from the CH_2Cl_2 solution into MeOH to give intramolecularly crosslinked $S_{21}BS_8$−OH ($S_{21}BS_8$(*cl*)−OH) as a white solid (1.11 g, 74.0%). The product was further purified by preparative SEC. ^{1}H NMR (400 MHz, $CDCl_3$): δ (ppm) 7.55−5.94 (m, 5H × *n* + 4H × *m*, −C_6H_5, −C_6H_4−), 6.06−4.82 (m, 3H × 0.15*m* + H × 0.85*m*, −C*H*=CH_2, −C*H*=C*H*−, −CH=CH_2), 3.62−3.23 (m, 2H, −CH_2OH), 3.14−0.64 (m, 7H × *m* + 3H × *n* + 9H, −C_6H_4CH_2−, −$C_6H_4CH_2$CH_2−, −C*H*(C_6H_5)−, −C*H*(C_6H_4−)−,

−C*H*$_2$CH(C$_6$H$_5$)−, −C*H*$_2$CH(C$_6$H$_4$−)−, C$_4$*H*$_9$−). $M_{n,SEC}$ = 2,790 (THF), $Đ$ = 1.18 (THF), the conversion of the terminal olefins = 85%.

5.2.5 Synthesis of block copolymer consisting of SBS(cl) and poly(rac-LA) (S$_{21}$BS$_8$(cl)−LA$_{20}$) via ring-opening polymerization of rac-LA using S$_{21}$BS$_8$(cl)−OH as an initiator.

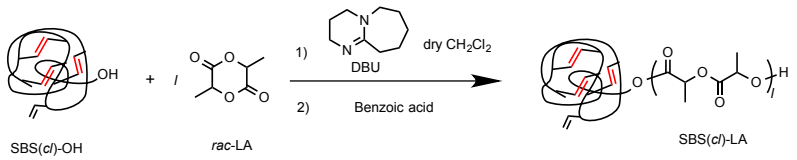

A typical procedure for the polymerization of *rac*-LA is as follows (method C). S$_{21}$BS$_8$(*cl*)−OH was freeze-dried from its absolute benzene solution three times prior to the polymerization. In the glovebox, S$_{21}$BS$_8$(*cl*)−OH ($M_{n,NMR}$ = 3,500, 234 mg, 66.9 μmol) and *rac*-LA (293 mg, 2.03 mmol) were dissolved in dry CH_2Cl_2 (4.10 mL). DBU (3.0 μL, 20 μmol) was then added to the CH_2Cl_2 solution to initiate the polymerization. After 8 min, the polymerization was quenched by the addition of benzoic acid. The mixture was purified by reprecipitation from the CH_2Cl_2 solution into MeOH to give S$_{21}$BS$_8$(*cl*)−LA$_{20}$ as a white solid (394 mg, 81.1%). The product was further purified by preparative SEC. ^{1}H NMR (400 MHz, $CDCl_3$): δ (ppm) 7.55−5.94 (m, 5H × *n* + 4H × *m*, −C$_6$*H*$_5$, −C$_6$*H*$_4$−), 6.06−4.82 (m, 3H × 0.15*m* + H × 0.85*m* + 1H × (2*l*-1), −C*H*=CH$_2$, −C*H*=C*H*−, −CH=C*H*$_2$, −OCOC*H*(CH$_3$)−), 4.43−4.28 (m, 1H, −C*H*(CH$_3$)OH), 4.07−3.78 (m, 2H, −C$_2$H$_4$C*H*$_2$OCO−), 3.14−0.64 (m, 7H × *m* + 3H × *n* + 3H × 2*l* + 9H, −C$_6$H$_4$C*H*$_2$−, −C$_6$H$_4$CH$_2$C*H*$_2$−, −C*H*(C$_6$H$_5$)−, −C*H*(C$_6$H$_4$−)−, −C*H*$_2$CH(C$_6$H$_5$)−, −C*H*$_2$CH(C$_6$H$_4$−)−, −OCOCH(C*H*$_3$)−, C$_4$*H*$_9$−). Conversion = 86%, $M_{n,NMR}$ = 6,430 ($CDCl_3$), the weight fraction of PLA = 0.46, $M_{n,SEC}$ = 14,900 (THF), $Đ$ = 1.06 (THF).

5.2.6 Bulk and thin film studies

Small-angle X-ray scattering (SAXS). The morphologies and *d* values of samples in the bulk state were investigated using SAXS. The experiments were performed on the BL-6A beamline at the Photon Factory in the High Energy Accelerator Research Organization (KEK, Tsukuba, Japan) using X-ray beams with λ = 1.5 Å. The two-dimensional scattering patterns were collected by a PILATUS3 1M detector (Dectris Ltd.), where the sample-to-detector distance was set to 1.5 m. The scattering angle (θ) was calibrated using silver behenate (Nagara Science Co., Ltd.) as the standard and subsequently converted to the scattering vector (q) using Bragg's equation ($q = (4\pi/\lambda)\sin(\theta/2)$). The *d* values of the samples were calculated according to $d = 2\pi/q^*$, where q^* is the principal scattering peak position. The bulk sample pieces obtained after the reprecipitation and vacuum dry were annealed at 180 °C for 1 h under vacuum and then exposed to X-ray directly for 1 min each.

Grazing incidence SAXS (GISAXS). The morphologies and *d* values of samples in the thin film state were investigated using GISAXS. The experiments were performed on the BL-6A beamline of KEK using X-ray beams with λ = 1.5 Å. The sample-to-detector distance was set to 2.0 m. The GISAXS profiles were acquired under ambient conditions for 20 s at a variety of incidence angles. The thin films for GISAXS experiments were prepared by spin-coating (2000 rpm for 1 min) the polymer solution in toluene (0.66 wt%) onto a Si substrate with $PS_{0.2}$-*stat*-$PMMA_{0.8}$ brush layer. The obtained thin film samples were annealed at 180 °C for 30 min. The film thickness was measured by ellipsometry (JASCO M-500S).

Transmission electron microscopy (TEM). Bright-field TEM images of the thinly sliced bulk samples were obtained using a JEM-3200FS electron microscope (JEOL) with an accelerating voltage of 100 kV. Bulk film samples prepared by drop-cast from the toluene

solutions were annealed at 180 °C for 1 h under vacuum and then embedded in a photocurable resin (Toagosei Co., Ltd., Alonix D-800). Sample slices with a thickness of ca.40 nm were obtained using a Leicca Ultracut S ultramicrotome equipped with a diamond knife (DiATOME, ultra sonic) at room temperature, and a piece of slice was transferred to copper grids. Sequentially, the samples on the grids were stained by exposing to the vapor of a 0.5% aqueous RuO_4 solution for 10 h.

Small-angle neutron scattering (SANS). The R_g of samples in the bulk state were analyzed using SANS. The experiments were performed by the time-of-flight small and wide angle neutron scattering instrument (TAIKAN) installed on the BL15 beamline at the Material and Life Science Experimental Facility (MLF) in Japan Proton Accelerator Research Complex (J-PARC, Tokai, Japan) using white neutron beams in the λ range of 0.7-7.8 Å. The scattering patterns were collected by 1608 ^{3}He one-dimensional position-sensitive detectors (Toshiba Electron Tubes & Devices Co., Ltd.) located in small-angle detector bank, where the sample-to-detector distance was set to 5.65 m. The scattering angle (θ) was converted to the scattering vector (q) using Bragg's equation ($q = (4\pi/\lambda)\sin(\theta/2)$). The binary blend samples composed of the deuterated polystyrene with DP of ca.80 (d-PS_{80}; M_n = 8,800, $Đ$ = 1.02, Polymer Source, Inc.) and the hydrogenous samples ($S_{65}BS_{28}$−OH or $S_{65}BS_{28}$(*cl*)−OH) were prepared as follows: The powder mix of d-PS_{80} (188 mg) and hydrogenous polystyrene (172 mg) was dissolved in toluene (500 μL) and vortexed for 1 h. The solution was then casted into the 15 mm diameter mold made by aluminum foil and dried at r.t. for 24 h, at 60 °C for 15h, and at 130 °C for 5h to completely remove the residual solvent. Finally, the sample was annealed at 130 °C for 2 h under vacuum, giving the polymer disc with the thickness of ca.2

mm. The obtained sample discs were directly exposed to the neutron beam without peeling the aluminum foil off for 30 min each.

Atomic force microscopy (AFM). The AFM phase images were realized using a Molecular Imaging PicoPlus atomic force microscope operating in the tapping mode with a silicon cantilever (Nanoworld AG, NANOSENSORS^{TM} PPP-NCH) having a resonant frequency and a force constant of 190 kHz and 48 N m^{-1}, respectively.

5.3 Results and Discussion

5.3.1 Synthesis of intramolecularly crosslinked block copolymers

The initial effort was directed to the synthesis of a series of block copolymers (BCPs) consisting of an intramolecularly crosslinked poly[styrene-*st*-(*p*-3-butenyl styrene)] and linear poly(*rac*-lactide), *i.e.*, P(S-*st*-BS)(*cl*)-*b*-PLAs (SBS(*cl*)−LA). In a previous study, the author established a synthetic pathway to the crosslinked−linear type BCP which involves the preparation of a linear−linear type BCP and subsequent intramolecular crosslinking of the one block.[34] However, such a pathway could cause variation in the degree of crosslinking among the samples with the varied PLA chain length. To avoid any potential effects of the structural variations due to the intramolecular crosslinking on the resulting morphology, the author established an alternative approach to the crosslinked−linear type BCP as shown in **Scheme 5.1**; the SBS(*cl*) block is initially prepared, then the PLA chain is extended from the hydroxyl chain end of the SBS(*cl*). By using a common SBS(*cl*), a series of SBS(*cl*)−LAs can be synthesized with varied PLA chain lengths while keeping the same molecular weight and degree of crosslinking of the SBS(*cl*) block, thus allowing the investigation into the pure effects of the PLA chain length on the resulting morphology. First, the hydroxyl-terminated P(S-*stat*-BS)s with a varied molecular weight (MW) and fixed BS mole fraction (f_{BS}), *i.e.*, $S_{21}BS_8$−OH (M_n = 3,600, $Đ$ = 1.08, f_{BS} = 0.29), $S_{33}BS_{14}$−OH (M_n = 5,760, $Đ$ = 1.04, f_{BS} = 0.30), and $S_{65}BS_{28}$−OH (M_n = 11,100, $Đ$ = 1.04, f_{BS} = 0.30) were prepared, wherein the subscript numbers denote the DP of each monomer. The obtained SBS−OHs were then subjected to the intramolecular olefin metathesis reaction using Grubbs' 2nd generation catalyst (G2) ($[SBS-OH]_0$ = 0.30 g L^{-1}, $[G2]_0/[BS\ unit]_0$ = 0.01), giving the corresponding

hydroxyl-terminated intramolecularly crosslinked SBS−OHs (SBS(*cl*)−OHs) with the olefin conversion of ≥85% (**Table S5.1,** the ^{1}H NMR and SEC results are presented in **Figures S5.1-S5.4**). Subsequently, the ring-opening polymerization of the *rac*-lactide was conducted using SBS(*cl*)−OHs as a macroinitiator to produce the crosslinked−linear type SBS(*cl*)−LAs, in which the weight fraction of the PLA block (F_{LA}) was systematically varied from 0.46 to 0.92 (the ^{1}H NMR and SEC results are presented in **Figures S5.5-S5.10**). The author successfully obtained three series of the SBS(*cl*)−LAs, *i.e.*, $S_{21}BS_{8}$(*cl*)−LAs, $S_{33}BS_{14}$(*cl*)−LAs, and $S_{65}BS_{28}$(*cl*)−LAs, which are denoted by the low-, middle-, and high-MW series, respectively. In addition, the linear−linear type $S_{65}BS_{28}$−LA_{466} ($M_{n,SBS}$ = 11,100, $M_{n,LA}$ = 46,600, F_{LA} = 0.86) was also synthesized by the PLA extension from the $S_{65}BS_{28}$−OH macroinitiator in order to compare the microphase separation behaviors between the crosslinked−linear BCPs and linear−linear counterpart (the ^{1}H NMR and SEC results are presented in **Figure S5.11**). The molecular characteristics of the studied BCPs are summarized in **Table 5.1**.

Table 5.1. Molecular and morphological characteristics of SBS(*cl*)–LAs

sample name	molecular characteristics				morphological characteristics				
	$M_{n,SBS(cl)}$ [a]	$M_{n,LA}$ [a]	F_{LA} [b]	$Đ$ [c]	morphology	d [d] (nm)	$l_{SBS(cl)}$ [e] (nm)	l_{LA} [e] (nm)	R_a [f]
$S_{21}BS_8(cl)$–LA_{20}	3,500	2,930	0.46	1.05	disorder	–	–	–	–
$S_{21}BS_8(cl)$–LA_{45}	3,500	6,550	0.65	1.04	A-LAM	14.1	5.3	8.8	1.66
$S_{21}BS_8(cl)$–LA_{70}	3,500	10,100	0.74	1.05	A-LAM	16.7	–	–	–
$S_{21}BS_8(cl)$–LA_{110}	3,500	15,900	0.82	1.03	HEX	17.2	–	–	–
$S_{33}BS_{14}(cl)$–LA_{33}	5,600	4,750	0.46	1.06	DG	13.0	–	–	–
$S_{33}BS_{14}(cl)$–LA_{72}	5,600	10,400	0.65	1.07	A-LAM	18.7	6.8	11.9	1.75
$S_{33}BS_{14}(cl)$–LA_{112}	5,600	16,200	0.74	1.05	A-LAM	20.6	6.5	14.1	2.17
$S_{33}BS_{14}(cl)$–LA_{201}	5,600	28,900	0.84	1.06	HEX	22.5	–	–	–
$S_{65}BS_{28}(cl)$–LA_{74}	10,800	10,700	0.50	1.09	DG	19.0	–	–	–
$S_{65}BS_{28}(cl)$–LA_{160}	10,800	23,000	0.68	1.06	A-LAM	25.2	8.9	16.3	1.83
$S_{65}BS_{28}(cl)$–LA_{223}	10,800	32,100	0.75	1.06	A-LAM	31.7	8.7	23.0	2.64
$S_{65}BS_{28}(cl)$–LA_{459}	10,800	66,100	0.86	1.09	A-LAM	41.3	9.2	32.1	3.49
$S_{65}BS_{28}(cl)$–LA_{684}	10,800	98,600	0.90	1.14	ill-defined	–	–	–	–
$S_{65}BS_{28}(cl)$–LA_{923}	10,800	133,000	0.92	1.10	ill-defined	–	–	–	–

[a]Determined by ^{1}H NMR in $CDCl_3$. [b]PLA weight fraction calculated by $M_{n,LA}/(M_{n,SBS(cl)}+M_{n,LA})$. [c]Determined by SEC in THF using polystyrene standards. [d]Determined by SAXS. [e]Determined by correlation function analysis of SAXS profiles. [f]Asymmetric ratio of LAM phases calculated by $l_{LA}/l_{SBS(cl)}$.

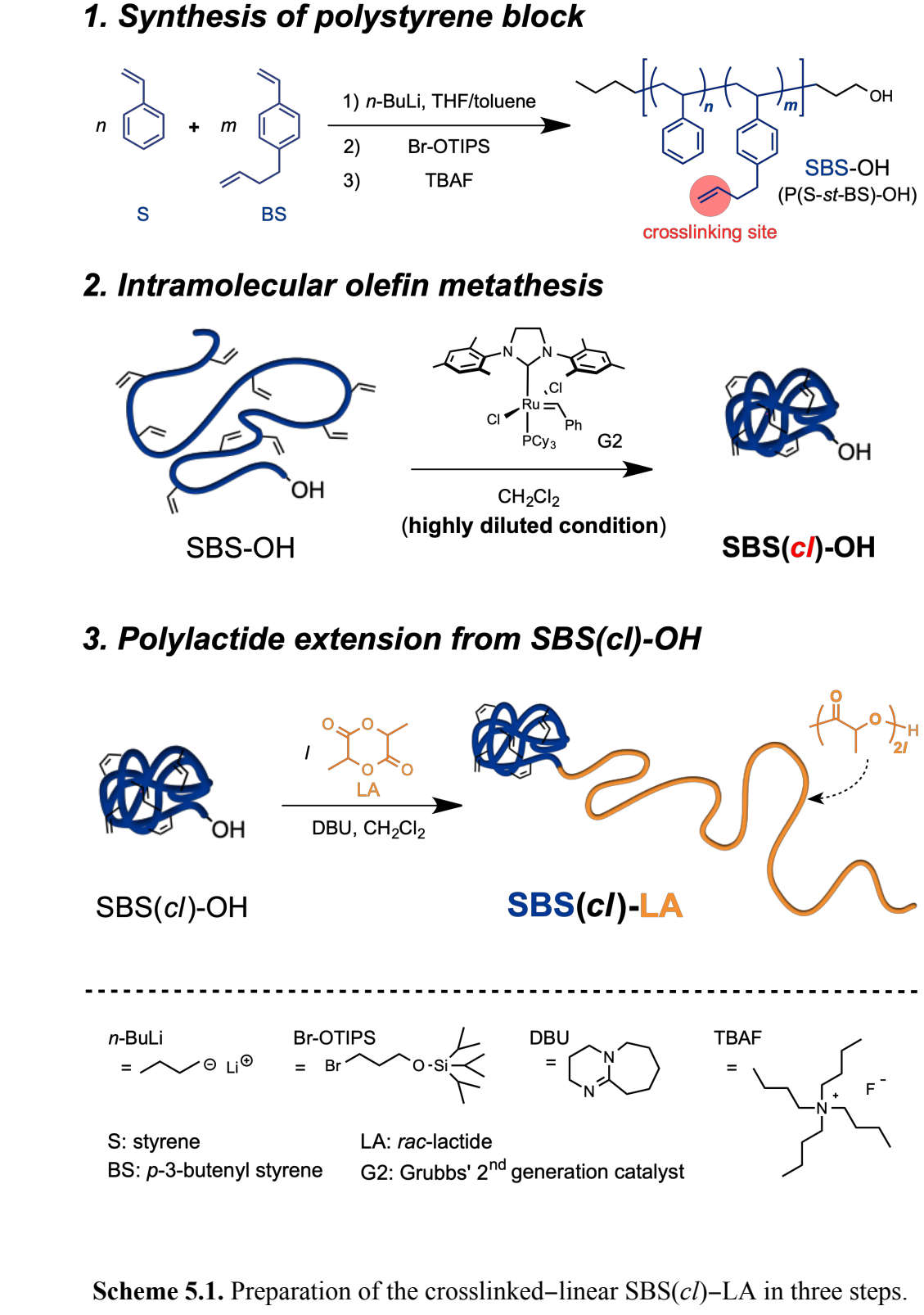

Scheme 5.1. Preparation of the crosslinked–linear SBS(*cl*)–LA in three steps.

5.3.2 Microphase separation behavior in bulk state

In order to elucidate the whole picture of the microphase-separation behavior of the SBS(*cl*)–LAs, a small-angle X-ray scattering (SAXS) study was carried out on their bulk samples. Prior to the SAXS experiments, the samples were thermally annealed for 1 h under vacuum at 150 °C. The resulting morphological characteristics of all the samples are summarized in **Table 5.1**.

The SAXS results of the low-MW $S_{21}BS_8$(*cl*)–LA series confirmed the morphological transition of the resulting nanostructures with the increasing F_{LA} value. First, the SAXS profile of the lowest molecular weight $S_{21}BS_8$(*cl*)–LA_{20} (F_{LA} = 0.46) showed only a broad scattering peak (q^*) corresponding to the disordered state, suggesting that the total DP of this BCP was insufficient to form an ordered nanostructure (**Figure 5.1**(a)). The SAXS profile of $S_{21}BS_8$(*cl*)–LA_{45} (F_{LA} = 0.65) exhibited a principal scattering peak at q^* of 0.447 nm^{-1} as well as the higher-ordered scattering peaks at the integer multiples of q^*, indicative of a lamellar (LAM) morphology (**Figure 5.1**(b)). The domain-spacing (d) value of the microphase-separated structures can be calculated based on the relationship of $d = 2\pi/q^*$, which was 14.1 nm for this LAM structure. The SAXS profile of $S_{21}BS_8$(*cl*)–LA_{75} having a longer PLA block (F_{LA} = 0.74) is also assignable to the LAM morphology (d = 16.7 nm) in spite of such an asymmetric block composition. $S_{21}BS_8$(*cl*)–LA_{115} with the longest PLA block (F_{LA} = 0.83) was found to form the hexagonally close-packed cylinder (HEX) morphology (d = 17.2 nm), as is evident from the scattering peaks at the relative q-values of 1: √3: 2: √7: 3 in the SAXS profile (**Figure 5.1**(d)). The middle-MW $S_{33}BS_{14}$(*cl*)–LA series showed a similar tendency; a morphological transition from LAM to HEX was observed upon increasing the

F_{LA}, in which LAM morphology was maintained up to F_{LA} of 0.74 (**Figures 5.1**(f)-(h)). Interestingly, the SAXS profile of the compositionally symmetric $S_{33}BS_{14}(cl)$–LA_{33} (F_{LA} = 0.46) exhibited multiple scattering peaks at the relative q-values of √6: √8: √14: √16: √20: √22, which agrees with the assignment of the highly ordered double gyroid (DG) morphology (**Figures 5.1**(e)). When the molecular weight of the SBS(*cl*) block was further increased (high-MW $S_{65}BS_{28}(cl)$–LA series), the LAM region expanded toward an even higher F_{LA}. Similar to the case of $S_{33}BS_{14}(cl)$–LA_{33}, the SAXS profile of the compositionally symmetric $S_{65}BS_{28}(cl)$–LA_{74} (F_{LA} = 0.50) exhibited a scattering pattern of the DG morphology (**Figure 5.2**(a)). On the other hand, the compositionally asymmetric BCPs, *i.e.*, $S_{65}BS_{28}(cl)$–LA_{160} (F_{LA} = 0.68), $S_{65}BS_{28}(cl)$–LA_{459} (F_{LA} = 0.75), and $S_{65}BS_{28}(cl)$–LA_{459} (F_{LA} = 0.86), self-assembled into the well-ordered LAM morphologies as supported by the appearance of more than four scattering peaks in the SAXS profiles (**Figures 5.2**(b)-(d)). Importantly, the author succeeded in visualizing the morphologies of $S_{65}BS_{28}(cl)$–LA_{74} (DG) and $S_{65}BS_{28}(cl)$–LA_{160} (LAM) in the bulk by transmission electron microscopy (TEM) observation of the microtomed samples. For $S_{65}BS_{28}(cl)$–LA_{74}, the typical pattern of the (211), (111), and (110) planes of the DG morphology was clearly observed (**Figures 5.2**(g), **S5.12**(a), and **S5.12**(b), respectively). The TEM image of $S_{65}BS_{28}(cl)$–LA_{160} showed the line pattern corresponding to the LAM morphology that consisted of the bright SBS(*cl*) and dark LA phases, where the estimated d value (22.5 nm) was roughly matched with that determined from the SAXS measurement (25.2 nm) (**Figure 5.2**(h)). Upon further increasing the F_{LA} values to 0.9 or higher, the well-defined morphology was no longer observed. The SAXS profiles of $S_{65}BS_{28}(cl)$–LA_{684} (F_{LA} = 0.90) and $S_{65}BS_{28}(cl)$–LA_{923} (F_{LA} = 0.92) exhibited the

broad primary scattering peaks (denoted by triangles) and the weak higher-ordered ones, indicative of the ill-defined nanostructures without the characteristic periodic structure (**Figures 5.2**(e) and (f)).

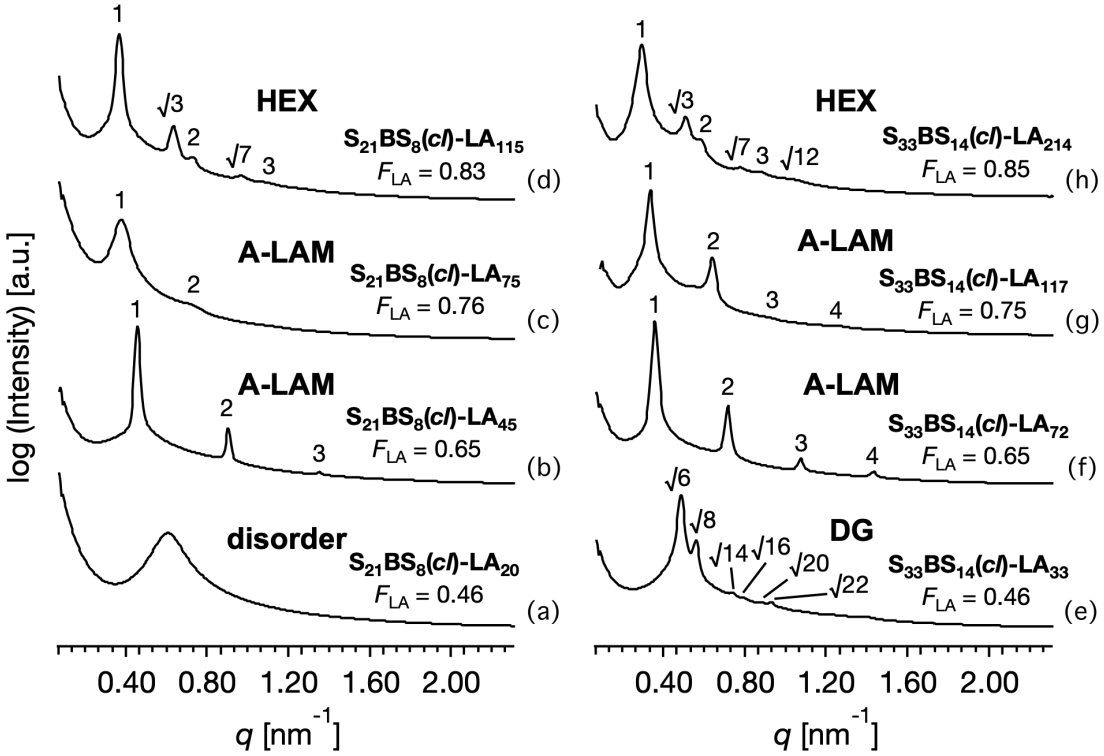

Figure 5.1. SAXS profiles of (a)-(d) $S_{21}BS_8(cl)$–LAs and (e)-(h) $S_{33}BS_{14}(cl)$–LAs (SBS and LA domains are shown in blue and yellow, respectively).

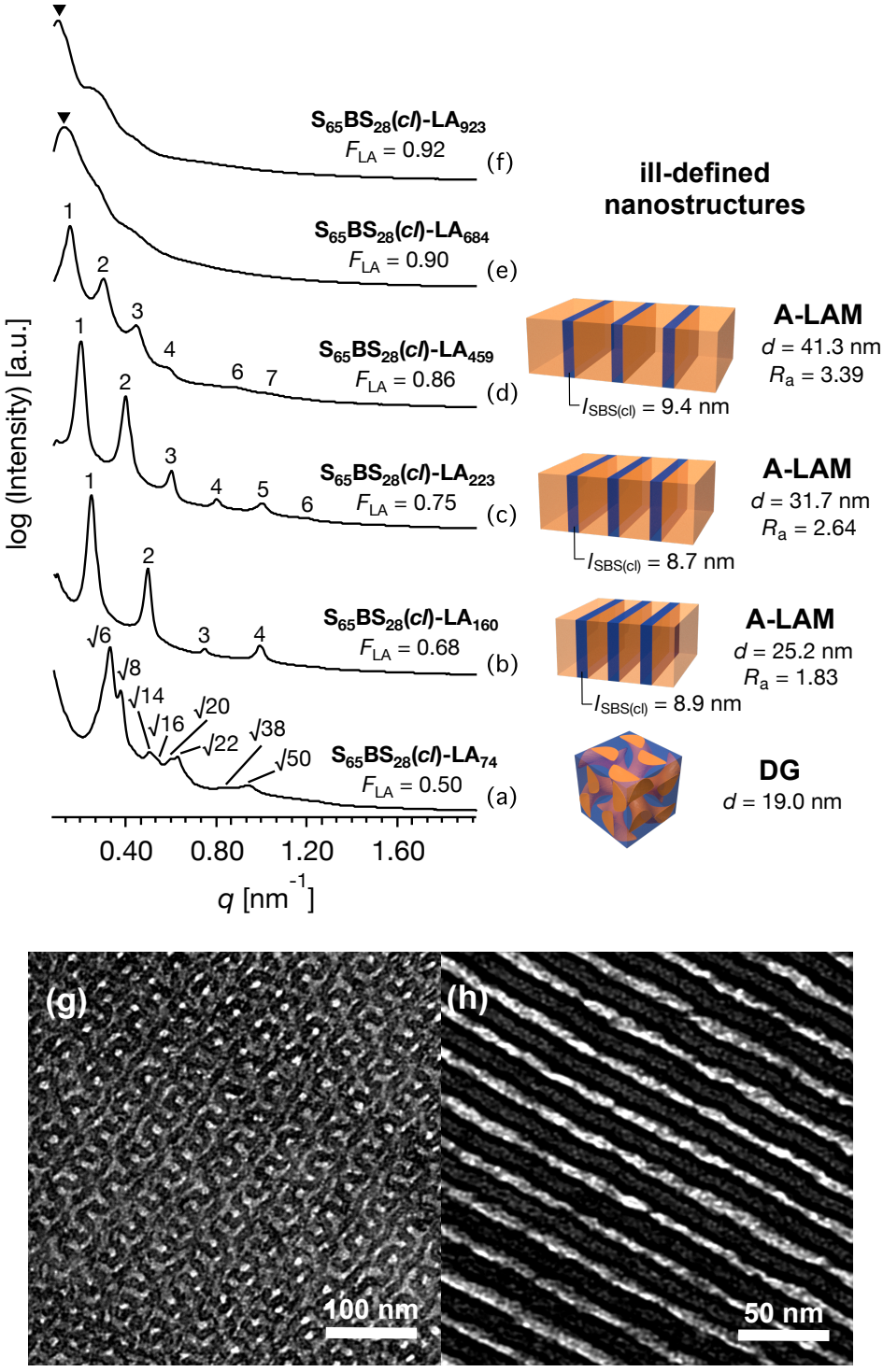

Figure 5.2. (a)-(f) SAXS profiles of $S_{65}BS_{28}(cl)$–LAs with the schematic illustration of each morphology (SBS and LA domains are shown in blue and yellow, respectively). TEM image of the microtomed (g) $S_{65}BS_{28}(cl)$–LA_{160} and (h) $S_{65}BS_{28}(cl)$–LA_{74} samples stained by RuO_4 vapor for 10 h.

Based on the previopus SAXS studies, the author constructed a phase diagram of the crosslinked–linear BCP with respect to F_{LA} and MW of SBS(*cl*) block ($M_{n,SBS(cl)}$) (**Figure 5.3**). The previous data for $S_{45}BS_{20}$(*cl*)–LA_{57} ($M_{n,SBS(cl)}$ = 7,710, $M_{n,LA}$ = 8,250, F_{LA} = 0.52, f_{BS} of linear prepolymer = 0.31) were also plotted since its molecular structure should be almost identical to the samples prepared in this study.[34] As expected, the LAM window was shifted toward the higher composition of the PLA block compared to the typical phase diagram of the linear–linear BCPs, resulting in the A-LAM morphologies over a wide range of block compositions.

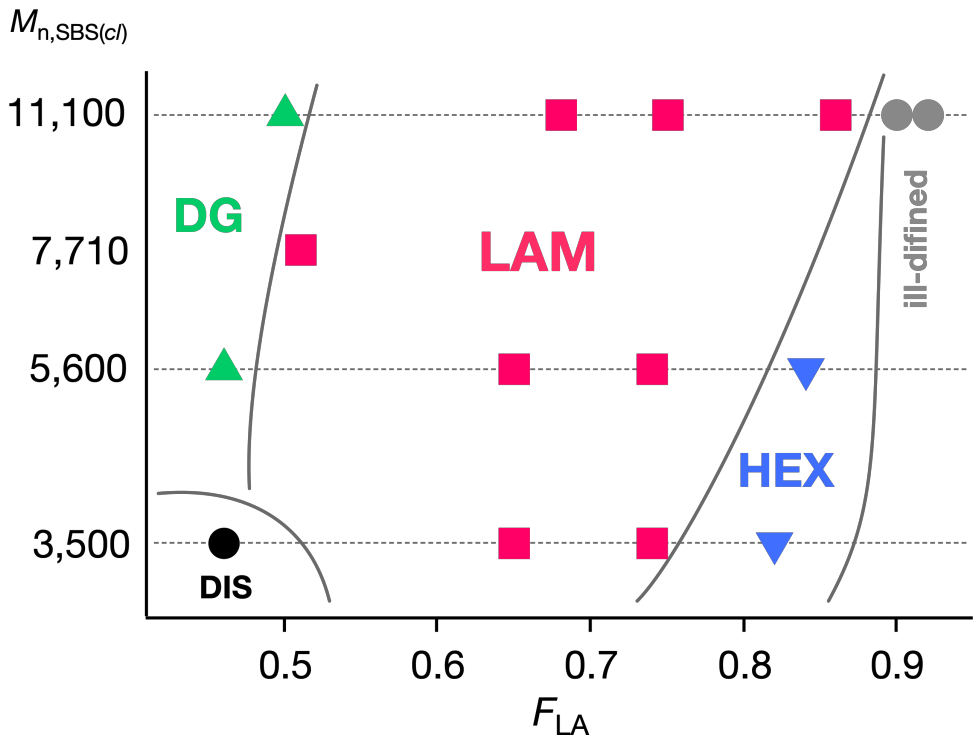

Figure 5.3. Experimentally constructed phase diagram for SBS(*cl*)–LAs. Points are plotted depending on F_{LA} and $M_{n,SBS(cl)}$. Red squares, red open-square, green triangles, blue inverted triangles, and gray circles denote LAM, DG, HEX, and ill-defined morphologies, respectively. Black circle denotes disordered state. Gray lines indicate the phase boundary.

Since the determination of the width of each domain in A-LAM is important for evaluating the degree of asymmetry, the author employed the correlation function analysis of the obtained SAXS profile (See Supporting Information for the detail). For the low-MW $S_{21}BS_8(cl)$–LA_{45} ($M_{n,SBS(cl)}$ = 3,500), the widths of SBS(*cl*) and LA domains ($l_{SBS(cl)}$ and l_{LA}, respectively) were determined to be 5.3 nm and 8.8 nm, respectively, from which the asymmetric ratio ($R_a = l_{LA}/l_{SBS(cl)}$) was calculated to be 1.66. To the best of the author's knowledge, such a 5-nm domain width is the smallest width among the LAM morphologies obtained so far from the PS–PLA system. Arguably, from the previous literature,[30] the compositionally symmetric linear–linear PS–PLA with the PS block of ca. 3,500 g mol^{-1} is not capable of forming the ordered LAM structure (and produces the disordered state) due to the insufficient overall molecular weight. Noteworthy here is the achievement of the exceptionally small LAM domain (ca. 5 nm) was clearly due to the ability of the crosslinked–linear SBS(*cl*)–LA to form the A-LAM, wherein the long PLA chain contributed to increase the BCP molecular weight and thus exceed the critical χN. By applying the same analysis, the domain widths and R_as of LAM morphologies generated by the middle-MW series were determined as follows: R_a = 1.75 for $S_{33}BS_{14}(cl)$–LA_{72} ($l_{SBS(cl)}$ = 6.8 nm, l_{LA} = 11.9 nm) and R_a = 2.17 for $S_{33}BS_{14}(cl)$–LA_{117} ($l_{SBS(cl)}$ = 6.5 nm, l_{LA} = 14.1 nm). These results consolidated the formation of the A-LAM morphologies; however, the maximum F_{LA} values allowing the LAM formation is around 0.75~0.80 for the low- and middle-MW series, which is comparable to that for the miktoarm star BCP system.[26,27]

For the high-MW $S_{65}BS_{28}(cl)$–LA series with the $M_{n,SBS(cl)}$ of 10,800, the formation of the A-LAM morphology was observed at F_{LA} up to 0.86. It is worth mentioning that the SAXS profile of the linear-linear type $S_{65}BS_{28}$–LA_{466} with the asymmetric composition (F_{LA} =

0.86) exhibited the scattering pattern of the HEX morphology (**Figure S5.13**). This result demonstrated that the unusual phase behavior of the crosslinked–linear type SBS(*cl*)–LAs is definitly caused by the intramolecularly crosslinked SBS(*cl*) block. The formation of the ill-defined nanostructures at F_{LA} over 0.90, on the other hand, is reasonably understandable because this region should be positioned near the order-disorder boundary in the phase diagram. Considering that $S_{45}BS_{20}$(*cl*)–LA_{57} with F_{LA} of 0.52 exhibited the LAM morphology, the DG–LAM phase boundary of the high-MW $S_{65}BS_{28}$(*cl*)–LA series might exist at $F_{LA} \approx 0.5$, which indicates the unusually large LAM region. Such a widespread LAM formation could not be achieved by the AB_n miktoarm BCP system, even the branching number n is increased to over 5, demonstrating the astonishing capability of the crosslinked–linear BCPs to generate the A–LAM morphology. The author attributed this phenomenon to a decrease in the domain interfacial curvature arising from the bulkiness and stiffness of the SBS(*cl*) block. The intramolecularly crosslinked structure is unfavorable to be packed into a curved microdomain, like a cylinder or sphere, due to a large packing frustration, resulting in the LAM morphologies with a less curved domain interface. Based on the correlation function analysis, the R_a values for $S_{65}BS_{28}$(*cl*)–LA_{160} ($l_{SBS(cl)}$ = 8.9 nm and l_{LA} = 16.3 nm), $S_{65}BS_{28}$(*cl*)–LA_{223} ($l_{SBS(cl)}$ = 8.7 nm and l_{LA} = 23.0 nm), and $S_{65}BS_{28}$(*cl*)–LA_{459} ($l_{SBS(cl)}$ = 9.2 nm and l_{LA} = 32.1 nm) were determined to be 1.83, 2.64, and 3.49, respectively (**Figure S5.14**), which indeed revealed the highly asymmetric line patterns. Notably, both the SAXS (**Figure 5.2**(b), the third-ordered scattering peak was suppressed[35]) and the TEM results (**Figure 5.2**(h)) of $S_{65}BS_{28}$(*cl*)–LA_{160} indicate that the width ratio between the two different phases of ca. 1:2, which is reasonably consistent with the result of the correlation function analysis (R_a = 1.83).

Interestingly, the $l_{SBS(cl)}$ values for the A-LAM morphologies were found to be constant among each series, *i.e.*, ca. 6.5 nm and 9.0 nm for the middle-MW $S_{33}BS_{14}(cl)$–LA and high-MW $S_{65}BS_{28}(cl)$–LA series, respectively. This result indicates that the $S_{65}BS_{28}(cl)$ blocks were packed in a similar manner in its narrow microdomain, regardless of the molecular weight of the counter LA block. The packing model for A-LAM morphologies is discussed in more detail below.

Meanwhile, one of the reasons for the DG formation by $S_{33}BS_{14}(cl)$–LA_{33} (F_{LA} = 0.46) and $S_{65}BS_{28}(cl)$–LA_{74} (F_{LA} = 0.50) is quite clear; even though these BCPs possess the symmetric block composition, the bulkiness of the SBS(*cl*) block created a driving force to bend the interface to the PLA domain side, resulting in the slightly curved nanostructure, *i.e.*, the DG morphology. Moreover, it has been simulated that the hybrid molecules consisting of a rigid nanosphere and flexible polymer potentially stabilize the DG morphology due to the reduction of the packing frustration.[36] Since the crosslinked–linear BCPs can be considered as a rigid nanosphere–flexible BCP system, the range of the DG formation may be wider than the classical linear–linear BCPs.

Overall, the presented intramolecularly crosslinked BCPs were found to self-assemble into the microphase-separated structures according to the totally different phase behavior from that of typical linear diblock copolymer. Remarkably, the upper F_{LA} limit of the LAM formation shifted toward a higher value upon increasing the MW of the crosslinked block, eventually resulting in the unusually wide LAM region.

5.3.3 Chain packing model in A-LAM morphology

The author's special interest was elucidating what the driving force behind the formation of the unusual A-LAM morphologies is; in other words, how the asymmetric crosslinked–linear BCP molecules are packed within the A-LAM microdomains. In order to understand this issue, the author investigated the relationship between the domain widths and radius of gyration (R_g) of the SBS(*cl*) block. The small-angle neutron scattering (SANS) measurement was performed on $S_{65}BS_{28}$(*cl*)–OH as well as its linear precursor, $S_{65}BS_{28}$–OH, in the bulk state (50% mixture in deuterated polystyrene with M_n of 8,800 g mol^{-1}) to identify their R_g values (See Supporting Information for details). **Figure 5.4**(a) shows the Guinier's plots of these two samples obtained from the corresponding SANS profiles (**Figure S5.15**). The R_gs of $S_{65}BS_{28}$–OH ($R_{g,SBS}$) and $S_{65}BS_{28}$(*cl*)–OH ($R_{g,SBS(cl)}$) were determined to be 2.9 and 2.5 nm, respectively, by the approximation based on Guinier's law, which should be reliable values because $R_{g,SBS}$ (2.9 nm) is very close to that of polystyrene with the same DP in theta solvent (2.7 nm, see Supporting Information). In addition, it is worth mentioning that the R_g value decreased upon the intramolecular crosslinking, as expected.

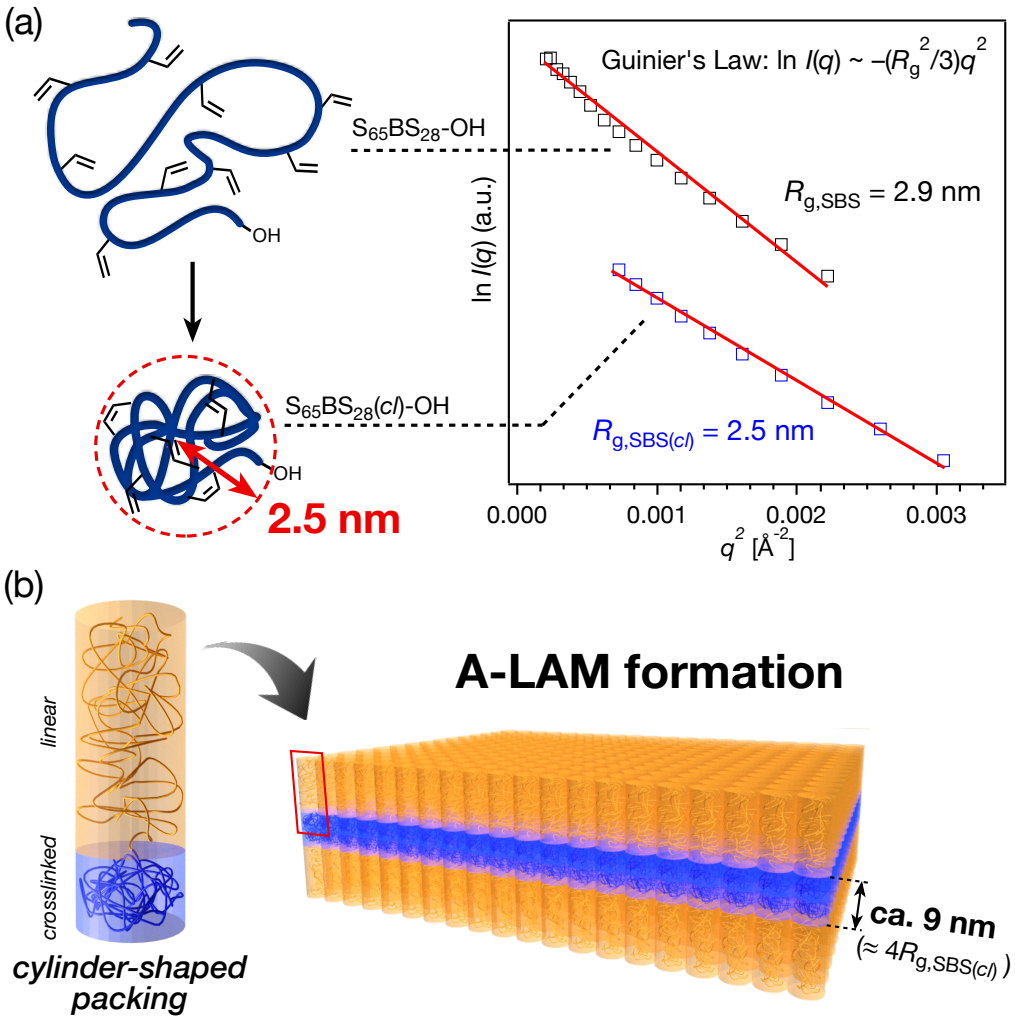

Figure 5.4. (a) Guinier plots of the SANS data measured from $S_{65}BS_{28}$–OH (black) and $S_{65}BS_{28}(cl)$–OH (blue). The R_g values were calculated based on Guinier's low: ln $I(q)$ ~ $-(R_g^2/3)q^2$. (b) Schematic representation of the cylinder-shaped packing of the crosslinked–linear BCPs and its arrangement into the A-LAM morphology.

As already mentioned, the widths of the SBS(*cl*) phases ($l_{SBS(cl)}$) for the three A-LAM morphologies formed by $S_{65}BS_{28}(cl)$–LA_{160}, $S_{65}BS_{28}(cl)$–LA_{223}, and $S_{65}BS_{28}(cl)$–LA_{459} were found to be comparable at around 9 nm irrespective of the PLA chain length. Notably, $4R_{g,SBS(cl)}$ (10.0 nm) is roughly consistent with the $l_{SBS(cl)}$ value, indicating that the conformation of the $S_{65}BS_{28}(cl)$ blocks were almost unchanged from its original single-chain state even after the arrangement into the A-LAM microdomain. Based on this fact, the author can assume the chain packing model of the intramolecularly crosslinked asymmetric BCPs as compared to that of the typical linear one. It is well known that a linear–linear BCP with an asymmetric block composition is packed into a cone shape in order to minimize the interfacial energy and maximize the conformational entropy (**Figure S5.16**(a)). Importantly, the minority block chain need to be stretched from its original state to achieve the tapered cone-shaped packing because the chain volume must be intact.[37] Upon the self-assembly of such a cone-shaped molecule, the curved morphology, like HEX and BCC, is formed. On the contrary, the asymmetric crosslinked–linear BCP is difficult to be packed into the cone shape since the chain-stretch of the intramolecularly crosslinked block is restricted by its intrinsic stiffness. As a consequence, the bulky and stiff intramolecularly crosslinked block needs to be packed into a non-tapered space, resulting in the cylinder-shaped packing of the crosslinked–linear BCP, which in turn self-assembles into the lamellar structure without any interfacial curvature (**Figures 4**(b) and **S5.16**(b)).

5.3.4 Microphase separation behavior in thin film state

Since the control over the microdomain orientation in the thin film is quite important for the pattern transfer to the underlying substrate in BCP lithography, the author finally focused on the fabrication of the perpendicularly oriented A-LAM using $S_{65}BS_{28}$(*cl*)–LA_{160}, $S_{65}BS_{28}$(*cl*)–LA_{459}, and $S_{65}BS_{28}$(*cl*)–LA_{459}. In order to quantitatively evaluate the morphology and the structural orientation inside the thin films, grazing incidence SAXS (GISAXS) was performed on the thin film samples. The author first tried the thin film preparation by spin-coating the BCPs (0.66 wt% in toluene, 2000 rpm for 1 min) onto a Si-substrate without any treatment, resulting in ca.20-nm-thick films, which were then thermally annealed at 180 °C for 30 min. However, the 2D GISAXS images of the annealed thin films showed no diffraction patterns (**Figure S5.17**), indicating that the microphase-separated structures were not successfully developed. Therefore, the author applied a polystyrene-*random*-poly(methyl methacrylate) (PS-*r*-PMMA) underlayer on the Si-substrate, by which the perpendicular LAM morphologies have been accomplished in the PS-*b*-PLA thin films.[12] In this study, PS-*r*-PMMA with an ca. 20 mol% PS composition ($PS_{0.2}$-*r*-$PMMA_{0.8}$) was grafted onto a Si-substrate (detailed preparation procedure is explained in the Supporting Information), then $S_{65}BS_{28}$(*cl*)–LAs were spin-coated on it with the same conditions as already described. The GISAXS images of the three as-cast films showed the reflection spots along the in-plane direction of thin films in addition to the weak diffraction ring, revealing the preorganization of the mixed-orientation nanostructures with a higher population of the perpendicular compartments (**Figures 5.5**(a)-(c)). After the thermal annealing, the GISAXS image of the $S_{65}BS_{28}$(*cl*)–LA_{160} thin film exhibited the intense Bragg rods (reflection stripes extended in the vertical direction) and the second-ordered reflection

spots along the in-plane direction, whose relative scattering vector lengths from the specular reflection position are 1 and 2, respectively, strongly suggesting the development of perpendicularly-oriented LAM morphologies (**Figure 5.5**(d)). By analyzing the in-plane scattering profile extracted along the $2\theta_f$ direction at α_f of 0.116°, the *d*-value was determined to be 24.7 nm, which reasonably matched with the *d* in the bulk (25.2 nm, **Figure S5.18**(a)). The GISAXS image of the $S_{65}BS_{28}(cl)$–LA_{223} thin film exhibited a similar diffraction pattern corresponding to the perpendicular LAM with the *d*-value of 29.9 nm (*d* in the bulk = 31.7 nm) (**Figures 5.5**(e) and **S5.18**(b)). Significantly, considering that the above two images contain no diffraction spots in the out-of-plane directions, the LAM structures were perfectly perpendicular throughout the entire thin film depth. On the other hand, the $S_{65}BS_{28}(cl)$–LA_{459} thin film exhibited the distinct GISAXS pattern from the other two; the 2D image contains two weak and broad reflection spots with the relative scattering vector lengths of 1 and 2 in both the in-plane and out-of-plane directions as well as the weak diffraction ring, which coincides with the LAM morphology with a mixed orientation. As the polarity of $S_{65}BS_{28}(cl)$–LA_{459} is much higher than those of the other two BCPs, the underlayer should be replaced by a more hydrophilic one to obtain the perpendicularly-oriented LAM. Interestingly, the *d* value for the horizontal LAM (d_H: 17.7 nm) was exactly half that for the perpendicular one (d_P: 35.7 nm) (**Figure S5.19**). Taking the thickness of this thin film (ca. 20 nm) into account, the d_H might correspond to the height of the horizontally expanded BCP monolayer (**Figure S5.20** (a)) while d_P should be the domain-spacing of the perpendicularly-oriented LAM structure (**Figure S5.20**(b)).

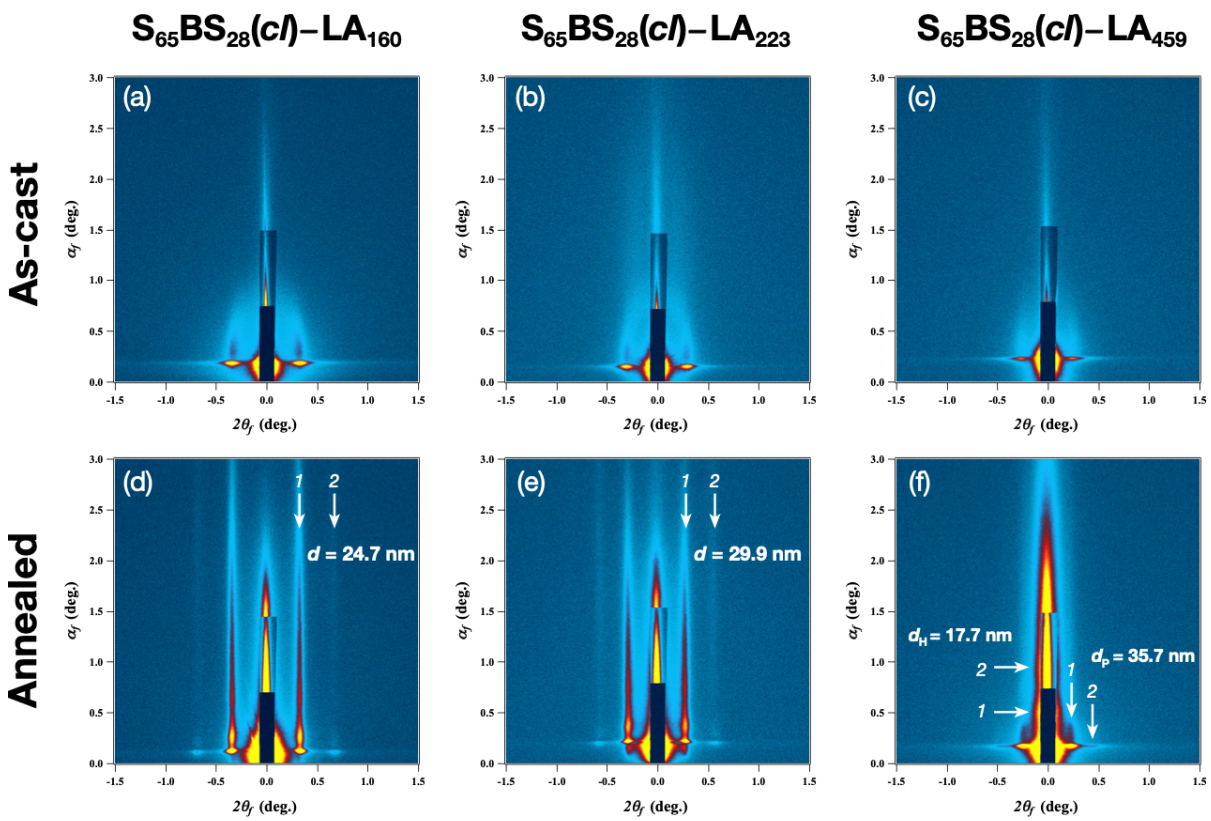

Figure 5.5. 2D GISAXS images of (a)(d) $S_{65}BS_{28}(cl)$–LA_{160}, (b)(e) $S_{65}BS_{28}(cl)$–LA_{223}, and (c)(f) $S_{65}BS_{28}(cl)$–LA_{459}. The measurement was performed on as-cast (upper) and thermally annealed (lower) thin films.

Finally, the thin film surface morphologies were visualized using atomic force microscopy (AFM) observations. The AFM phase images of the $S_{65}BS_{28}(cl)$–LA_{459} thin film showed an unclear patterned surface, supporting the GISAXS data (**Figures S5.21**). Strikingly, the fingerprint patterns were clearly observed in the phase images of the $S_{65}BS_{28}(cl)$–LA_{160} and $S_{65}BS_{28}(cl)$–LA_{223} thin films in a huge area, indeed revealing the development of the highly-organized perpendicular LAM morphologies (**Figures 5.6**(a)(b) and **S5.22**). The *d* values extracted from the 2D fast Fourier transform (FFT) profiles were 24.9 nm and 30.9 nm

for $S_{65}BS_{28}(cl)$−LA_{160} and $S_{65}BS_{28}(cl)$−LA_{223}, respectively, which are in good agreement with those estimated from GISAXS. Quite importantly, the line width of the bright LA microdomains is obviously greater than the dark SBS(*cl*) microdomain, which also surely demonstrated the formation of the A-LAM morphology in the thin film state. The highly-asymmetric patterns, especially for $S_{65}BS_{28}(cl)$−LA_{223}, can also be confirmed from the cross-sectional images extracted along with the red lines in the AFM phase images (**Figure 5.6**(c)).

Overall, the author has successfully obtained the perpendicularly-oriented A-LAM by combining the brush random copolymer layer and the simple thermal annealing. This fact strongly indicates that the intramolecularly-crosslinked BCP possesses the promising potential to be applied for the next-generation BCP lithography technology.

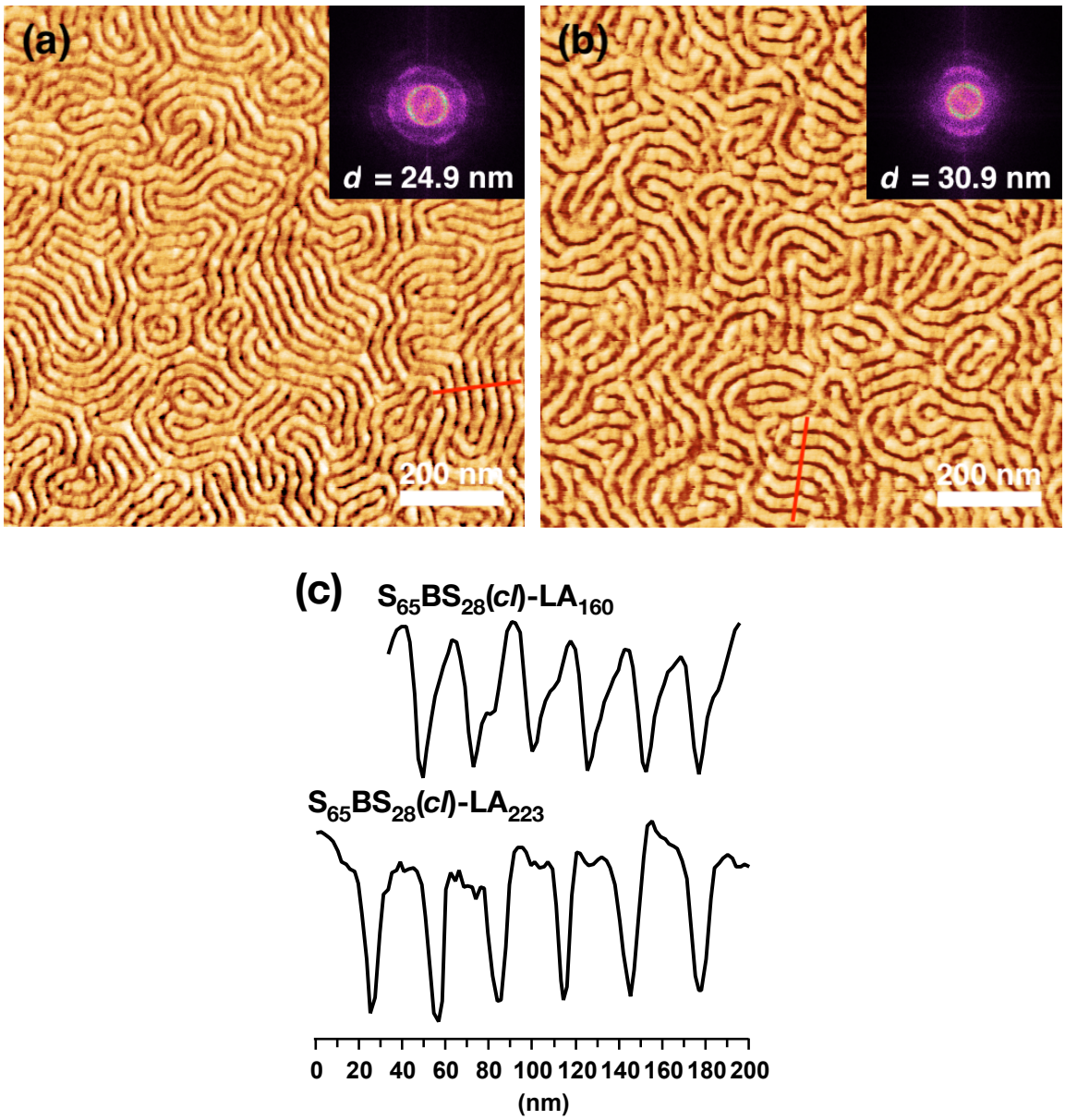

Figure 5.6. AFM phase images of (a) $S_{65}BS_{28}(cl)$–LA_{160} and (b) $S_{65}BS_{28}(cl)$–LA_{223} thin films on the $PS_{0.2}$-*stat*-$PMMA_{0.8}$ brush underlayer. The insets show the 2D FFT profiles obtained from the phase images. Scale bars are 200 nm. (c) AFM phase cross sectional images along with the red lines in (a) (upper) and (b) (lower).

5.4 Conclusion

In summary, the author have designed the compositionally asymmetric crosslinked–linear type SBS(*cl*)–LAs with a long PLA block (F_{LA} ~ 0.92) and successfully elucidated their unusual microphase-separation behavior. According to the experimentally constructed phase diagram, the LAM window of the SBS(*cl*)–LA was expanded to the wide range of the block composition in the higher F_{LA} regime, resulting in the A-LAM morphologies with an asymmetric ratio R_a up to 3.39. This unusual phase behavior arguably arose from the bulky and stiff conformation of the SBS(*cl*) block. Note that the widths of the minor SBS(*cl*) domain, corresponding to the line part of the L/S structure on the lithographic process, obtained in this study were sub-10 nm in all the MW range. Additionally, since the space width should be controllable while maintaining the line width unchanged in the L/S design for a logic device, the fact that the A-LAM morphologies were successfully obtained with the constant and varied widths of thinner and thicker domains, respectively, is quite significant for lithographic applications. The author also indicated the stabilization of the DG morphology in the crosslinked–linear BCP system; if that is the case, it provides the presented intramolecular crosslinking protocol with the remarkable opportunity to be expanded for exciting applications, such as electronic[38,39] and optical[40-42] materials. Most importantly, the intensive thin film studies by GISAXS and AFM demonstrated the capability of the SBS(*cl*)–LAs to produce the perpendicularly-oriented A-LAM morphology with the use of the PS-*r*-PMMA neutral underlayer, revealing the potential as the lithographic mask for the asymmetric L/S fabrication.

5.5 References

1. Stoykovich, M. P.; Nealey, P. F. Block Copolymers and Conventional Lithography. *Mater. Today* **2006**, *9* (9), 20–29.
2. Li, M.; Ober, C. K. Block Copolymer Patterns and Templates. *Mater. Today* **2006**, *9* (9), 30–39.
3. Jeong, S. J.; Kim, J. Y.; Kim, B. H.; Moon, H. S.; Kim, S. O. Directed Self-Assembly of Block Copolymers for next Generation Nanolithography. *Mater. Today* **2013**, *16* (12), 468–476.
4. Koo, K.; Ahn, H.; Kim, S. W.; Ryu, D. Y.; Russell, T. P. Directed Self-Assembly of Block Copolymers in the Extreme: Guiding Microdomains from the Small to the Large. *Soft Matter* **2013**, *9* (38), 9059–9071.
5. Bates, C. M.; Maher, M. J.; Janes, D. W.; Ellison, C. J.; Willson, C. G. Block Copolymer Lithography. *Macromolecules* **2014**, *47* (1), 2–12.
6. Rodwogin, M. D.; Spanjers, C. S.; Leighton, C.; Hillmyer, M. A. Polylactide-Poly(dimethylsiloxane)-Polylactide Triblock Copolymers as Multifunctional Materials for Nanolithographic Applications. *ACS Nano* **2010**, *4* (2), 725–732.
7. Luo, Y.; Montarnal, D.; Kim, S.; Shi, W.; Barteau, K. P.; Pester, C. W.; Hustad, P. D.; Christianson, M. D.; Fredrickson, G. H.; Kramer, E. J.; Hawker, C. J. Poly(Dimethylsiloxane-*b*-Methyl Methacrylate): A Promising Candidate for Sub-10 nm Patterning. *Macromolecules* **2015**, *48* (11), 3422–3430.
8. Cushen, J. D.; Otsuka, I.; Bates, C. M.; Halila, S.; Fort, S.; Rochas, C.; Easley, J. A.; Rausch, E. L.; Thio, A.; Borsali, R.; Willson, C. G.; Ellison, C. J. Oligosaccharide/Silicon-Containing Block Copolymers with 5 nm Features for Lithographic Applications. *ACS Nano* **2012**, *6* (4), 3424–3433.
9. Kwak, J.; Mishra, A. K.; Lee, J.; Lee, K. S.; Choi, C.; Maiti, S.; Kim, M.; Kim, J. K. Fabrication of Sub-3 nm Feature Size Based on Block Copolymer Self-Assembly for Next-Generation Nanolithography. *Macromolecules* **2017**, *50* (17), 6813–6818.
10. Zhang, W.; Huang, M.; Abdullatif, S. Al; Chen, M.; Shao-Horn, Y.; Johnson, J. A. Reduction of (Meth)acrylate-Based Block Copolymers Provides Access to Self-Assembled Materials with Ultrasmall Domains. *Macromolecules* **2018**, *51* (17), 6757–6763.
11. Poelma, J. E.; Ono, K.; Miyajima, D.; Aida, T.; Satoh, K.; Hawker, C. J. Cyclic Block Copolymers for Controlling Feature Sizes in Block Copolymer Lithography. *ACS Nano* **2012**, *6* (12), 10845–10854.
12. Isono, T.; Otsuka, I.; Kondo, Y.; Halila, S.; Fort, S.; Rochas, C.; Satoh, T.; Borsali, R.; Kakuchi, T. Sub-10 nm Nano-Organization in AB_2- and AB_3-Type Miktoarm Star Copolymers Consisting of Maltoheptaose and Polycaprolactone. *Macromolecules* **2013**, *46* (4), 1461–1469.

13. Shi, W.; Tateishi, Y.; Li, W.; Hawker, C. J.; Fredrickson, G. H.; Kramer, E. J. Producing Small Domain Features Using Miktoarm Block Copolymers with Large Interaction Parameters. *ACS Macro Lett.* **2015**, *4* (11), 1287–1292.
14. Yue, K.; Liu, C.; Huang, M.; Huang, J.; Zhou, Z.; Wu, K.; Liu, H.; Lin, Z.; Shi, A. C.; Zhang, W. Bin; Cheng, S. Z. D. Self-Assembled Structures of Giant Surfactants Exhibit a Remarkable Sensitivity on Chemical Compositions and Topologies for Tailoring Sub-10 nm Nanostructures. *Macromolecules* **2017**, *50* (1), 303–314.
15. Gartner, T. E.; Kubo, T.; Seo, Y.; Tansky, M.; Hall, L. M.; Sumerlin, B. S.; Epps, T. H. Domain Spacing and Composition Profile Behavior in Salt-Doped Cyclic vs Linear Block Polymer Thin Films: A Joint Experimental and Simulation Study. *Macromolecules* **2017**, *50* (18), 7169–7176.
16. Mansky, P.; Liu, Y.; Huang, E.; Russell, T. P.; Hawker, C. Controlling Polymer-Surface Interactions with Random Copolymer Brushes. *Science* **1997**, *275* (5305), 1458–1460.
17. Bates, C. M.; Seshimo, T.; Maher, M. J.; Durand, W. J.; Cushen, J. D.; Dean, L. M.; Blachut, G.; Ellison, C. J.; Willson, C. G. Polarity-Switching Top Coats Enable Orientation of Sub-10-nm Block Copolymer Domains. *Science* **2012**, *338* (6108), 775–779.
18. Kim, S.; Wang, H. S.; Choe, Y.; Choi, S. H.; Bang, J. Controlling the Microdomain Orientation in Block Copolymer Thin Films via Cross-Linkable Random Copolymer Neutral Layer. *Polym. J.* **2016**, *48* (4), 333–340.
19. Nakatani, R.; Takano, H.; Chandra, A.; Yoshimura, Y.; Wang, L.; Suzuki, Y.; Tanaka, Y.; Maeda, R.; Kihara, N.; Minegishi, S.; Miyagi, K.; Kasahara, Y.; Sato, H.; Seino, Y.; Azuma, T.; Yokoyama, H.; Ober, C. K.; Teruaki, H. Perpendicular Orientation Control without Interfacial Treatment of RAFT-Synthesized High-χ Block Copolymer Thin Films with Sub-10 nm Features Prepared via Thermal Annealing. *ACS Appl. Mater. Interfaces* **2017**, *9* (37), 31266–31278.
20. Lee, W.; Kim, Y.; Jo, S.; Park, S.; Ahn, H.; Ryu, D. Y. Irreversible Physisorption of PS-*b*-PMMA Copolymers on Substrates for Balanced Interfacial Interactions as a Versatile Surface Modification. *ACS Macro Lett.* **2019**, 519–524.
21. Han, S. H.; Pryamitsyn, V.; Bae, D.; Kwak, J.; Ganesan, V.; Kim, J. K. Highly Asymmetric Lamellar Nanopatterns via Block Copolymer Blends Capable of Hydrogen Bonding. *ACS Nano* **2012**, *6* (9), 7966–7972.
22. Shi, W.; Hamilton, A. L.; Delaney, K. T.; Fredrickson, G. H.; Kramer, E. J.; Ntaras, C.; Avgeropoulos, A.; Lynd, N. A. Creating Extremely Asymmetric Lamellar Structures via Fluctuation-Assisted Unbinding of Miktoarm Star Block Copolymer Alloys. *J. Am. Chem. Soc.* **2015**, *137* (19), 6160–6163.
23. Huang, M.; Yue, K.; Huang, J.; Liu, C.; Zhou, Z.; Wang, J.; Wu, K.; Shan, W.; Shi, A. C.; Cheng, S. Z. D. Highly Asymmetric Phase Behaviors of Polyhedral Oligomeric

Silsesquioxane-Based Multiheaded Giant Surfactants. *ACS Nano* **2018**, *12* (2), 1868–1877.

24. Lo, T. Y.; Krishnan, M. R.; Lu, K.-Y.; Ho, R.-M. Silicon-containing block copolymers for lithographic applications. *Prog. Polym. Sci.* **2018**, *77*, 19–68.
25. Son, J. G.; Gotrik, K. W.; Ross, C. A. High-Aspect-Ratio Perpendicular Orientation of PS-*b*-PDMS Thin Films under Solvent Annealing. *ACS Macro Lett.* **2012**, *1* (11), 1279–1284.
26. Matsen, M. W.; Schick, M. Microphase Separation in Starblock Copolymer Melts. *Macromolecules* **1994**, *27* (23), 6761–6767.
27. Grason, G. M.; Kamien, R. D. Interfaces in Diblocks: A Study of Miktoarm Star Copolymers. *Macromolecules* **2004**, *37* (19), 7371–7380.
28. Hosono, N.; Gillissen, M. A. J.; Li, Y.; Sheiko, S. S.; Palmans, A. R. A.; Meijer, E. W. Orthogonal Self-Assembly in Folding Block Copolymers. *J. Am. Chem. Soc.* **2013**, *135* (1), 501–510.
29. Perez-Baena, I.; Asenjo-Sanz, I.; Arbe, A.; Moreno, A. J.; Lo Verso, F.; Colmenero, J.; Pomposo, J. A. Efficient Route to Compact Single-Chain Nanoparticles: Photoactivated Synthesis via Thiol-Yne Coupling Reaction. *Macromolecules* **2014**, *47* (23), 8270–8280.
30. Zalusky, A. S.; Olayo-Valles, R.; Wolf, J. H.; Hillmyer, M. A. Ordered Nanoporous Polymers from Polystyrene-Polylactide Block Copolymers. *J. Am. Chem. Soc.* **2002**, *124* (43), 12761–12773.
31. Keen, I.; Yu, A.; Cheng, H.; Jack, K. S.; Nicholson, T. M.; Whittaker, A. K.; Blakey, I. Control of the Orientation of Symmetric Poly(styrene)-*block*-Poly(D,L-lactide) Block Copolymers Using Statistical Copolymers of Dissimilar Composition. *Langmuir* **2012**, *28* (45), 15876–15888.
32. Zhang H.; Ruckenstein, E. Selective Living Anionic Polymerization of a Novel Bifunctional Monomer 4-(Vinylphenyl)-1-butene and the Preparation of Uniform Size Functional Polymers and Amphiphilic Block Copolymers. *Macromolecules*, **1999**, *32* (17), 5495–5500.
33. Burdyńska, J.; Li, Y.; Aggarwal, A. V.; Höger, S.; Sheiko, S. S.; Matyjaszewski, K. Synthesis and Arm Dissociation in Molecular Stars with a Spoked Wheel Core and Bottlebrush Arms. *J. Am. Chem. Soc.* **2014**, *136* (36), 12762–12770.
34. Watanabe, K.; Katsuhara, S.; Mamiya, H.; Yamamoto, T.; Tajima, K.; Isono, T.; Satoh, T. Downsizing Feature of Microphase-Separated Structures via Intramolecular Crosslinking of Block Copolymers. *Chem. Sci.* **2019**, *10* (11), 3330–3339.
35. Hamley, I. W.; Castelletto, V. Small-Angle Scattering of Block Copolymers in the Melt, Solution and Crystal States. *Prog. Polym. Sci.* **2004**, *29* (9), 909–948.
36. Iacovella, C. R.; Horsch, M. A.; Glotzer, S. C. Local Ordering of Polymer-Tethered Nanospheres and Nanorods and the Stabilization of the Double Gyroid Phase. *J. Chem. Phys.* **2008**, *129* (4).

37. Grason, G. M. The Packing of Soft Materials: Molecular Asymmetry, Geometric Frustration and Optimal Lattices in Block Copolymer Melts. *Phys. Rep.* **2006**, *433* (1), 1–64.
38. Crossland, E. J. W.; Kamperman, M.; Nedelcu, M.; Ducati, C.; Wiesner, U.; Smilgies, D. M.; Toombes, G. E. S.; Hillmyer, M. A.; Ludwigs, S.; Steiner, U.; Snaith, H. J. A Bicontinuous Double Gyroid Hybrid Solar Cell. *Nano Lett.* **2009**, *9* (8), 2807–2812.
39. Robbins, S. W.; Beaucage, P. A.; Sai, H.; Tan, K. W.; Werner, J. G.; Sethna, J. P.; DiSalvo, F. J.; Gruner, S. M.; Van Dover, R. B.; Wiesner, U. Block Copolymer Self-Assembly-Directed Synthesis of Mesoporous Gyroidal Superconductors. *Sci. Adv.* **2016**, *2* (1), e1501119.
40. Urbas, A. M.; Maldovan, M.; DeRege, P.; Thomas, E. L. Bicontinuous Cubic Block Copolymer Photonic Crystals. *Adv. Mater.* **2002**, *14* (24), 1850–1853.
41. Vignolini, S.; Yufa, N. A.; Cunha, P. S.; Guldin, S.; Rushkin, I.; Stefik, M.; Hur, K.; Wiesner, U.; Baumberg, J. J.; Steiner, U. A 3D Optical Metamaterial Made by Self-Assembly. *Adv. Opt. Mater.* **2012**, *24* (10), 23–27.
42. Dolan, J. A.; Wilts, B. D.; Vignolini, S.; Baumberg, J. J.; Steiner, U.; Wilkinson, T. D. Optical Properties of Gyroid Structured Materials: From Photonic Crystals to Metamaterials. *Adv. Opt. Mater.* **2015**, *3* (1), 12–32.

5.6 Supporting Information

5.6.1 Experimental

Synthesis of *ω*-end hydroxy-functionalized statistical copolymer of S and BS ($S_{33}BS_{14}$−OH). Method A was used for the living anionic copolymerization of S (5.5 g, 53 mmol) and BS (3.6 g, 23 mmol) with *n*-BuLi (1.21 mL, 1.61 mmol as a 1.33 mol L^{-1} stock solution in *n*-hexane) and Br−O−TIPS (1.53 g, 5.17 mmol) in mixture solvent of dry toluene (100 mL) and dry THF (50 mL) for 6 h followed by the deprotection with TBAF (15.5 mL, 15.5 mmol as a 1.0 mol L^{-1} stock solution in THF) in dry THF (50 mL) to give $S_{33}BS_{14}$−OH. Yield: 8.02 g (88 %). $M_{n,NMR}$ = 5,760 ($CDCl_3$), f_{BS} = 0.30, $M_{n,SEC}$ = 6,070 (THF), $Đ$ = 1.04 (THF).

Synthesis of *ω*-end hydroxy-functionalized statistical copolymer of S and BS ($S_{65}BS_{28}$−OH). Method A was used for the living anionic copolymerization of S (5.5 g, 53 mmol) and BS (3.6 g, 23 mmol) with *n*-BuLi (0.92 mL, 0.82 mmol as a 0.89 mol L^{-1} stock solution in *n*-hexane) and Br−O−TIPS (1.41 g, 4.79 mmol) in mixture solvent of dry toluene (100 mL) and dry THF (50 mL) for 6 h followed by the deprotection with TBAF (14.4 mL, 14.4 mmol as a 1.0 mol L^{-1} stock solution in THF) in dry THF (50 mL) to give $S_{65}BS_{28}$−OH. Yield: 8.02 g (88 %). $M_{n,NMR}$ = 11,100 ($CDCl_3$), f_{BS} = 0.30, $M_{n,SEC}$ = 11,200 (THF), $Đ$ = 1.04 (THF).

Intramolecular crosslinking of $S_{33}BS_{14}$−OH via olefin metathesis reaction. Method B was used for the intramolecular crosslinking of $S_{33}BS_{14}$−OH ($M_{n,NMR}$ = 5,760, 1.50 g, 3.74 mmol olefin-containing units) with G2 (31.7 mg, 37.4 μmol) in dry CH_2Cl_2 (3000 mL) for 3 h to give $S_{33}BS_{14}$(*cl*)−OH as a white solid (1.20 g, 80.0 %)). The product was further

purified by preparative SEC prior to each measurement. $M_{n,SEC}$ = 4,880 (THF), $Đ$ = 1.09 (THF), $conv._{olefin}$ = 86%.

Intramolecular crosslinking of $S_{65}BS_{28}$−OH via olefin metathesis reaction. Method B was used for the intramolecular crosslinking of $S_{65}BS_{28}$−OH ($M_{n,NMR}$ = 5,760, 1.00 g, 2.49 mmol olefin-containing units) with G2 (21.2 mg, 24.9 μmol) in dry CH_2Cl_2 (3330 mL) for 3 h to give $S_{65}BS_{28}$(*cl*)−OH as a white solid (740 mg, 74.0 %)). The product was further purified by preparative SEC prior to each measurement. $M_{n,SEC}$ = 7,870 (THF), $Đ$ = 1.06 (THF), $conv._{olefin}$ = 88%.

Synthesis of block copolymer consisting of SBS(*cl*) and poly(*rac*-LA) ($S_{21}BS_8$(*cl*)−LA_{45}) via ring-opening polymerization of *rac*-LA using $S_{21}BS_8$(*cl*)−OH as an initiator. Method C was used for the ring-opening polymerization of *rac*-LA (375 mg, 2.60 mmol) with $S_{21}BS_8$(*cl*)−OH ($M_{n,NMR}$ = 3,500, 150 mg, 42.9 μmol) and DBU (3.9 μL, 26 μmol) in dry CH_2Cl_2 (5.2 mL) for 15 min to give $S_{21}BS_8$(*cl*)−LA_{45} as a white solid (409 mg, 77.9%)). The product was further purified by preparative SEC prior to the intramolecular crosslinking reaction and each measurement. $M_{n,NMR}$ = 10,100 ($CDCl_3$), F_{LA} = 0.65, $M_{n,SEC}$ = 15,500 (THF), $Đ$ = 1.04 (THF).

Synthesis of block copolymer consisting of SBS(*cl*) and poly(*rac*-LA) ($S_{21}BS_8$(*cl*)−LA_{70}) via ring-opening polymerization of *rac*-LA using $S_{21}BS_8$(*cl*)−OH as an initiator. Method C was used for the ring-opening polymerization of *rac*-LA (488 mg, 3.38 mmol) with $S_{21}BS_8$(*cl*)−OH ($M_{n,NMR}$ = 3,500, 130 mg, 37.1 μmol) and DBU (5.1 μL, 34 μmol) in dry CH_2Cl_2 (6.8 mL) for 25 min to give $S_{21}BS_8$(*cl*)−LA_{70} as a white solid (469 mg, 75.9%)). The product was further purified by preparative SEC prior to the intramolecular crosslinking

reaction and each measurement. Conversion = 85%, $M_{n,NMR}$ = 20,900 ($CDCl_3$), F_{LA} = 0.65, $M_{n,SEC}$ = 11,700 (THF), $Đ$ = 1.05 (THF).

Synthesis of block copolymer consisting of SBS(*cl*) and poly(*rac*-LA) ($S_{21}BS_8$(*cl*)−LA_{110}) via ring-opening polymerization of *rac*-LA using $S_{21}BS_8$(*cl*)−OH as an initiator. Method C was used for the ring-opening polymerization of *rac*-LA (531 mg, 3.69 mmol) with $S_{21}BS_8$(*cl*)−OH ($M_{n,NMR}$ = 3,500, 85 mg, 24.3 μmol) and DBU (5.5 μL, 37 μmol) in dry CH_2Cl_2 (7.4 mL) for 35 min to give $S_{21}BS_8$(*cl*)−LA_{70} as a white solid (407 mg, 66.1%)). The product was further purified by preparative SEC prior to the intramolecular crosslinking reaction and each measurement. Conversion = 76%, $M_{n,NMR}$ = 19,400 ($CDCl_3$), F_{LA} = 0.82, $M_{n,SEC}$ = 25,200 (THF), $Đ$ = 1.03 (THF).

Synthesis of block copolymer consisting of SBS(*cl*) and poly(*rac*-LA) ($S_{33}BS_{14}$(*cl*)−LA_{33}) via ring-opening polymerization of *rac*-LA using $S_{33}BS_{14}$(*cl*)−OH as an initiator. Method C was used for the ring-opening polymerization of *rac*-LA (293 mg, 2.03 mmol) with $S_{33}BS_{14}$(*cl*)−OH ($M_{n,NMR}$ = 5,600, 234 mg, 41.8 μmol) and DBU (3.0 μL, 20 μmol) in dry CH_2Cl_2 (4.1 mL) for 12 min to give $S_{33}BS_{14}$(*cl*)−LA_{33} as a white solid (386 mg, 73.2%)). The product was further purified by preparative SEC prior to the intramolecular crosslinking reaction and each measurement. Conversion = 85%, $M_{n,NMR}$ = 10,400 ($CDCl_3$), F_{LA} = 0.46, $M_{n,SEC}$ = 14,900 (THF), $Đ$ = 1.06 (THF).

Synthesis of block copolymer consisting of SBS(*cl*) and poly(*rac*-LA) ($S_{33}BS_{14}$(*cl*)−LA_{72}) via ring-opening polymerization of *rac*-LA using $S_{33}BS_{14}$(*cl*)−OH as an initiator. Method C was used for the ring-opening polymerization of *rac*-LA (375 mg, 2.60 mmol) with $S_{33}BS_{14}$(*cl*)−OH ($M_{n,NMR}$ = 5,600, 150 mg, 26.8 μmol) and DBU (3.9 μL, 26

μmol) in dry CH_2Cl_2 (5.2 mL) for 23 min to give $S_{33}BS_{14}(cl)$–LA_{72} as a white solid (415 mg, 79.0%)). The product was further purified by preparative SEC prior to the intramolecular crosslinking reaction and each measurement. Conversion = 79%, $M_{n,NMR}$ = 16,000 ($CDCl_3$), F_{LA} = 0.65, $M_{n,SEC}$ = 23,200 (THF), $Đ$ = 1.07 (THF).

Synthesis of block copolymer consisting of SBS(*cl*) and poly(*rac*-LA) ($S_{33}BS_{14}(cl)$–LA_{112}) via ring-opening polymerization of *rac*-LA using $S_{33}BS_{14}(cl)$–OH as an initiator. Method C was used for the ring-opening polymerization of *rac*-LA (479 mg, 3.32 mmol) with $S_{33}BS_{14}(cl)$–OH ($M_{n,NMR}$ = 5,600, 130 mg, 23.2 μmol) and DBU (5.0 μL, 33 μmol) in dry CH_2Cl_2 (6.6 mL) for 35 min to give $S_{33}BS_{14}(cl)$–LA_{112} as a white solid (446 mg, 73.2%)). The product was further purified by preparative SEC prior to the intramolecular crosslinking reaction and each measurement. Conversion = 82%, $M_{n,NMR}$ = 21,800 ($CDCl_3$), F_{LA} = 0.74, $M_{n,SEC}$ = 29,800 (THF), $Đ$ = 1.05 (THF).

Synthesis of block copolymer consisting of SBS(*cl*) and poly(*rac*-LA) ($S_{33}BS_{14}(cl)$–LA_{201}) via ring-opening polymerization of *rac*-LA using $S_{33}BS_{14}(cl)$–OH as an initiator. Method C was used for the ring-opening polymerization of *rac*-LA (531 mg, 3.69 mmol) with $S_{33}BS_{14}(cl)$–OH ($M_{n,NMR}$ = 5,600, 85.0 mg, 24.3 μmol) and DBU (5.5 μL, 37 μmol) in dry CH_2Cl_2 (7.4 mL) for 55 min to give $S_{33}BS_{14}(cl)$–LA_{201} as a white solid (451 mg, 73.2%)). The product was further purified by preparative SEC prior to the intramolecular crosslinking reaction and each measurement. Conversion = 88%, $M_{n,NMR}$ = 34,500 ($CDCl_3$), F_{LA} = 0.82, $M_{n,SEC}$ = 39,900 (THF), $Đ$ = 1.06 (THF).

Synthesis of block copolymer consisting of SBS(*cl*) and poly(*rac*-LA) ($S_{65}BS_{28}(cl)$–LA_{74}) via ring-opening polymerization of *rac*-LA using $S_{65}BS_{28}(cl)$–OH as

an initiator. Method C was used for the ring-opening polymerization of *rac*-LA (143 mg, 990 μmol) with $S_{65}BS_{28}$(*cl*)−OH ($M_{n,NMR}$ = 10,800, 100 mg, 9.35 μmol) and DBU (1.5 μL, 1.0 μmol) in dry CH_2Cl_2 (2.0 mL) for 20 min to give $S_{65}BS_{28}$(*cl*)−LA_{74} as a white solid (181 mg, 74.5%)). The product was further purified by preparative SEC prior to the intramolecular crosslinking reaction and each measurement. Conversion = 68%, $M_{n,NMR}$ = 21,500 ($CDCl_3$), F_{LA} = 0.50, $M_{n,SEC}$ = 18,800 (THF), $Đ$ = 1.09 (THF).

Synthesis of block copolymer consisting of SBS(*cl*) and poly(*rac*-LA) ($S_{65}BS_{28}$(*cl*)−LA_{160}) via ring-opening polymerization of *rac*-LA using $S_{65}BS_{28}$(*cl*)−OH as an initiator. Method C was used for the ring-opening polymerization of *rac*-LA (185 mg, 1.28 mmol) with $S_{65}BS_{28}$(*cl*)−OH ($M_{n,NMR}$ = 10,800, 65.0 mg, 6.07 μmol) and DBU (1.9 μL, 1.3 μmol) in dry CH_2Cl_2 (2.6 mL) for 45 min to give $S_{65}BS_{28}$(*cl*)−LA_{160} as a white solid (184 mg, 73.6%)). The product was further purified by preparative SEC prior to the intramolecular crosslinking reaction and each measurement. Conversion = 74%, $M_{n,NMR}$ = 33,800 ($CDCl_3$), F_{LA} = 0.68, $M_{n,SEC}$ = 32,100 (THF), $Đ$ = 1.06 (THF).

Synthesis of block copolymer consisting of SBS(*cl*) and poly(*rac*-LA) ($S_{65}BS_{28}$(*cl*)−LA_{223}) via ring-opening polymerization of *rac*-LA using $S_{65}BS_{28}$(*cl*)−OH as an initiator. Method C was used for the ring-opening polymerization of *rac*-LA (213 mg, 1.48 mmol) with $S_{65}BS_{28}$(*cl*)−OH ($M_{n,NMR}$ = 10,800, 50.0 mg, 4.67 μmol) and DBU (2.2 μL, 1.5 μmol) in dry CH_2Cl_2 (3.0 mL) for 65 min to give $S_{65}BS_{28}$(*cl*)−LA_{223} as a white solid (185 mg, 93%)). The product was further purified by preparative SEC prior to the intramolecular crosslinking reaction and each measurement. Conversion = 78%, $M_{n,NMR}$ = 42,900 ($CDCl_3$), F_{LA} = 0.75, $M_{n,SEC}$ = 40,700 (THF), $Đ$ = 1.06 (THF).

Synthesis of block copolymer consisting of SBS(*cl*) and poly(*rac*-LA) ($S_{65}BS_{28}$(*cl*)−LA_{459}) via ring-opening polymerization of *rac*-LA using $S_{65}BS_{28}$(*cl*)−OH as an initiator. Method C was used for the ring-opening polymerization of *rac*-LA (249 mg, 1.72 mmol) with $S_{65}BS_{28}$(*cl*)−OH ($M_{n,NMR}$ = 10,800, 35.0 mg, 3.27 μmol) and DBU (2.6 μL, 1.7 μmol) in dry CH_2Cl_2 (3.4 mL) for 90 min to give $S_{65}BS_{28}$(*cl*)−LA_{459} as a white solid (232 mg, 81.4%)). The product was further purified by preparative SEC prior to the intramolecular crosslinking reaction and each measurement. Conversion = 83%, $M_{n,NMR}$ = 76,900 ($CDCl_3$), F_{LA} = 0.86, $M_{n,SEC}$ = 56,000 (THF), $Đ$ = 1.09 (THF).

Synthesis of block copolymer consisting of SBS(*cl*) and poly(*rac*-LA) ($S_{65}BS_{28}$(*cl*)−LA_{684}) via ring-opening polymerization of *rac*-LA using $S_{65}BS_{28}$(*cl*)−OH as an initiator. Method C was used for the ring-opening polymerization of *rac*-LA (249 mg, 1.72 mmol) with $S_{65}BS_{28}$(*cl*)−OH ($M_{n,NMR}$ = 10,800, 25.0 mg, 2.34 μmol) and DBU (2.6 μL, 1.7 μmol) in dry CH_2Cl_2 (3.4 mL) for 110 min to give $S_{65}BS_{28}$(*cl*)−LA_{684} as a white solid (236 mg, 86.2%)). Conversion = 92%, $M_{n,NMR}$ = 109,000 ($CDCl_3$), F_{LA} = 0.90, $M_{n,SEC}$ = 60,600 (THF), $Đ$ = 1.14 (THF).

Synthesis of block copolymer consisting of SBS(*cl*) and poly(*rac*-LA) ($S_{65}BS_{28}$(*cl*)−LA_{923}) via ring-opening polymerization of *rac*-LA using $S_{65}BS_{28}$(*cl*)−OH as an initiator. Method C was used for the ring-opening polymerization of *rac*-LA (257 mg, 1.78 mmol) with $S_{65}BS_{28}$(*cl*)−OH ($M_{n,NMR}$ = 10,800, 18 mg, 1.68 μmol) and DBU (2.7 μL, 1.8 μmol) in dry CH_2Cl_2 (3.6 mL) for 140 min to give $S_{65}BS_{28}$(*cl*)−LA_{923} as a white solid (226 mg, 82.1%)). The product was further purified by preparative SEC prior to the intramolecular

crosslinking reaction and each measurement. Conversion = 82%, $M_{n,NMR}$ = 144,000 ($CDCl_3$), F_{LA} = 0.92, $M_{n,SEC}$ = 60,200 (THF), $Đ$ = 1.10 (THF).

5.6.2 Additional data

Table S5.1. Characterization data of SBS−OHs and SBS(*cl*)−OHs

sample name	f_{BS} [a]	conv.$_{olefin}$ [a] (%)	$M_{n,NMR}$ [a]	$M_{n,SEC}$ [b]	$Đ$ [b]	R_g [d] (nm)
$S_{21}BS_8$−OH	0.29	–	3,600	3,920	1.08	–
$S_{21}BS_8$(*cl*)−OH	–	85	3,500	2,790	1.18	–
$S_{33}BS_{14}$−OH	0.30	–	5,760	6,070	1.04	–
$S_{33}BS_{14}$(*cl*)−OH	–	86	5,600	4,880	1.09	–
$S_{65}BS_{28}$−OH	0.30	–	11,100	11,200	1.04	2.9
$S_{65}BS_{28}$(*cl*)−OH	–	88	10,800	7,870	1.06	2.5

[a]Determined by ^{1}H NMR in $CDCl_3$. [b]Determined by SEC in THF using polystyrene standards. [c]Determined by DSC at the heating rate of 10 °C min^{-1}. [d]Determined by SANS in the bulk.

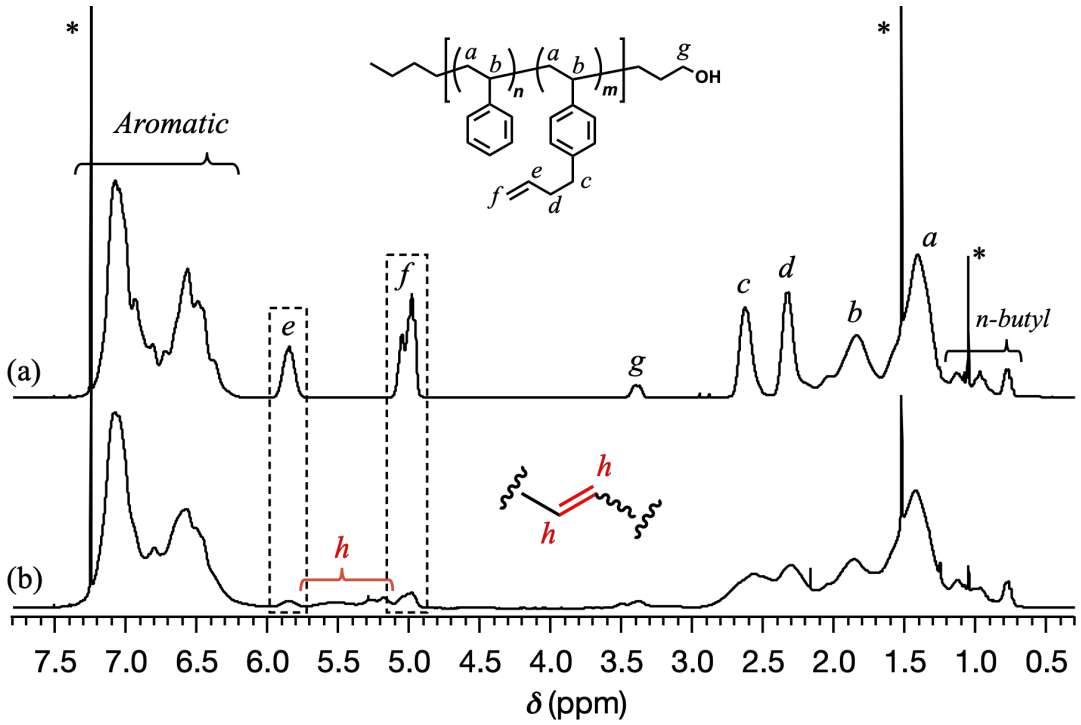

Figure S5.1. ^{1}H NMR spectra of (a) $S_{21}BS_8$−OH and (b) $S_{21}BS_8$(*cl*)−OH in $CDCl_3$ (400 MHz).

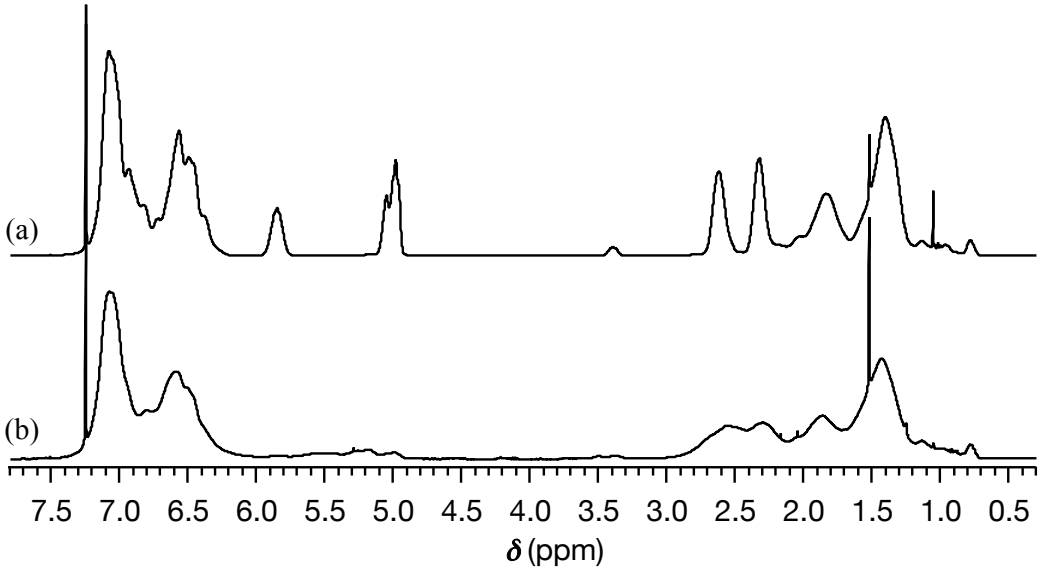

Figure S5.2. ^{1}H NMR spectra of (a) $S_{33}BS_{14}$–OH and (b) $S_{33}BS_{14}$(*cl*)–OH in $CDCl_3$ (400 MHz).

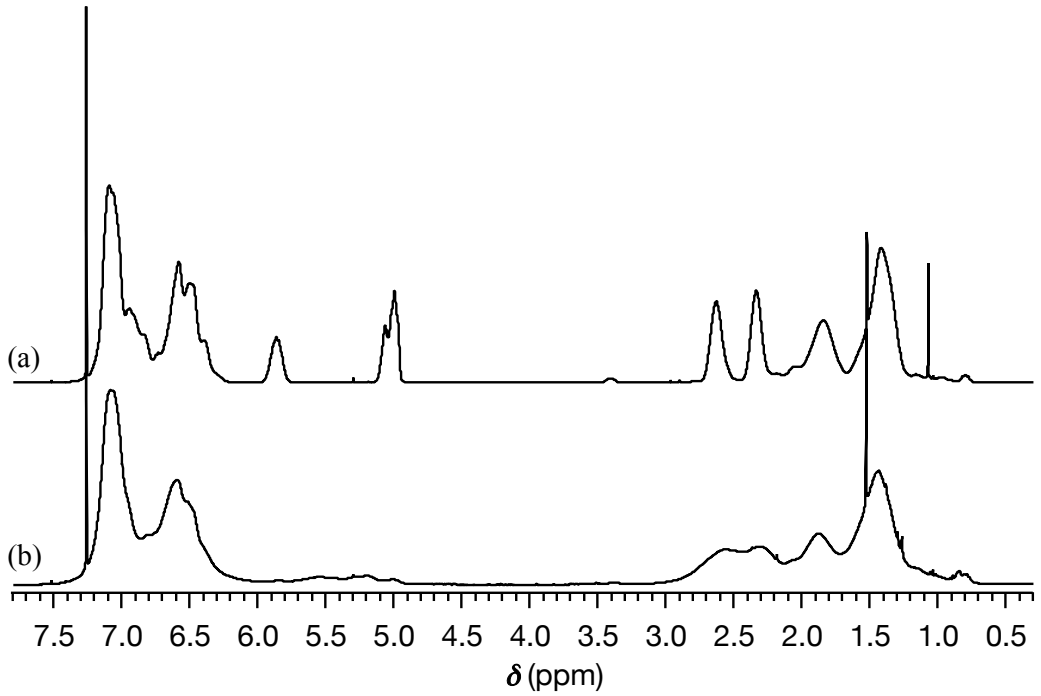

Figure S5.3. ^{1}H NMR spectra of (a) $S_{65}BS_{28}$–OH and (b) $S_{65}BS_{28}$(*cl*)–OH in $CDCl_3$ (400 MHz).

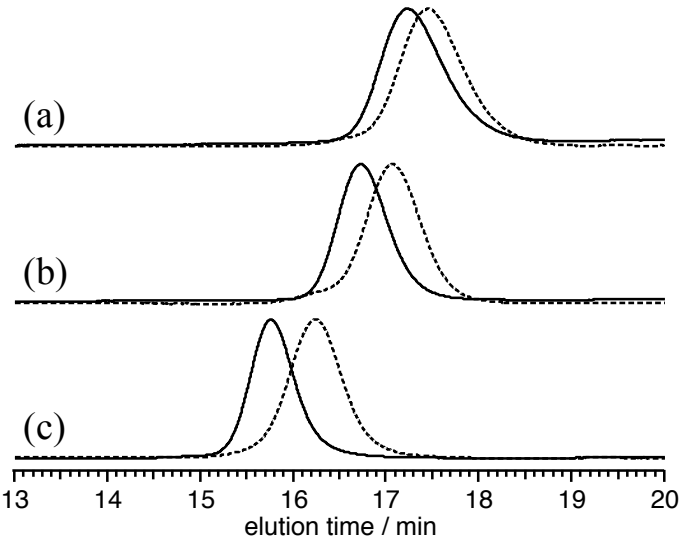

Figure S5.4. SEC traces of (a) $S_{21}B_8$–OH and $S_{21}BS_8$(*cl*)–OH, (b) $S_{33}BS_{14}$–OH and $S_{33}BS_{14}$(*cl*)–OH, and (c) $S_{65}BS_{28}$–OH and $S_{65}BS_{28}$(*cl*)–OH (eluent, THF; flow rate, 1.0 mL min^{-1}). SBS–OHs and SBS(*cl*)–OHs are presented using solid and dashed lines, respectively.

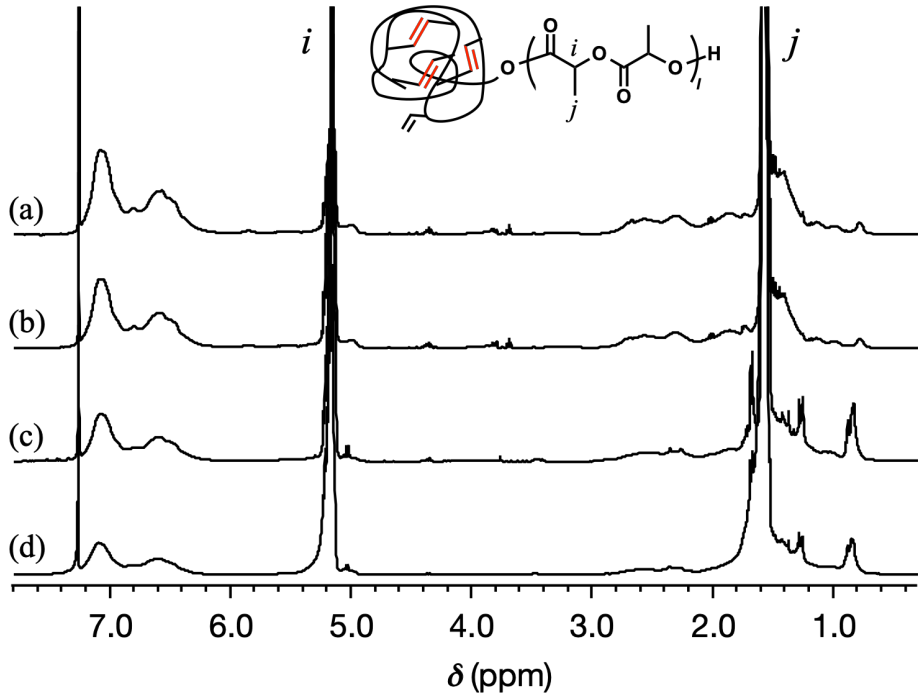

Figure S5.5. ^{1}H NMR spectra of (a) $S_{21}BS_8$–LA_{20}, (b) $S_{21}BS_8$(*cl*)–LA_{45}, (c) $S_{21}BS_8$(*cl*)–LA_{75}, and (d) $S_{21}BS_8$(*cl*)–LA_{115} in $CDCl_3$ (400 MHz).

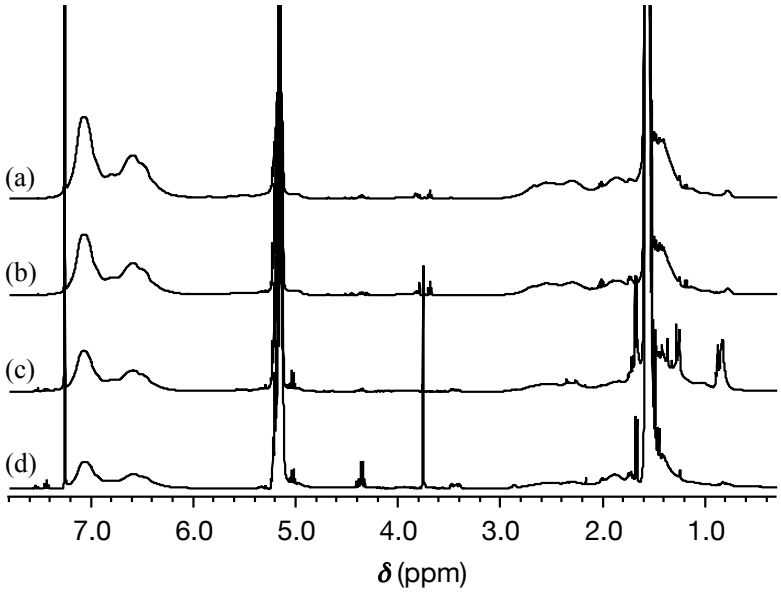

Figure S5.6. ^{1}H NMR spectra of (a) $S_{33}BS_{14}$–LA_{33}, (b) $S_{33}BS_{14}$(*cl*)–LA_{72}, (c) $S_{33}BS_{14}$(*cl*)–LA_{117}, and (d) $S_{33}BS_{14}$(*cl*)–LA_{214} in $CDCl_3$ (400 MHz).

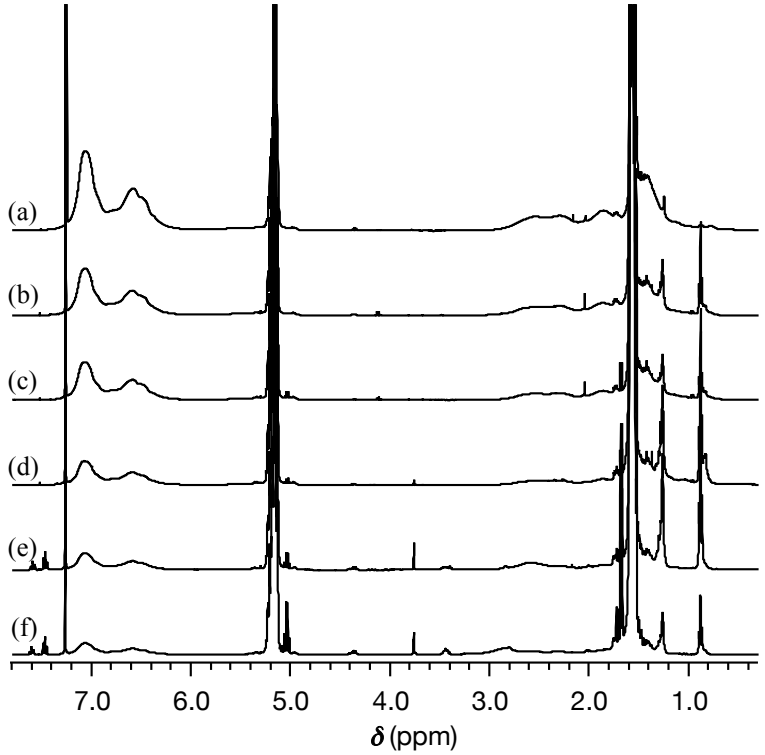

Figure S5.7. ^{1}H NMR spectra of (a) $S_{65}BS_{28}$–LA_{74}, (b) $S_{65}BS_{28}$(*cl*)–LA_{160}, (c) $S_{65}BS_{28}$(*cl*)–LA_{223}, (d) $S_{65}BS_{28}$(*cl*)–LA_{459}, (e) $S_{65}BS_{28}$(*cl*)–LA_{684}, and (f) $S_{65}BS_{28}$(*cl*)–LA_{923} in $CDCl_3$ (400 MHz).

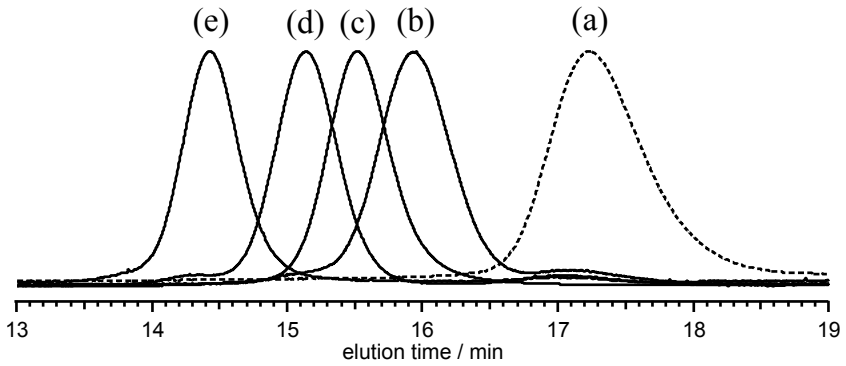

Figure S5.8. SEC traces of (a) $S_{21}BS_8(cl)$–OH macroinitiator, (b) $S_{21}BS_8$–LA_{20}, (c) $S_{21}BS_8(cl)$–LA_{45}, (d) $S_{21}BS_8(cl)$–LA_{75}, and (e) $S_{21}BS_8(cl)$–LA_{115} (eluent, THF; flow rate, 1.0 mL min^{-1}).

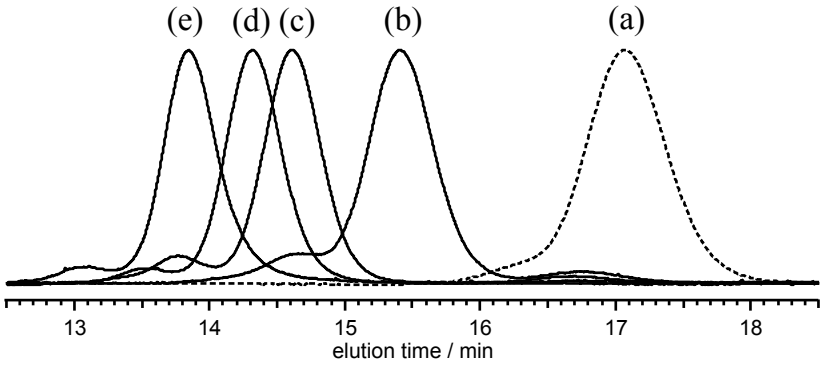

Figure S5.9. SEC traces of (a) $S_{33}BS_{14}(cl)$–OH macroinitiator, (b) $S_{33}BS_{14}$–LA_{33}, (c) $S_{33}BS_{14}(cl)$–LA_{72}, (d) $S_{33}BS_{14}(cl)$–LA_{117}, and (e) $S_{33}BS_{14}(cl)$–LA_{214} (eluent, THF; flow rate, 1.0 mL min^{-1}).

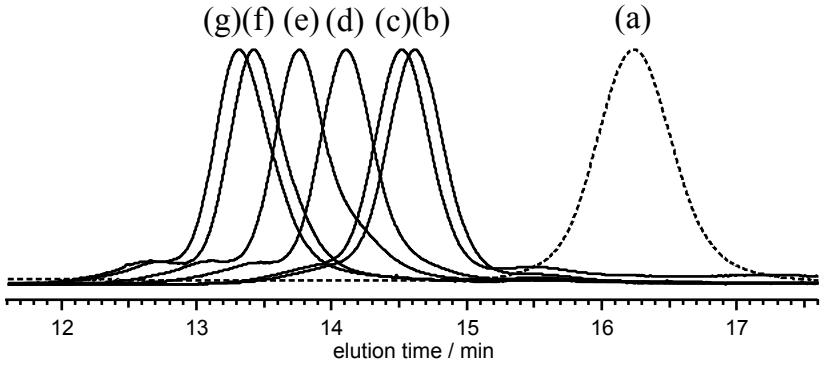

Figure S5.10. SEC traces of (a) $S_{65}BS_{28}(cl)$–OH macroinitiator, (b) $S_{65}BS_{28}$–LA_{74}, (c) $S_{65}BS_{28}(cl)$–LA_{160}, (d) $S_{65}BS_{28}(cl)$–LA_{223}, (e) $S_{65}BS_{28}(cl)$–LA_{459}, (f) $S_{65}BS_{28}(cl)$–LA_{684}, and (g) $S_{65}BS_{28}(cl)$–LA_{923} (eluent, THF; flow rate, 1.0 mL min^{-1}).

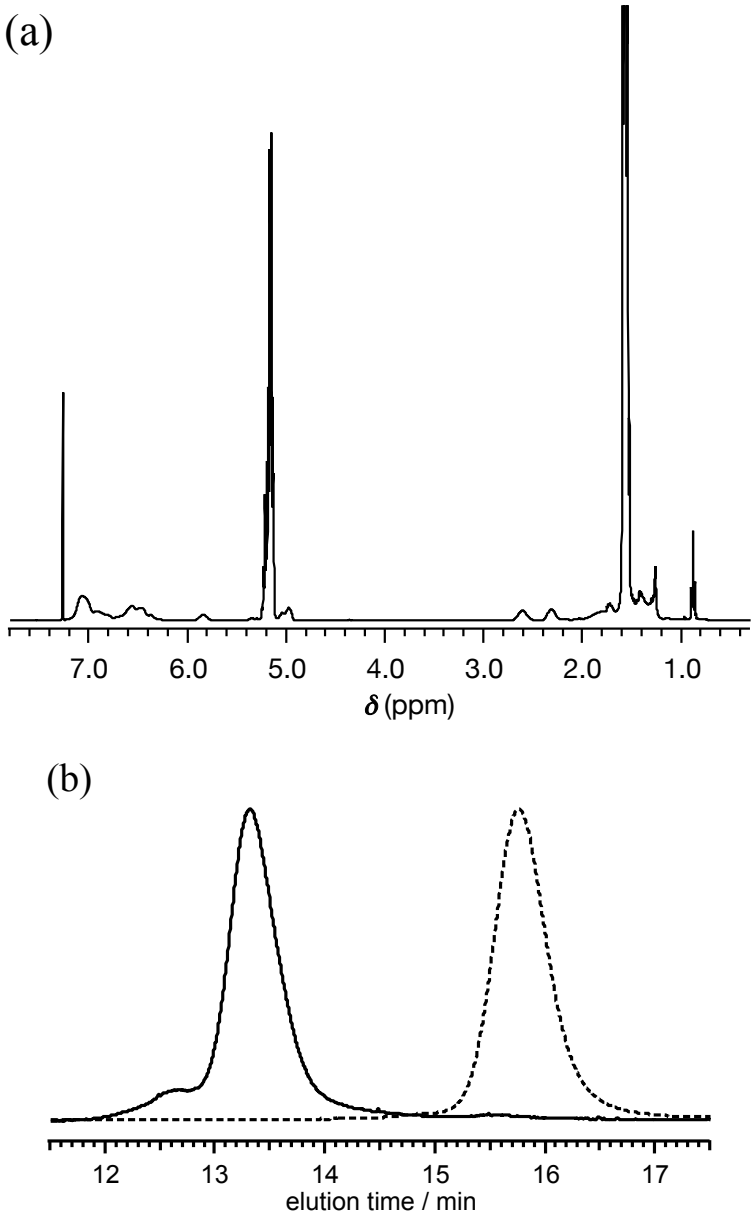

Figure S5.11. (a) ^{1}H NMR spectra of $S_{65}BS_{28}$−LA_{466} in $CDCl_3$ (400 MHz) and (b) SEC traces of $S_{65}BS_{28}$−OH macroinitiator (dashed line) and $S_{65}BS_{28}$−LA_{466} (solid line) (eluent, THF; flow rate, 1.0 mL min^{-1}).

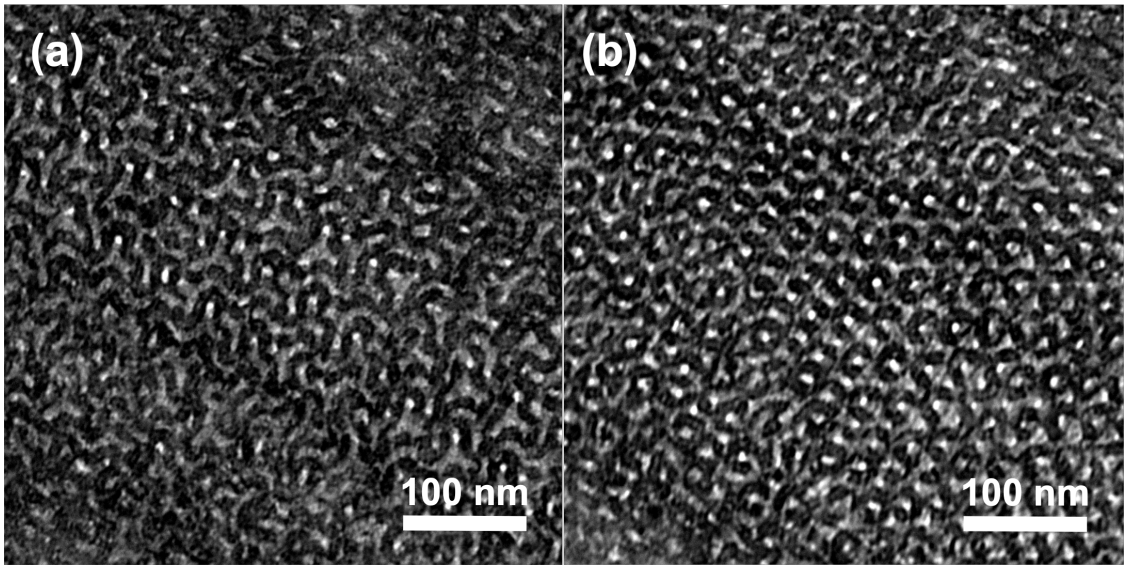

Figure S5.12. TEM images of the microtomed $S_{65}BS_{28}(cl)$–LA_{74} samples stained by RuO_4 vapor for 10 h. Images show the patterns of (a) (111) and (b) (110) planes of the DG morphology.

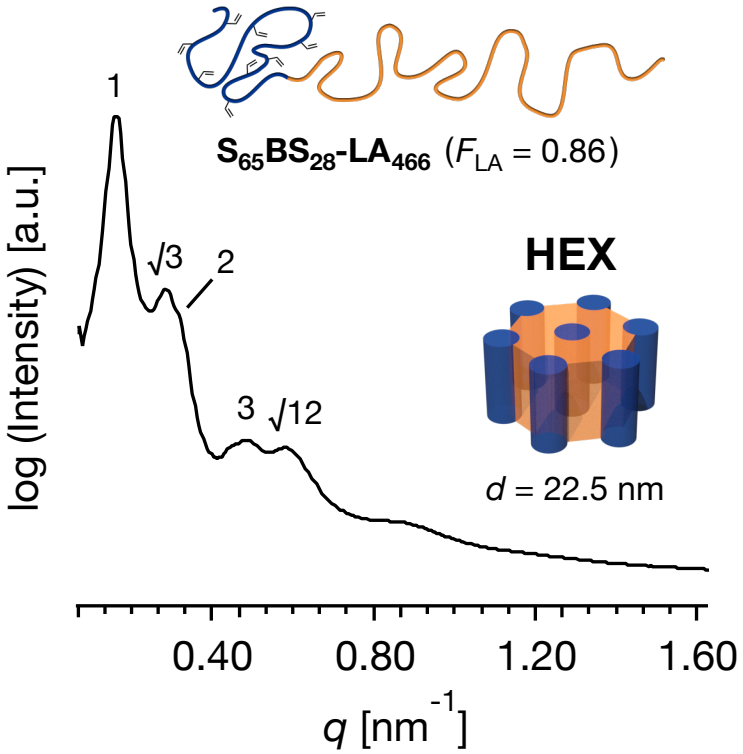

Figure S5.13. SAXS profile of $S_{65}BS_{28}$–LA_{466} with the schematic illustration of HEX morphology (SBS and LA domains are shown in blue and yellow, respectively)

Correlation Function Analysis

The width of one domain (l_a) as well as domain-spacing (d) in A-LAM structures were estimated by the correlation function analysis of the SAXS profiles of the samples using a following equation:

$$\Gamma(x) = \frac{1}{Q*}\int_0^\infty I(q)q^2 cos(qx)dq$$

wherein Q* stands for the scattering invariant. The l_as were assigned to the x value of intersection point of fitting and horizontal line drew from the first peak as seen in **Figure S5.18**. The width of the other domain (l_b) can be calculated according to $l_b = d - l_a$. Considering the facts that the width of SBS(cl) domain ($l_{SBS(cl)}$) should be smaller than that of LA one (l_{LA}) and l_b value is increased by increasing the molecular weight of PLA block, l_a and l_b must be $l_{SBS(cl)}$ and l_{LA}, respectively.

$$\Gamma(x) = \frac{\int_0^\infty I(q)q^2 cos(qx)dq}{\int_0^\infty I(q)q^2 dq}$$

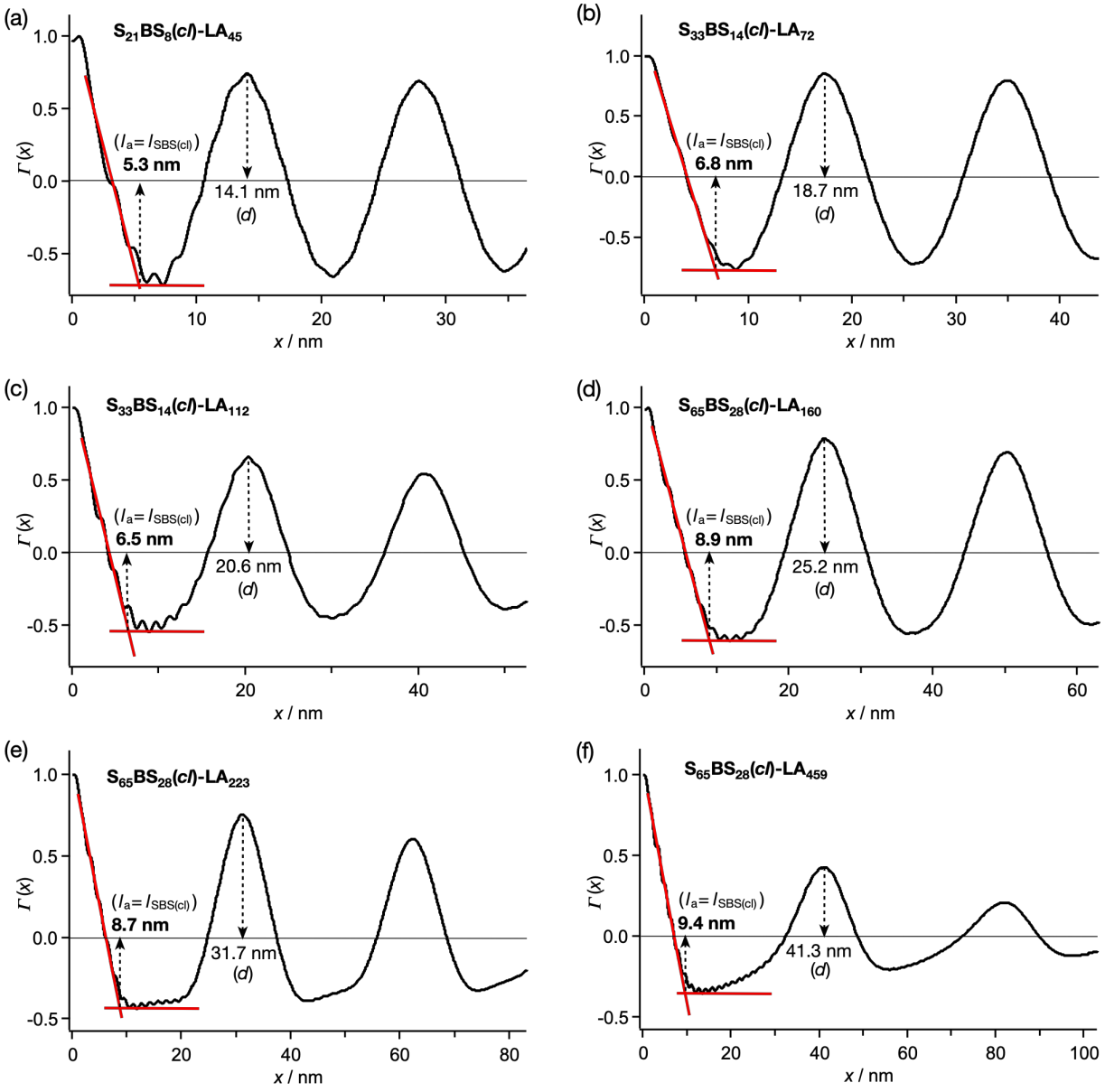

Figure S5.14. Correlation functions obtained by the Fourier transformation of the SAXS of (a) $S_{21}BS_8(cl)$–LA_{45}, (b) $S_{33}BS_{14}(cl)$–LA_{72}, (c) $S_{33}BS_{14}(cl)$–LA_{112}, (d) $S_{65}BS_{28}(cl)$–LA_{160}, (e) $S_{65}BS_{28}(cl)$–LA_{223}, and (f) $S_{65}BS_{28}(cl)$–LA_{459}.

Guinier Analysis of SANS Data

The radius of gyration (R_g) of the samples in the bulk was approximated by the Guinier analysis of the scattering data (**Figure S5.19**(a)) at the low q region according to the following equation (Guinier's low):

$$\ln I(q) = \ln I_0(q) - \frac{q^2 {R_g}^2}{3}$$

where $I_0(q)$ is the incident beam intensity. This approximation must satisfy the maximum qR_g of less than 1.33. Within this condition, the obtained scattering data can be plotted into a log$I(q)$ *vs.* q^2 curve (**Figure S5.19**(b)), wherein the resulting slope of the curve m is used to give the approximate R_g values by the following equation:

$$R_g = \sqrt{-3m}$$

There is the steep increase in the intensity at low q region in the SANS profile of $S_{65}BS_{28}(cl)$–OH due to the parasitic scattering coming from the air gaps in the bulk sample. Therefore, the Guinier analysis was performed by discarding the data at very low-q region.[1]

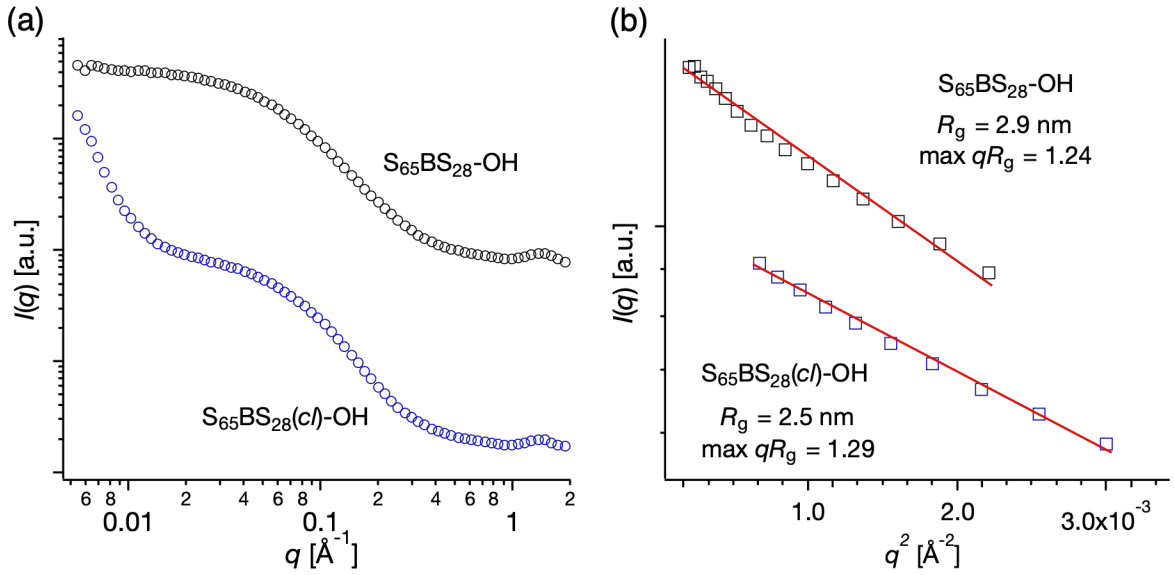

Figure S5.15. (a) SANS profiles and (b) Guinier plots of $S_{65}BS_{28}$–OH (black) and $S_{65}BS_{28}(cl)$–OH (blue). The $I(q)$ data were vertically shifted by multiplying arbitrary constants.

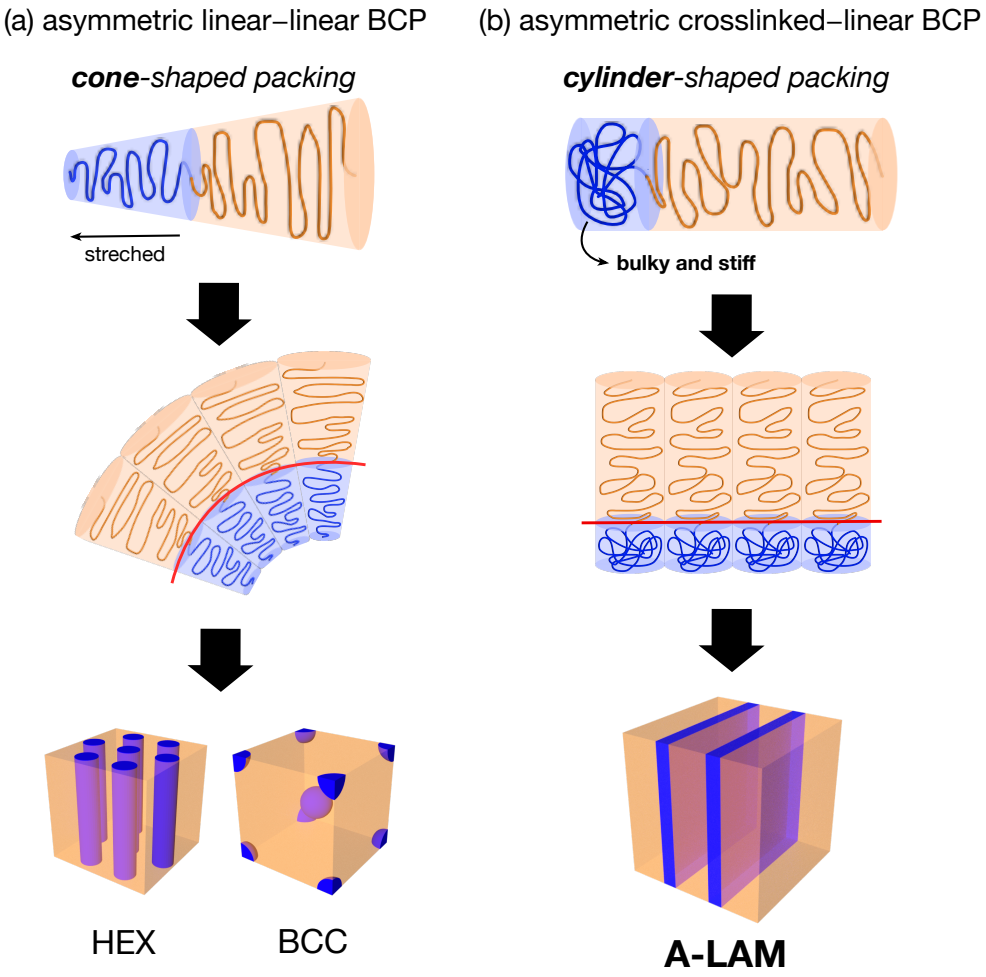

Figure S5.16. Schematic illustration of the packing models for the compositionally asymmetric (a) linear–linear and (b) crosslinked–linear BCPs.

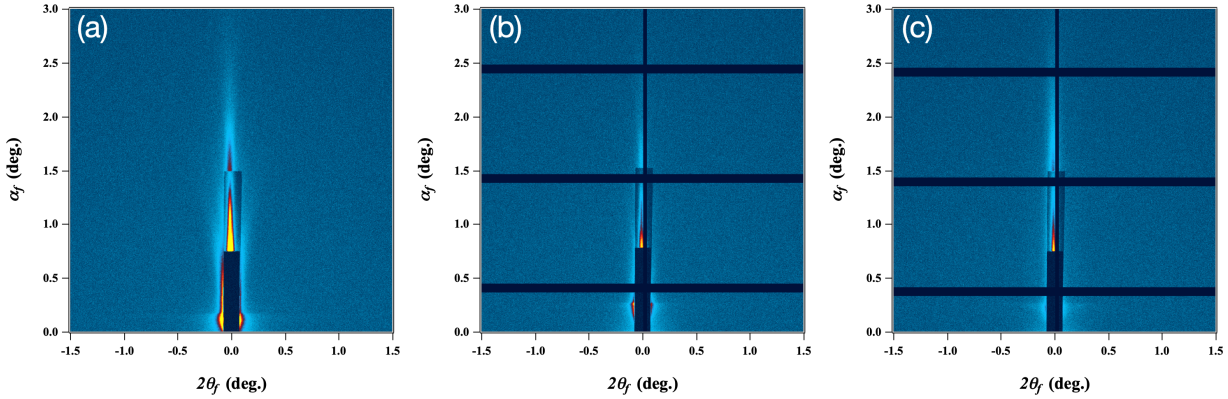

Figure S5.17. 2D GISAXS images of the thermally annealed (a) $S_{65}BS_{28}(cl)$–LA_{160}, (b) $S_{65}BS_{28}(cl)$–LA_{223}, and (c) $S_{65}BS_{28}(cl)$–LA_{459} thin films on a Si-substrate without any treatment.

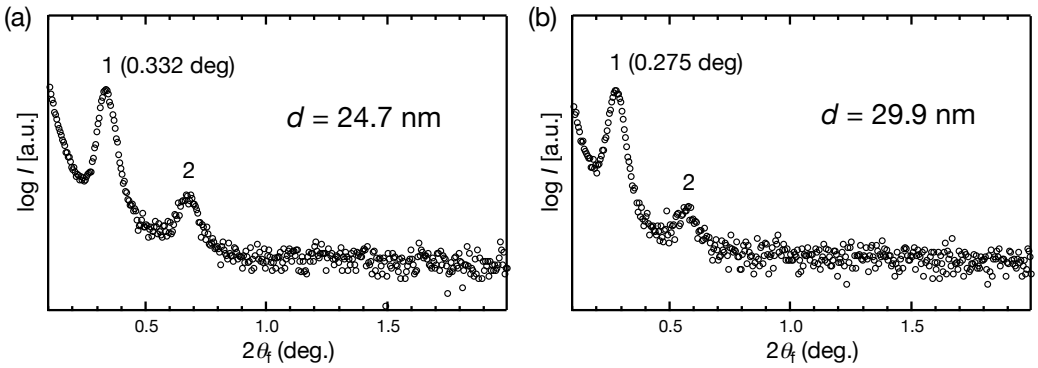

Figure S5.18. The in-plane scattering profiles extracted from the GISAXS images of (a) $S_{65}BS_{28}(cl)$–LA_{160} and (b) $S_{65}BS_{28}(cl)$–LA_{223} thin films along the $2\theta_f$ direction at α_f of 0.116° and 0.271°, respectively.

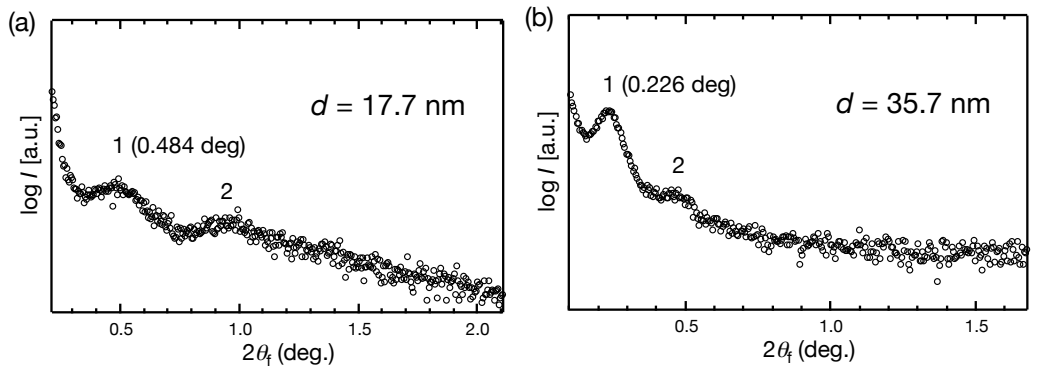

Figure S5.19. The (a) out-of-plane and (b) in-plane scattering profiles extracted from the GISAXS images of $S_{65}BS_{28}(cl)$–LA_{459} thin film along the α_f direction at $2\theta_f$ of -0.096° and $2\theta_f$ direction at α_f of 0.232°, respectively.

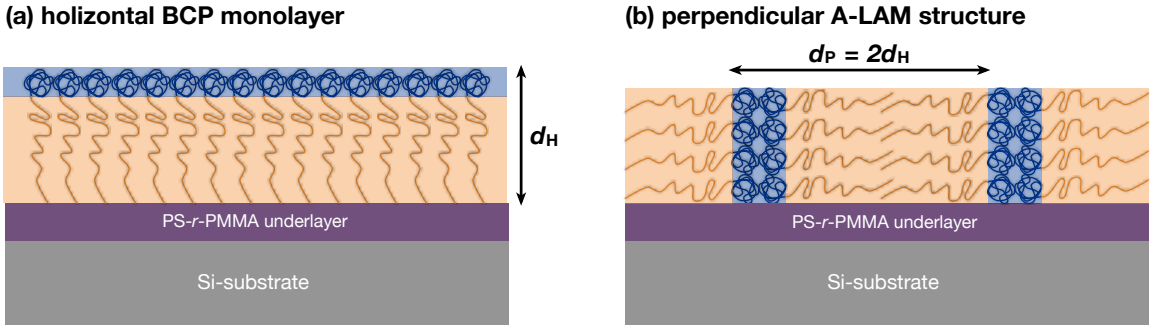

Figure S5.20. Schematic illustration of the (a) horizontally expanded BCP monolayer and (b) perpendicularly oriented LAM in $S_{65}BS_{28}(cl)$–LA_{459} thin film.

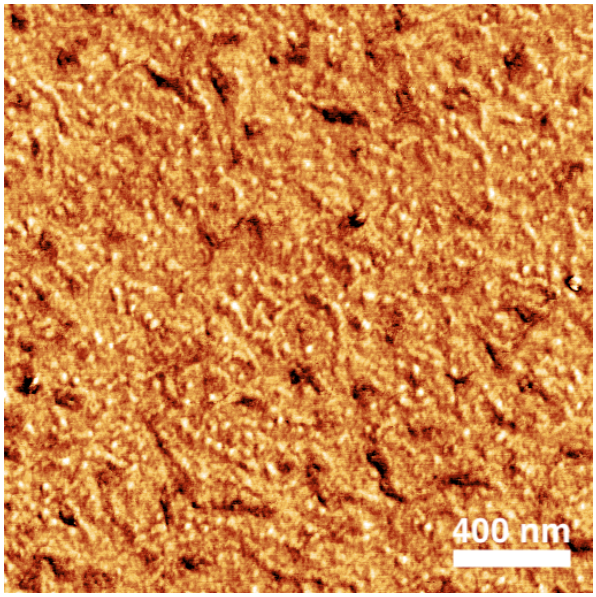

Figure S5.21. AFM phase image of $S_{65}BS_{28}(cl)$–LA_{459} thin film on the $PS_{0.2}$-*stat*-$PMMA_{0.8}$ brush underlayer. Scale bar is 400 nm.

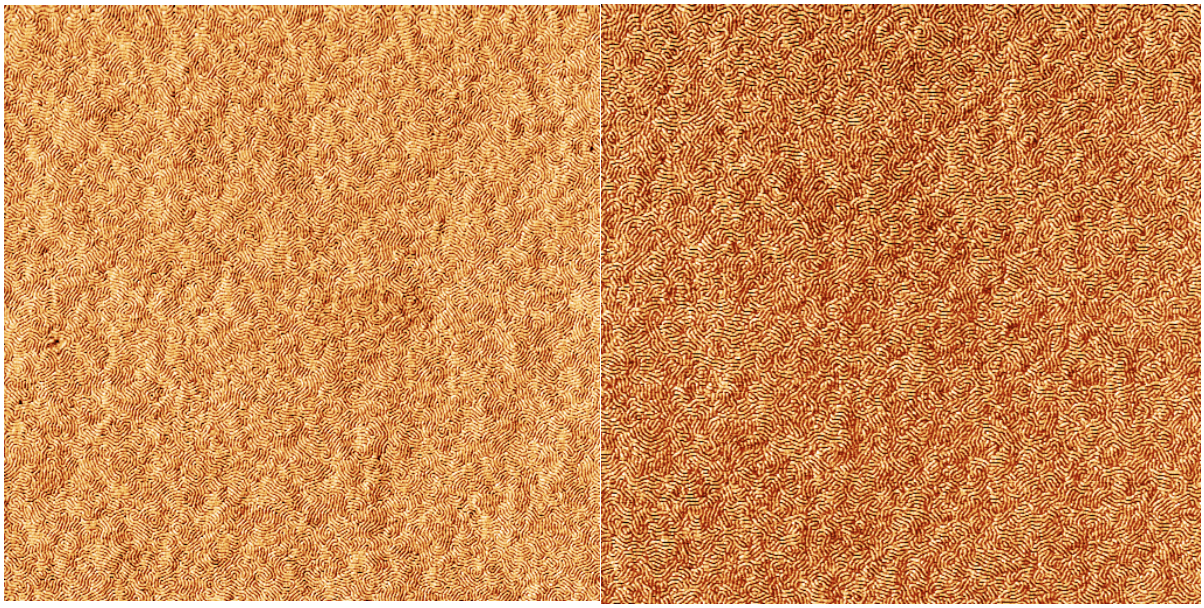

Figure S5.22. AFM phase images of (a) $S_{65}BS_{28}(cl)$–LA_{160} and (b) $S_{65}BS_{28}(cl)$–LA_{223} thin films on the $PS_{0.2}$-*stat*-$PMMA_{0.8}$ brush underlayer. The images are 5 μm square.

Reference

1. Anderson, K. S.; Hillmyer, M. A. Melt Chain Dimensions of Polylactide. *Macromolecules* **2004**, *37* (5), 1857–1862.

Chapter 6

Conclusions

In this dissertation, the author established the intramolecular crosslinking protocol using the Ru-catalyzed olefin metathesis reaction, which is applicable to a wide variety of olefin-containing polymers. In order to provide the novel approaches for downsizing of the microphase-separated structures and fabrication of the asymmetric lamellar (A-LAM) morphology, poly[styrene-*st*-(*p*-3-butenyl styrene)]-*b*-poly(*rac*-lactide)s (SBS–LAs) and SBS-*b*-poly(allylglycolide) (SBS–AG) were intramolecularly crosslinked to give the crosslinked–linear-type BCPs (SBS(*cl*)–LAs) and crosslinked–crosslinked-type BCP ((SBS–AG)$_{cl}$), respectively. Their self-assembling behaviors were intensively studied in both the bulk and the thin film states. A summary of the important achievements and findings in the present study is as follows:

Chapter 2. Intramolecular Olefin Metathesis for Synthesis of Single-Chain Nanoparticles in a Size-Controlled Manner

A series of single-chain nanoparticles (SCNPs) have been successfully synthesized via the Ru-catalyzed intramolecular olefin metathesis of a series of linear prepolymers possessing pendant olefin groups. The comprehensive investigation using poly[(*n*-butyl methacrylate)-*co*-(3-butenyl methacrylate)] (P(BMA-*co*-3BMA)s) as the model prepolymer system revealed that the size of the resultant SCNP can be precisely controlled by adjusting the following three factors: (1) the olefin contents of the prepolymer (crosslinking density), (2) molecular weight of the prepolymer, and (3) the poor solvent content in the reaction medium (which eventually affected the conformation of the linear prepolymer in the solution). In addition, the author found that the solvent quality affected not only the SCNP size, but also the morphology of the SCNPs; the resultant SCNPs appeared to form a globular morphology

with the increasing poor solvent content in the reaction medium. Moreover, the established intramolecular olefin metathesis was successfully applied to the poly(acrylate), poly(ester), and poly(styrene-*block*-methacrylate) precursors, demonstrating the versatility of this methodology.

Chapter 3. Downsizing of Microphase-Separated Structures via Intramolecular Crosslinking of Block Copolymers with One Olefin-Containing-Block

The crosslinked–linear BCPs (SBS(*cl*)–LAs) have been successfully synthesized from the linear–linear BCPs consisting of the crosslinkable SBS segment possessing pendant double bonds and the LA segment (SBS–LA) via intramolecular olefin metathesis under a highly diluted condition. Morphological analyses of the obtained BCPs in the bulk state by SAXS measurement clearly revealed that the SBS(*cl*)–LAs had lower *d* values in their lamellar (LAM) and hexagonally close-packed cylinder (HEX) morphologies as compared to the corresponding SBS–LAs due to the restricted chain dimensions of the SBS(*cl*) segments. Importantly, the degree of *d* decrease was controllable by varying the content of the crosslinking sites, in which the greatest decrease (22%) was achieved with the LAM morphology with ca. 50% of the crosslinkable BS unit incorporated into the SBS block. The author also demonstrated the downsizing of the HEX morphology in the thin film state by atomic force microscopy (AFM) observations, presenting the applicability of this approach to the BCP lithography technology. This is the first evaluation regarding the effect of the intramolecular crosslinking of the BCPs on their microphase separation behavior.

Chapter 4. Further Downsizing of Microphase-Separated Structures via One-Shot Intramolecular Crosslinking of Olefin-Containing Block Copolymer

The author has successfully demonstrated the one-shot intramolecular crosslinking of the linear BCP bearing crosslinkable olefins along the whole chain (SBS–AG) via olefin metathesis reaction, giving a Janus BCP particle (Janus (SBS–AG)$_{cl}$). The intensive solution studies clearly revealed not only the folded and compact conformation, but also the compartmentalized block localization of the Janus (SBS-*b*-AG)$_{cl}$. The generation of this unique product was presumably related to the higher reactivity of the spatially closer olefin pairs compared to the farther ones. Most significantly, the bulk microphase-separated structure of the Janus (SBS–AG)$_{cl}$ was found to be 47% smaller as compared to that of the linear SBS–AG prepolymer, representing the unprecedented degree of downsizing among the BCP architectural control approach. The presented "one-shot crosslinking" of the BCP, therefore, is a remarkably robust methodology to downsize the microphase-separated structures.

Chapter 5. Fablication of Asymmetric Lamellar Structures by Intramolecularly Crosslinked Block Copolymers with Highly-Asymmetric Composition

The author has designed the compositionally asymmetric crosslinked–linear type SBS(*cl*)–LAs with a long PLA block (F_{LA} ~ 0.92) and successfully elucidated their unusual microphase-separation behavior. According to the experimentally-constructed phase diagram, the LAM window of the SBS(*cl*)–LA was expanded to the higher F_{LA} regime, resulting in the A-LAM morphologies with an asymmetric ratio up to 3.39. This unusual phase behavior arguably arose from the bulky and stiff conformation of the SBS(*cl*) block. Since the space width should be controllable while maintaining the line width unchanged in the L/S design for

logic devices, the fact that the A-LAM morphologies were successfully obtained with the constant and varied widths of thinner and thicker domains, respectively, is quite significant for lithographic applications. Most importantly, the intensive thin film studies by grazing incidence SAXS and AFM demonstrated the capability of the SBS(*cl*)–LAs to produce the perpendicularly oriented A-LAM morphology with the use of the neutral underlayer, revealing the potential as the lithographic mask for the asymmetric L/S fabrication.

In conclusion, the author has established the intramolecular crosslinking system as a novel and robust methodology to downsize the feature and fabricate the A-LAM morphology in the microphase separation of the BCPs. Considering the excellent functional group tolerance and sufficient reactivity of the Ru-catalyzed olefin metathesis, the presented intramolecular olefin metathesis approach is expandable to a wide variety of BCPs bearing the olefin functionality. The author, therefore, believes that the presented intramolecular crosslinking system offers better guidance to control the microphase-separated structures, thus opening a novel vista and platform into the BCP lithography field.